Statistical and Dynamical Aspects in the Study of Compound Nucleus and Nuclear Fission

By

YOGESH KUMAR GUPTA

Enrollement No: PHYS01200804002

Bhabha Atomic Research Centre, Mumbai

A thesis submitted to the

Board of Studies in Physical Sciences

In partial fulfillment of requirements

For the Degree of

DOCTOR OF PHILOSOPHY

of

HOMI BHABHA NATIONAL INSTITUTE

September, 2012

Homi Bhabha National Institute

Recommendations of the Viva Voce Board

As members of the Viva Voce Board, we certify that we have read the dissertation prepared by Yogesh Kumar Gupta entitled "Statistical and Dynamical Aspects in the Study of Compound Nucleus and Nuclear Fission" and recommend that it may be accepted as fulfilling the dissertation requirement for the Degree of Doctor of Philosophy.

Chairman: Dr. A. Chatterjee   Date: 12/3/2013

Guide/Convener: Dr. D. C. Biswas   Date: 12/3/2013

Member 1: Dr. R. K. Choudhury   Date: 12-3-2013

Member 2: Dr. B. V. John   Date: 12/3/2013

Member 3: Prof. I. Mazumdar   Date:

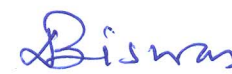External Examiner: Prof. Umesh Garg   Date: 12.03.2013

Final approval and acceptance of this dissertation is contingent upon the candidate's submission of the final copies of the dissertation to HBNI.

I hereby certify that I have read this dissertation prepared under my direction and recommend that it may be accepted as fulfilling the dissertation requirement.

Date: 12/3/2013

Place: BARC

(Dr. D. C. Biswas)
Guide

STATEMENT BY AUTHOR

This dissertation has been submitted in partial fulfillment of requirements for an advanced degree at Homi Bhabha National Institute (HBNI) and is deposited in the Library to be made available to borrowers under rules of the HBNI.

Brief quotations from this dissertation are allowable without special permission, provided that accurate acknowledgement of source is made. Requests for permission for extended quotation from or reproduction of this manuscript in whole or in part may be granted by the Competent Authority of HBNI when in his or her judgment the proposed use of the material is in the interests of scholarship. In all other instances, however, permission must be obtained from the author.

12/3/13

Yogesh Kumar Gupta

DECLARATION

I, hereby declare that the investigation presented in the thesis has been carried out by me. The work is original and has not been submitted earlier as a whole or in part for a degree/diploma at this or any other Institution/University.

Yogesh Kumar Gupta

12/3/13

Dedicated to my parents

ACKNOWLEDGMENTS

List of Publications in Referred Journals:

1. "Enhanced α-particle emission in ^{12}C + ^{232}Th fission due to transfer-breakup process", **Y. K. Gupta**, D. C. Biswas, B. V. John, B. K. Nayak, A. Chatterjee, and R. K. Choudhury, Phys. Rev. **C 86**, 014615(2012).

2. "Systematics of pre- and near-scission α-particle multiplicities in heavy-ion induced fusion-fission reactions", **Y. K. Gupta**, D. C. Biswas, R. K. Choudhury, A. Saxena, B. K. Nayak, Bency John, K. Ramachandran, R. G. Thomas, L. S. Danu, B. N. Joshi, K. Mahata, S. K. Pandit, and A. Chatterjee, Phys. Rev. **C 84**, 031603(R)(2011).

3. "Pulse height and timing characteristics of CsI(Tl)-Si(PIN) detector for γ-rays and fission fragments", **Y. K. Gupta**, D. C. Biswas, P. Roy, B. K. Nayak, R. G. Thomas, A. L. Inkar, R. P. Vind, B. John, A. Saxena, and R. K. Choudhury, Nucl. Instr. Meth. **A 629**, 149(2011).

4. "Nuclear level-density parameter of nuclei in Z$\sim$70 and A$\sim$180 mid-shell regions", **Y. K. Gupta**, D. C. Biswas, Bency John, B. K. Nayak, A. Saxena, and R. K. Choudhury, Phys. Rev. **C 80**, 054611(2009).

5. "Angular momentum dependence of nuclear level-density parameter around Z$\sim$50", **Y. K. Gupta**, Bency John, D. C. Biswas, B. K. Nayak, A. Saxena, and R. K. Choudhury, Phys. Rev. **C 78**, 054609(2008).

6. "Collisions of Rare Earth Nuclei - a New Reaction Route for Synthesis of Super Heavy Nuclei", R. K. Choudhury, and **Y. K. Gupta** arXiv:1211.4380 [nucl-th].

7. "Projectile structure effects in multi-nucleon and cluster transfers in ^{16,18}O+^{164}Dy, ^{208}Pb reactions", D. C. Biswas, Pratap Roy, **Y. K. Gupta**, B. N. Joshi, B. K. Nayak, L. S. Danu, B. V. John, R. P. Vind, N. N. Deshmukh, S. Mukherjee, A. K. Jain, and R. K. Choudhury, J. Phys. Conf. Ser., **381**, 012091(2012).

8. "Heavy cluster knockout reaction $^{16}O(^{12}C, 2\,^{12}C))^4He$ and the nature of the ^{12}C - ^{12}C interaction potential", B. N. Joshi, A. K. Jain, **Y. K. Gupta**, D. C. Biswas, A. Saxena, B. V. John, L. S. Danu, R. P. Vind, ans R. K. Choudhury, Phys. Rev. Lett. **106**, 022501(2011).

9. "Systematic study of projectile-structure effect on the fusion-barrier distribution", Pratap Roy, A. Saxena, B. K. Nayak, E. T. Mirgule, B. John, **Y. K. Gupta**, L. S. Danu, R. P. Vind, Ashok Kumar, and R. K. Choudhury, Phys. Rev. **C 84**, 011602 (R)(2011).

10. "Fission fragment angular distributions in the ^9Be + ^{232}Th reaction", S. Appannababu, R. G. Thomas, L. S. Danu, P. K. Rath, **Y. K. Gupta**, B. V. John, B. K. Nayak, D. C. Biswas, A. Saxena, S. Mukherjee, and R. K. Choudhury, Phys. Rev. **C 83**, 067601 (2011).

11. "Breakup threshold anomaly in the near-barrier elastic scattering of $^6Li + {}^{116,112}Sn$", N. N. Deshmukh, S. Mukherjee, D. Patel, N. L. Singh, P. K. Rath, B. K. Nayak, D. C. Biswas, S. Santra, E. T. Mirgule, L. S. Danu, **Y. K. Gupta**, A. Saxena, R. K. Choudhury, R. Kumar, J. Lubian, C. C. Lopes, E. N. Cardozo, and P. R. S. Gomes, Phys. Rev. **C 83**, 024607 (2011).

12. "Charged particle identification by pulse shape discrimination with single-sided segmented silicon-pad detectors", Bency John, A. Topkar, R. P. Vind, A. L. Inkar, D. C. Biswas, A. Saxena, **Y. K. Gupta**, and S. Kailas, Nucl. Instr. Meth. **A609**, 24 (2009).

13. "Evidences for Coulomb effects on fusion barrier distribution for deformed projectile nuclei", B. K. Nayak, R. K. Choudhury, A. Saxena, P. K. Sahu, R. G. Thomas, D. C. Biswas, B. V. John, E. T. Mirgule, **Y. K. Gupta**, M. Bhike and H. G. Rajprakash, Phys. Rev. **C 75**, 054615 (2007).

List of Publications in National and International Symposia/Workshops:

1. "New insight to the fission dynamics using α-particle emission as a probe", **Y. K. Gupta**, An invited talk in DAE-BRNS Symposium on Nucl. Phys. **Vol. 56** (2011)43 - 51.

2. "Observation of ^{8}Be breakup in α-particle multiplicities for ^{12}C + ^{232}Th system", **Y. K. Gupta**, D. C. Biswas, B. K. Nayak, B. V. John, R. K.Choudhury, and A. Chatterjee, DAE-BRNS Symposium on Nucl. Phys. **Vol. 56** (2011)590 - 591.

3. "Measurement of fission fragment anisotropies and excitation functions in ^{6,7}Li + ^{232}Th reactions ", G. Prajapati, **Y. K. Gupta**, D. C. Biswas, R. P. Vind, A.L.Inkar, B. K. Nayak, L. S. Danu, P. Roy, B. N. Joshi, and B. V. John, DAE-BRNS Symposium on Nucl. Phys. **Vol. 56** (2011)494 -495.

4. "Contribution of α - ^{12}C resonance in ^{16}O(^{12}C, 2 ^{12}C))^{4}He reaction at 118.8 MeV", B. N. Joshi, A. K. Jain, **Y. K. Gupta**, D. C. Biswas, A. Saxena, B. V. John, ans R. K. Choudhury, DAE-BRNS Symposium on Nucl. Phys. **Vol. 56** (2011)584 -585.

5. "Study of fusion barrier distributions from quasi-elastic scattering in ^{6,7}Li + ^{209}Bi systems", D. Patel, B. K. Nayak, S. Mukherjee, D. C. Biswas, E. T. Mirgule, B. V. John, **Y. K. Gupta**, S. Mukhopadhyay, G. Prajapati, L. S. Danu, P. K. Rath, V. Desai, N. N. Deshmukh, and A. Saxena, DAE-BRNS Symposium on Nucl. Phys. **Vol. 56** (2011)624 -625.

6. "A two-dimensional cathode strip gas detector for fission fragments ", R. P. Vind, D. C. Biswas, A. Inkar, R. V. Jangale, **Y. K. Gupta**, and R. K. Choudhury, DAE-BRNS Symposium on Nucl. Phys. **Vol. 56** (2011)1126 - 1127.

7. "Pulse height and timing characteristics of CsI(Tl)Si(PIN) detector for fission fragments", **Y. K. Gupta**, D. C. Biswas, Pratap Roy, B. K. Nayak, A. L. Inkar,

R. P. Vind, B. John, and R. K. Choudhury, DAE-BRNS Symposium on Nucl. Phys. **Vol. 55** (2010)712-713.

8. "Comparative study of elastic scattering in ^{16,18}O + ^{209}Bi reactions", Pratap Roy, D. C. Biswas, B. K. Nayak, L. S. Danu, B. N. Joshi, B. John, R. P. Vind, **Y. K. Gupta**, N. N. Desmukh, S. Mukherjee, and R. K. Choudhury, DAE-BRNS Symposium on Nucl. Phys. **Vol. 55** (2010)286-287.

9. "Elastic scattering of ^{6}Li + ^{112}Sn system near barrier energies", N. N. Deshmukh, S. Mukherjee, B. K. Nayak, D. C.Biswas, E. T. Mirgule, S. Santra, D. Patel, L. S. Danu, **Y. K. Gupta**, A. Saxena, R. K. Choudhury, R. Kumar, S. Appannababu, N. L. Singh, R. Kumar, J. Lubian, and P. R. S. Gomes, DAE-BRNS Symposium on Nucl. Phys. **Vol. 55** (2010)290-291.

10. "Systematic study of effect of target and projectile structure on fusion barrier distribution", Pratap Roy, A. Saxena, B. K. Nayak, E. T. Mirgule, B. John, **Y. K. Gupta**, L. S. Danu, R. P. Vind, and R. K. Choudhury, DAE-BRNS Symposium on Nucl. Phys. **Vol. 55** (2010) 240-241.

11. "Fission time scale of ^{16}O + ^{209}Bi (E$_x$ = 55 MeV) reaction from α-particle multiplicity", **Y. K. Gupta**, D. C. Biswas, R. G. Thomas, L. S. Danu, P. Roy, B. N. Joshi, B. K. Nayak, K. Ramachandran, Bency John, A. Saxena, R. K. Choudhury, V. Nanal, and R. G. Pillay, International Nuclear Physics Conference, Vancouver, July 4-9, 2010.

12. "Energy and time response of CsI(Tl)-PIN detector for γ-rays and fission fragments", **Y. K. Gupta**, D. C. Biswas, P. Roy, R. G. Thomas, B. K. Nayak, R. P. Vind, A. Inkar, Bency John, A. Saxena, and R. K. Choudhury, DAE- BRNS symposium on nuclear instrumentation, NSNI, **109** (2010).

13. "Development of charged particle detector array", Bency John, A. Topkar, S. Venketramanan, Manish Kumar, S. Sunil Kumar, A. L. Inkar, A. Saxena, R. P.

Vind, **Y. K. Gupta**, D. C. Biswas, B. K. Nayak, R. G. Thomas, L. S. Danu, R. K. Choudhury and S. Kailas, National symposium on nuclear instrumentation, NSNI, **323** (2010).

14. "Characteristics of CsI(Tl) crystal coupled with PIN photodiode for gamma rays and charged particles", **Y. K. Gupta**, D. C. Biswas, B. K. Nayak, A. Inkar, R. P. Vind, R. G. Thomas, Bency John, A. Saxena, L. S. Danu, and R. K. Choudhury, DAE-BRNS International Symposium on Nucl. Phys. **Vol. 54** (2009)654-655.

15. "α-particle emission in ^{11}B, ^{12}C + ^{232}Th fission reactions", **Y. K. Gupta**, D. C. Biswas, R. G. Thomas, B. K. Nayak, K. Ramachandran, B. V. John, A.Saxena, L. S. Danu, K. Mahata, B. N. Joshi, S. K. Pandit, A. Chatterjee, and R. K. Choudhury, DAE-BRNS International Symposium on Nucl. Phys. **Vol. 54** (2009)342-343.

16. "The ^{16}O(C, 2C))^{4}He reaction and the nature of the short range C-C interaction", B. N. Joshi, A. K. Jain, **Y. K. Gupta**, D. C. Biswas, A. Saxena, B. V. John, L. S. Danu, R. P. Vind, and R. K. Choudhury, DAE-BRNS International Symposium on Nucl. Phys. **Vol. 54** (2009)260-261.

17. "Finite range analysis of the 119 MeV ^{16}O(C, 2C))^{4}He reaction and the C-C elastic scattering", A. K. Jain, B. N. Joshi, **Y. K. Gupta**, D. C. Biswas, A. Saxena, B. V. John, L. S. Danu, R. P. Vind, and R. K. Choudhury, DAE-BRNS International Symposium on Nucl. Phys. **Vol. 54** (2009)262-263.

18. "Study of fission fragment angular distributions for ^{9}Be + ^{232}Th", S. Appannababu, R. G. Thomas, B. V. John, A. Saxena, D. C. Biswas, B. K. Nayak, **Y. K. Gupta**, L. S. Danu, P. K. Rath, and R. K. Choudhury, DAE-BRNS International Symposium on Nucl. Phys. **Vol. 54** (2009) 340-341.

19. "Determination of the ^{234}Pa (n, f) reaction crossection by hybrid surrogate ratio method", B. K. Nayak, L. S. Danu, **Y. K. Gupta**, R. G. Thomas, A. Saxena,

D. C. Biswas, E. T. Mirgule, S. Santra, R. P. Vind, and R. K. Choudhury, DAE-BRNS International Symposium on Nucl. Phys. **Vol. 54** (2009)358-359.

20. "A search for sensitivity of nuclear level-density parameter with angular momentum in ^{12}C + ^{181}Ta reaction", **Y. K. Gupta**, Bency John, D. C. Biswas, A. Saxena, B. K. Nayak, R. P. Vind, and R. K. Choudhury, DAE-BRNS Symposium on nuclear physics, **Vol. 53** (2008)511-512.

21. "Near Scission emission of alpha particles in ^{11}B + ^{232}Th reaction", **Y. K. Gupta**, A. Saxena, K. Ramachandran, R. G. Thomas, D. C. Biswas, Bency John, B. K. Nayak, L. S. Danu, R. P. Vind, A. Chatterjee, and R. K. Choudhury, DAE-BRNS Symposium on nuclear physics, **Vol. 53** (2008)397-398.

22. "Elastic scattering studies in ^{16}O, ^{18}O + ^{164}Dy reactions at above barrier energies", B. N. Joshi, D. C. Biswas, **Y. K. Gupta**, B. K. Nayak, B. V. John, A. Saxena, R. P. Vind, A. K. Jain, and R. K. Choudhury, DAE-BRNS Symposium on nuclear physics, **Vol. 53** (2008)413-414.

23. "Study of clustering in ^{16}O through ^{12}C knockout using 119 MeV ^{12}C-beam", B. N. Joshi, A. K. Jain, **Y. K. Gupta**, D. C. Biswas, A. Saxena, B. V. John, R. G. Thomas, L. S. Danu, R. P. Vind, B. srinivasan, R. K. Choudhury, V. Nanal, and R. G. Pillay, DAE-BRNS Symposium on nuclear physics, **Vol. 53** (2008)377-378.

24. "Effect of N=40 shell closure on fusion barrier distribution in ^{18}O + ^{58,62}Ni reactions", L. S. Danu, B. K. Nayak, A. Saxena, D. C. Biswas, E. T. Mirgule, B. V. John, B. V. John, R. G. Thomas, **Y. K. Gupta**, and R. K. Choudhury, DAE-BRNS Symposium on nuclear physics, **Vol. 53** (2008)363-364.

25. "Effect of N=40 shell closure on barrier distribution in ^{18}O + ^{58,62}Ni reactions", L. S. danu, B. K. Nayak, A. Saxena, D. C. Biswas, B. V. John, R. G. Thomas, **Y. K. Gupta**, and R. K. Choudhury, AIP conference proceedings, **1098** (2008)270.

26. "Evidence for Coulomb reorientation effects of deformed projectile on fusion barrier distribution", B. K. Nayak, R. K. Choudhury, A. Saxena, P. K. Sahu, R. G. Thomas, D. C. Biswas, B. V. John, E. T. Mirgule, **Y. K. Gupta**, M. Bhike, and H. G. Rajprakash, International nuclear physics conference (INPC, Tokyo Japan), June 3-8, 2007.

27. "Sensitivity of nuclear level density parameter with angular momentum in midshell mass region", **Y. K. Gupta**, Bency John, D. C. Biswas, A. Saxena, B. K. Nayak, R. P. Vind, and R. K. Choudhury, DAE-BRNS Symposium on nuclear physics, **Vol. 52** (2007)383-384.

28. "Multinucleon and cluster transfer in ^{16,18}O + ^{164}Dy, ^{208}Pb reactions", D. C. Biswas, **Y. K. Gupta**, B. K. Nayak, B. V. John, A. Saxena, R. P. Vind, A. Inkar, B. N. Joshi, R. K. Jain, and R.K.Choudhury, DAE-BRNS Symposium on nuclear physics, **Vol. 52** (2007)425-426.

29. "Determination of the ^{233}Pa(n, f) reaction cross-section from 10.5 to 16.5 MeV neutron energy by surrogate ratio method", B. K. Nayak, A. Saxena, D. C. Biswas, E. T. Mirgule, B. V. John, S. Santra, R. P. Vind, **Y. K. Gupta**, R. K. Choudhury *et. al.*, DAE-BRNS Symposium on nuclear physics, **Vol. 52** (2007)303-304.

30. "Angular momentum dependence of Nuclear level density parameter in mass regions of $A \sim$120 and $A \sim$180", **Y. K. Gupta**, Bency John, D. C. Biswas, A. Saxena, B. K. Nayak, P. K. Sahu, R. G. Thomas, and R. K. Choudhury, International nuclear physics conference (INPC, Tokyo Japan), June 3-8, (2007)425-426.

31. "Nuclear level density investigation in mass region around $A \sim$120", **Y. K. Gupta**, Bency John, D. C. Biswas, A. Saxena, B. K. Nayak, P. K. Sahu, R. G. Thomas, and R. K. Choudhury, DAE-BRNS Symposium on nuclear physics, **Vol. 51** (2006)377-378.

32. "Hybrid detector telescope for fission fragments and heavy-ions", D. C. Biswas, **Y. K. Gupta**, B. V. John, A. N. Raghav, A. Inkar, B. K. Nayak, A. Saxena, A. Topkar, and R. K. Choudhury, DAE-BRNS Symposium on nuclear physics, **Vol. 51** (2006)584-585.

33. "Pulse shape discriminator for charged particles in segmented silicon detectors", Bency John, D. C. Biswas, A. Saxena, B. K. Nayak, P. K. Sahu, A. L. Inkar, **Y. K. Gupta**, R. P. Vind, A. Topkar, and R.K.Choudhury, DAE-BRNS Symposium on nuclear physics, **Vol. 51** (2006)594-595.

34. "Coulomb reorientation effect of deformed projectile on fusion barrier distribution", B. K. Nayak, A. Saxena, D. C. Biswas, E. T. Mirgule, B. V. John, **Y. K. Gupta**, M. Bhike, R. K. Choudhury, and H. G. Rajprakash, DAE-BRNS Symposium on nuclear physics, **Vol. 51** (2006)353-354.

35. "Gamma multiplicity gated alpha evaporation spectra in ^{16}O + ^{164}Dy reaction", **Y. K. Gupta**, Bency John, D. C. Biswas, A. Saxena, B. K. Nayak, P. K. Sahu, R. G. Thomas, and R. P. Vind, DAE-BRNS Symposium on nuclear physics, **Vol. 50** (2005)314.

36. "Luminescence characteristics of PVT based thin film scintillation detectors", Bency John, D. C. Biswas, A. K. Pandey, Suparna Sodaye, **Y. K. Gupta**, DAE-BRNS Symposium on nuclear physics, **Vol. 50** (2005)443.

37. "Effect of projectile structure on fusion barrier distribution in ^{16}O + ^{115}In and ^{28}Si + ^{115}In reactions derived from quasi elastic scattering", B. K. Nayak, A. Saxena, P. K. Sahu, R. G. Thomas, B. V. John, **Y. K. Gupta**, D. C. Biswas, E. T. Mirgule, R. P. Vind, and H. G. Rajprakash, DAE-BRNS Symposium on nuclear physics, **Vol. 50** (2005)312.

Other Publications

1. "Understanding of ternary fission in heavy-ion induced reactions", **Y. K. Gupta**, R. K. Choudhury, and A. Chatterjee, BARC News Letter, ISSUE NO. **324**, Jan.-Feb., 6 (2012).

2. "Systematics of pre- and near-scission α-particle multiplicities in heavy-ion fusion-fission", **Y. K. Gupta**, 29$^{\text{th}}$ IPS colloquium for young physicists (YPC - 2011).

Contents

SYNOPSIS OF THE THESIS TO BE SUBMITTED TO THE HOMI BHABHA NATIONAL INSTITUTE FOR THE DEGREE OF DOCTOR OF PHILOSOPHY IN PHYSICS

Name of the candidate	: Yogesh Kumar Gupta
Name of the guide	: Dr. D. C. Biswas Nuclear Physics Division, Bhabha Atomic Research Centre, Mumbai, 400 085
Registration number	: PHYS01200804002
Date of registration	: 1/09/2008
Title of the thesis	: Statistical and Dynamical Aspects in the Study of Compound Nucleus and Nuclear Fission
Place of research	: Nuclear Physics Division, Bhabha Atomic Research Centre, Mumbai, 400 085

(Candidate)   **(Research Guide)**

Synopsis

The domain of nuclear physics encompasses the whole range of questions starting from the microscopic behaviour of many body quantum systems to the macroscopic behaviour of the stars. While doing so one deals with the study of excitation and decay of nuclei in the two dimensional space of excitation energy (E_X) and angular momentum (J). With heavy-ion collisions it is now possible to study the excited nuclei of a variety of choices in a wide range of E_X and J by varying the Z and A of the projectile and target nuclei. In a heavy-ion collision different types of reactions take place such as elastic, inelastic, and transfer of nucleons for larger impact parameters to deep inelastic and fusion for the smaller impact parameters. The fusion reaction leads to compound nucleus formation where complete amalgamation of projectile and target takes place. Depending on the projectile bombarding energy, the compound nucleus (CN) has a certain amount of initial excitation energy and a broad J distribution. The CN decays to the ground state by sequential emission of several particles and γ rays, which are governed by the statistical properties of nuclei in the decay process. In case of heavier CN, where fission decay competes with particle emission, the dynamical effects play an important role along with the statistical ones in understanding the gross properties of the decay process. The first part of the present thesis deals with the statistical aspects in the decay of medium heavy compound nuclei, in particular the spin dependence of the nuclear level-density. In the second part of the thesis, the dynamical aspects involved in the nuclear fission decay are addressed.

The nuclear level-density (NLD) is one of the basic statistical parameters which plays crucial role in determining the decay channels of the excited nucleus. Practical applications of the NLD are quite widespread in various phenomena such as nuclear fission, decay of excited nuclei by particle evaporation, production of elements in stellar processes, etc. From the theoretical point of view, the NLD contains important information not only on the statistical aspects, but also the microscopic features of

an excited nucleus. It is a key ingredient in the calculation of reaction cross sections using the framework of Hauser-Feshbach (HF) theory of compound nuclear reactions [1, 2]. Applications of HF theory require global knowledge of nuclear level densities as a function of E_X and J. This is best served by using a phenomenological level-density function, known in the literature as back-shifted Fermi-gas (BSFG) formula [3, 4]. The phenomenological descriptions mainly ignore the residual interactions of nucleons except for pairing which is partly taken into account by the back-shift-energy [3, 4]. There are two fundamental parameters in the BSFG formula which are tuned to reproduce the experimental data and they are the level-density parameter, 'a' and the spin cut-off parameter, σ^2 [3, 4]. In the Fermi-gas model, the level-density parameter 'a' is related to the single particle level-density around the Fermi surface, g via $a = \pi^2 g/6 = \pi^2 A/4\epsilon_f$, where ϵ_f is the Fermi energy [4]. According to this relation, it is expected that the parameter 'a' should vary smoothly with A. However, it is seen experimentally from the neutron resonances data that there is a considerable deviation from a constant value [5], implying the presence of unaccounted microscopic features in the Fermi-gas assumption. These microscopic effects have been identified with the influence of single particle shells prevailing at low excitation energies. Many phenomenological improvements [6, 7] have been carried out for the level-density parameter to account for the shell effects. The spin cut-off parameter in the Fermi-gas model, is determined according to $\sigma^2 = \langle m^2 \rangle gt = \Im t/\hbar^2$ where $\langle m^2 \rangle$ is the average of the squares of the single-particle spin projections, t is thermodynamic temperature, and $\Im$ is the nuclear moment of inertia [4]. Since the thermodynamic temperature t, is directly related to the level-density parameter 'a', the uncertainty in the determination of σ^2 is not only because of the parameter $\Im$, but also the parameter 'a' itself. Experimentally, σ^2 can be determined only from spin distribution of low-lying discrete levels [8, 9]. These measurements correspond to a low value of compound nuclear spin of $\sim 5\hbar$. At higher excitation energies and angular momenta the exclusive determination of the cut-off parameter becomes problematic due to higher level densities and

the absence of the reliable observables sensitive to this parameter. In the absence of reliable experimental information on angular momentum distribution of levels over a wide range of J to validate σ^2, the Fermi-gas model values are used as such in reaction cross section calculations.

At high excitation energies and spins, the major source of information about the nuclear level-density is obtained from particle-evaporation spectra in heavy-ion fusion reactions analyzed in the framework of the phenomenological descriptions involving the level-density parameters 'a' and σ^2 [10–15]. The moment of inertia, $\Im$ required in determination of σ^2, can be obtained with a good extent of accuracy at higher excitation energies from rotating liquid drop model [16], and thus the uncertainty in the cut-off parameter σ^2, remains dominantly due to the parameter 'a'. Therefore, information about the parameter 'a' at high E_X and J becomes crucial. The excitation energy dependence of the parameter 'a' has been investigated earlier from particle evaporation measurements for a wide variety of excited nuclei [14, 15]. The level-density parameter 'a' determined from these measurements is an averaged quantity over a range of excitation energies and angular momenta [10, 11]. The studies of the level-density parameter 'a' with angular momentum selection are very few [17] and as a result the value of 'a' is essentially unknown in high angular momentum domains for a great majority of nuclei. Therefore, it is important to carry out these investigations and this forms the basis of first part of the present thesis work.

We have developed a method for extracting the inverse level density parameter ($K = A/a$) as a function of angular momentum from γ-ray fold gated α-particle evaporation spectra in heavy-ion fusion reactions. The measured γ-ray multiplicity fold gated α-particle evaporation spectra are least squares fitted with statistical model calculations using the code PACE2 [18]. The parameter K is obtained as a function of angular momentum at an average excitation energy around 35 MeV for a number of nuclei in the shell region of $Z \sim 50$ and in mid-shell region of $Z \sim 70$. Around the

the shell closure region of $Z=50$, the 'gross' K value (summed over all J) is seen to be in the range 9.0 - 10.5 MeV, which is within liquid drop model estimate [19]. The variation of K as a function of angular momentum in the range of 5 to $30\hbar$ for the shell closure region, shows several interesting features not accounted by the shell and angular momentum corrected values of K used in PACE2 calculation [19]. However, in the mid-shell region the average value of K is 8.2 ± 1.1 MeV [20], and remains essentially constant around the average value in the angular momentum range of 15 to $30\hbar$ [20]. The present results for nuclei in shell closure region and in the mid-shell region would serve as important inputs for microscopic theories to understand the statistical properties of nuclei in different mass regions.

In case of heavy compound nuclear systems ($Z \simeq 80$ and $A \simeq 200$) populated in heavy-ion reactions, fission competes with particle emission and the dynamical effects become important along with the statistical ones. The dynamical effects in nuclear collisions have also been recognized in the pre-equilibrium emission and in the multi-fragmentation in a large number of studies [21]. But all of these processes proceed on a rather fast time scale. The manifestation of the dynamics on longer time scale, e.g., the fission time scale is of particular interest. The fission dynamics between saddle to scission has been of continued interest and is an important question that has received much attention over the years. It is still debated whether fission is an adiabatic (fast) or dissipative (slow) process. Various probes such as neutrons, charged particle [22–24], GDR γ rays [25] and FF kinetic energies [26] have been employed to address the above question. These experimental observations indicate that nuclear motion from compound nucleus to the scission point is over damped and energy dissipation during fission is essential to understand the fission dynamics. However, at the time of scission the actual tearing up of the neck joining the two nascent fission fragments is still not clearly understood. A suitable probe sensitive to scission point needs to be employed to address the scission mechanism.

In heavy-ion induced fusion-fission reactions, neutron and charged-particle (mainly proton and α-particle) emission is observed to take place from various stages, namely (i) the fissioning compound nucleus (prescission), (ii) the accelerated fission fragments (postscission), and (iii) close to scission (rupture) point between the main two fission fragments termed as ternary emission or near scission emission (NSE) [22, 23, 27, 28]. The ternary emission events of the fission process are very much sensitive to the scission configuration and therefore can provide information about the rupture process of the neck. In low energy fission (thermal neutron induced, photo-, and spontaneous fission) detailed investigations have been carried out for the ternary emission and are well documented in various review articles [26, 29, 30]. These investigations show that 90% of ternary charged particles are α-particles which are also called as long range alphas (LRA) in order to differentiate from less energetic alphas from radioactive decays. From low energy fission experiments, it is observed that the ternary charged particles exhibit characteristic energy and angular distributions resulting from strong focusing of the particles by the Coulomb forces of the nascent fission fragments. From these characteristic features of ternary α-particle emission, it is concluded that in low energy fission the near scission emission is a dynamical process [29].

Near scission α-particle emission in heavy-ion reactions has been studied only for a limited number of target-projectile systems due to the complexity of measurements and the analysis procedure [23, 27, 28, 31–33]. Some of the heavy-ion results do not agree with dynamical emission of ternary α particles [23, 27]. In the work of Ref. [21] it has been shown by measurement of relative ternary emission probabilities of intermediate mass fragments ($3 \leq Z \leq 20$) as a function of initial excitation energy that the ternary emission is a dynamical process even at higher excitation energies. But, later on it has been suggested by Moretto *et al.* [34] that the results obtained in the above work are consistent with statistical emission. Thus, at higher excitation energies, it is still not clear whether the NSE mechanism is a statistical evaporation or dynamical or a combination of both. There is no systematic study for the NSE over a large fissility (x)

range in heavy-ion induced fusion-fission reactions. Study of near scission emission of α-particles can provide information on the scission point characteristics of the fissioning nucleus (such as neck radius, elongation of scission configuration, kinetic energy of the fission fragments at the time of scission, etc.) and is important from the point of understanding the collective fission dynamics. In the second part of the present thesis, we describe the measurements of α-particle energy spectra in coincidence with fission fragments for the systems of ^{11}B (62 MeV) + ^{232}Th (Z^2/A=37.14) and ^{12}C (69 MeV) + ^{232}Th (Z^2/A=37.77) in a wide range of relative angles with respect to FF emission direction. The measured spectra are fitted with moving source model calculations to extract the α-particle multiplicities corresponding to different emission stages of the fusion-fission process. The obtained results in ^{11}B+ ^{232}Th reaction have been analyzed along with data from literature over a wide range of excitation energy (E_{CN}) and fissility (x) of the compound system to develop the systematic features of prefission and near-scission emission as a function of α-particle emission Q-value and Z^2/A of the compound system.

The fraction of near-scission multiplicity (α_{nse}) is observed to be nearly same at around 10% of the total prescission multiplicity ($\alpha_{pre} + \alpha_{nse}$) for various systems over a wide range of Z^2/A and excitation energy suggesting that the near scission emission of α-particles is a statistical process in heavy-ion induced fission reactions [35]. It is seen that prescission α-particle multiplicity (α_{pre}) normalized to $E_{CN}^{2.3}$ show a systematic linearly increasing trend with α-particle emission Q-value [35, 36]. The above observations indicate that the α-particle emission from the neck is a statistical decay process at higher excitation energies, in contrast to low energy and spontaneous fission where the neck-emission is a dynamical or fast process. Therefore, it can be inferred that nuclear collective motion during scission exhibits a change over from super-fluid to viscous nature with increasing excitation energy.

In case of ^{12}C (69 MeV) + ^{232}Th reaction, the α_{nse} appears to be anomalously en-

hanced with respect to the above systematics [37], indicating that there is some other source of α-particle emission in ^{12}C + ^{232}Th reaction in addition to pre-, post, and near scission emission stages. At the same time, in the two-dimensional particle identification plot, a high energy component of varying intensity depending on laboratory angle is also observed which corresponds to summed energy of two α particles entering the detector simultaneously (2α-events from ^{8}Be breakup). From these circumstantial evidences and also from transfer product angular distributions measured earlier for the present reaction [38], we have identified the new source of enhanced α_{nse} in the ^{12}C (69 MeV) + ^{232}Th reaction, as due to a single α-particle entering the particle detector from ^{8}Be transfer product breakup [37]. Accounting this source in the analysis, the extracted α_{pre} and α_{nse} are in agreement with the above systematics [35, 37].

The research work carried out and compiled here in the form of thesis has been published in peer reviewed journals [19, 20, 35–37, 39]. An overview of the thesis content grouped under six chapters is as follows:

Chapter 1:

The chapter begins with a preamble about some of the important features of the compound nucleus. Further, this chapter is divided into two parts corresponding to statistical and dynamical aspects of the excited nuclei. The first part begins with an overview about the statistical aspects of compound nucleus populated in heavy-ion reactions. Further, the concept of the nuclear level-density is introduced followed by a description of different methods, experimental as well as theoretical, of determining the nuclear level densities. After sketching a literature overview about the level-density parameters, the motivation for the first part of the thesis is described. In the second part of the chapter, after providing an overview about the saddle to scission dynamics, an introduction to the ternary fission is outlined, describing the characteristic features of the near-scission emission in low energy fission. At the end, the present understanding of the near scission α-particle emission in heavy-ion induced reactions is discussed

to provide the motivation for the second part of the thesis work.

Chapter 2:

This chapter describes performance characteristics of various radiation detectors used to carry out the experiments discussed in the present thesis work. Following detectors have been used; (i) For charged particle: Si-surface barrier and CsI(Tl)-Si(PIN), (ii) For γ rays; BGO and BaF$_2$ scintillation detectors, and (iii) For fission fragments; 32-strip silicon and a position sensitive gas ionization chamber telescope. In particular, the CsI(Tl)-Si(PIN) detector has been characterized quite rigorously for pulse height and timing response of fission fragments and γ rays. The chapter also discusses two particle identification techniques applied in the thesis work. Further, a brief description about the preparation of the targets used in the present thesis work is outlined. At the end, a brief introduction to the BARC-TIFR Pelletron accelerator facility at Mumbai is presented.

Chapter 3:

The chapter is divided into two parts. The first part begins with the methodology of the γ-ray multiplicity fold gated α-particle evaporation spectra measurement. It discusses different experimental aspects including background subtraction from α-spectra, detector energy calibration, validation of the BGO setup, etc. It also discusses about the extraction of first two moments of the γ-ray multiplicity distribution, the angular momentum carried away by the evaporated α-particle, the CN residue average angular momentum, and the conversion procedure of each γ-ray fold value to a corresponding average angular momentum. The second part, first introduces the statistical model code PACE2 followed by describing the method of calculating angular momentum gated α-particle spectra using the code. It also discusses the least squares fit method used to extract the inverse level-density parameter K, by comparing the experimental data with the PACE2 predictions. Finally, the results on level-density parameter K obtained for compound nuclear systems around the shell closure and in the mid-shell regions are

discussed.

Chapter 4:

The chapter begins with the methodology of the α-particle measurement in coincidence with fission fragments at different relative angles with respect to the fragment emission direction in ^{11}B (62 MeV) + ^{232}Th (Z^2/A=37.14) and ^{12}C (69 MeV) + ^{232}Th (Z^2/A=37.77) reactions. Further, this chapter deals with the moving source analysis which is used to disentangle the different components of the α-particle multiplicity. Finally, the results obtained for both the fissioning systems are compared.

Chapter 5:

The chapter is divided into two parts. The first part begins with the statistical model calculations using the code JOANNE2 to reproduce the prescission α-particle multiplicities for both reactions. The systematics of pre- and near-scission emission is developed using the present results along with available data from literature over a wide range of Z^2/A and the excitation energy of the compound system. In the second part of the chapter, the anomalous results obtained in the ^{12}C induced fission are explained in terms of transfer-breakup process.

Chapter 6:

This chapter gives a brief summary of the research work carried out in this thesis along with a future outlook.

References

[1] R. Stokstad, *Treatise on heavy-ion science, edited by D. A. Bromley*, vol. 3 (Plenum, New York, 1985).

[2] T. Ericson, Adv. Phys. **9**, 425 (1960).

[3] A. Gilbert and A. G. W. Cameron, Can. J. Phys. **43**, 1446 (1965).

[4] J. R. Huizenga and L. G. Moretto, Annu. Rev. Nucl. Sci. **22**, 427 (1972).

[5] A. S. Iljinov, M. V. Mebel, N. Bianchi, E. D. Sanctis, C. Guaraldo, V. Lucherini, V. Muccifora, E. Polli, A. R. Reolon, and P. Rossi, Nucl. Phys. **A 543**, 517 (1992).

[6] A. V. Ignatyuk, G. N. Smirenkin, and A. S. Tishin, Sov. J. Phys. **21**, 255 (1975).

[7] S. K. Kataria, V. S. Ramamurthy, and S. S. Kapoor, Phys. Rev. **C 18**, 549 (1978).

[8] P. Hille, P. Sperr, M. Hille, K. Rudolph, W. Assmann, and D. Evers, Nucl. Phys. **A 232**, 157 (1974).

[9] C. C. Lu, L. C. Vaz, and J. R. Huizenga, Nucl. Phys. **A 197**, 321 (1972).

[10] B. John, S. K. Kataria, B. S. Tomar, A. Goswami, G. K. Gubbi, and S. B. Manohar, Phys. Rev. **C 56**, 2582 (1997).

[11] B. John, R. K. Choudhury, B. K. Nayak, A. Saxena, and D. C. Biswas, Phys. Rev. **C 63**, 054301 (2001).

[12] A. Mitra, D. R. Chakrabarty, V. M. Datar, S. Kumar, E. T. Mirgule, and H. H. Oza, Nucl. Phys. **A 707**, 343 (2002).

[13] A. Mitra, D. R. Chakrabarty, V. M. Datar, S. Kumar, E. T. Mirgule, H. H. Oza, V. Nanal, and R. G. Pillay, Nucl. Phys. **A 765**, 277 (2006).

[14] A. Chbihi, L. G. Sobotka, N. G. Nicolis, D. G. Sarantites, D. W. Stracener, Z. Majka, D. C. Hensley, J. R. Beene, and M. L. Halbert, Phys. Rev. **C 43**, 666 (1991).

[15] D. Fabris and et al., Phys. Rev. **C 50**, R 1261 (1994).

[16] A. J. Sierk, Phys. Rev. **C 33**, 2039 (1986).

[17] S. Henss, A. Ruckelshausen, R. D. Fischer, W. Kuhn, V. Metag, R. Novotny, R. V. F. Janssens, T.L.Khoo, D. Habs, D. Schwalm, et al., Phys. Rev. Lett. **60**, 11 (1988).

[18] A. Gavron, Phys. Rev. **C 21**, 230 (1980).

[19] Y. K. Gupta, B. John, D. C. Biswas, B. K. Nayak, A. Saxena, and R. K. Choudhury, Phys. Rev. **C 78**, 054609 (2008).

[20] Y. K. Gupta, D. C. Biswas, B. John, B. K. Nayak, A. Saxena, and R. K. Choudhury, Phys. Rev. **C 80**, 054611 (2009).

[21] R. Yanez, T. A. Bredeweg, E. Cornell, B. Davin, K. Kwiatkowski, V. E. Viola, R. T. de Souza, R. Lemmon, and R. Popescu, Phys. Rev. Lett. **82**, 3585 (1999).

[22] K. Ramachandran, A. Chatterjee, A. Navin, K. Mahata, A. Shrivastava, V. Tripathi, S. Kailas, V.Nanal, R.G.Pillay, A. Saxena, et al., Phys. Rev. **C 73**, 064609 (2006).

[23] J. P. Lestone, J. R. Leigh, J. O. Newton, D. J. Hinde, J. X. Wei, J. X. Chen, S. Elfstrom, and M. Z. Pfabe, Nucl. Phys. **A 559**, 277 (1993).

[24] H. Ikezoe, N. Shikazono, Y. Nagame, Y. Sugiyama, Y. Tomita, K. Ideno, I. Nishinaka, B. J. Qi, H. J. Kim, A. Iwamoto, et al., Phys. Rev. **C 46**, 1922 (1992).

[25] P. Paul, Annu. Rev. Nucl. Sci. **44**, 65 (1994).

[26] R. Vandenbosch and J. R. Huizenga, *Nuclear Fission* (Academic, New York, 1973).

[27] M. Sowinski, M. Lewitowicz, R. Kupczak, A. Jankowski, N. K. Skobelev, and S. Chojnacki, Z. Phys. A **324**, 87 (1986).

[28] B. Lindl, A. Brucker, M. Bantel, H. Ho, R. Muffler, L. Schad, M. G. Trauth, and J. P. Wurm, Z. Phys. A **328**, 85 (1987).

[29] I. Halpern, Annu. Rev. Nucl. Sci. **21**, 245 (1971).

[30] A. K. Sinha, D. M. Nadkarni, and G. K. Mehta, Pramana J. Phys. **33**, 85 (1989).

[31] L. Schad, H. Ho, G.-Y. Fan, B. Lindl, A. Pfoh, R. Wolski, and J. P. Wurm, Z. Phys. A **318**, 179 (1984).

[32] K. Siwek-Wilczynska, J. Wilczynski, H. K. W. Leegte, R. H. Siemssen, H. W. Wilschut, K. Grotowski, A. Panasiewicz, Z. Sosin, and A. Wieloch, Phys. Rev. **C 48**, 228 (1993).

[33] W. W. Wilcke, J. P. Kosky, J. R. Birkelund, M. A. Butler, A. D. Dougan, J. R. Huizenga, W. U. Schroder, H. J. Wollersheim, and D. Hilscher, Phys. Rev. Lett. **51**, 99 (1983).

[34] L. G. Moretto, D. Breus, L. Phair, and G. J. Wozniak, Phys. Rev. Lett. **85**, 2645 (2000).

[35] Y.K.Gupta, D. C. Biswas, R.K.Choudhury, A. Saxena, B. K. Nayak, B. John, K. Ramachandran, R. G. Thomas, L. S. Danu, B. N. Joshi, et al., Phys. Rev. **C 84**, 031603 (R) (2011).

[36] Y. K. Gupta, R. K. Choudhury, and A. Chatterjee, BARC News Letter **324 Jan.-Feb.**, 6 (2012).

[37] Y. K. Gupta, D. C. Biswas, B. John, B. K. Nayak, A. Chatterjee, and R. K. Choudhury, Phys. Rev. **C 86**, 014615 (2012).

[38] D. C. Biswas, R. K. Choudhury, B. K. Nayak, D. M. Nadkarni, and V. S. Ramamurthy, Phys. Rev. **C 56**, 1926 (1997).

[39] Y. K. Gupta, D. C. Biswas, P. Roy, B. K. Nayak, , R. G. Thomas, A.L.Inkar, R.P.Vind, B. John, A. Saxena, et al., Nucl. Instr. Meth. **A 629**, 149 (2011).

List of Figures

List of Tables

Chapter 1

Introduction

1.1 Preamble to nuclear physics

From the time immemorial, mankind has pondered over questions like, "what is the nature of the universe? What are its constituents?". Over the years emerging answers have been forming the core of human knowledge. The persistent zeal of the curious human mind to unraveling the ultimate structure of the physical world around us has lead to many new discoveries starting from Dalton's atomic picture of the matter and then subsequent discovery of radioactivity by Henri Becquerel to J.J. Thomson's discovery of electron during the last decade of 19th century. A major breakthrough came when Rutherford discovered the atomic nucleus during 1906–1911 at the university of Manchester which laid the foundation of the new field called *'nuclear physics'*. In subsequent years when protons and neutrons were identified as the constituents of the nucleus, it enthralled and provoked the human mind to carry out further investigations. It is now realized that the proton and neutron are not the elementary particles, as they exhibit signature of finite internal structure. With the advancements in the field of sophisticated accelerators and detectors, and at the same time sound theoretical developments, the present understanding has been that the elementary particles are leptons, quarks and the force carrying gauge bosons.

In the journey from atom to the elementary particle, the physicists from all over

the world have devoted a major fraction of time to understand the exotic phenomena that the atomic nucleus exhibits. The dense nucleus that lies at the center of every atom and carries more than 99.9% of the atomic mass in a 10^{-12} fraction of its volume is a quantum system with a finite number of strongly interacting fermions of two kinds: proton and neutron (together known as nucleons). In nuclear systems, all the fundamental forces hold sway–from the strong interactions that operate as nucleon-nucleon forces to form the basic building blocks-the hadrons, to the weak interactions that give rise to beta decay and initiate stellar burning, the electromagnetic interactions that limit the stability of heavy nuclei towards fission, and the gravity that constrains the structure of neutron stars. Thus, simultaneous manifestation of all the fundamental forces makes the atomic nucleus one of the richest and challenging quantum systems. So far it has not been possible to even describe the atomic nuclei having a few nucleons from the first principle starting from bare nucleon-nucleon interaction. Various models have been employed to understand theoretically the different nuclear phenomena observed experimentally. The short range and saturation properties of the nuclear forces make the nuclear fluid to behave like an incompressible drop of liquid. The liquid drop model (LDM) of the atomic nucleus has been proposed by George Gamow and then developed by N. Bohr and J. A. Wheeler to explain many ground state properties of nuclei. This is a crude model that does not explain all the properties of the nucleus, but does explain the spherical shape of most nuclei and roughly predicts the binding energies and masses of the nuclei. Measurements of the binding energy of atomic nuclei show systematic deviations with respect to those estimated from the LDM. In particular, some nuclei having certain values for the number of protons and/or neutrons (Z or $N = 2, 8, 20, 50, 82,$ and 126) are more tightly bound together than predicted by the LDM. Moreover, at these Z and N values nuclei show a discontinuous change in various properties such the nucleon separation energy, capture cross section, etc. Nuclei with these Z and N numbers are called singly/doubly magic nuclei. These observations lead to assume the existence of a shell structure of nucleons within the nucleus, like

that of electrons within an atom. In order to explain these magic numbers, a shell model was developed in 1949 following independent work by several physicists, most notably E. P. Wigner, Maria Goeppert-Mayer and J. H. D. Jensen, who shared the 1963 Nobel Prize in Physics for their contributions. In this model it is assumed that nucleons are in motion in a mean field potential modified by the spin-orbit interaction of the individual nucleons. The shell model not only explains the special behavior of the magic nuclei, but also predicts other properties with some success, in particular spin, parity, and magnetic moments of nuclei in their ground states, and to some extent their excited states as well. Furthermore, the observation of the collective phenomena exhibited by the nuclear quantum many body system adds to the diversity of nuclear physics. Hence, numerous models have been formulated since the inception of the subject to understand the various nuclear phenomena. Nuclear systems ranging from a few nucleons (deuterium, ^{3}He) to 10^{57} particles (neutron stars), exhibit almost all of the diverse phenomena characteristic of mesoscopic systems. In understanding the diverse nuclear phenomena, though a remarkable progress has been made, much remains still to be understood. This progress has been driven by new theoretical insights, improved experimental facilities, increased computational power, and access to new isotopes with a large excess of neutrons or protons away from the beta stability region.

Understanding the origin, structure, and evolution of baryonic matter in the universe lies close to the heart of nuclear physics. Approximately 7000 nuclei are believed to be bound by the strong and electromagnetic interactions having half-lives longer than 1 microsecond (i.e., bound to rapid-proton, neutron, alpha, and fission decays). Of this total, only approximately 300 are stable, with lifetimes in their ground states sufficiently long (>1 billion years). At the most basic level, more than 50% of the nuclei in the nuclear chart still remain to be discovered and characterized.

The quest for deeper insight into the origin and stability of nuclei implies studying the exotic regions in the nuclear chart, especially those close to the "drip lines". Of

particular interest in this subject of research are the so-called magic nuclei. It has been predicted by numerous theoretical models that for exotic nuclei close to the drip lines, the nature of shell-closure changes quite drastically in comparison to nuclei close to the line of stability. The study of the exotic nuclei with radioactive ion beam (RIBs) facilities has opened an exciting avenue to look up to some of the crucial issues in the context of both nuclear structure and astrophysics.

On the other extreme of the nuclear chart, an "island of stability" of super-heavy elements (SHE), has been predicted by macro-microscopic nuclear theories when approaching the closed spherical shells of $Z \sim 114$ and $N \sim 184$. Synthesis of super-heavy elements in the laboratory is one of the most challenging problems in nuclear physics. So far the synthesis of elements up to $Z = 118$ has been possible using heavy-ion fusion reactions. Efforts are on to synthesize still heavier elements in various laboratories all over the world such as GSI, Berkeley and Dubna. This journey of exploration of the nuclear chart is full of excitement and challenges.

Another open problem in nuclear physics is the identification and characterization of phase transitions such as the liquid-gas and quark gluon plasma, which have been predicted theoretically. Study of hot and dense nuclear matter is important from astrophysical processes point of view such as supernovae explosions and neutron stars dynamics.

Collisions between two heavy nuclei (heavy-ion collisions) provide an avenue to study the excited nuclei of a variety of choices in a wide range of excitation energy (E_X) and angular momentum (J). In heavy-ion collisions, measurement and subsequent analysis of outgoing particles provide the information on the nuclear properties in the two dimensional space of E_X and J. Complete understanding of the diverse nuclear phenomena using the stable beams around the stability line of the nuclear chart, is a "stepping-stone" in the journey of nuclear chart exploration.
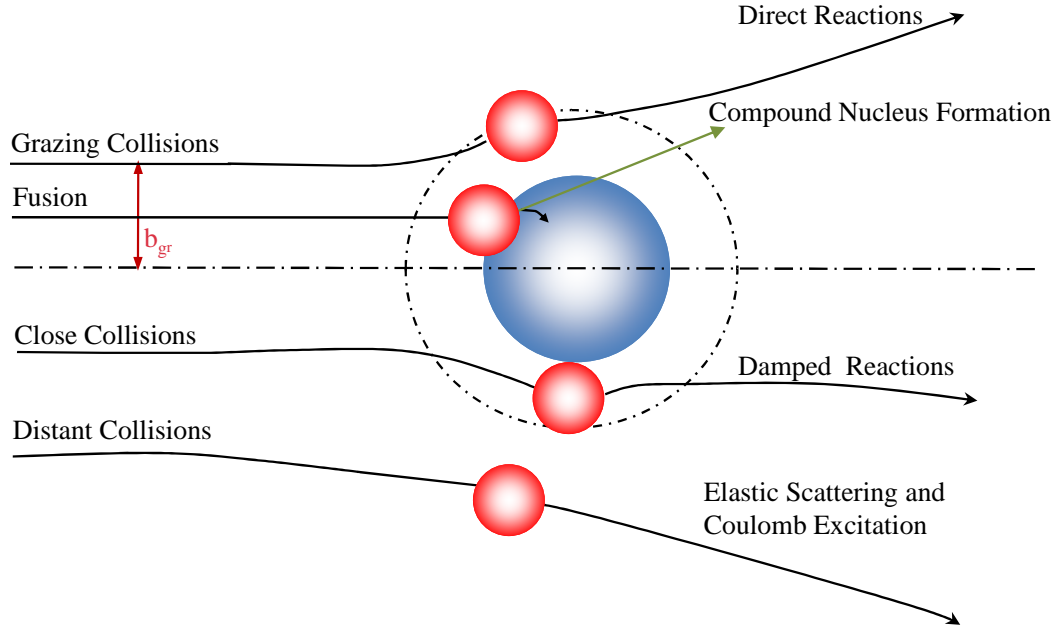
Figure 1.1: Schematic representation of different types of heavy-ion reactions as a function of impact parameter, 'b' [1].

1.2   Heavy ion collisions

Nucleus-nucleus collisions at moderate bombarding energies exhibit a broad spectrum of reaction types ranging from direct processes to fully equilibrated compound nuclear formation. Due to the small de Broglie wave length, heavy-ion collisions can be approximated by the semi-classical picture, where the trajectories of the collisions depend on initial conditions such as the impact parameter, relative velocity, Z and A of the colliding nuclei, as well as the long range Coulomb and short range nuclear forces acting between them. It is customary to use the impact parameter 'b' or the orbital angular momentum 'ℓ' to distinguish between different reaction processes. The impact parameter is the center to center distance of the target and projectile nuclei well before the collision. At a given impact parameter 'b', the entrance channel orbital angular momentum is $\vec{\ell} = \vec{b} \times \vec{p}$, where $\vec{p}$ is the momentum of the incident projectile in center-of-mass frame. Fig. 1.1 shows the classification of different reaction processes as a function of impact parameter, 'b' [1].

For very large values of '*b*', a negligible overlap of the colliding nuclei occurs, and interaction takes place mainly through the Coulomb field. These processes include Rutherford scattering, elastic scattering, and Coulomb excitation. The elastic scattering data have been extensively used to derive the internuclear potential by means of optical model analysis [2]. In Coulomb excitation, the electromagnetic forces between the two interacting nuclei excite the low lying excitations [3].

For grazing collisions, the most likely outcome is that the nuclei will scatter elastically, or the process may involve internal excitation to the intrinsic states of the interacting nuclei (inelastic scattering) [4]. For small overlapping encounters, nucleons may be exchanged, either in successive steps or as clusters resulting in both energy and angular momentum transfer from the relative motion into internal degrees of freedom (transfer reactions) [5]. For closer impacts, the two nuclei may partially coalesce for a short time before separating again. During these collisions, a noticeable dissipation of available kinetic energy and angular momentum takes place into the internal degrees of freedom of the reaction partners. The outgoing reaction partners have relatively good memory of the entrance channel parameters such as the mass, charge, etc. During these so called deep inelastic collisions, the composite system may undergo some amount of rotation before reaction partners (dominantly projectile and target like) re-separate [6]. In case of more central collisions, the two nuclei fuse together, where the total excitation energy and angular momentum is equilibrated inside the compound nucleus.

1.2.1   Compound nucleus formation

The nuclear reactions at moderate energies (typically less than 30 MeV/nucleon) can be classified in terms of a time scale [4, 7]. At one extreme, for "direct interaction" processes, the time interval between particle incidence and particle emission is close in magnitude to the time scale of transit of a nucleon across the nucleus ($\sim 10^{-22}$ s).

On the other extreme, for "compound nuclear" process, the particle emission is greatly retarded where the time scale is $\sim 10^{-19}$ to 10^{-16} s. There are indirect experimental evidences that for a particular reaction product, both types of processes occur simultaneously with substantial cross sections. Although it is rarely possible to measure the involved times directly, but there are indirect experimental arguments which can be exploited to discriminate CN processes from the direct ones. The most convincing evidence is provided by the observation of the reaction products with masses near to that of the CN [4]. The other arguments are based on the fact that direct processes tend to have the memory of the entrance channel whereas compound nuclear processes do not. Therefore, measurement of energy and angular distributions of the reaction products helps in discriminating these two distinct processes [4, 7].

The fusion reaction followed by CN formation can be considered as the most dissipative phenomenon observed in heavy-ion reactions. In this process, all the nucleons of the projectile and target are involved and the available kinetic energy is completely transformed into the intrinsic excitation energy of the compound system and all the initial angular momentum can be transformed into spin of the fused nucleus (the CN) [4]. Therefore, with a suitable combination of projectile and target nuclei and with varying beam energy, a variety of choices of the excited nuclei in a wide range of E_X and J can be populated through heavy-ion fusion reactions. One of the unique aspects of the heavy-ion fusion reactions is associated with the high angular momentum which can be imparted to the CN, offering the possibility of studying various nuclear phenomena in high angular momentum domains.

The expression 'compound nucleus' has a meaning that depends on the context [7]. The initial impetus for compound nuclear theory of nuclear reactions comes from the observations of narrow resonance widths in slow neutron absorption experiments where the compound nucleus is excited to discrete, sharp, resolved, and quantized energy levels and exists long enough for the mode of decay to be independent of formation. In

order to explain the long lifetimes ($\sim 10^{-16}$s) which these states implied, Bohr suggested [8] that the incident particle and target nucleus combine to form the compound nucleus in which the available excitation energy is shared among all the nucleons, and thus a long time, before enough energy is concentrated on one particle so that it can be re-emitted from the CN. The typical resonance spacing in the slow neutron experiments is of the order of 15-16 eV and it is around 10^6 times smaller than the single particle level spacings which is a sufficient evidence that the compound nuclear formation involves many degrees of freedom.

In the framework of medium energy heavy-ion nuclear reactions, the projectile and target amalgamate completely to form the compound nucleus (CN) in an energy region where enormous number of overlapping energy levels are excited. This process is referred to as complete fusion. Therefore the notations 'compound nuclear formation' and 'fusion' are used interchangeably. In the fusion process, the projectile and target nuclei pass through the fusion barrier (V_B) resulting from repulsive electrostatic mutual Coulomb, centrifugal, and attractive nuclear forces. In the partial waves expansion formalism the fusion cross section is [9];

$$\sigma_{fus}(E_{\text{c.m.}}) = \frac{\pi}{k^2} \sum_{\ell=0}^{\ell=\infty} (2\ell + 1)T_{\ell}, \tag{1.1}$$

where, T_{ℓ} is the fusion transmission probability for orbital angular momentum ℓ. Classically, the phenomenon of fusion can occur at center-of-mass energy ($E_{\text{c.m.}}$) only above V_B. In this classical sharp cut-off model, it is assumed that the $T_{\ell} = 1$ for $\ell < \ell_f$ and zero otherwise, where ℓ_f is the critical angular momentum of entrance channel below which fusion may occur [9]. In this approximation,

$$\sigma_{fus}(E_{\text{c.m.}}) = \frac{\pi}{k^2} \sum_{\ell=0}^{\ell=\ell_f} (2\ell + 1) \approx \frac{\pi}{k^2} \ell_f^2, \tag{1.2}$$

By inserting $\ell_f \hbar = \sqrt{2\mu(E_{\text{c.m.}} - V_B)}R_B$ and $k = \sqrt{2\mu(E_{\text{c.m.}})}/\hbar$ in the Eq. (1.2) (where μ is the reduced mass of the projectile and target nuclei) we get the well known classical formula for the fusion cross section as [9];

$$\sigma_{fus}(E_{\text{c.m.}}) = \begin{cases} \pi R_B^2 \left(1 - \frac{V_B}{E_{\text{c.m.}}}\right) & \text{if } E_{\text{c.m.}} > V_B \\ 0 & \text{if } E_{\text{c.m.}} < V_B \end{cases} \tag{1.3}$$

Classically, it is the fusion barrier which prevents the compound nuclei to be populated with lower excitation energies using heavy-ion fusion reactions. However, from the stand point of quantum mechanics, fusion is possible even for $E_{\text{c.m.}} < V_B$ due to the process of quantum mechanical tunneling [4, 9]. The nucleus-nucleus potential of the interacting nuclei plays significant role in determining the shape of the fusion barrier and hence the value of the fusion cross section. Different models have been employed to reproduce the experimental fusion cross sections, the simplest one is the one-dimensional barrier penetration model where the potential is the function of only relative distance between the interacting nuclei. The fusion process being a tunneling phenomenon, the strong interplay between nuclear structure and the reaction is observed at energies around the Coulomb barrier [10–12]. Particularly, the systematic variation of fusion cross section below and around the Coulomb barrier has revealed the involvement of various other degrees of freedom such as relative orientations, excitations, exchange of nucleons, etc. [13–15]. Using coupled channel calculations (CCFUS [16], CCDEF [17], CCFULL [18]), these internal degrees of freedom have been taken into account to a good extent in reproducing the experimental fusion cross sections. As far as the present thesis work is concerned, the beam energies are above the Coulomb barrier and hence no ambiguity in the results due to the fusion process.

1.2.2 Compound nucleus decay

The CN populated at high excitation energies in the heavy-ion fusion reactions have very short lifetime (10^{-21} to 10^{-20} s) in comparison to the CN populated through slow neutron absorption [4, 7]. The main features of these reactions can be understood in complete analogy to traditional concept of the CN, neglecting the possibility of pre-equilibrium emission. The populated CN is assumed to be fully equilibrated with
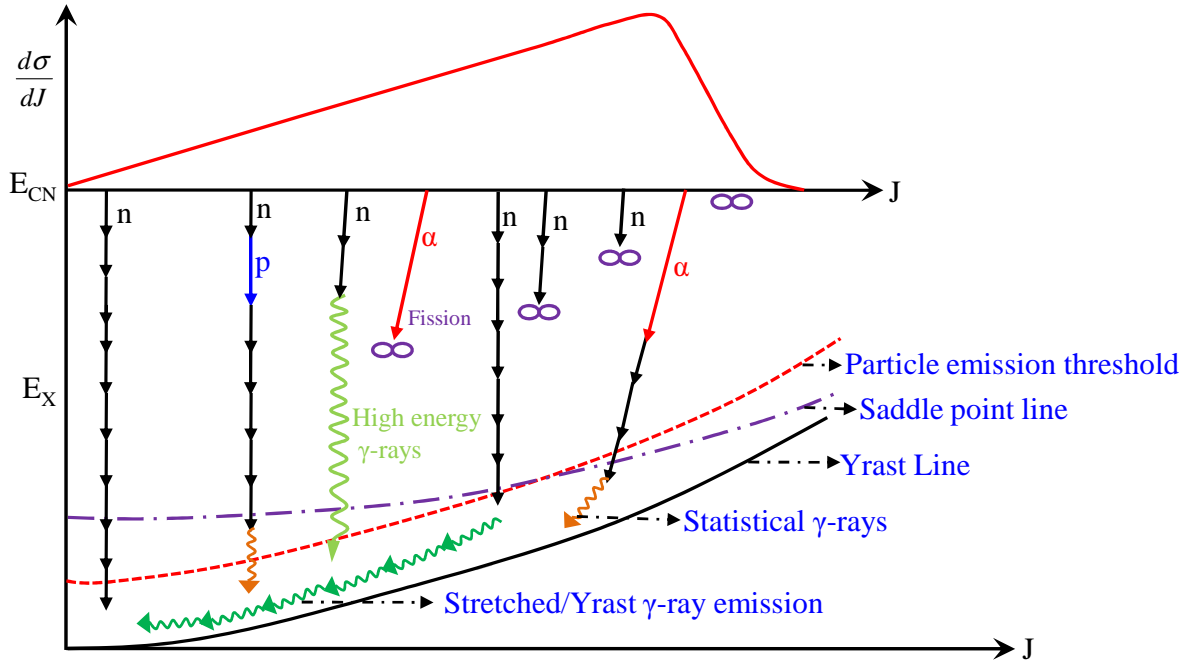
Figure 1.2: Schematic illustration of possible decay modes of a compound nucleus (CN) formed at a unique high excitation energy E_{CN} and over a broad range of spins J, with population cross section of $\frac{d\sigma}{dJ}$ [19]. Different decay paths such as particle (n, p, α) emission, γ-ray emission, and fission are sketched.

respect to all degrees of freedom and characterized by its total mass, charge, energy, and angular momentum. The CN has a certain amount of excitation energy E_{CN} depending on the projectile beam energy and fusion Q-value and a broad J-distribution as shown in the upper half of the Fig. 1.2. Once the CN is formed, its decay is completely determined by the statistical weights of various possible final states, forgetting the past history of the formation process except for the demand of the conservation laws [20, 21]. This essentially means that the cross section (σ) associated for the reaction $A(a, b)B$ can be written as;

$$\sigma(a + A \longrightarrow B + b) = \sigma(a + A \longrightarrow C^*)P(C^* \longrightarrow B + b) = \sigma(a + A \longrightarrow C^*)\frac{\Gamma_{C^* \longrightarrow B+b}}{\Gamma},$$

$$(1.4)$$

where $\sigma(a + A \longrightarrow C^*)$ is the cross section for populating the CN, C^* and $P(C^* \longrightarrow B + b)$ is the probability for the CN to decay into a particular channel $(B + b)$ which is equal to the ratio of partial width $(\Gamma_{C^*} \longrightarrow B + b)$ to the total width (Γ) of CN decay.

The CN decays to the ground state by sequential emission of several particles (n, p, and α-particle) and γ rays, which are governed by the statistical weight factors [20–22]. With less probability, the excited CN may also dissipate its energy and angular momentum by emitting d, t, ^{3}He and high energy γ rays (giant resonances). In the case of heavier CN, fission decay also competes with particle and γ-ray emission as shown in the Fig. 1.2. The branching ratios for different decay modes at a given excitation energy depend on the angular momentum distribution of the CN. In order to illustrate the correlation between angular momentum and decay of the CN, the possible decay paths of de-excitation for a medium heavy CN ($A \approx 200$) in excitation energy versus angular momentum plane are shown schematically in the Fig. 1.2 (taken from Ref. [19]). The accessible part of the plane is bounded by the yrast line which connects the states of lowest energy for each angular momentum J. At sufficiently high angular momentum, lowering of the fission barrier makes the fission to be the most suitable decay path of the CN. If the CN does not undergo fission, particle emission becomes favorable by which the CN lose a major part of the excitation energy, but only a small fraction of the angular momentum. Thus the evaporation of particles gives a steep descent towards the ground state as shown in Fig. 1.2. When the excitation energy of the CN reduces below the particle emission threshold, γ-ray emission takes over. The remaining excitation energy and angular momentum are then dissipated by a series of electromagnetic transitions which proceed initially as a "statistical cascade" towards the yrast line, and eventually through a sequence of low energy yrast γ rays to the ground state as shown in the Fig. 1.2. These yrast γ rays carry the major fraction of the angular momentum of the CN. Since the particle emission results with a small change in the CN angular momentum, the measurement of these multiplicity γ rays can provide information about the initial J-distribution of the CN.

1.3   Statistical aspects in the study of compound nuclear decay

The statistical model which relies on the assumption of equilibrium, rests on the premise that all the decay channels that are "open" are, on the average, equally likely to be populated [20–22]. By an open channel we mean a particular final state, specified by all the quantum numbers, which can be reached from the initial state without the hindrance of any barrier penetration. If a centrifugal, Coulomb or other type of barrier is present, the probability of population of that channel is simply reduced by the barrier penetration probability. The statistical model thus says that probability of decay to a particular channel is inversely proportional to the number of open channels. As mentioned earlier, various decay modes are possible, for convenience these modes can be put into three categories viz γ-ray emission, particle evaporation, and the fission. The average total decay rate $R(E_i, J_i)$ from the initial state of excitation energy E_i and angular momentum J_i is the sum of all the possible transitions that depopulate the level [22];

$$R(E_i, J_i) = R_\gamma + R_{\text{evap}} + R_{\text{fission}}, \tag{1.5}$$

where R_γ, R_{evap}, and R_{fission} are the average decay rates at which an ensemble of compound nuclei decay to final state (E_f, J_f) via γ-ray emission, particle evaporation, and the fission, respectively. Here, we will focus only on particle evaporation to understand the statistical decay of the CN. Consider an ensemble of compound nuclei in thermal equilibrium with energies E_i to $E_i + dE_i$ and angular momentum J_i, the evaporation decay rate can be written as [22];

$$R_{\text{evap}} dE = \sum_\mu \sum_{j,s} \int_{\epsilon=0}^{E_i - S_\mu} R_\mu(E_i, J_i; E_i - S_\mu - \epsilon, j, s) d\epsilon. \tag{1.6}$$

where the running variables μ, j, and s stands for the particle type, angular momentum, and intrinsic spin, respectively. S_μ and ϵ are the separation energy and

the kinetic energy of the particle, respectively. The probability that the CN will decay to channel x is [22];

$$P(E_i, J_i; x) = \frac{R(E_i, J_i; x)}{R(E_i, J_i)}. \tag{1.7}$$

Hence the cross section for the population of a given channel, x may be written as;

$$\sigma(x) = \sum_{J_i} \sigma(E_i, J_i) P(E_i, J_i; x). \tag{1.8}$$

where, $\sigma(E_i, J_i)$ is the so called inverse reaction cross section for production of equilibrated compound nucleus with excitation energy and angular momentum E_i and J_i, respectively [22]. In essence, we are utilizing the reciprocity theorem to simplify the formulation with the approximation that in CN reaction, $a + A \longrightarrow C^* \longrightarrow B + b$, the reaction cross section $\sigma(a + A \longrightarrow C^*)$ is equal to $\sigma(b + B \longrightarrow C^*)$. Ignoring the fact that the residual nucleus B may be left in the excited state, for practical calculations of inverse reaction cross section the residual nucleus B is assumed to be in ground state. Furthermore, minor difference between total reaction cross section and compound nuclear formation cross section is neglected [7].

The rate of decay for an ensemble of compound nuclei in thermal equilibrium with energies E_i to $E_i + dE_i$ and angular momentum J_i that emits particle μ with kinetic energy ϵ, spin s, orbital angular momentum l, and leaving the residual nuclei in the final state with the excitation energies E_f to $E_f + dE$ and spin j, can be written as [22];

$$R_\mu(E_i, J_i; E_f, j, s) = \frac{1}{h} \sum_{S=|j-s|}^{|j+s|} \sum_{l=|J_i-S|}^{J_i+S} T_l(\epsilon) \frac{\rho(E_f, j)}{\rho(E_i, J_i)} dE, \tag{1.9}$$

where, $E_f = E_i - S_\mu - \epsilon$. In the Eq. (1.9), the $T_l(\epsilon)$ is the optical model transmission coefficient for the formation of compound nucleus in a time reversed reaction of the emitted particle and the residual nucleus with excitation energy E_f and angular momentum j. $\rho(E_i, J_i)$ and $\rho(E_f, j)$ are the level densities of the initial and final states. For relative decay widths of different particles, the initial level densities will be the same, it is the density of final states which controls the competition among different decay modes.

Equations (1.5) - (1.9) forms the basis of Hauser-Feshbach (HF) theory of the statistical decay of the compound nucleus. The quantities, level-density and transmission coefficients of Eq. (1.9) play significant role in the statistical decay of the CN. In the context of present thesis work we will focus on the level-density in the subsequent sections.

1.4   Nuclear level-density

Nuclear level-density (NLD) defines the number of energy levels per unit energy at any excitation energy, E_X, is a characteristic property of every nucleus [23]. From the experimental observations, it is seen that at high excitation energy more than one nucleon can be excited to the higher orbits and hence a widespread mixing of different J^π configurations results in rapidly increasing nuclear density. In a typical example, for $A = 100$, even a few MeV excitation energy may give rise the level-density of the order of 10^6 MeV^{-1} [22]. The NLD is a function of various constant of the motion, e.g., excitation energy, angular momentum, parity, isospin, etc. As discussed in the previous section, the NLD is one of the basic statistical parameters which plays crucial role in determining the decay channels of the excited nucleus. It is a key ingredient in the calculation of reaction cross sections using the framework of Hauser-Feshbach (HF) theory of compound nuclear reactions [7, 21, 22, 24]. Hence, the knowledge of nuclear level densities of various nuclei is a crucial input in various fields/applications that include:

- **Design of nuclear reactors, ADSS, and radioactive-ion beams (RIBs):**
  The neutron capture cross sections as well the yields of different radio-nuclide produced in the nuclear reactors depend critically on the NLD. An important applied field where the NLD information is quite important is the accelerated driven sub-critical system (ADSS) which can be used for energy production as well as transmutation of nuclear waste in hybrid reactors. Design of ADSS re-

quire precise knowledge of different nuclide production cross section in order to predict the amount of radioactive isotopes produced inside the spallation target. Further, in order to explore the outer regions of the nuclear chart beyond the line of stability, especially those close to the so called proton and neutron drip lines, researchers need beams of unstable (radioactive) nuclei. Model predictions of the yields of radio-nuclides far from stability are needed to optimize experimental conditions for the production of these beams. An improved knowledge of nuclear level densities will significantly improve the accuracy of statistical model calculations used in these applications [25].

- **Nucleosynthesis:** In astrophysical environments, explosive nuclear burning produces a variety of nuclei spanning almost whole the nuclear chart. Experimentally, very few reaction rates are measurable, especially at the energies of astrophysical interest. In order to predict the relative abundance of different nuclei in astrophysical environments, the precise knowledge of nuclear level-density is an essential input [26].

- **Structure of nuclear fission barrier:** To understand fission barrier structure, experimentally, fission cross section are measured as a function of energy around the barrier. The level-density values play crucial role in determining the barrier structure from these measurements.

- **Nuclear medicine:** To optimize production of radioactive isotopes for therapeutic purposes reaction cross-sections are needed. These depend on Level Densities.

Apart from our practical needs, the theoretical study of NLD provides a fundamental insight into the microscopic features of an excited nucleus. The knowledge of NLD provides information about the internal structure of any nucleus, which determines the manner in which the nucleus participates in a physical process. The nuclear level-density $\rho(E, J)$ of an excited nucleus is the number of energy levels lying between

energy E and $E + dE$ at an angular momentum value J. Since the nuclear energy level at angular momentum J has $2J + 1$ degenerate magnetic states with projection M on the quantization axis, thus $\omega(E, J) = (2J + 1)\rho(E, J)$ is the state density counting all the (J, M) configurations.

The calculation of a nuclear level-density at energy E, amounts to determining the number of different ways in which individual nucleon can be placed in the various single-particle orbitals, such that the excitation energy lies in the range of E and $E + dE$. It is thus a combinatorial problem, in which physics is contained in the specification of the single particle orbitals if the nucleons are non-interacting and require correction of the residual interaction if they do interact. There are three main methods of obtaining the level-density from the single particle levels [22, 23];

1. **Thermodynamical or statistical approach:** The thermodynamical or statistical approach is one of the oldest and the most efficient method which will be discussed in the next section.

2. **Combinatorial method:** The Combinatorial methods relies on large computers, where different configuration are generated by cycling the occupation number of each of the single particle level over its all allowable values. The levels are then sorted out in terms of particle number, excitation energy, angular momentum, and any other possible quantum number. One of the advantage of such a method is the exact counting of the energy levels. But the disadvantage is that even after using large computers, theses calculations are limited to small excitation energies due to rapid increase of the level density with the excitation energy and the level densities are handled in a numerical manner.

3. **Spectral distribution method:** To understand the concept of this method for calculating the NLD, it would be insightful to begin with the distribution of eigen values also referred to as the density function or the density of states.

The distribution of shell model states with fixed angular momentum projection M for many fermions in a large but finite set of single-particle states interacting with two nucleon forces, is close to a Gaussian. Hence we can calculate these shell model state densities without having all the eigen states exactly but by directly calculating the first few moments (centroid, width, skewness, etc.) of the Hamiltonian for a fixed value of M [27, 28]. These shell model level densities are essentially based on a finite spectroscopic space. Beyond some excitation energy $\bar{E}$, higher single-particle states should be included. Hence the shell model level densities coincide with the actual level-density of the system up to the excitation energy $\bar{E}$. This method has been quite successful in predicting E_X and J dependence of the NLD for lighter nuclei in a narrow region of E_X and J.

1.4.1 Thermodynamical or statistical approach to calculate the NLD

In this technique, the basis (single particle levels) are the same as used in the combinatorial methods. It differs only in the mathematical technique used to obtain the level-density. Statistical mechanics provides a framework for relating the microscopic properties of individual particles (nucleons) to the macroscopic bulk properties (or thermodynamical properties) such as entropy, temperature, volume, etc. [29]. Though the number of nucleons within the nucleus are not adequate for the statistical mechanics to be applicable, it is the large value of the NLD which justifies to use the statistical mechanics for deducing the various macroscopic properties of the nucleus. Thus, it is reasonable to develop thermodynamic concepts such as temperature and entropy, for nuclear systems.

Bethe [30] and Weisskopf [31] did pioneering work in introducing the concept of a nuclear temperature. An individual nucleus is one of the Nature's most perfect examples of an isolated system. Equilibrium within the excited nucleus is linked closely to the nuclear temperature. We invoke the fundamental quantities of the statistical

mechanics and their inter-links to define the nuclear temperature. Let us consider a whole ensemble of isolated nuclear systems. Let $\Gamma(E, N)$ specify the number of states of a given system with fixed volume and particle number N that lie in the vicinity (ΔE) of energy E. It immediately follows that [31];

$$\Gamma(E, N) = \omega(E, N)\Delta E, \tag{1.10}$$

where $\omega(E, N)$ is the density of states in the vicinity ΔE of energy E. The entropy of the system $S(E, N)$ is given by;

$$S(E, N) = \ln \Gamma(E, N) = \ln \omega(E, N) + \ln \Delta E. \tag{1.11}$$

With these quantities, the definition of temperature provided by statistical mechanics is [29, 31];

$$\frac{1}{T} = \frac{\partial S(E, N)}{\partial E} = \frac{\partial \ln \omega(E, N)}{\partial E} = \frac{1}{\omega}\frac{\partial \omega(E, N)}{\partial E}, \tag{1.12}$$

here we have taken ΔE to be independent of E. Thus the nuclear temperature, T gives the information about the change of density of states with excitation energy.

Now let us come to the main motivation of calculating the density of states using mathematical techniques of statistical mechanics, where a grand partition function contains all the essential information. Let the nucleus is defined by its number of neutrons N, protons Z and energy E, then the grand partition function can be written as [23];

$$e^{\Omega} = \sum_{N', Z'} \int \omega(E', N', Z') \exp(\alpha_N N' + \alpha_Z Z' - \beta E') \mathrm{d}E', \tag{1.13}$$

where α_N, α_Z, and β are the Lagrange multipliers associated with the particle number and energy. Of particular significance is the quantity $t = 1/\beta$ which is commonly known as the statistical or thermodynamical temperature. In the Eq. (1.13), the $\omega(E', N', Z')$ represent the density of states. Thus the grand partition function is the Laplace transformation of the density of states which can be obtained by inverse transformation employing some mathematical tools. In addition to the number of protons, neutrons and total energy, by introducing the total magnetic quantum number,

M in the Eq. (1.13), the angular momentum dependence of the density of states can be obtained. In order to calculate the analytic expression for the state density, it is the grand partition function which depends on nuclear models.

System of non interacting fermions:

If we approximate the isolated nuclear system to be consisting of non-interacting fermions (Fermi gas model), the partition function can be easily evaluated. Let the constants of motion are the neutron and proton numbers N, Z, the energy E, and the projection of angular momentum M. In this case an approximate expression for the state density is obtained to be [23];

$$\omega(E, N, Z, M) = \omega(E, N, Z)\frac{\exp(-M^2/2\sigma^2)}{\sqrt{2\pi\sigma^2}}, \tag{1.14}$$

where $\omega(E, N, Z)$ is the total state density. The quantity σ^2 is called the spin cut off parameter, determines the width of the M distribution. Bethe suggested that dependence of the nuclear level-density on angular momentum (J) can be obtained in the following way [23];

$$\rho(E, N, Z, J) = \omega(E, N, Z, M = J) - \omega(E, N, Z, M = J + 1) \tag{1.15}$$

or

$$\rho(E, N, Z, J) = -\left[\frac{d}{dM}\omega(E, N, Z, M)\right]_{M=J+1/2} \simeq \frac{2J+1}{2\sqrt{2\pi}\sigma^3}\omega(E, N, Z)\exp\left[-\frac{(J+1/2)^2}{2\sigma^2}\right] \tag{1.16}$$

Thus, for a nuclear system of non-interacting fermions, we can get an analytic expression for the excitation energy and angular momentum dependent nuclear level-density if the total state density, $\omega(E, N, Z, M)$ is known to us. There are some highly simplified cases where the total state density can be calculate analytically.

Equidistant Fermi gas model:

If we further simplify the system of non interacting fermions in which the single particle level spacing decrease with square root of energy to the case where all the single particle

levels are equidistant, the total density of states for a gas of two components neutrons and protons is calculated to be [32];

$$\omega(E, N, Z) = \frac{\sqrt{\pi}}{12} \frac{\exp(2\sqrt{aE})}{E^{5/4}a^{1/4}} \qquad (1.17)$$

where $a = \pi^2 g/6$ and g is the sum of neutron and proton single particle level densities of a Fermi gas evaluated at the Fermi Surface, ϵ_f. Thus the nuclear temperature is given by [22];

$$\frac{1}{T} = \frac{\partial \ln \omega}{\partial E} = \left(\frac{a}{E}\right)^{1/2} - \frac{5}{4E}, \qquad (1.18)$$

The nuclear temperature is roughly the average energy per excited nucleon around the Fermi surface. In the limit of large excitation energies, the thermodynamic temperature $\frac{1}{t} = \frac{dS}{dE} = \sqrt{(a/E)}$ becomes equal to the nuclear temperature T [22]. By inserting the total state density from Eq. (1.17) into the Eq. (1.16), we get the expression of the nuclear level-density as [22, 23];

$$\rho(E, J) = \frac{2J+1}{12}\sqrt{a}\left(\frac{\hbar^2}{2\Im}\right)^{3/2}\frac{1}{E^2}\exp\left(2\sqrt{aE} - \frac{(J+1/2)^2}{2\sigma^2}\right) \qquad (1.19)$$

where $\sigma^2 = \langle m^2 \rangle gt = \Im t/\hbar^2$ where $\langle m^2 \rangle$ is the average of the squares of the single-particle spin projections, t is thermodynamic temperature, and $\Im$ is the nuclear moment of inertia [23]. In the context of $E_{rot} << E$, where $E_{rot} = \frac{\hbar^2}{2\Im}J(J+1)$ is the rotational energy, the Eq. (1.19) is written in the compact form [33];

$$\rho(E, J) = \frac{2J+1}{12}\sqrt{a}\left(\frac{\hbar^2}{2\Im}\right)^{3/2}\frac{1}{E^2}\exp\left(2\sqrt{a(E-E_{rot})}\right). \qquad (1.20)$$

The excitation energy and spin dependent level-density given by the Eq. (1.20) is most widely used in the statistical models, with some suitable adjustment of the parameters. The interpretation of the exponential factor $\exp\left(-\frac{(J(J+1))}{2\sigma^2}\right)$ in the Eq. (1.19) is that the energy in the form of rotation is unavailable for random excitation of the system and therefore does not contribute to the "intrinsic" level-density.

In this Fermi gas picture, the parameter 'a' is only a function of the mass number A of the excited nucleus;

$$a = \frac{\pi^2 g}{6} = \frac{\pi^2 A}{4\epsilon_f} \approx A/15. \qquad (1.21)$$

This simple estimate does not yield the experimentally determined mass dependence, the experimental values of the parameter 'a' at lower excitation energies are systematically larger than the calculated by the Eq. (1.21) and at higher excitation energies these two values are of similar magnitude. These discrepancies have been attributed to the diffused nuclear surface and effective nucleon mass in the nuclear medium [34], there are many other experimental observations which deviates from the equidistant Fermi gas model of the nuclear level-density [22, 23].

1.4.2 NLD beyond the Fermi gas picture: Phenomenological description

The Fermi gas formalism of the nuclear level-density is too simplistic which does not include the very important nuclear aspects such as the shell effects, pairing corrections, and the effect of nuclear deformation [22, 35, 36]. A vast amount of experimental accurate data from slow neutron resonance have been available from where experimental absolute values of the nuclear level densities can be obtained at an excitation energy around 8 MeV [37, 38]. The Fermi-gas picture explain only the average trend of the nuclear level densities as a function of excitation energy and mass number.

Since the level-density parameter is directly related to the single particle density g around the Fermi surface, shell model picture of the nucleus reveals that there are large gaps just above the major shells, we therefore expect marked deviations in the value of the parameter 'a' around the closed shells at moderately low excitation energies. From compilation of neutron resonance data it is seen that on the average the parameter 'a' increases with the mass number A, but rapidly decrease near the shell closures. These systematic deviations imply the presence of unaccounted microscopic features in the Fermi-gas assumption. These microscopic effects have been identified with the influence of single particle shells prevailing at low excitation energies. However the shell effects present in the ground state or at low E_X, are seen to wash out with increasing E_X [39]. Many phenomenological improvements [40–47] have been carried out for the

level-density parameter to account for the shell effects.

Within the Fermi gas picture it is assumed that the nucleons are non-interacting, but the short range strong nuclear force among the nucleons should definitely lead to some residual interactions. In particular, the paring interaction will alter the energy dependence of the density of levels. The effect of pairing is to partially block levels near the Fermi surface such that unpaired nucleon can not occupy them, thus reducing the density of levels [22]. These pairing effects are prominent only at lower values of E_X and J. In the phenomenological descriptions of the nuclear level-density, the pairing is partly taken into account by the back-shift-energy (calculated from odd-even nuclei mass differences) [47].

The Fermi gas model of nuclear level-density also does not take into account the effect of deformation. The effect of deformation on level-density is three fold: (i) the spacing and order of single particle levels depend on the shape of the nuclear potential, and therefore, the density of single particle levels at the Fermi surface depends on the deformation [22]. (ii) introduction of new levels associated with collective degrees of freedom, i.e., the rotational and vibrational levels, which increase the intrinsic level-density [37, 48, 49]. This effect is termed as the collective enhancement of the NLD. (iii) The increase of moment of inertia due to deformation should reduce the rotational energy at a given J, thus enhancing the intrinsic excitation energy available for excitations [50]. Thus, the deformation effect on the NLD is quite complicated, but the deformation being a shell effect which washes out with increasing excitation energy, these effects are more prominent at low excitation energies.

A survey of literature would lead to a vast amount of theoretical studies, that have been dedicated to incorporate the observed shell effects [40–46], pairing effects [47, 51–54], and the collective enhancement [37, 48, 49] . Various schemes based on phenomenology have been proposed to reproduce the experimental data mainly obtained from neutron resonance [23, 37, 41, 47]. One of such scheme is the Back Shifted

Fermi Gas (BSFG) model [47] in which the expression for the E_X and J dependent NLD is almost similar to the Fermi gas formalism except for: (i) the pairing is partly taken into account by the back-shift-energy, (ii) the level-density parameter 'a' is modulated to take into account for the shell effects. The BSFG model have been quite successful in reproducing the experimental data mainly at lower values of E_X and J, with suitable tuning of the level-density parameter, 'a' and the spin cut-off parameter, σ^2 [23, 47].

Here it is worth to mention that in the literature, the microscopic approaches have also been pursued [40, 54–61] to reproduce the experimental data regarding the NLD with an accuracy competing with BSFG type successful model. Unfortunately, all these microscopic approaches have limited success only in the narrow region of the E_X and J. For higher values of E_X and J, one has to depend on the phenomenological description of the NLD.

1.4.3 Experimental techniques to determine the NLD

Various experimental techniques have been enabling us to extract the information about the NLD [23]. Since the majority of the data are analyzed with in the phenomenological description of the NLD, where various parameters are tuned, the prime motivation of gathering more and more experimental data is to reduce the uncertainties in the fitted parameters.

Neutron and charged particle resonance:
The earliest and most extensive source of information on absolute value of the NLD came from the low energy neutron resonance (s-wave) data [37, 38, 62, 63] at an excitation energy just exceeding the neutron binding energy. In this approach the exact counting of the levels is possible for almost all stable nuclei of the entire periodic table. But at the same time, disadvantage is that it is limited to narrow region of spin and excitation energy of the nucleus to be studied. Similar to the neutron resonance,

the charged particle resonance has also enabled us to extract the NLD, but only for light and medium mass nuclei due to the presence of Coulomb barrier [23, 64, 65]. The study of charged particle resonance gives level-density information for a number of nuclei for which neutron resonance spectroscopy can not be studied.

Inelastic scattering and nuclear reactions:

The neutron and charged particle resonances give the NLD information of the compound nuclei. The experimental information about the variation of the NLD with E_X and J in residual nuclei can be obtained from inelastic scattering and various nuclear reactions [23, 66, 67]. The typical nuclear reactions which have been employed are (p, p'), (n, n'), (α, α'), and (p, α'). Although the energy resolution [1 - 10 keV] achieved in these measurements is order of magnitude poorer than the particle resonances experiments, however, the information obtained from this technique in conjunction with particle capture resonance data gives a more critical test of the phenomenological prescriptions of the NLD.

Measuring the excitation function of the isolated levels:

Since the cross section for the formation of an isolated level in the residual nucleus is governed by the competition of decay probability through this channel to that for all other channels, it was pointed out by Ericson [21] that measurement of the excitation function in compound nuclear reactions for an isolated level of a residual nucleus can give the excitation energy dependence and absolute measurement of the NLD. However, this technique suffers from the exponentially decreasing cross section with energy of a single particle level and the possible admixture by direct reaction process, still the information about the excitation energy dependence has been helpful to improve the phenomenological prescription of the NLD [23].

Ericson fluctuation width analysis [68]:

With increasing excitation energy of the CN, the average spacing between the nuclear

levels becomes comparable or larger than the average width of the levels. In such case the measured nuclear reaction cross section fluctuates as a function of well defined beam-energy. The average width of the CN energy levels can be obtained from the correlation functions of the fluctuating cross sections of the different compound nuclear reactions. This average width of the CN is related by statistical theory to the sum of partial widths of all the exit channels. Thus, if we can get information on the exit channels from other measurements, the level-density of the CN at a high excitation energy of around 20 MeV can be obtained. For a long time this was the only technique to get the NLD at energy around 20 MeV.

Measuring the NLD from particle evaporation spectra

The techniques discussed above give absolute value of the NLD but they are limited to the lower values of excitation energies and angular momenta. At high E_X and J, the major source of information about the nuclear level-density is obtained from particle-evaporation spectra in heavy-ion fusion reactions. According to Hauser-Feshbach (HF) theory of compound nuclear reactions [21, 22, 24], the shapes of the energy and angular distributions of evaporated particles are mainly governed by the the E_X and J dependence of the NLD. Thus, from particle evaporation measurements, however, we can not get the absolute values of the level densities, but its variation as a function of E_X and J can be studied for a large variety of nuclear systems and most importantly in a wide range of E_X and J [34, 50, 69–73].

The slope of the high energy part of the spectra is directly related to the average nuclear temperature and hence the level density parameter 'a'. More hard energy spectra correspond to the high value of the temperature implying a slow variation of the NLD with E_X and hence a low value of the parameter 'a'. To further illustrate this let us consider two nuclei of mass number A=150 and 200, if both have same E_X=50 MeV, the slope of the particle spectra for A=200 will be more steep than A=150. Thus the particle spectra can provide the information about the level-density parameter 'a',

but averaged over a range of excitation energy.

The efficient detection methods for charged particles in comparison to the neutrons makes them superior probes. In case of charged particle emission (proton and α-particle) the high energy part well above the emission barrier is free from barrier penetration uncertainties related to the choice of the transmission coefficients required to calculate the inverse reaction cross section. Hence, by analyzing the only high energy part of the charged particle spectra one can study the E_X and J dependence of the NLD without any ambiguity due to barrier penetration factors.

This technique has two drawbacks [50]: (i) the particle evaporation spectrum is a result of multi-step decay leading to a average NLD, however by tagging the residual nucleus of well defined mass and charge this problem can be surmounted. Otherwise also, if we restrict to the high energy part of the spectra, the particle evaporation is almost close to the first chance decay of the CN populated at not too high an excitation energy. (ii) due to this multi-step decay process, the source velocity is not unique in the second and the following steps, only an average center-of-mass particle spectrum can be calculated from the measured laboratory spectra.

1.5 Angular momentum dependence of the NLD: Motivation of the first part of the thesis

The angular momentum, J dependence of the NLD has been a complicated and least studied topic. The general feature of the J-dependence of the NLD at a given E_X is a broad bump due to the multiplicative factors $(2J + 1)$ and $\exp\left(-\frac{(J(J+1))}{2\sigma^2}\right)$, which yield a maximum NLD at a J-value which increases slowly with E_X [69]. The factor $(2J + 1)$ corresponds to the increasing sub-levels at each J and hence the increasing NLD. But at the same time, with increasing J the rotational energy $E_{rot} = \frac{\hbar^2}{2\Im} J(J + 1)$ will increase with corresponding reduction in the intrinsic excitation energy hence reducing the NLD. Thus, these two multiplicative factors $(2J + 1)$ and $\exp\left(-\frac{(J(J+1))}{2\sigma^2}\right)$ results

in a modified Gaussian-shaped J dependence of the NLD. The width of this Gaussian function is determined by the spin-cut off parameter σ^2. It is the shape of yrast line which determine the increase of rotational energy as a function of J and hence the width σ^2. At a given E_X, the entire excitation energy will be locked in the rotational energy at a certain larger value of the J which will yield zero NLD, justifying the notation *"spin cut-off parameter"* for σ^2.

The spin cut-off parameter in the Fermi-gas model, is determined according to $\sigma^2 = \langle m^2 \rangle \, gt = \Im t/\hbar^2$, where $\langle m^2 \rangle$ is the average of the squares of the single-particle spin projections, t is thermodynamic temperature, and $\Im$ is the nuclear moment of inertia [23]. Since the thermodynamic temperature, t is directly related to the level-density parameter 'a', the uncertainty in the determination of σ^2 is not only because of the parameter $\Im$, but also the parameter 'a' itself. Experimentally, σ^2 can be determined only from spin distribution of low-lying discrete levels [74, 75]. These measurements correspond to a low value of compound nuclear spin of $\sim 5\hbar$. At higher excitation energies and angular momenta, the exclusive determination of the cut-off parameter becomes problematic due to higher level densities and the absence of the reliable observables sensitive to this parameter. In the absence of reliable experimental information on angular momentum distribution of levels over a wide range of J to validate σ^2, the Fermi-gas model values are used as such in reaction cross section calculations.

As discussed earlier, at high excitation energies and spins, the major source of information about the nuclear level-density is obtained from particle-evaporation spectra in heavy-ion fusion reactions analyzed in the framework of the phenomenological descriptions involving the level-density parameters 'a' and σ^2 [34, 69–73]. The moment of inertia, $\Im$ required in determination of σ^2, can be obtained with a good extent of accuracy at higher excitation energies from rotating liquid drop model [76], and thus the uncertainty in the cut-off parameter σ^2, remains dominantly due to the parameter

'*a*'. Therefore, information about the parameter '*a*' at high E_X and J becomes crucial. The excitation energy dependence of the parameter '*a*' has been investigated earlier from the particle evaporation measurements for a wide variety of excited nuclei [34, 73]. The level-density parameter '*a*' determined from these measurements is an averaged quantity over a range of excitation energies and angular momenta [71, 72]. The studies of the level-density parameter '*a*' with angular momentum selection are very few [77] and as a result the value of '*a*' is essentially unknown in high angular momentum domains for a great majority of nuclei. Therefore, it is important to carry out these investigations and this forms the basis of first part of the present thesis work. Since the α-particle spectra are more sensitive to yrast line than the protons, they provide a better scope to understand the J-dependence of the parameter '*a*'.

1.6 Statistical versus dynamical aspects of fission

As discussed earlier, in statistical decay of the heavy CN, fission is also a competing channel along with particle and γ-ray emission [22]. Unlike particle and γ-ray emission, fission is a quite complex process. During the fission process, the nuclear many-body system evolves through a large scale rearrangement of the nucleons and subsequently divides into two fragments of more or less equal masses [78, 79]. The splitting of a nucleus into two fission fragments is termed as binary fission. The fission process has been of continued interest starting from its mysterious discovery by Hahn and Strassmann [80] during 1939 in attempts to populate trans-uranium elements to the present contemporary physics of super heavy element formation where fission plays crucial role in determining the survival probability of the super heavy nucleus [81].

The liquid drop model (LDM) provided the first qualitative picture of the fission process, which has been developed over the years by Bohr and Wheeler [82], Swiatecki [83] and others [84]. During the complex nuclear fission dynamics, various degrees of freedom such as the elongation (deformation), mass asymmetry, etc. are involved in
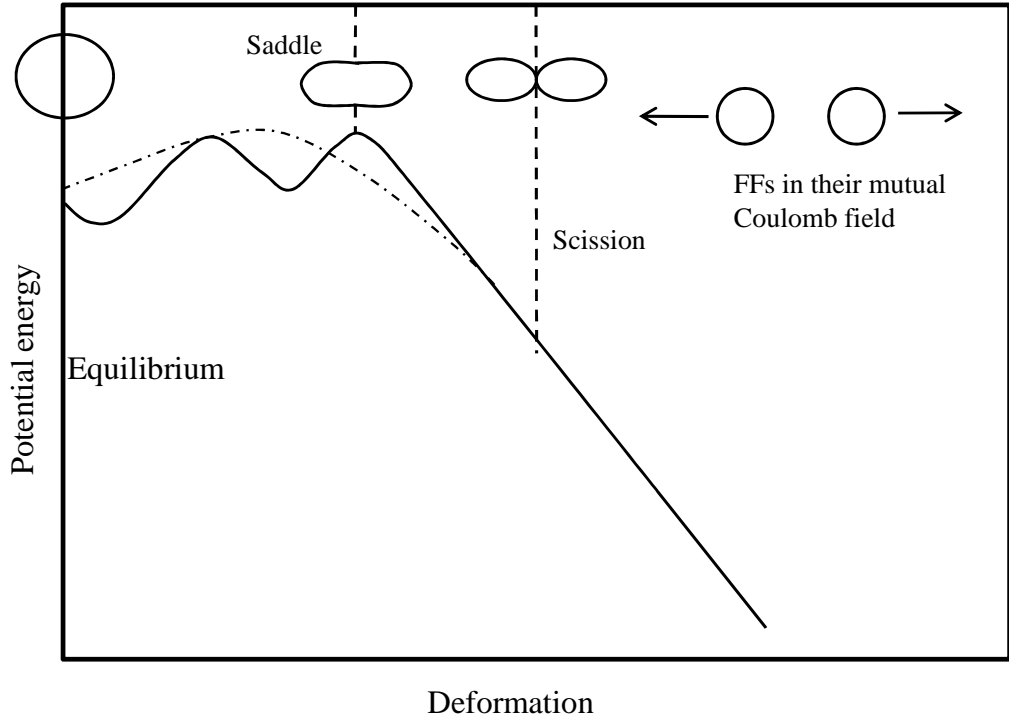
Figure 1.3: Schematic diagram of potential energy as a function of deformation calculated using liquid drop model (dashed line) and after incorporating the shell corrections (solid line).

the multi-dimensional potential energy surface which governs the dynamical evolution of the fissioning nucleus from ground state to the stage where two fission fragments are in just touching configuration [85, 86]. In the description of the LDM, the collective motion in the fission degree of freedom is resulted due to the oppositely varying surface and Coulomb energies as a function of deformation [78]. In addition to the macroscopic aspects of bulk matter such as surface and Coulomb energies, the fission process is also influenced by the microscopic effects of the finite number of fermions (e.g., shell correction) [87]. On the basis of the LDM one gets the smooth variation of the potential energy with deformation as shown by the dashed line in the Fig. 1.3, and after incorporating the shell effects, the potential energy curve is modified to double hump shape as shown by the solid line in Fig. 1.3 [87]. Existence of double hump barrier explains various low energy fission observables such as asymmetric mass distribution, occurrence of spontaneous fission isomers, etc. [78].

There are two landmark points during the fission process: saddle point and scission point. The maxima in the potential energy curve along the deformation axis is called the fission saddle point and its height with respect to the ground state represents the fission barrier. Beyond the saddle point the potential energy decreases and at some stage, called the scission point, the nucleus divides into two fragments and their motion is governed by the mutual Coulomb repulsion between them. Although the fission barrier height is much smaller than the total energy released in fission, it is the fission barrier which plays significant role in deciding the many characteristic properties of the fission process such as the spontaneous decay probability, fission cross section, fission fragment angular distribution, etc. [78]. The fission barrier height decreases as a function of fissility (a decisive parameter) of the fissioning nucleus. The fissility, x is defined as [88];

$$ x = \frac{Z^2/A}{50.883[1 - 1.7826I^2]}, \tag{1.22} $$

where Z and A refer to the fissioning nucleus and $I = (A - 2Z)/A$ is the measure of neutron excess. Larger fissility implies less stability against fission and saddle point shapes are close to the equilibrium ones, whereas the nuclei with lesser fissility are more stable against the fission having similar shapes for saddle and scission points.

1.6.1 Statistical fission decay width

The fission decay rate (or fission width) is conceptually different from particle and γ-ray emission widths, where density of states in residual nucleus determines the respective decay widths [22]. In case of fission, as such there is no residual nucleus. Despite these apparent differences, the fission can be treated in a manner almost analogous to the light charged particle emission [22] for which the decay width is expressed by Eq. (1.9). The transmission coefficient of Eq. (1.9) can be taken to be unity, if the total available energy is in excess of the fission barrier and zero otherwise (sharp-cut-off approximation). This is a good approximation in heavy-ion induced fusion-fission reactions. Following the Eq. (1.9), Bohr and Wheeler [8] formulated first quantitative

description of the fission decay width (Γ_{BW}) based on non-viscous liquid drop model;

$$\Gamma_{BW} = \frac{1}{2\pi\rho(E_{CN})} \int_0^{E_{CN}-B_f} \rho^*(E_{CN} - B_f - \epsilon)d\epsilon, \qquad (1.23)$$

where E_{CN}, B_{f}, and ϵ are the compound nucleus initial excitation energy, the fission barrier height, and the kinetic energy at the saddle point. The term $\rho^*(E_{\mathrm{CN}} - B_{\mathrm{f}} - \epsilon)$ is the level density at the saddle point, where most of the available energy has gone into the deformation and the available energy for intrinsic excitation and hence the density of intrinsic levels may be quite small. This is illustrated schematically in the Fig. 1.4 (taken from Ref. [22]), where the notation 'μ' refers to the different type of particles such as neutron, proton, α-particle, etc. and B_μ is the separation energy of the particle. A simplified expression for fission decay width is obtained if the level density is approximated by the Fermi gas model where $\rho(E) \sim \exp(2\sqrt{aE})$, $E = aT^2$ and with the condition $E_{CN} >> B_f$;

$$\Gamma_{BW} = \frac{T}{2\pi} \exp(-B_f/T), \qquad (1.24)$$

where a and T are the level-density parameter and the nuclear temperature, respectively. This description yields just the statistical fission width depending on nuclear temperature and fission barrier without invoking the dynamical features of the nuclear fission. The fission width derived from liquid drop based transition state model has been quite successful in explaining fission decay rates in low energy fission. But, the picture becomes more complicated with increasing excitation energy, where Bohr and Wheeler fission width fails in explaining the fission decay rates [89, 90].

1.6.2   Dynamics of nuclear fission: Nuclear Viscosity

Understanding the dynamics of nuclear fission from equilibrium to the scission point has received considerable attention over the years. It has been debated whether fission is an adiabatic (fast) or dissipative (slow) process [78]. Various experimental probes [90] and at the same time various models [91–94] have been explored to understand
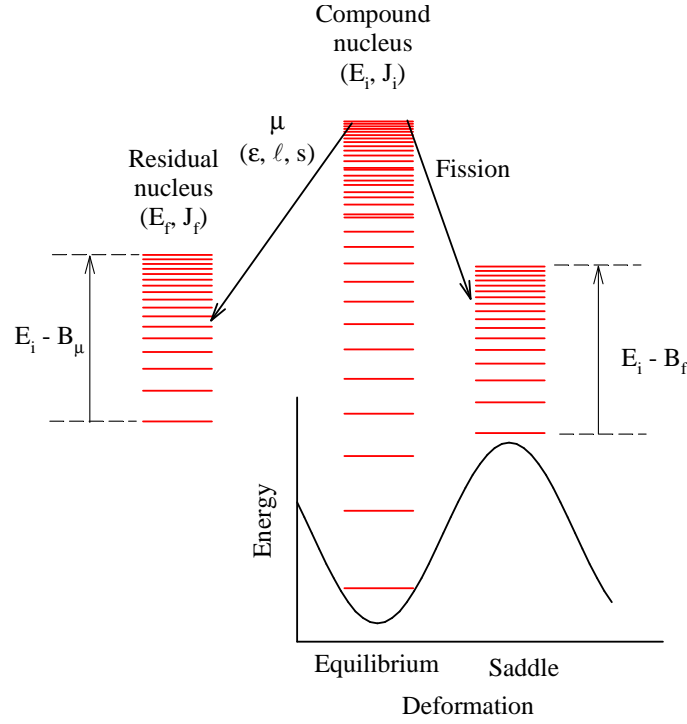
Figure 1.4: Schematic diagram showing the compound nuclear fission as a statistical decay. Notation 'μ' refers to the different type of particles such as neutron, proton, α-particle, etc. and B_μ is the separation energy of the particle.

the fission dynamics. A spate of experimental data from heavy-ion fission studies have resulted in the interesting observations of unexpectedly large prescission yields of neutrons [88, 90, 95], charged particles [96–98], GDR γ rays [99] from the compound system before fission. The standard statistical model underestimates the prescission yield of particles and γ rays, the discrepancy being larger at higher excitation energies ($\geq$ 40 MeV) [90]. These observations led one to think that sufficient time is not available for particles to evaporate prior to fission. In other words, the fission width calculated on the basis of phase space argument is overestimated by the statistical model at higher excitation energies. Since at lower excitation energies, the fission width is quite small and does not affect the particle emission width, the standard statistical model calculations hold good in lower excitation energy regime.

This realization motivated one to look beyond the statistical model and carry out more rigorous calculations of fission width invoking the dynamical effects which slow

down the fission process. The need for slowing down mechanism naturally suggests one to consider the effect of nuclear friction (viscosity) on fission lifetime [89, 90]. The 'non-viscous' liquid drop based transition state model does not invoke any dynamical feature and hence independent of the nuclear friction (or viscosity). It is however interesting to note that it is mentioned in the addendum of Bohr's paper [100] that 'non-viscous' fluid can hardly be maintained in view of the close coupling between the motions of the individual nuclear particles". Kramer took up this point [91] and prescribed the fission decay width as $\Gamma_{K_r} = K_r\Gamma_{BW}$, where Γ_{BW} is the Bohr and Wheeler fission width and K_r is the Kramer's factor. The factor $K_r = \left[\sqrt{1 + \gamma^2} - \gamma\right]$, where $\gamma = \frac{\beta}{2\omega_o}$ is friction coefficient, β is the dissipation coefficient, and ω_o is the potential curvature at the saddle point. The Kramer's idea emerged as a successful tool in explaining the heavy-ion fission cross sections.

Contributions to nuclear viscosity may arise from either nucleons colliding with a moving potential wall (wall and window one-body model) or from two-body collisions (as for ordinary fluids) between the nucleons [89, 90, 101–103]. The "two-body (or short mean free path)" dissipation mechanism is contradictory to the "one-body (or long mean free path)" mechanism, in which the exchange of energy between collective and microscopic degrees of freedom proceeds through collisions of the particles with a moving boundary of the system. One-body dissipation has the opposite effect on the prescission dynamical path compared to ordinary two-body viscosity which shifts the dynamical path toward increased fragment elongation. This occurs because neck formation is a process that involves large velocity gradients and that is consequently hindered by two-body viscosity [102]. In contrast, one-body dissipation shifts the dynamical path towards a more compact configuration. Understanding of the precise nature and magnitude of the nuclear viscosity and hence the energy dissipation during fission, remains one of the interesting aspects in nuclear physics. The temperature dependence of the nuclear viscosity is the contemporary physics interest extending up to the nuclear matter produced in relativistic heavy-ion collisions (RHIC) [104].

1.7 Probes to understand the nuclear viscosity during fission

In order to choose the suitable probe to understand the nuclear viscosity, we can divide the entire evolution from equilibrium to the scission point into three regions: (i) from equilibrium to the saddle (or pre-saddle), (ii) saddle to scission, and (iii) during rupture of the neck (during scission). The influence of dissipation during these stages of fission can be drastically different. The strength and nature of nuclear dissipation might be different at equilibrium deformation, the saddle, and the scission point, i.e., shape dependent [90]. It is the saddle to scission motion which is very sensitive to the nature (one-body versus two-body) and the magnitude of the nuclear viscosity. Nuclear dissipation might also be temperature dependent [90]. If the viscosity is very large which would result in over damped motion during the fission, the hot composite system would take more time to reach the saddle point configuration and cools down by emitting more particles and γ rays compared to the normal (non-viscous) motion. Due to this cooling effect, some of the nuclei which would otherwise have proceeded to fission, may not be able cross the fission barrier. This leads to an enhancement in the evaporation residue (ER) cross section and reduction in the fission cross section. Thus, the study of ER (or fission) excitation function can provide the information about the nuclear viscosity, but only in pre-saddle region. Following probes have been employed to gain information about the nuclear viscosity in the full dynamical region from equilibrium to the scission point:

1.7.1 Fission fragment kinetic energy

As mentioned above, the nuclear viscosity plays crucial role in determining the fission fragment shapes at the scission point and hence the kinetic energy of the fission fragments (FFs). By examining the FF kinetic energy in a large fissility range, some insight about the nuclear viscosity may be obtained. In low energy fission, the viscosity

effects are buried under the single particle effects (such as the shell and pairing effects). Therefore, FF kinetic energy data can not provide the information about the nuclear viscosity in low energy fission. However, at high excitation energies where the single particle effects are relatively small and most probable mass division is into two equal mass fragments, it could be considered as a suitable probe.

For heavy-ion fission, Davies *et al*. [101, 102] have compared the calculated and experimental most probable FF kinetic energies for the fission of nuclei over a wide mass range. The results calculated for non-viscous flow agree with the experimental values for light nuclei but are higher than the experimental values for heavy nuclei. This discrepancy may be removed either by two-body or by one-body dissipation, but the detailed manner in which this occurs is different in the two cases.

The final translational kinetic energy of the fission fragments at infinity may be decomposed conceptually into the contribution that is acquired prior to scission and the remaining contribution that is acquired from the scission point onwards due to mutual Coulomb repulsion [102]. For light nuclei, the relatively small distance between the saddle and scission points means that the prescission kinetic energy is always small. However, for heavy nuclei the relatively large distance between the saddle and scission points leads to a substantial prescission kinetic energy when the hydrodynamical flow is non-viscous. This prescission kinetic energy is reduced either by two-body or one-body dissipation. The two-body viscosity leads to a more elongated scission shape, the postscission kinetic energy would be lesser in this case than the non-viscous flow if viscosity coefficient μ is assumed to be infinite. The experimental FF kinetic energies are reproduced satisfactorily in terms of two-body viscosity when the viscosity coefficient μ has the value [101, 102];

$$\mu = 0.015 \pm 0.005 \text{ TP} = (9 \pm 3) \times 10^{-24} \text{ MeVsec/fm}^3 \qquad (1.25)$$

where TP termed as the terapoise. For comparison, the viscosity of water is 1.002 cp (centipoise) at 20°C, which is less than the above nuclear viscosity coefficient by a
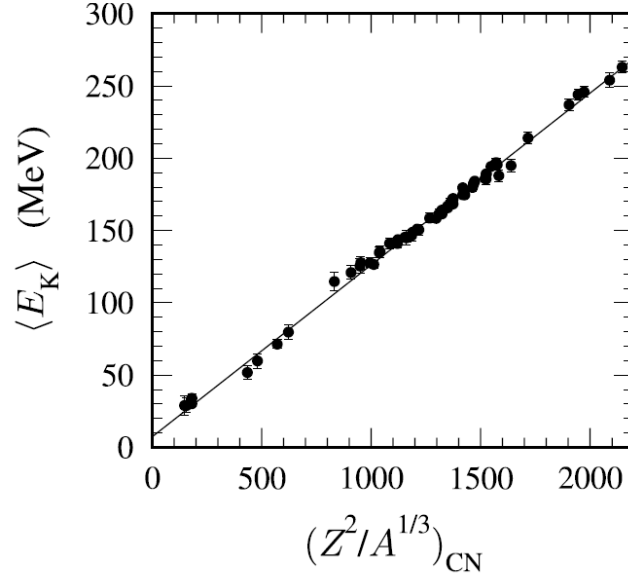
Figure 1.5: Mean FF kinetic energy $\langle E_K \rangle$ as a function of the Coulomb parameter $(Z^2/A^{1/3})_{CN}$ of the fissioning compound nucleus. The solid line represent the most recent fit to the data (Viola systematics [105]).

factor of $\sim 10^{12}$.

Because the one-body dissipation leads to more compact scission shape, postscission kinetic energy is large. The combined effect of the decreased prescission kinetic energy and increased postscission kinetic energy fit the experimental data of FF kinetic energies. Thus experimental FF kinetic energy data are explained by both the one-body and two-body dissipation mechanisms, which clearly indicate that the reproduction of fission fragment kinetic energy alone is not sufficient to understand the magnitude and nature of nuclear viscosity.

Moreover, as mentioned earlier, most of the available excitation energy of the fissioning nucleus is lost prior to scission via particle or γ-ray emission, the FF kinetic energy remains almost constant with varying excitation energy of the nucleus. Fig. 1.5 depicts a plot of the most probable kinetic energy release $\langle E_K \rangle$ vs. the Coulomb parameter $Z^2/A^{1/3}$, in the rest frames for a large number of fissioning systems over a range of excitation energies. The solid line is a result of the least squares linear fit to
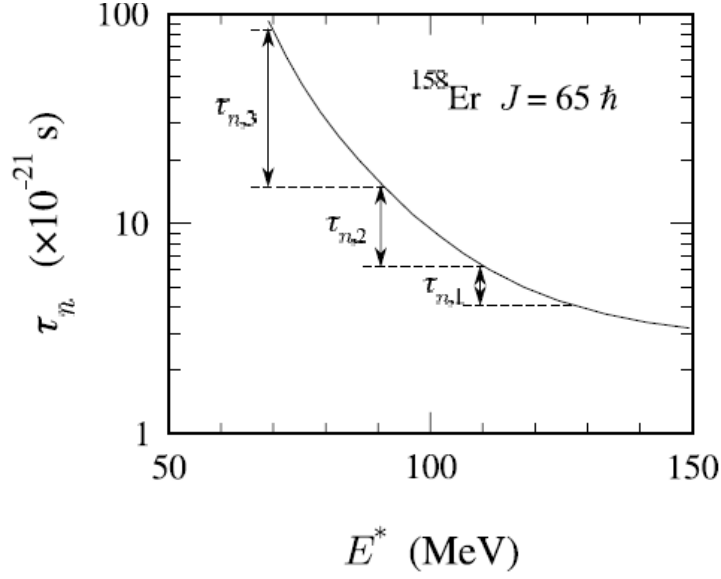
Figure 1.6: Dependence of the neutron evaporation time on excitation energy of the emitting system. The mean evaporation time of the ith neutron in a cascade are schematically indicate by τ_i, taken from Ref. [90].

the data which leads to the relation [105]:

$$< E_K >= (0.1189 \pm 0.0011)\frac{Z^2}{A^{1/3}} + 7.3(\pm 1.5) \text{ MeV}, \qquad (1.26)$$

where Z and A refer to the fissioning nucleus. This seemingly simple expression is commonly referred to as the Viola systematics [105]. Thus, the FFs kinetic energy data spanning a wide range of excitation energies are just determined by the parameter $Z^2/A^{1/3}$, leaving no scope to extract the temperature dependence of the nuclear viscosity.

1.7.2 Prescission neutron or charged particle emission

Prior to scission, an excited heavy-nucleus can decay by sequential emission of neutrons or charged particles. Measurement of evaporated charged particle and neutron multiplicities emitted during the fission process have been used as a "clock" to allow estimation of the dynamical fission time scale [90, 95]. This quantity is critically dependent on the magnitude of nuclear viscosity. The basic idea of this method is to measure the number of evaporated light particles prior to and post the scission point.

The mean evaporation time for one particle (either neutron or any charged particle), defined as $\tau_p = \hbar/\Gamma_p$, where Γ_p is the particle decay width and is an exponential decreasing function of the instantaneous excitation energy of the emitting system as shown in the Fig. 1.6 as a typical example for the case of neutron emission (from Ref. [90]). The particles are assumed to be emitted sequentially from the excited nucleus, with an increasing mean time between emissions as the available excitation energy decreases. The prescission lifetime of the fissioning nucleus can be estimated by summing the emission times of the prescission particles in an event [95];

$$\tau_{pre} = \sum_{i=1}^{M_{pre}} \tau_{p,i} = \sum_{i=1}^{M_{pre}} \frac{\hbar}{\Gamma_{p,i}}. \tag{1.27}$$

where M_{pre} is the prescission particle multiplicity. Eq. (1.27) forms the principle of prescission particle clock. Prescission particles can be distinguished from the postscission ones by examining their angular distributions relative to direction of motion of the emitting source. Such measurements have shown that at lower excitation energies and fissility, agreement with statistical model calculations using standard parameters can be obtained but at higher excitation energies and/or fissility, the experimental yields exceed significantly those calculated with statistical models [95]. This can be explained in quite general terms. In the statistical model described above, the time scale for fission at a certain step i^{th} in the evaporation chain can be defined as $\tau_{stat} = \hbar/\Gamma_{tot}^i$ where $\Gamma_{tot}^i = \Gamma_f^i + \Gamma_p^i$. Due to higher excitation energies and/or fissility, the time scale τ_{stat} can become very short (10^{-22} s or less). It is not realistic to expect a complex collective phenomenon such as the nuclear fission to occur on such a short time scale. Indeed, classical hydrodynamical calculation for a nucleus without any fission barrier and considering 'non-viscous' nuclear fluid, show that it takes several 10^{-21}s for the nucleus to move from saddle to scission configuration. In the realistic case, in addition to the time delay due to large scale rearrangement of nucleons, the effect of nuclear viscosity is to slow the motion towards the scission point. A longer saddle to scission time will result in a higher prescission particle multiplicity, thus the latter quantity can be used

to gain information on nuclear viscosity in a rather direct way. Further, the effect of viscosity is to delay the onset of fission, due to time delay in establishing the equilibrium population at the saddle point. Sum of the time delay before the onset of fission and the saddle to scission transit time, both of which depend on viscosity, is described as the dynamical fission time scale. The difference of dynamical fission time scale with respect to the statistical fission time scale (τ_{stat}) is referred as the fission-delay [95].

In last several years extensive measurements have been carried out for prescission neutron and α-particle multiplicities with the motivation mainly to extract the fission time scales and gain information about the nuclear viscosity. In 1986 Gavron *et al.* [106], Hinde *et al.*, [107], and Zank *et al.* [108] explained the excess multiplicity in their measurements in terms of reduced nuclear dissipation coefficient (β). Gavron *et al.* arrived at an upper limit of $\beta \leq 5 \times 10^{21}$ s^{-1} for the reduced nuclear dissipation coefficient. Zank *et al.* obtained a viscosity coefficient, μ to be 0.1 TP assuming two-body viscosity which corresponds to a total fission time of 30-120 zs (1 zs = 10^{-21} s) to explain the excess neutron multiplicity. Hinde *et al.* explained the excess neutron multiplicity in their measurement as arising from the delayed onset of fission with a delay time (compared to standard statistical model) of 70 zs or a slow saddle-to-scission transition of 30 zs. In summary, all deduced dissipation coefficients are consistent with an over damped motion of a fissioning nucleus.

As far as prescission charged particle emission is concerned, despite their low multiplicities they offer some advantages over neutron emission such as; (i) easy detection and (ii) very sensitive to the deformation of the emitting source. The prescission α-particle multiplicities (α_{pre}) have been measured for a variety of compound nuclear systems. In the work by Ikezoe *et al.* [98], the excess multiplicity could be explained in terms of deformation of the fissioning nuclei. Before reaching the scission point, the nucleus deforms continuously and this leads to a lowering of the emission barrier for charged particle emission. This reduction in the barrier enhances charged particle

emission. But, their work did not consider changes in the particle binding energies arising due to deformation. In 1991 Lestone *et al.* [109] have pointed out this fact and shown that fission has to be considered blocked for ∼60 zs in order to explain the results of their measurement of prescission charged particle multiplicity.

Later on, the prescission neutron, proton, and α particle multiplicities have also been measured simultaneously for some of the systems to improve the knowledge of fission time scale [97, 98, 110]. Thus, substantial efforts have been made, both experimentally and theoretically, but the precise nature and magnitude of nuclear viscosity remains one of the major problems as yet unsolved in nuclear physics. So far there exist no clear experimental evidence from prescission particle yields on temperature dependence of nuclear viscosity. The difficulty is simply due to the fact that at high temperature the cooling time by light particle evaporation is considerably smaller than any characteristic time for collective motion. In other words, with increasing excitation energy the neutron decay time decreases exponentially, therefore, if we increase the excitation energy, accordingly neutron multiplicity increases, leaving no scope to study the temperature dependence of the nuclear viscosity [90].

1.7.3   GDR-γ-ray emission

Very similar to above described prescission particle multiplicity, the emission of high-energy γ rays from the giant dipole resonance (GDR) excited in the hot fissioning compound nucleus prior to scission has been used as a probe to gain new insights into the properties of nuclear dissipation [99]. This technique became available after it was realized in the mid-1980s that the GDR of a hot nucleus could be measured easily and after its properties were established systematically as a function of nuclear mass and temperature. In the case of particle emission, the decomposition between pre- and post-scission components is obtained by their angular correlations with respect to the emitting source. In the case of GDR γ rays, the fission fragment contribution must

be subtracted carefully from the total spectrum. The GDR in the hot nucleus emits γ rays according to the strength function;

$$F(E_\gamma) = 2.09 \times 10^{-5} \frac{NZ}{A} . S. \frac{\Gamma_{GDR} E_\gamma^4}{(E_\gamma^2 - E_{GDR}^2)^2 + \Gamma_{GDR}^2 E_\gamma^2}, \qquad (1.28)$$

where N, Z, A refer to the fissioning nucleus, S is the classical sum rule strength, E_γ and Γ_{GDR} are the GDR γ-ray energy and width, respectively. It is the Γ_{GDR} which is very sensitive to the deformation and hence play crucial role in decomposing the total GDR yield into pre- and post-scission components. The GDR energies are essentially unaffected by temperature ($\pm$ 3%) and can thus be taken from ground-state systematics. Thus the GDR clock has several advantageous features: (a) the simplicity of the GDR strength function and the absence of truly free parameters; (b) the fact that its rate does not depend on transmission factors; (c) the GDR vibrational time scale $\hbar\omega$ = 10 - 15 MeV, which is much faster than all fission time scales and thus ensures that the strength function follows the evolving deformation of the fissioning nucleus; and (d) the sensitivity of the GDR strength distribution and the γ-ray fission angular correlation to the deformation of the nucleus at the time of γ-ray emission. The prescission GDR γ-ray multiplicity has been determined for a variety of compound nuclear systems. It is seen that similar to prescission particle multiplicities, the prescission GDR γ-ray yield also exceeds the standard statistical model predictions, indicating the fission hindrance. According to this probe the dissipation sets in rather rapidly at nuclear excitation energies above >40 MeV, depending somewhat on the reaction and mass of the compound system. These excitation energies correspond to compound nucleus temperatures of T $\sim$ 1.3 MeV. In addition, the GDR clock demonstrates that above this temperature, strong dissipation is present inside the barrier, with a dissipation constant γ_i = 10($\pm$3), as well as outside the saddle, with γ_o = 5 ($\pm$ 1) [99]. Thus the mass motion is strongly over damped everywhere. Majority of the data are consistent with a two-body viscosity inside the saddle and one-body viscosity outside the saddle.

1.8 Near-scission emission (ternary fission)

Employing above probes the effect of nuclear viscosity inside and out side the saddle has been understood to a good extent. However, at the time of scission, the actual tearing up of the neck joining the two nascent fission fragments is still not clearly understood. Moreover, the probes mentioned above are not suitable in a wide energy regime from spontaneous fission to the heavy-ion fission. A suitable probe sensitive to scission point needs to be employed to address the above questions. Ternary fission presents a good choice for studying the nuclear viscosity at scission in the wide energy regime [90]. The energy spectra and angular distributions of the ternary particles show that they are generated close to the scission (rupture) point, between the two main fission fragments. Ternary fission is thus often referred to as near-scission emission (NSE). Using the NSE as a probe, the scission point characteristics such as the kinetic energy of the FFs, neck radius, FF separation, etc. can be determined. The kinetic energy at scission point carries important information about the transition from saddle to scission and energy dissipation during this transition. Thus the NSE can provide the information not only during the scission process but also during the descent from saddle to scission. In the present work, the NSE has been used as a probe to gain insight about the nuclear viscosity. In low energy fission (spontaneous, thermal neutron, and photo-fission) detailed investigations have been carried out for the ternary fission [78, 111, 112] and their characteristics are discussed briefly here.

1.9 Characteristics of near scission emission in low energy fission

Investigations from low energy fission show that 90% of ternary particles are the α-particles which are also called as long range alphas (LRA) in order to differentiate from less energetic alphas from radioactive decays. Other particles such as triton, deuteron, and proton have significantly lower probability of emission in ternary fission. There is

a very rare process that generates a third light charged fragment close to the direction of motion of the main two fission fragments. This is often called polar emission. To distinguish the dominant ternary-fission process from the rare polar emission, they are sometimes referred to as equatorial ternary fission (ETF) and polar ternary fission (PTF), respectively [113]. In this thesis work, we have studied mainly the ETF for understanding the fission dynamics. Their various characteristics from low energy ternary fission are discussed in following sub-sections.

1.9.1 Probability of ternary charged particle emission

Probability of different ternary charged particle emission is closely related to the average energy cost (E_c) of the near scission emission. The larger the value of E_c, the smaller the expected likelihood for the particle emission. Halpern [111] gave a simplistic formulation of the energy cost according to which the average energy required for removing a particular third particle from one of the binary fragments and place it in the midway between the two fragments will be;

$$E_c = B + \Delta V + K_e \qquad (1.29)$$

where B refers to the binding energy of the third particle in the mother fragment, which can be calculated using the experimental masses. In Eq. (1.29), K_e is the average kinetic energy with which the third particle is born, which is a model dependent parameter. ΔV is average Coulomb potential energy (V) difference between the corresponding binary and ternary configurations;

$$\Delta V = V(\text{Ternary.Configuration}) - V(\text{Binary.Configuration}). \qquad (1.30)$$

To calculate the value of ΔV, in the Halpern's description it is assumed that for given binary fragments of charges Z_1 and Z_2, the third fragment Z_3 appears midway between Z_1 and Z_2 in the corresponding ternary configuration as shown in the Fig. 1.7(a). In this figure the particle Z_3 has been taken entirely from Z_2 and displaced the residual
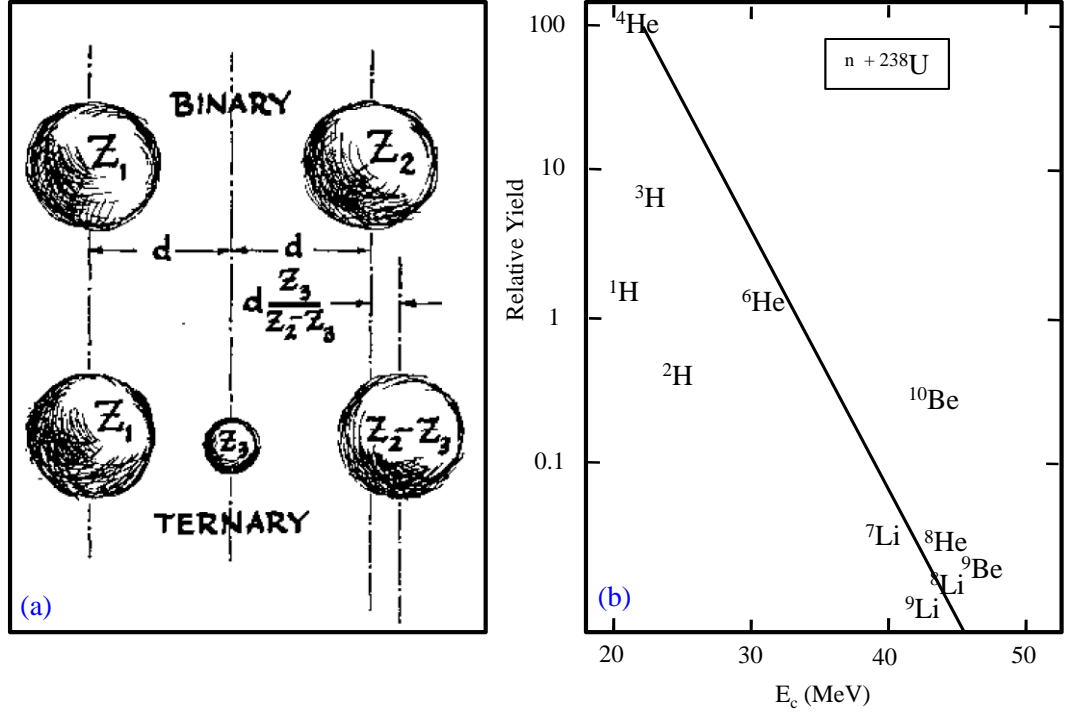
Figure 1.7: (a) A diagram to show how much larger the inter-particle Coulomb energy is in a ternary configuration than the corresponding binary configuration. The third particle (Z_3) is removed from one of the binary fragments (Z_2) and placed at a point midway between Z_1 and Z_2 while the residual fragment (Z_2-Z_3) is displaced slightly in order to keep the center-of-mass at the same place for both configurations. (b) The measured relative yields of various ternary particles as a function of energy cost (E_c) in the fission of ^{235}U with slow neutrons. The yields are given as percentages of the α-particle yield. Both the figures are taken from Ref. [111].

fragment (Z_2-Z_3) so that the center-of-mass of the entire system has not moved, which leads to:

$$\Delta V = \left(\frac{Z_2 Z_3}{d} + \frac{Z_1 Z_3}{4d} \right) e^2, \qquad (1.31)$$

where d is half of the center-to-center distance of two fragments in their binary configuration as shown in the Fig. 1.7(a). Eq. (1.31) reveals that as the third particle charge increases, the Coulomb contribution to the energy cost increases and it remains same for different isotopes of a given element. The energy cost for α-particle and proton are similar, because reduction in binding energy of α-particle in the mother fragment is compensated by reduced ΔV of hydrogen isotopes. Assuming $K_e = 2$ MeV, Halpern [111] calculated the E_c for various ternary charged particles observed in ^{235}U(n, f) re-

action, and plotted the relative yields as a function of E_c as shown in the Fig. 1.7(b). It is seen that other than hydrogen isotopes all the third particle yields are following the decreasing trend with increasing energy cost. The discrepancy of hydrogen isotopes from the trend is least for the heaviest triton (a factor of ten from its place).

However, it may be noted that the above model is an oversimplification of the real situation. It does not include nuclear-force, fragment deformation, and final state interaction effects in the calculation of the energy cost.

1.9.2 Energy distributions

The observed ternary charged particle energy spectra are nearly Gaussian in shape. The simplest interpretation of the Gaussian shape is that the final energy of the emitted ternary particle is determined by the relatively independent initial variables such as the position, direction, and kinetic energy with which it was born. In the low energy fission it is observed that the peak (or mean) energy of a given third charged particle decreases with increasing mass as shown in the Fig. 1.8(a) for He-isotopes [111, 112]. The peak energy of the ternary α-particle is constant between 15-16 MeV irrespective of the Z and A of the fissioning nucleus as shown in the Fig. 1.8(b). The shape of the scission configuration and the kinetic energies of the FFs at the time of scission play significant role in the determination of the α-particle final energy. It should be noted here that the final energies of the ternary α particles are much less than the energy cost, E_c. The width (FWHM) of the ternary α-particle is quite large ($\sim$10 MeV) which results from the dispersion in the initial conditions. Similar to the peak energy the energy-width is also nearly constant for all the fissioning nuclei.

Since experimentally we measure the final energies of the FFs as well as the characteristics of the third particle, using inverse trajectory calculations the scission point parameters can be determined. If it is assumed that at the time of scission the FFs are either stationary or moving very slowly and the initial kinetic energy of the α particle
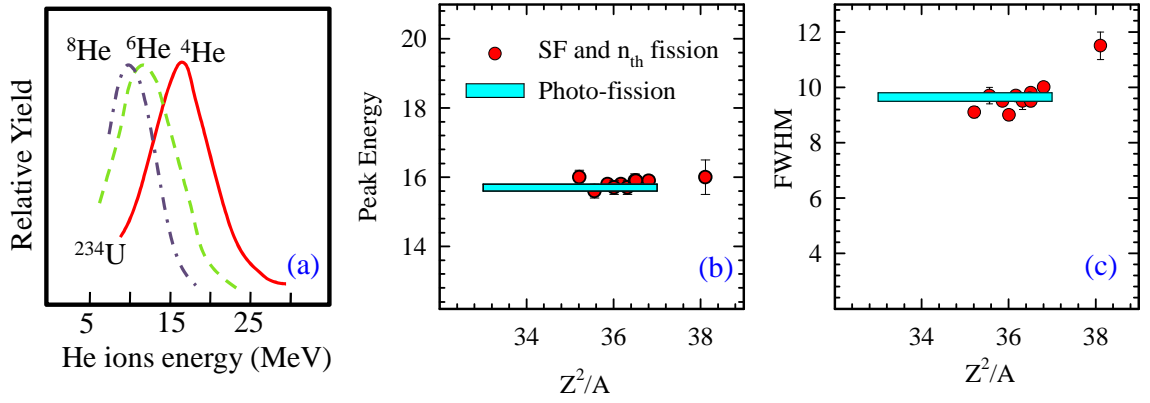
Figure 1.8: (a) Energy distributions of the ternary He-isotopes produced in the fission of ^{234}U [111]. Peak energy [in (b)] and width (FWHM) [in (c)] of the energy distributions for the ternary α particles produced from various fissioning systems in low energy fission [spontaneous fission (SF), thermal neutron (n_{th}), and photo-fission], taken from Refs. [78, 111, 112].

is very small (say 2 MeV), then it is observed that the calculated asymptotic kinetic energies of the α particles are much larger than the experimentally observed values. The large computed values are essentially because the third particle is so much lighter than the FFs that they acquire a large component of potential energy if they are given a slight start. The difference between experimental and calculated values indicate about the large kinetic energy of the FFs at the time of scission. According to the two-body viscosity, the kinetic energy of FFs at the scission point increases with the fissility [102], reducing the Coulomb potential energy to be taken away by the α-particle. This results in constant peak energy of the ternary α particles for all the fissioning nuclei. However, from trajectory calculations [114–117] no unique set of scission point parameters could be obtained mainly because of larger number of scission parameters and limited amount of experimental information relevant to the scission configuration.

1.9.3 Angular distributions

Similar to the energy distribution, the angular distribution of the ternary α-particles is Gaussian in shape [111, 112]. For the symmetric fission, the Coulomb forces exerted by the two nascent FFs on the third charge particle will make it to be emitted pref-

(a): Symmetric Fission   (b): Asymmetric Fission
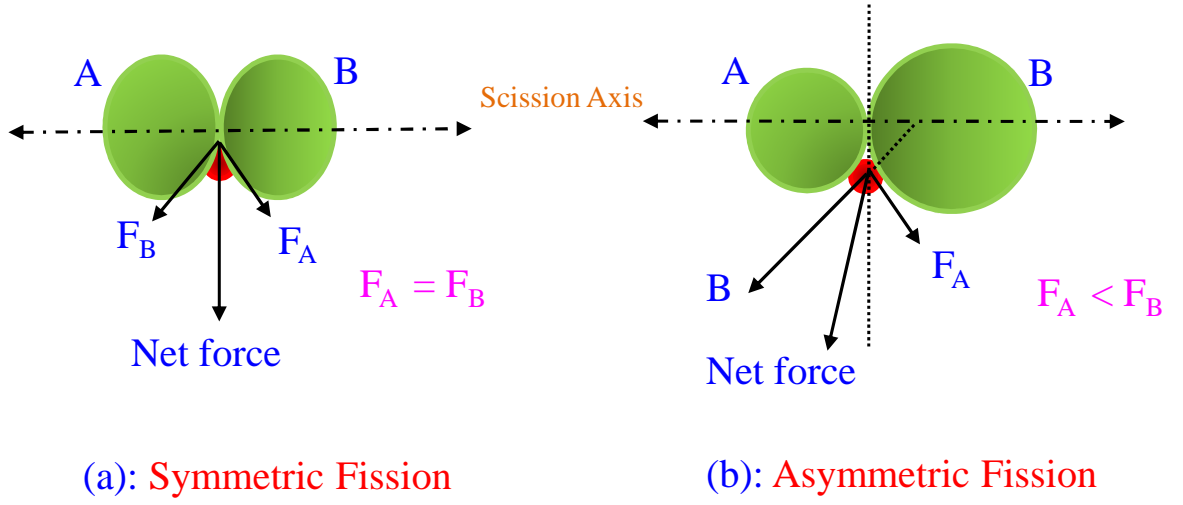
Figure 1.9: Cartoons depicting the ternary fission process. In symmetric fission (a), cancellation of the scission-axis parallel components of the Coulomb forces on the ternary particle (F_A and F_B) exerted by the two equal mass fragments A and B, gives rise the characteristic angular and energy distributions of the ternary α particles. In case of asymmetric fission (b), the unequal Coulomb forces make the angular distribution to peak at an angle slightly less than 90° with respect to the scission axis.

erentially perpendicular to the scission axis as shown schematically in Fig. 1.9(a). In the low energy fission, since the mass distribution is asymmetric the Coulomb force exerted by the heavy fragment is more than the light fragment which results in more than 90° with respect to the heavy fragment and less than 90° with respect to light fragment [Fig. 1.9(b)]. In the low energy fission, the angular distributions for all the light charged particles follow the similar trend as observed for the α-particles. In ternary fission, a correlation between average kinetic energy of the α-particle and the angle of emission has been observed. The kinetic energy of the α-particle increases as the angle changes away from the most probable one. Conversely, this effect can be described as broadening of the angular distribution for α-particles with energies considerably above the average energy [118, 119].

The width of the angular distribution is attributed to position and momenta of the particles at the time of scission. The broader the angular distribution, the larger the separation between the main FFs at scission and larger their kinetic energy at
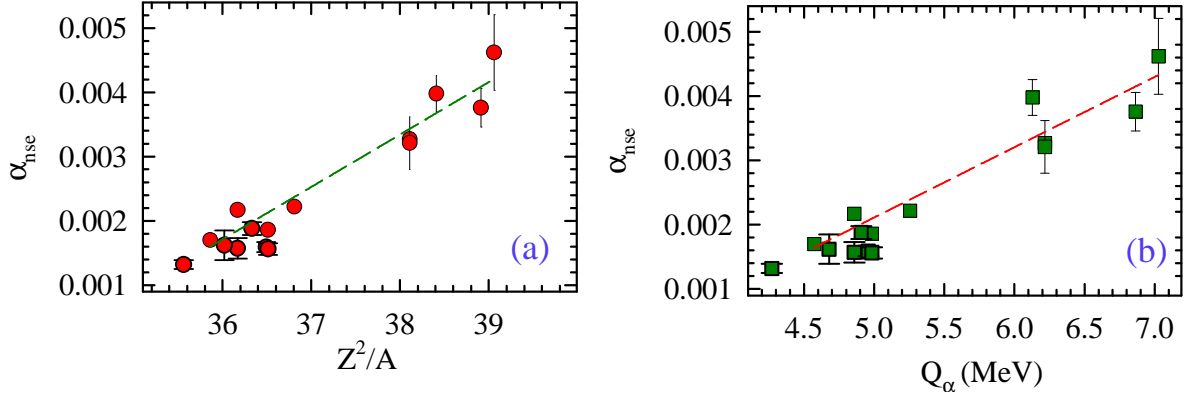
Figure 1.10: Near scission α-particle multiplicity (α_{nse}) as a function of Z^2/A [in panel (a)] and α-particle emission Q-value (Q_α) [in panel (b)] from low energy fission data.

that time. There is still some disagreement among experimenters about the widths of these distributions. The most detailed measurement for ^{252}Cf gives the FWHM of the α-particle angular distribution as 32.5° [120]. There is another measurement, however, which gives only $\sim$0.7 of this value [115]. There are also two measurements of the distributions from the slow neutron fission of ^{235}U, one with emulsions and the other with counters, resulting the FWHM to be 29° and 20°, respectively [111]. To further complicate the picture, the angular distribution in the fission of ^{238}U with protons is found to be about 50% wider than that from the spontaneous fission of ^{252}Cf [121].

1.9.4 Dependence of the ternary α-particle yield on Z^2/A

From the compilation of all the low energy fission data, it is observed that α-particle yield increases almost linearly with the fissility parameter Z^2/A and α-particle emission Q-value (Q_α) as shown in the Fig. 1.10(a) and (b), respectively. This observation is consistent with the idea that the ternary yield is dependent on the amount of deformation at the time of scission. Liquid drop model calculations have shown an increase in the deformation energy at the scission with increasing Z^2/A [78, 112]. This is due to the fact that with increasing fissility, the saddle shapes are close to the equilibrium shape and change in potential energy between saddle and scission points increases.
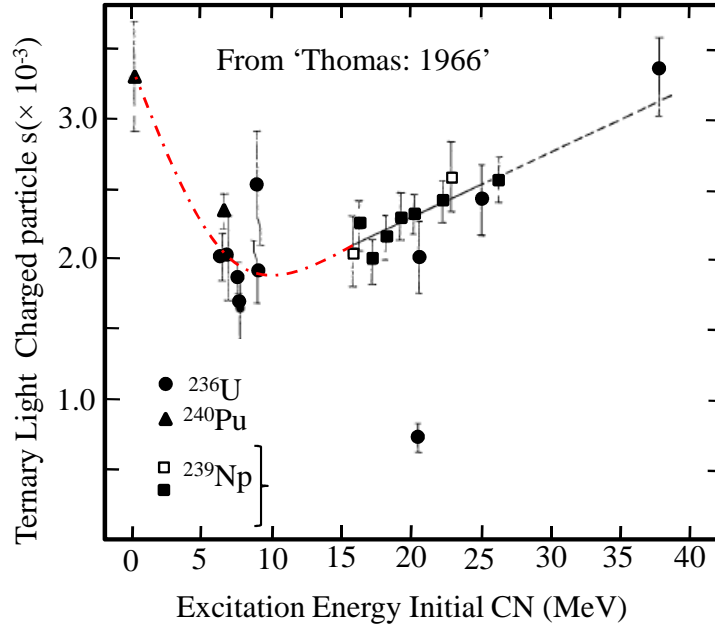
Figure 1.11: Excitation energy dependence of the ternary light charged particles from low energy fission. The dashed and dash-dot lines are shown to guide the eye.

This behavior is consistent with the viscous stretching of the nuclear system during saddle to scission motion, more precisely it indicates about the presence of two-body viscosity during saddle to scission motion which favors the stretched scission configuration. Since Q_α also increases with Z^2/A, the α_{nse} values in low excitation energy fission appears to be increasing with Q_α.

1.9.5 Excitation energy dependence of the ternary α-particle yield

The excitation energy dependence of the ternary α-particle yield is observed to be fairly weak in the region of 6 - 20 MeV as shown in the Fig. 1.11. But at the same time it has also been conclusively established that the ternary yield in thermal or 1-MeV neutron induced fission (corresponding $E_{CN} = 6$ - 8 MeV) is less than in spontaneous fission of the same fissioning nuclei [122–124]. This behavior suggest that there might be a minimum in the α-particle yield if measured at various energies in the interval of 1 to 20 MeV as indicated by the dashed line in the Fig. 1.11. This possibility is

supported by the studies of light charged particle induced fission, where one finds that ternary α-particle yield increases very slowly with the excitation energy above 15 MeV up to 30 MeV as shown in the Fig. 1.11. In any case, the α-particle yield depends only weakly on excitation energy in the range of 6 - 20 MeV. Perhaps this behavior is connected with the observation that average fragment kinetic energies are essentially independent of the initial excitation energy.

1.9.6   Possible models to explain ternary fission

The models which are successful in describing binary fission are difficult to apply for ternary fission. In the binary fission models the introduction of third particle is not foreseen. Various models have been attempted to understand the characteristics of the ternary fission data observed from low energy fission. All the models can be grouped into the three categories: (i) statistical models (ii) dynamical models, and (iii) combination of both.

1.9.6.1   Statistical evaporation of the ternary particles

As discussed earlier, energy dissipation takes place during the fission from collective degrees of freedom to the internal excitations of nucleons. Therefore at the time of scission some excitation energy is available which gets transferred to the fission fragments in binary fission. One can argue that similar to compound nuclear evaporation, the ternary charged particles are also evaporated at the time of scission [111]. The relative probability of ternary fission over binary fission is dominated by the factor $\exp\left(-E_c/T\right)$, where E_c is the mean energy cost of emitting a third particle and T is the nuclear temperature (Boltzman factor) at the time of scission. As mentioned earlier, the energy cost E_c for α-particle is $\sim$20 MeV and the nuclear temperature $T \leq 1$ MeV. These values imply the ternary α-particle yield to be order of magnitude smaller than the experimentally observed results. The Boltzman factor implies the steep excitation energy dependence which is contradictory to the experimental observation of

weak excitation energy dependence. Moreover, the observation of constant peak energy of the ternary α-particle irrespective of the Z and A of the fissioning system, is inconsistent with a statistical emission mechanism in which emission barriers follow a standard Z dependence. Therefore, standard statistical evaporation can be ruled out at least in low energy ternary fission. This has led many authors to conclude that ternary fission is a dynamical process and not associated with an evaporative process in low energy fission.

1.9.6.2 Dynamical emission of the ternary particles

Halpern suggested that if the approach from saddle to scission is non-adiabatic then the energy stored initially in distortions can be transferred non statistically to a third particle at the time of scission [78]. According to this model [111, 125], the neck joining the two nascent fragments collapses suddenly (very fast) and a light charged particle in the neck region feels a rapid change in the nuclear potential energy. This rapid change in the nuclear potential can result in the gain of an individual particle. A slow collapse of the neck would warm up the whole nucleus and the only possibility remain is the statistical emission and there would be trouble in accounting for the emission rates as discussed above. But if the neck collapse is fast enough, there are small but finite chances for individual particles to acquire sufficient energy from rapidly changing nuclear potential in the region between the two fragments to find themselves free and unbound.

However, the initial suggestion of Halpern has not been used to obtain a quantitative description of ternary fission, but qualitatively main features of ternary α-particle emission from low energy fission are consistent with this model, for example: (i) the linear increase of α-particle yield as a function of Z^2/A of the fissioning system is consistent with liquid drop model calculations for dynamical emission of α-particles near the scission configuration as the gain in potential energy from saddle to scission increases with Z^2/A [78, 112], (ii) the weak excitation energy dependence of the α-

particle yield is in favor of the dynamical model, (iii) constant mean energy of the α particles also favors the dynamical model.

Over the years, many other dynamical models have been developed with a motivation to understand the ternary fission observables quantitatively. These include models involving an extension of the theory of particle emission from actinide ground states to a rapidly evolving system in the last phase of the fission process, double-neck rupture, and other dynamical models reviewed in Ref. [126]. Although each of these dynamical models has had limited success in reproducing some of the features observed in the experimental data, no satisfactory simultaneous reproduction of a large amount of experimental data has been achieved.

1.9.6.3 Combination of statistical and dynamical emission

A combined statistical and dynamical model of ternary fission has been recently introduced by Lestone [113, 127]. In this model, statistical theory is used to calculate the probability that the particles are evaporated from the nuclear surface with insufficient energy to surmount the Coulomb barrier. These quasi-evaporated particles exist between the nuclear surface and the Coulomb barrier for a short period of time before returning to the nuclear fluid. Potential ternary particles are first quasi-evaporated into the region surrounding the prescission neck material. Then, due to the rapid collapse of the neck material, quasi-evaporated particles above the neck-rupture location experience a rapid rise in their nuclear potential and are ejected perpendicular to the direction of the main fragments via a purely classical process. This particle emission mechanism can be viewed as a coupling of the sudden approximation first suggested by Halpern and particle evaporation, and has been used to explain many of the properties of ^{235}U (n_{th}, f) ternary fission [113]. However, others have suggested that the classical concepts used in the combined statistical and dynamical model are invalid, and that the results are not consistent with an evaporative process occurring in low-energy ternary fission [113].

1.10 Ternary emission in heavy-ion fission: Motivation of the second part of the thesis

In heavy-ion induced fusion-fission reactions, neutron and charged-particle (mainly proton and α-particle) emission takes place from various stages namely from the fissioning compound nucleus (prescission) and from the accelerated fission fragments (postscission) [96, 97] as schematically shown in the Fig. 1.12. Prescission neutron and charged particle emission spectra and multiplicities provide important information on the statistical and dynamical aspects of the fusion-fission process [96, 97]. The prescission neutron multiplicity, ν_{pre} has been shown to have a linearly increasing dependence on the compound nucleus excitation energy (E_{CN}) [88, 128], whereas prescission charged-particle multiplicities increase non-linearly with E_{CN} [98, 128]. Although there have been many studies on prescission α-particle emission in heavy-ion induced fusion-fission reactions [96–98, 129–132], a global systematics is yet to be developed. In case of α-particle emission, it is observed that particles are also emitted very near the neck region in the fission process just before scission, akin to the ternary fission events in low energy fission [129–133]. This part of prescission α-particles emitted near the neck region is termed as near scission emission (NSE). Although there have been many studies on prescission α-particle emission in many heavy-ion induced fusion-fission reactions [96–98, 129–132], a global systematics is yet to be developed. In low energy fission, NSE is a dominant channel [78, 111, 112] and exhibits characteristic energy and angular distributions corresponding to strong focusing of the particles by the Coulomb field of the fragments, as discussed earlier. The features of the NSE observed in low energy fission have been understood qualitatively with sudden neck collapse dynamic model suggested by Halpern [111]. However, the validity of such a model has not been proven at elevated excitation energies and over a wide range of Z^2/A of fissioning nuclei typically encountered in heavy-ion induced fusion-fission reactions.

In the work by Lestone *et al.* [97], it is observed that the NSE α-particle yield
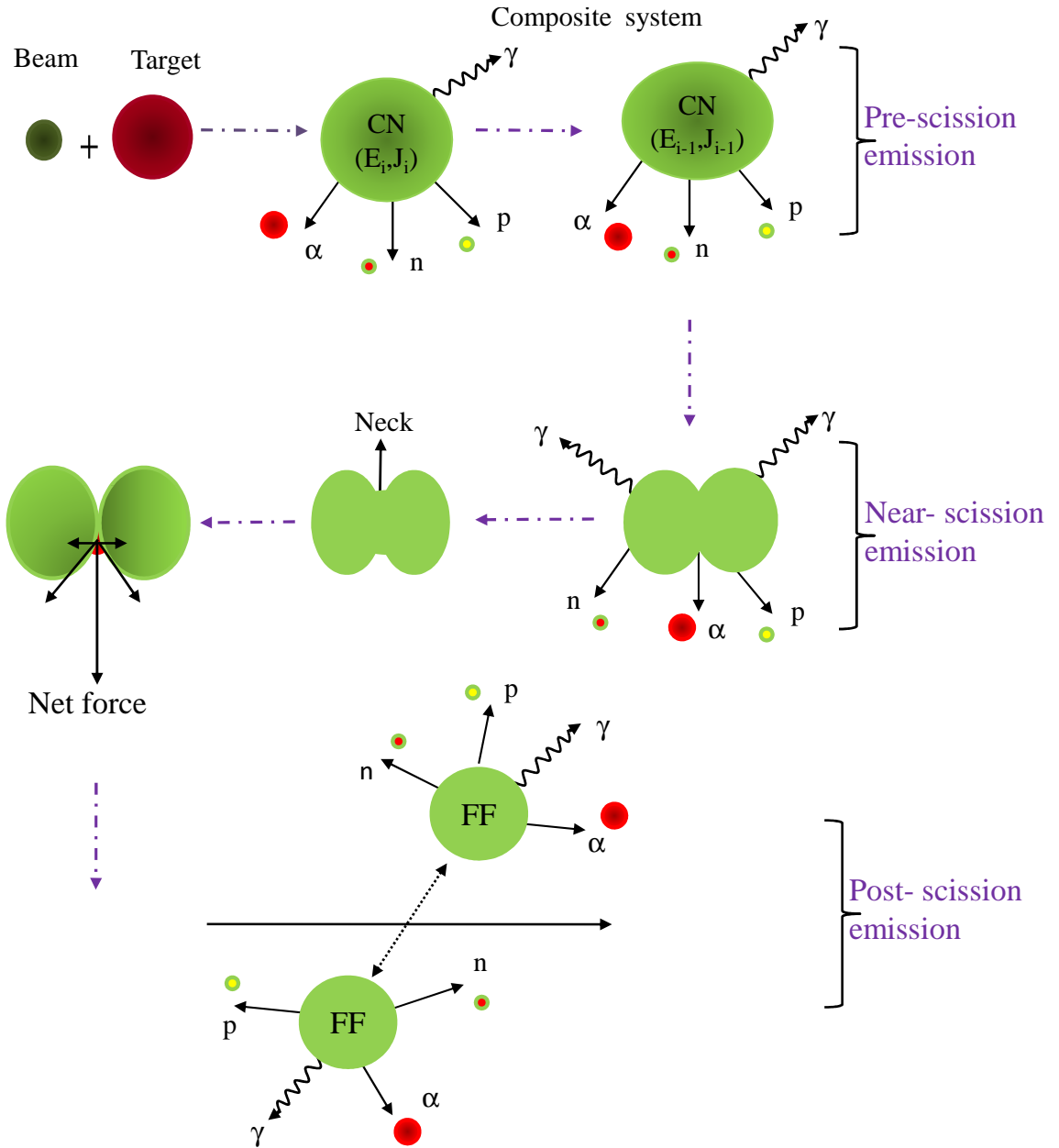
Figure 1.12: Schematic illustration of the different stages of the particle emission in heavy-ion induced fission.

increases quite strongly with increasing excitation energy around 75 MeV which is completely in contrast to the observation of a weak excitation energy dependence in low energy fission. The observations by Sowinski *et al.* [130] of similar NSE α-particle yields for two projectile-target systems with similar excitation energy but widely different Z^2/A values are also against dynamical emission of the α-particle yields. Whereas, in the work of Ref. [134] it has been shown by measurement of relative ternary emission probabilities of intermediate mass fragments ($3 \leq Z \leq 20$) as a function of initial excitation energy that the ternary emission is a dynamical process even at higher excitation energies. But, later on it has been suggested by Moretto *et al.* [135] that the results obtained in the above work are consistent with statistical emission. Thus, at higher excitation energies, it is still not clear whether the NSE mechanism is a statistical evaporation or dynamical or a combination of both.

Understanding of the near scission emission mechanism can provide information on the scission point characteristics of the fissioning nucleus and is important from the point of understanding the collective fission dynamics. In particular, investigation of near scission emission in a wide energy range from spontaneous fission to heavy ion fission, can provide insight about the nuclear viscosity in saddle to scission region and during the scission itself. Extensive systematic study are available in low energy fission but there are no systematic studies so far in heavy-ion induced fusion-fission reactions for the NSE over a large fissility (x) range. Therefore, it is important to carry out systematic study of prescission and near-scission α-particle multiplicities and this forms the basis for the second part of the present thesis work.

1.11   Outline of the thesis

The first part of the thesis deals with the study of the statistical aspects of compound nuclei, where α-particle evaporation spectra and γ-ray multiplicities have been measured for various target-projectile systems corresponding to residual nuclei in the shell

region of $Z \sim 50$ and mid-shell region of $Z \sim 70$ with excitation energy of 30-40 MeV. The high energy part of the evaporation spectra have been analyzed using the statistical model code PACE2 [136] to derive values of the inverse level-density parameter (K). Angular momentum dependence of the inverse level-density parameter is investigated using γ-ray multiplicity data. The parameter K is obtained as a function of angular momentum at an average excitation energy around 35 MeV for a number of nuclei. Around the shell-closure region of $Z=50$, the 'gross' K value (summed over all J) is seen to be in the range 9.0 - 10.5 MeV, which is within liquid drop model estimate [137]. The variation of K as a function of angular momentum in the range of 5 to $30\hbar$ for the shell-closure region, shows several interesting features not accounted by the shell and angular momentum corrected values of K used in PACE2 calculation [137]. However, in the mid-shell region the average value of K is 8.2 ± 1.1 MeV [138], and remains essentially constant around the average value in the angular momentum range of 15 to $30\hbar$ [138]. The present results for nuclei in shell-closure region and in the mid-shell region would serve as important inputs for microscopic theories to understand the statistical properties of nuclei in different mass regions.

The aim of the second part of the thesis is to investigate the dynamical aspects involved in nuclear fission. Measurements of α-particle energy spectra in coincidence with fission fragments are carried out for the systems of ^{11}B (62 MeV) + ^{232}Th (Z^2/A = 37.14) and ^{12}C (69 MeV) + ^{232}Th ($Z^2/A = 37.77$) in a wide range of relative angles with respect to FF emission direction [139, 140]. The measured spectra are fitted with moving source model calculations to extract the α-particle multiplicities corresponding to different emission stages of the fusion-fission process. In case of ^{12}C (69 MeV) + ^{232}Th reaction an extra source of α-particle emission other than pre-, post-, and near-scission emission stages, is observed which is attributed to ^{8}Be breakup in α-transfer induced fission reactions [140].

The obtained results from ^{11}B (62 MeV) + ^{232}Th reaction, have been analyzed

along with the data from literature over a wide range of excitation energy (E_{CN}) and fissility of the compound system to develop the systematic features of prefission and near-scission emission as a function of α-particle emission Q-value and Z^2/A of the compound system. It is seen that prescission α-particle multiplicity (α_{pre}) normalized to $E_{CN}^{2.3}$ show a systematic linearly increasing trend with α-particle emission Q-value [139]. The fraction of near-scission multiplicity (α_{nse}) is observed to be nearly same at around 10% of the total prescission multiplicity ($\alpha_{pre} + \alpha_{nse}$) for various systems over a wide range of Z^2/A and excitation energy suggesting that the near scission emission of α-particles in heavy-ion induced fission is a statistical process [139, 141]. This is in contrast to low energy and spontaneous fission where the neck-emission is a dynamical or fast process. Therefore, it can be inferred that nuclear collective motion during scission exhibits a change over from super-fluid to viscous nature with increasing excitation energy.

CsI(Tl)-Si(PIN) detectors used in these experiments for charged particle measurements are characterized for various aspects [142]. The energy dependence of the scintillation light output for FFs has been studied by degrading the energies of the FFs produced from a ^{252}Cf source in P-10 gas at different gas-pressures. The light output for both the heavy and light mass groups increases linearly in the energy interval 0.2 to 0.9 MeV/A and for the heavy mass fragments it is more than that for light mass fragments at a given energy. Time response of the detector has also been investigated and the time resolution for γ rays is determined to be 134 $\pm$3 ns.

The structure of the thesis is as follows;

1. **Chapter one** introduces the historical preamble and the physics motivation of the research work described in this thesis.

2. **Chapter two** describes performance characteristics of various radiation detectors used to carry out the experiments of the present thesis work. The chapter also discusses two particle identification techniques applied in the thesis work.

Further, brief descriptions about the target-preparation and the BARC-TIFR Pelletron accelerator facility at Mumbai, are presented.

3. **Chapter three** is divided into two parts. The first part describes in detail the methodology to determine the γ-ray multiplicity and fold gated α-particle spectra. The second part, introduces the statistical model code PACE2 followed by a description of the method for calculating fold-gated α-particle spectra using the code. It also discusses the least squares fit method used to extract the inverse level-density parameter K. Finally, the results on level-density parameter K obtained for compound nuclear systems around the shell-closure and in the mid-shell regions are discussed.

4. **Chapter four** begins with the methodology of the α-particle measurement in coincidence with fission fragments at different relative angles with respect to the fragment emission direction in ^{11}B (62 MeV) + ^{232}Th ($Z^2/A = 37.14$) and ^{12}C (69 MeV) + ^{232}Th ($Z^2/A = 37.77$) reactions. Further, this chapter deals with the moving source analysis which is used to disentangle the different components of the α-particle multiplicity. Finally, the results obtained for both the fissioning systems are compared.

5. **Chapter five** is divided into two parts. The first part begins with the statistical model calculations using the code JOANNE2 to reproduce the prescission α-particle multiplicities for both reactions. The systematics of pre- and near-scission emission is developed using the present results from ^{11}B (62 MeV) + ^{232}Th reaction along with available data from literature over a wide range of Z^2/A and the excitation energy of the compound system. In the second part, the anomalous results obtained in the ^{12}C induced fission are explained in terms of transfer-breakup process.

6. **Chapter six** gives a brief summary of the research work carried out in this thesis along with a future outlook.

Chapter 2

Detection techniques and instrumentation

2.1 Introduction

Detectors, signal processing electronics, thin targets, radioactive sources, and accelerators are the essentials in the study of experimental nuclear physics. Particularly the detectors along with associated electronics form the backbone of the nuclear experiments. The radiation detector is a device used to detect, track, and/or identify the particles produced in nuclear reactions. Over the years, radiation detectors have gone through an amazing evolution in size, faster time response, better energy resolution, enhanced position sensitivity, stability, resistivity to radiation damage, and cost effectiveness. Advances in the cutting edge technologies in the field of nuclear materials and electronics, have been stimulating the parallel development of various type of sophisticated detectors. In the present thesis work, a variety of detectors have been used and their characteristics are discussed briefly in the present chapter. However, the CsI(Tl)-Si(PIN) detectors have been discussed in details since these detectors are characterized quite rigorously for their use in charged particle measurements. The particle identification techniques used in the thesis work, are also discussed. A brief description about target preparation techniques and different radioactive sources used in the present work is also presented. All the experimental investigations were carried out

Table 2.1: Various parameters of ^{252}Cf spontaneous fission, from Ref. [78, 143–147].

$\langle A_L \rangle$	$\sigma(A_L)$	$\langle A_H \rangle$	$\sigma(A_H)$	$\langle TKE \rangle$ MeV	$\sigma(TKE)$ MeV
108.5 ± 0.1	7.1 ± 0.1	143.5 ± 0.1	7.1 ± 0.1	185.9 ± 0.5	11.6 ± 0.1

$\langle E_L \rangle$ MeV	$\sigma(E_L)$ MeV	$< E_H >$ MeV	$\sigma(E_H)$ MeV	$M_n{}^1$	$M_\gamma{}^2$
105.7 ± 0.2	5.8 ± 0.1	80.2 ± 0.2	8.5 ± 0.1	3.8	$7 - 10$

[1] From Ref. [78].
[2] From Refs. [144–147].

using 14UD BARC-TIFR Pelletron accelerator facility at Mumbai. A brief description about the accelerator facility is presented in the present chapter.

2.2 Radioactive sources

The radioactive sources with the known parameters such as the half-life, energy of the emitted radiation, branching ratio, etc. play an important role in the study of experimental nuclear physics. Particularly, the characterization and calibration of the different detectors are performed using various radioactive sources. A brief description about the sources used in the present thesis work is as follows;

(i) ^{252}**Cf for fission fragments:** Californium is a radioactive metallic actinide, the sixth transuranium element. The element was first made at the University of California, Berkeley in 1950 by bombarding ^{248}Cm with α particles and was named as californium. Its decay half-life is 2.645 years and dominantly decay via α-emission (96.908%) and remaining by spontaneous fission [148]. Although, five discrete α-particle energies are observed, only two of them dominate *i. e.*, 6.118 MeV (81.6%) and 6.075 MeV (15.2%). The fission fragments (FFs) produced from spontaneous fission of the ^{252}Cf can be grouped into two categories according to their masses and energies, the light (L) and heavy (H) mass groups. The various aspects of the each
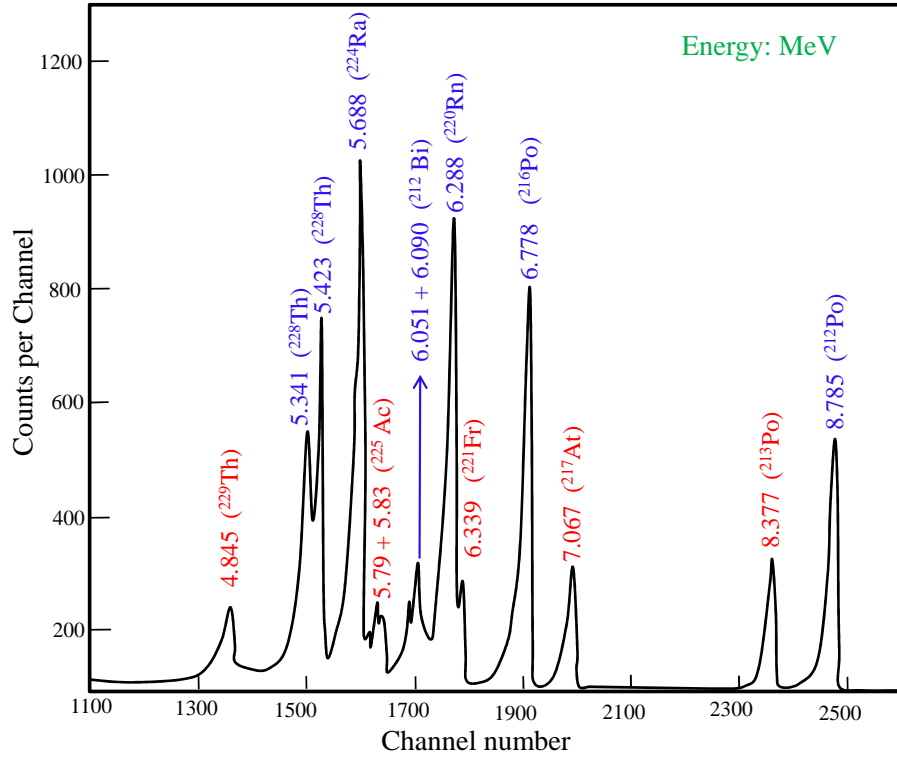
Figure 2.1: The α-particle energy spectrum from ^{228,229}Th source taken from Ref. [149].

mass group, such as the average masses($\langle A_L \rangle$ and $\langle A_H \rangle$), energies ($\langle E_L \rangle$ and $\langle E_H \rangle$) and their variances; mass variances ($\sigma(A_L)$ and $\sigma(A_H)$) and energy variances ($\sigma(E_L)$ and $\sigma(E_H)$), are listed in the Table 2.1 (from Ref. [143]).

The average total kinetic energy released in the fission process ($\langle TKE \rangle$) and its variance $\sigma(TKE)$, mean number of neutrons (M_n) and γ rays (M_γ) emitted per binary fission, are also listed in the Table 2.1 (from Ref. [143]). In this thesis work, ^{252}Cf has been used to validate the BGO setup used for γ-ray multiplicity measurements, to investigate the light output response of the CsI(Tl) detector for FFs, and testing of various gas detectors.

(ii) ^{241}**Am-**^{239}**Pu and** ^{228,229}**Th for** α **particles:** Many unstable heavy nuclei attain the stability by α-decay where certain amount of energy (Q-value) is released depending on mass difference of the parent and daughter nuclei. The α-decay can lead to any of the excited state of the daughter nucleus (E_X), and accordingly the α-particle
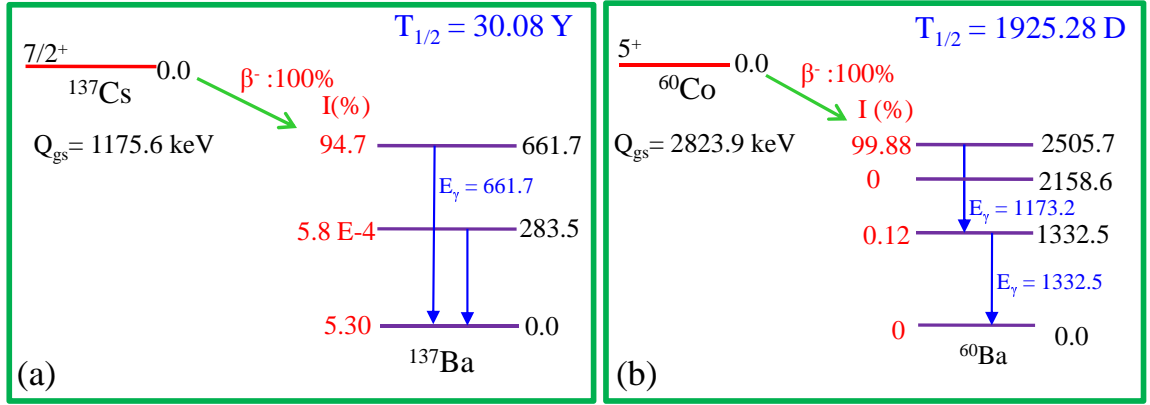
Figure 2.2: Decay schemes from Ref. [148]; (a) for ^{137}Cs which emits predominantly a γ-ray of energy 661.7 keV. (b) for ^{60}Co which emits predominantly two simultaneous γ rays of energies 1173.2 and 1332.5 keV.

kinetic energy is observed to be $E_\alpha = Q_{\text{eff}}[1 - 4.0/A]$, where $Q_{\text{eff}} = Q - E_X$, and A is the mass number of the parent nucleus. Both ^{241}Am as well as ^{239}Pu emit α particles of various discrete energies but only few of them are dominant. In case of ^{241}Am, the dominant energies are 5.486 MeV (84.8%) and 5.443 MeV (13.1%), whereas in the case of ^{239}Pu these are 5.155 MeV (70.77%), 5.144 MeV (17.11%), and 5.105 MeV (11.94%) [148]. The half lives of ^{241}Am and ^{239}Pu are 432.6 years and 24110 years, respectively [148]. In the case of ^{228,229}Th source, the discrete energies of the α particles as shown in the Fig. 2.1 are due to further α-decay of the short lived daughter products [149]. The half-life of ^{228}Th is 1.912 years which is much smaller than that of ^{229}Th for which it is 7340 years [148]. In the present work, we have used ^{241}Am-^{239}Pu and ^{228,229}Th α-sources to characterize and calibrate various charged particle detectors.

(iii) ^{137}**Cs and** ^{60}**Co sources for** γ **rays:** The majority of the unstable nuclei when emit an α- or β-particle, the daughter nuclei are usually left in the excited states which come to ground states by emitting γ rays of discrete energies in the complete analogy to the atomic X-ray emission. We have used ^{137}Cs source which emits predominantly a 661.7 keV γ-ray as shown in the Fig. 2.2, for setting up the energy thresholds, estimating the cross-talk probability, and determining the efficiency of the BGO setup. The ^{60}Co source which emits predominantly two simultaneous γ

rays of energies 1173.2 and 1332.5 keV as shown in the Fig. 2.2 (from Ref. [148]), has been used to measure the time resolution of the CsI(Tl)-Si(PIN) detector using the γ-γ coincidence method.

2.3   Detectors

In the present work, various types of the detectors have been employed such as; (i) Gas detectors - ionization chambers, (ii) Semiconductor detectors- Si-surface barrier and Si-strips, and (iii) Scintillation detectors - CsI(Tl), BGO, and BaF$_2$. A brief description about these detectors is presented here. Detailed characteristics of the detectors have been documented in various reference books [150, 151].

2.3.1   Gas detectors

The gas detectors are the simplest and easiest devices used for radiation detectors. The striking features of the gas detectors in comparison to other type of detectors are the versatility of construction in various configuration, variation in thickness by selecting appropriate gas pressure, and immunity to the radiation damage. The simplest form of a gas detector is essentially a parallel plate capacitor in which the region between the plates is filled with a gas suitable for ionization when a radiation passes through it. As ionizing radiation passes through the gas volume, it dissipates some or all of its energy in collisions with the gas molecules, and thus creates electron-ion pairs. In the absence of the electric field between the plates, the motion of electrons and positive ions would be random, and they would eventually recombine to form neutral molecules. However, when a voltage is applied between the plates, the electrons are accelerated and acquire a net drift velocity in the direction of the anode plate. Likewise, the positive ions acquire a net velocity in the direction of the cathode plate. The space charge resulting from the creation of the electron-ion pairs and their subsequent motion within the electric field, causes an induced electric current at the electrode plates. This induced
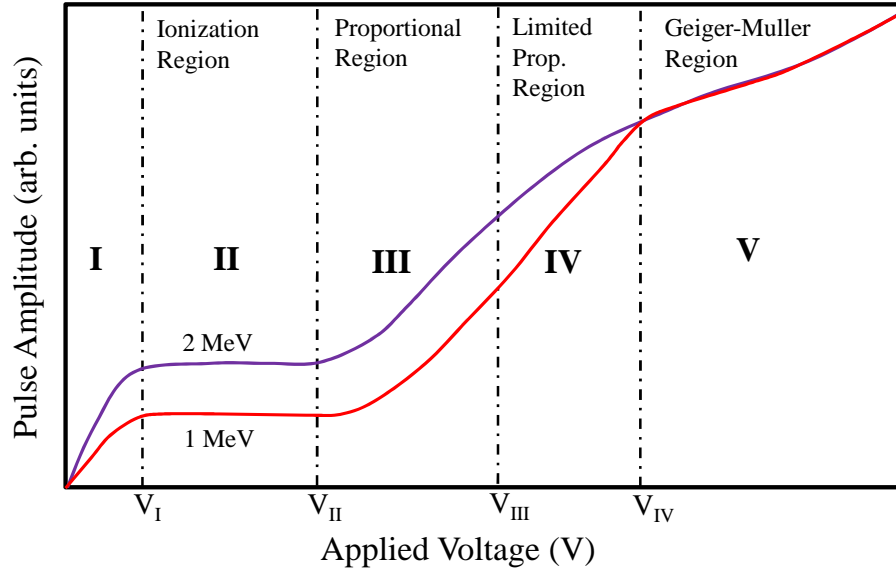
Figure 2.3: The different regions of operation of a pulse mode gas detector. The pulse amplitude is plotted for two different energies of the radiation, taken from Ref. [150].

current continues to flow until all of the charge has been collected. Measurement of the induced current or voltage pulse provides the detector signal.

Behavior of the gas detector varies as a function of applied electric field. With all other parameters being fixed (detector geometry, gas type, pressure, etc.) the gas detectors exhibit different characteristics in the different domains of the applied field as shown in the Fig. 2.3 (from Ref. [150]). Fig. 2.3 shows the pulse amplitude as a function of the applied field, displaying the different regions of the gas detector operation such as, Ionization, Proportional, Limited Proportional, and the Geiger-Mueller (GM) region.

In the present work, we have used the gas detectors operated in the pulse mode ionization region, hence we will focus on the characteristics of the pulse mode ionization chambers only. For the ionization chambers, the collection time of the massive positive ions is about 1000 times larger than that for electrons, therefore, the ionization chambers are operated in the electron sensitive mode to avoid the pulse-pileup. In this mode, a time constant is chosen that is intermediate between electron and the ion collection times. The amplitude of the pulse reflects only the drifts of electrons and
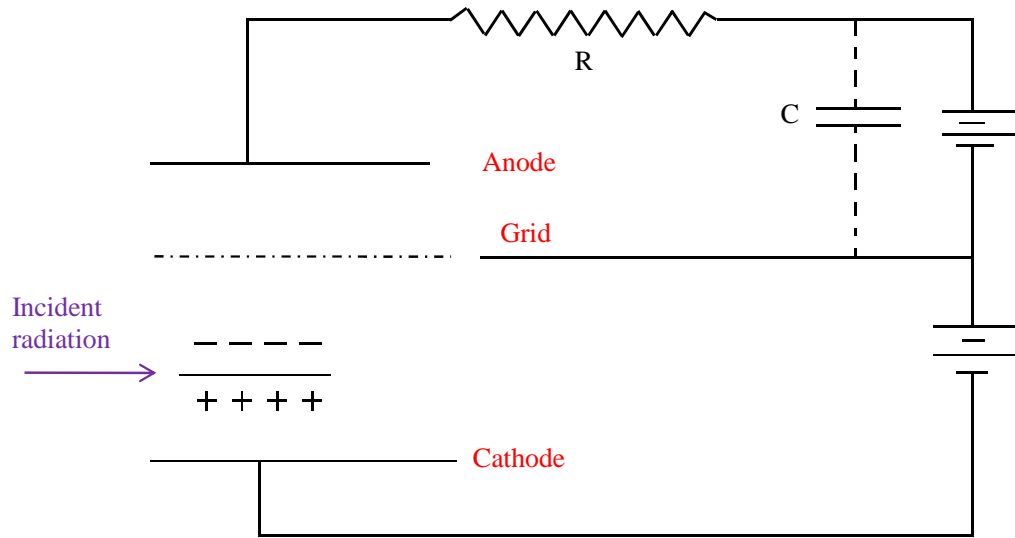
Figure 2.4: Schematic diagram of a parallel plate, pulse mode gridded gas-ionization chamber.

have much faster rise time. However, the amplitude of the pulse becomes sensitive to the initial position of the interacting radiation in the chamber. The use of a gridded chamber overcomes this shortcoming to a large extent.

2.3.1.1 Gridded gas ionization chambers

A simple parallel plate gridded ionization chamber has been designed to understand the characteristics of the ionization region. Schematic geometry of the chamber is shown in the Fig. 2.4, where rectangular copper plates act as anode and cathode. A Frisch grid with 95% transmission is placed between anode and cathode. P-10 gas (90% Ar + 10% CH_4 mixture) is used in continuous flow mode within the chamber. The gas pressure is kept constant at around 500 mbar. The cathode is grounded and the grid is maintained at an intermediate potential of the two electrodes. In the transverse geometry, the electric field in the cathode-grid and grid-anode regions is normal to the planes of cathode, anode, and the gird. An α-source is placed in front of the entrance window of the chamber such that the α particles are incident perpendicular to the electric field in the cathode-grid region as shown in the Fig. 2.4. Electrons and
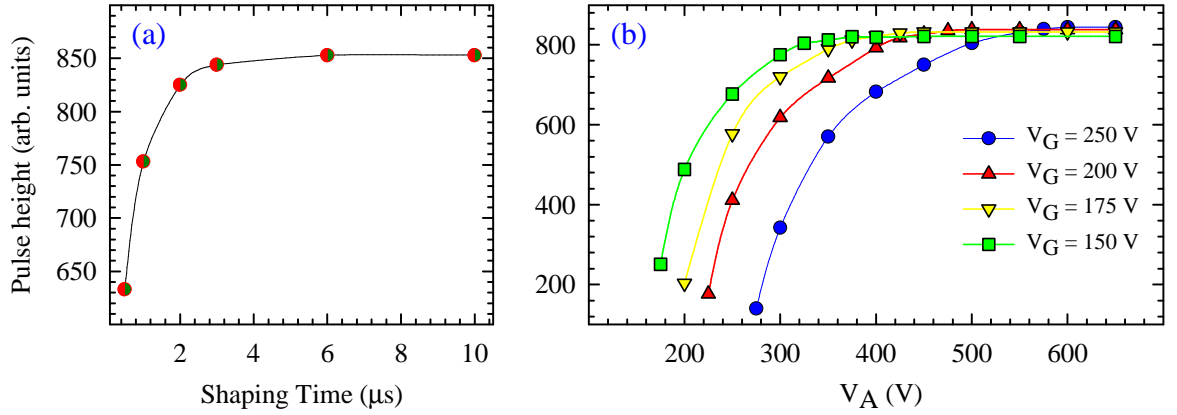
Figure 2.5: Pulse amplitude of 5.155 MeV α particles produced from ^{239}Pu source as a function of shaping time of the spectroscopic amplifier (a) and anode voltage, V_A at various grid voltages, V_G (b).

positive ions are generated in the interaction volume. Positive ions drift towards the cathode and electrons towards the grid. A load resistor, R is connected in the circuit in such a way that neither the downward drift of the ions nor the upward drift of the electrons up to the grid, produces any measurable current across the load resistor. Once the electrons pass through the grid on their way to the anode, the grid-anode voltage begins to drop and proportionally signal voltage pulse develops across the load resistor.

The ionization chamber has been tested with α particles of energy 5.155 MeV produced from a ^{239}Pu source and characterized the effect of shaping time of the spectroscopic amplifier and voltage settings of grid and anode on the pulse amplitude. The pulse amplitude increases with increasing the shaping time from 0.5 μs to 3.0 μs, and after 3.0 μs the pulse amplitude is saturated as shown in the Fig. 2.5 (a). This behavior is attributed to the charge integration of the pre-amplifier output pulse. For further investigations, the shaping time of the spectroscopic amplifier is kept fixed at 3.0 μs to have reasonably fast and complete pulse formation. The characteristic curves of pulse amplitude as a function of anode-voltage (V_A) at various grid-voltages (V_G) have been obtained as shown in the Fig. 2.5(b). At a given V_G, the pulse amplitude initially
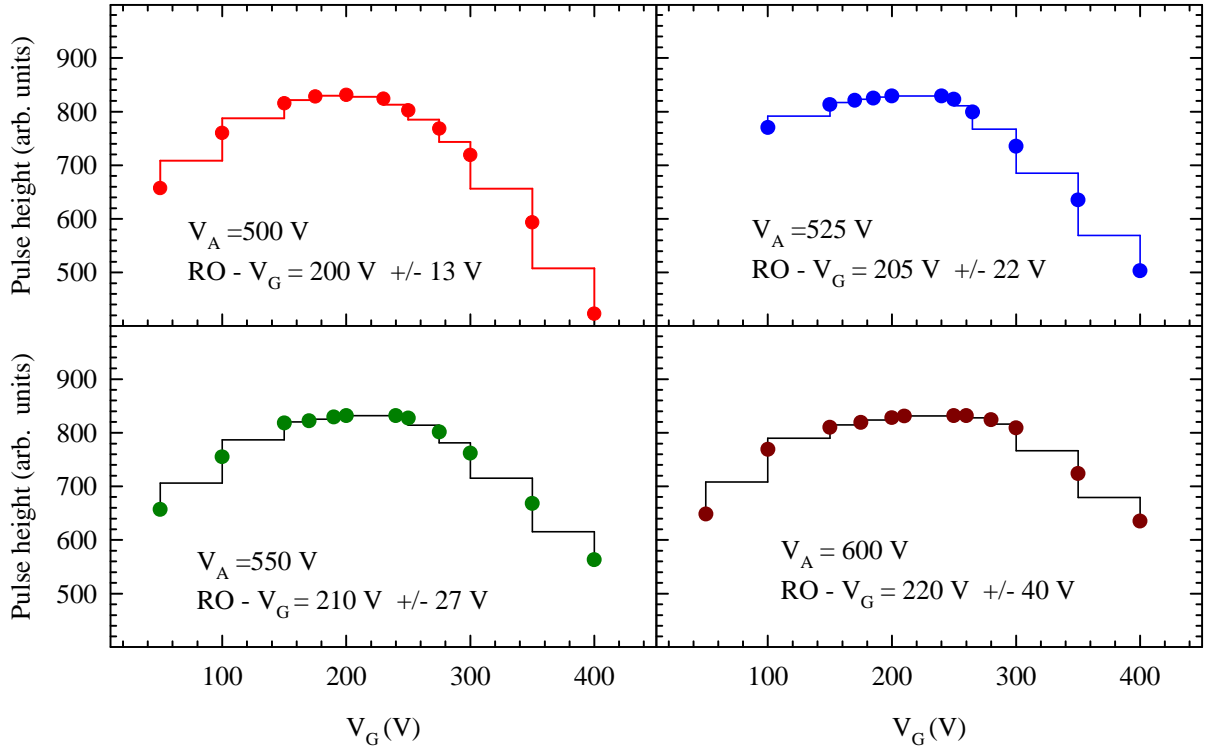
Figure 2.6: The pulse amplitude of 5.155 MeV α particles produced from ^{239}Pu source as a function of grid voltage at various anode voltages.

increases up to a certain V_A value, after that it is saturated. The anode voltage, where saturation occurs for a given grid voltage, is termed as the knee voltage. Since the higher grid voltage would suppress the electron motion between the grid and anode, therefore, the knee-voltage increases with increasing grid-voltage.

Further, we investigated the pulse amplitude as a function of V_G at various V_A settings as shown in the Fig. 2.6. The anode voltage is set to sufficiently higher voltage than that of grid. By increasing the V_G from a certain minimum value, more number of electrons are fed to the grid-anode region from cathode-grid region which results in increased pulse amplitude. By further increasing the V_G the chamber approaches to the ionization region where amplitude pulse gets saturated. If we still increase the V_G, the electric field in the grid-anode region is decreased which results in reduced pulse amplitude as reflected in the Fig. 2.6. It is also noted from the Fig. 2.6 that the range of grid voltage settings (RO-V_G) where pulse saturation occurs, increases with
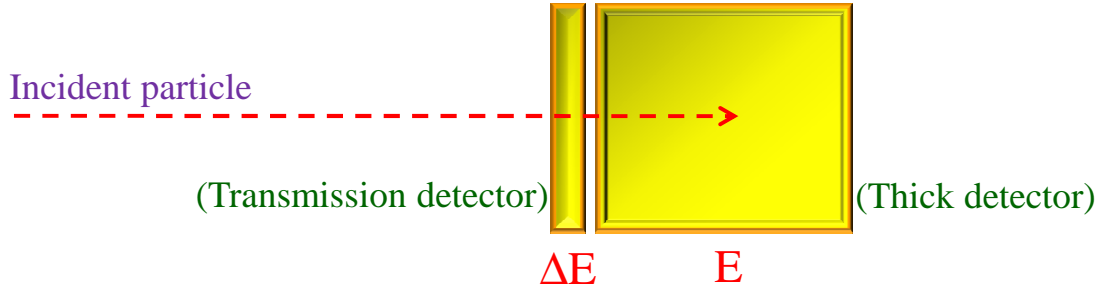
Figure 2.7: Schematic diagram of telescopic arrangement of ΔE and E detectors, where ΔE is a transmission type thin detector and E is a thick detector.

increasing V_A. The values of RO-V_G are mentioned at the bottom of each panel in the Fig. 2.6. The α-particle energy spectra are also obtained using a ^{241}Am-^{239}Pu source at different V_G and V_A values. The best energy resolution for α particles of energies around 5 MeV is obtained to be 118 keV for $V_G =$225 V and $V_A =$475 V.

The gridded gas ionization chambers have shown their potential use in not only energy but also the particle identification and angle measurements, specially for heavy fragments. In the subsequent sections, fragment identification and their position information using a gas ionization chamber have been discussed.

2.3.1.2 ΔE–E Telescope

Identification of different reaction products is one of the primary requirements in the study of experimental nuclear physics. Energy loss measurement is one of the efficient techniques employed for this purpose. This technique is based on the fact that for different particles of the same energy, the specific energy loss $(\mathrm{d}E/\mathrm{d}x)$ on passing through a material are different. In this technique, the particles are first allowed to traverse through a thin transmission type detector, where partial energy (ΔE) is lost and remaining energy of the incident particle is deposited in the thick E-detector, hence it is referred as ΔE - E technique. The thickness of the ΔE detector is chosen very small in comparison to the particle range. Schematic diagram of this telescopic arrangement of ΔE and E detectors is depicted in the Fig. 2.7. The $\mathrm{d}E/\mathrm{d}x$ of charged

particle passing through a medium is described by the well known Bethe-Bloch formula which can be approximated for a non-relativistic particle as [150];

$$\frac{dE}{dx} \propto \frac{M Z_{eff}^2}{E}, \tag{2.1}$$

where M is the mass of the ion with incident energy E and charge Z_{eff}. The energy loss in the transmission detector is obtained by [150];

$$\Delta E = \int_0^{x_t} \frac{dE}{dx} \mathrm{dx}, \tag{2.2}$$

where x_t is the detector thickness. The product $E \times \frac{dE}{dx}$ is a measure of $M Z_{eff}^2$, thus different parabolas in the ΔE vs. E plot correspond to different particles as shown in the Fig. 2.8(a) obtained using the silicon detector telescope (ΔE_{Si} - E_{Si}) in a heavy-ion reaction. The total energy of the incident particle is obtained from the sum of pulse height signals from ΔE and E detectors. Employing Si-detectors in this technique, an excellent separation is obtained only for lower Z values ($Z \leq 10$) with a suitable thickness of the ΔE detector. For larger Z, the different combinations of M and Z values may lead to the same $M Z_{eff}^2$, thus rendering the method unsuitable [150].

Combination of gas ionization chamber as a ΔE-detector and a thick E-detector (either gas or any other suitable) makes a hybrid telescope which can provide a very good separation between heavy fragments and light charged particles. By tuning the gas pressure, the energy loss in the ΔE_{gas}-detector can be varied and the telescope can be made suitable to different mass ranges of the fragment [152, 153]. We have used ΔE_{gas} vs. E_{gas} telescopes to separate the fission fragments and light charged particles. To achieve this goal in a simplest way, the anode plate of the above described ionization chamber was segmented into two parts corresponding to ΔE and E. At P-10 gas pressure of 150 mbar and voltage settings of V_A=400 V, V_G= 200 V, and cathode = -10 V, response of this simplest gas ionization telescope is shown in the Fig. 2.8(b) for fission fragments produced from ^{252}Cf source, where a clear separation between
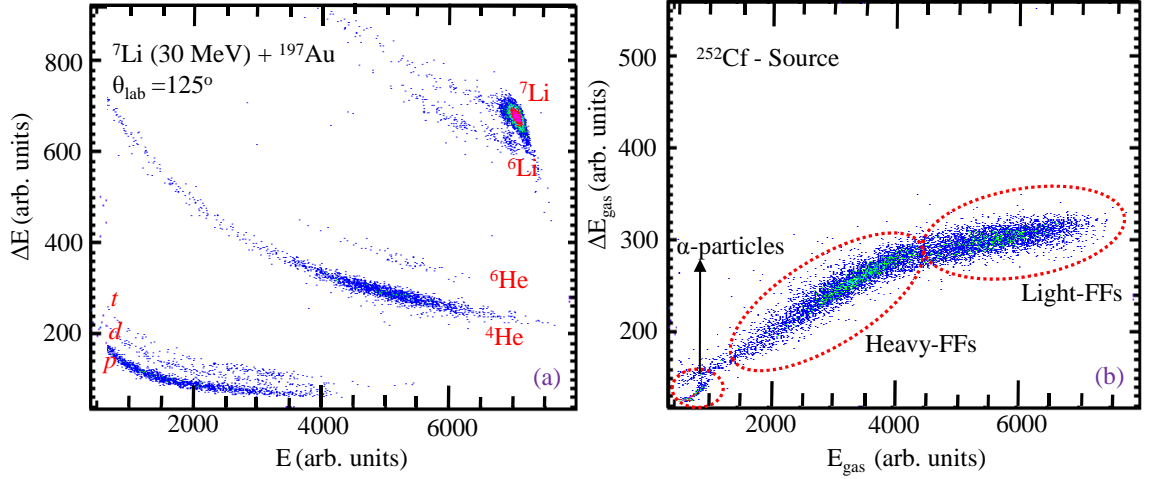
Figure 2.8: Typical two-dimensional spectra obtained using the ΔE - E telescopes. (a) Separation between different charged particles produced from ^{7}Li (30 MeV) + ^{197}Au reaction at θ_{lab}=125° using a Si-telescope (ΔE_{Si} - E_{Si}). (b) Separation between FFs and α particles produced from ^{252}Cf source using a gas-ionization telescope (ΔE_{gas} - E_{gas}).

fission fragments and α particles is obtained. It should be noted here that the slope of the ΔE vs. E plot for fission fragments is opposite to that of the light charged particles as shown in the Fig. 2.8(a) and (b). This is because the Z_{eff} of the fission fragment increases with its energy which results in more dE/dx with increasing the energy, whereas for light charged particles Z_{eff}=Z and therefore, dE/dx decreases with increasing energy [153].

2.3.1.3 A position sensitive gas ionization telescope

In the applications where the large solid-angle detectors are employed, the position information is of absolute necessity. The position information can be obtained in two basic architectures: (i) direct read-out, where 1D/2D arrays of small pixels with one read-out per pixel is used and (ii) interpolating read-out, where the measurement parameters (signal magnitude and time) of the large area detector are position dependent. Since the direct read-out requires a large number of read-out channels, interpolating schemes are attractive for large area coverage. The charge division and delay line
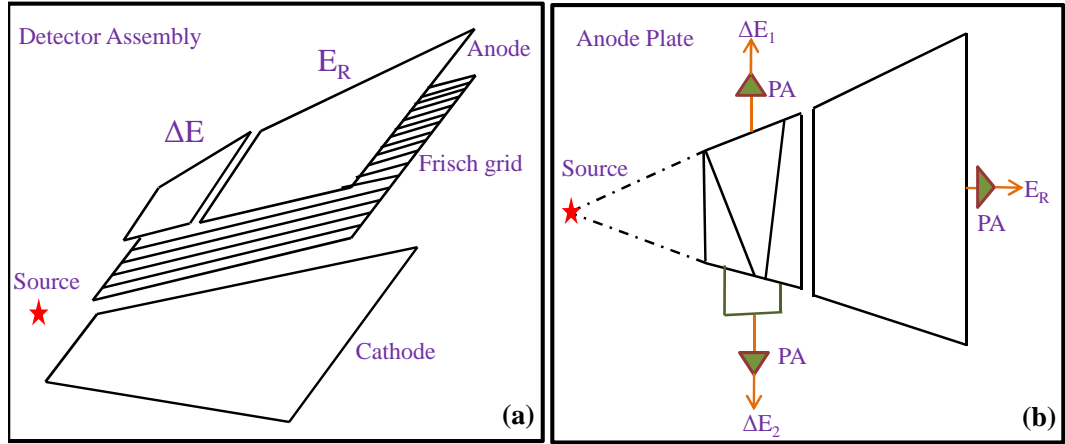
Figure 2.9: Schematic diagram of detector assembly (a) and anode plate (b) for ΔE_{gas} - E_{gas} position sensitive ionization chamber, see Ref. [156].

read-out methods belong to the second category of the interpolating read-out.

In a back-to-back geometry of the ionization chamber with a common cathode and two sets of grid and anode, angle measurements of the FFs produced from ^{235}U (n_{th}, f) reaction with respect to the electric field have been reported earlier [154, 155]. The back-to-back geometry of the ionization chamber has been suitable only for neutron induced fission but for charged particle induced fission, other alternatives have to be looked for. In the present thesis work, the charge-division as well as delay-line read-out methods have been used for this purpose.

The gas ionization chamber used here is of trapezoidal shape and the main body of the detector is machined from stainless steel material, as discussed in detail in Ref. [156]. Fig. 2.9(a) shows the schematic diagram of the detector electrode assembly which consists of a cathode, a Frisch grid and an anode plate, all having trapezoidal shapes and mounted on supporting teflon rods and spacers. The separation between the cathode and grid is kept at 40 mm and the grid to anode at 10 mm. The cathode is made of one sided Cu-plated fiber glass. The Frisch grid is constructed by first making a trapezoidal frame out of fiber glass and then attaching a sheet of electro-formed mesh to the frame. The mesh is made of 0.001 inch thick Ni and has about 95% transmission.
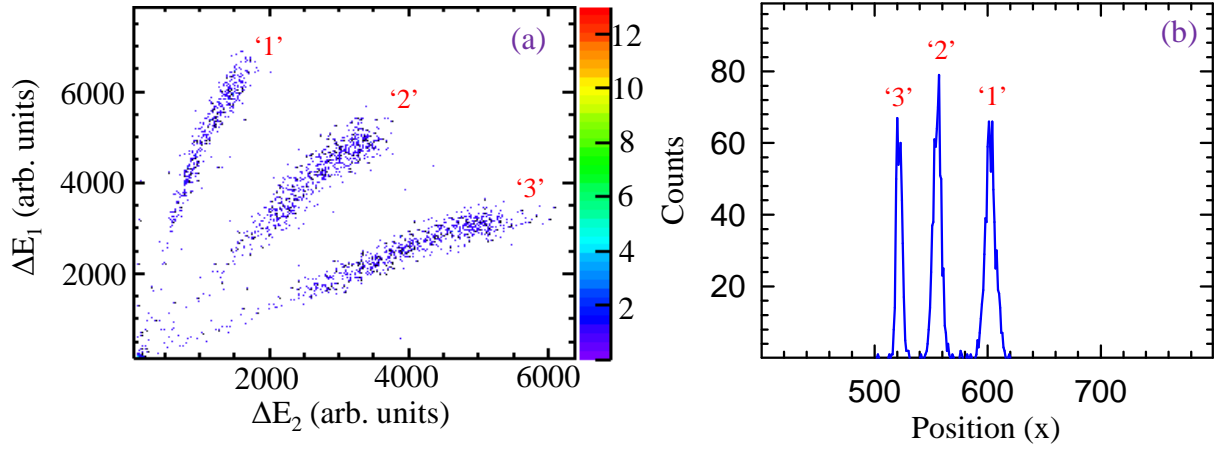
Figure 2.10: (a) A two-dimensional spectrum of ΔE_1 vs. ΔE_2 using ^{252}Cf fission source obtained from position sensitive ionization chamber having a three slit mask at the entrance window. The notations '1', '2', and '3' correspond to the three slit openings. (b) The corresponding position spectrum using the Eq. (4.2) (see text).

The anode plate made of Cu-plated fiber glass is splitted into two trapezoidal parts of length 45 mm (ΔE) and 90 mm (E). A stretched 1.5 μm thick mylar foil is fixed on a window frame and supported by a Ni mesh having 95% transmission. The active area of the window is (42×12 mm^2) which enables an angular coverage of 30° for the detector distance of 8.5 cm from the target.

The ΔE part is further divided into two segments ΔE_1 and ΔE_2 as shown in Fig. 2.9 (b) in such a way that the average dE/dx is almost equal in both the regions for the FFs entering the central line of the detector. The FFs, passing at any other angle will lose energies proportional to their path lengths in ΔE_1 and ΔE_2 regions. The position information is derived by using the charge division method for the signals collected by the ΔE_1 and ΔE_2 sections. The detector has been tested using a ^{252}Cf spontaneous fission source. At P-10 gas pressure of 140 mbar and voltage settings of cathode = -50 V, grid = +125 V, and anode = +250 V, the detector operates in the ionization region. The position parameter is defined as [156];

$$x = \frac{\Delta E_1 - K_g \Delta E_2}{\Delta E_1 + K_g \Delta E_2},\qquad(2.3)$$

where K_g is a ratio of electronic gains of ΔE_1 to ΔE_2, and was measured to be 2.25

during the detector characterization. The parameter x is proportional to the FFs position and is related to the scattering angle. Position resolution has been measured by attaching a mask of three slits each of 2 mm width and 10 mm separation in front of the detector window. For this masked entrance window, the ΔE_1 vs. ΔE_2 plot and extracted position information are shown in the Figs. 2.10(a) and (b), respectively. In the Fig 2.10(a), the three-slits openings are denoted by '1', '2', and '3' which correspond to three peaks in position spectrum as shown in the Fig 2.10(b). The position resolution is determined to be 1.1 mm which translates to $\sim 1°$ of angle resolution which is quite good for studying the angular distribution of FFs in heavy-ion reactions.

2.3.2   Semiconductor detectors

The semiconductor-detectors have wide spread applications in various field such as medical imaging, space, particle and nuclear physics research, etc. In particular, the advancement in the semiconductor detector technology has revolutionized the research in the field of nuclear and particle physics by virtue of their better energy resolution, fast timing response, and compact geometry.

The basic operating principle of semiconductor detector is analogous to gas ionization chambers. Instead of the gas, the medium is now a solid semiconductor. The passage of ionizing radiation creates electron-hole pairs instead of electron-ion pairs, which are then collected by an electric field. In a semiconductor material the band-gap between the valence band and the conduction band is small $\approx 1 - 2$ eV. Therefore, the advantage of semiconductor material, is that the average energy required to create an electron-hole pair is around 10 times smaller than that for gas ionization. Thus, the number of charge carriers produced for a given energy deposited in a semiconductor material is a order of magnitude larger than gas ionization chambers, resulting in better energy resolution. Because of their high density, the semiconductor detectors are compact in size and hence very fast timing response. The most suitable semiconductor
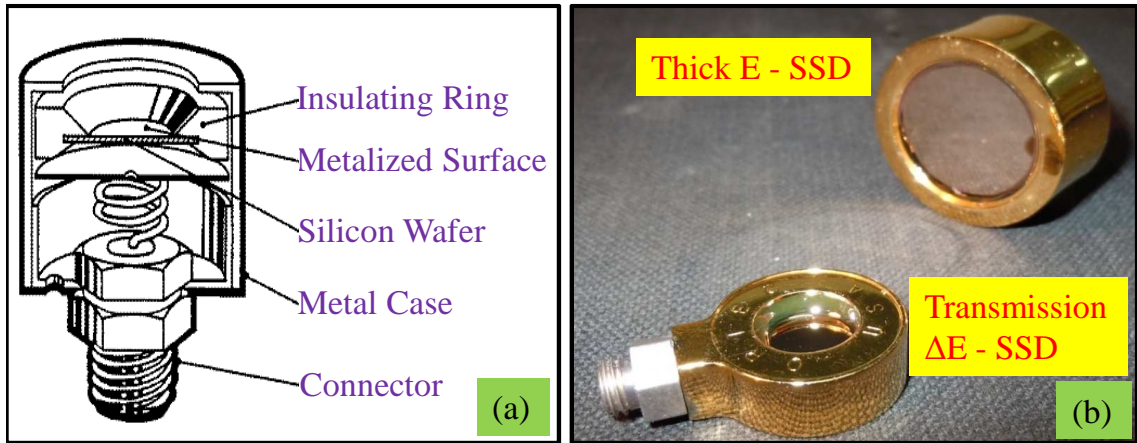
Figure 2.11: Schematic, (a) and real, (b) views of typical Si-surface barrier detectors.

materials that are used to fabricate these detectors are the silicon (Si) and germanium (Ge), which are characterized by the band-gap of 1.115 and 0.665 eV (at room temperature) [150], respectively. The major drawback of these detectors is that being crystalline material, they have greater sensitivity to radiation damage which limits their long term use.

For charged particle detection, Si is the most widely used semiconductor material because it has advantage of room temperature operation and wide availability. The depletion region (ideal for radiation detection) in Si may be created in a number of ways which result in a number of different type of Si-detectors such as the diffused junction diode, surface barrier, ion-implanted diode, and lithium drifted silicon (Si(Li)), etc. Each type of Si-detector have certain merits and de-merits, therefore depending on the application a suitable selection is made. We have used Si-surface barrier detectors for light charged particles and a 32-strips Si-detector with a delay-line read-out for fission fragment measurements. In the present chapter we will discuss briefly about only Si-surface barrier detectors and the 32-strips Si-detector is discussed in a later chapter.

The Si-surface barrier detectors (SBD) rely on the junction formed between a semiconductor and certain metal, usually *n–type* silicon with gold or *p–type* Si with

aluminum [150, 151]. In most commercially available SBDs, the *n–type* silicon is oxidized on one side and coated with a thin gold layer to form thin *p–type* material and a rectifying electrical contact. The other side of *n–type* material is coated with aluminum for electrical contact. Reverse bias is applied with positive voltage on the *n–type* side through the aluminum contact. The junction is mounted in an insulating ring with metalized surfaces for electrical contacts, as shown in the Fig. 2.11(a). Typical transmission type and thick Si-detectors are shown in the Fig. 2.11(b). The SBDs can be fabricated with varying thickness from 10 μm to 2 - 5 mm. The thin SBDs can be fully depleted by applying suitable reverse bias voltage, the depletion zone extends through the entire thickness of the silicon wafer. The fully depleted detectors are very useful as transmission detectors to be used for particle identification in ΔE-E telescopes as discussed in the previous section.

2.3.3   Scintillation detectors

The scintillation detectors make use of the fact that certain material emit a small flash of light, i.e., a scintillation when struck by an incoming nuclear radiation. These scintillations can be converted into electrical pulses when the scintillator is coupled to an electronic light sensor such as a photomultiplier tube (PMT) or a photodiode, which can be analyzed subsequently to extract the information about the incident radiation. The scintillators exhibit various desired properties required in radiation detection such as high density, fast timing response, low cost, radiation hardness, production capability, and durability of operational parameters.

The scintillators can be grouped into two categories viz. the inorganic scintillators such NaI(Tl), CsI(Tl), BGO, BaF$_2$, etc., and the organic scintillators such the plastic, anthracene, stilbene, etc. [150, 151]. The organic scintillators are characterized by fast timing response (2 - 30 ns), low density, and large signal non-linearity due to large ionization quenching. In the study of nuclear physics, the organic scintillators
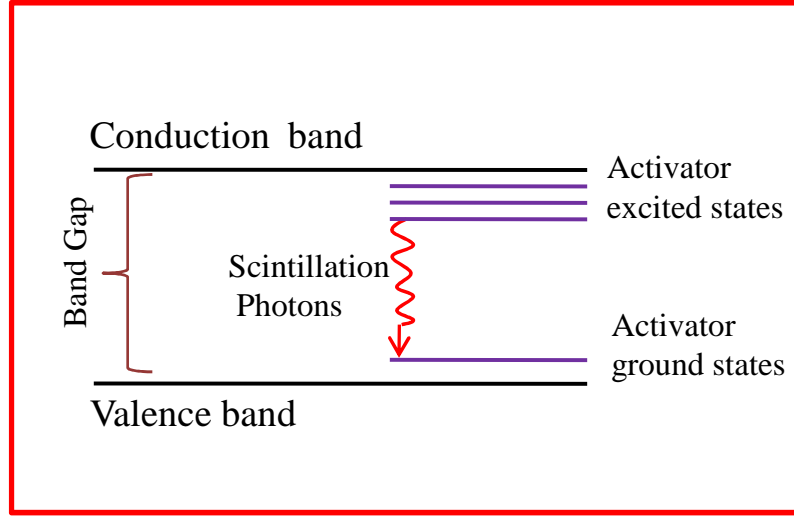
Figure 2.12: Schematic energy band structure of an activated inorganic scintillator, taken from Ref. [150].

are mostly used for neutron detection, where an excellent discrimination of γ rays can be obtained. Whereas, an inorganic scintillator exhibits specific features which makes them attractive for a specific application in the field of nuclear physics. The NaI(Tl) is one of the oldest detector which produce maximum light output when coupled to a PMT among all the inorganic scintillators. However, for charged particle measurements the CsI(Tl) coupled with photodiode is superior to NaI(Tl) as discussed in the following sections. In present thesis work, the CsI(Tl) has been characterized quite rigorously and used for charged particle measurements.

The CsI(Tl) and NaI(Tl) are the crystals of the alkali halides containing small amount of thallium as an activator. The basic scintillation mechanism in these materials depends on the discrete energy states determined by the crystal lattice as shown in the Fig. 2.12. The energy deposited by the incident radiation in the crystal results in the excitation of an electron from valence band to the conduction band. In the pure crystal (without Tl activator), the emission of photon due to electron transition from conduction band to valence band, is an inefficient process because of self absorption. Moreover, the typical band-gap of a pure crystal is too high which would make
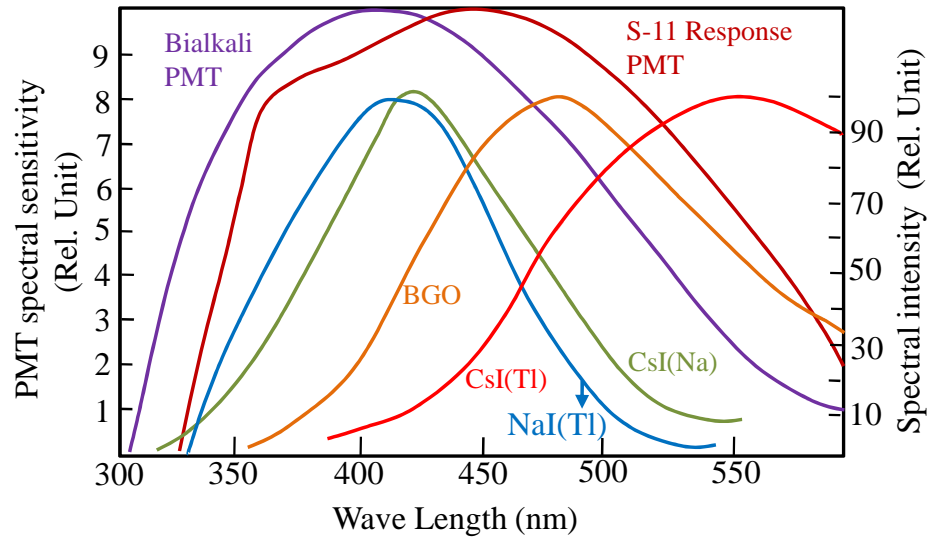
Figure 2.13: The emission spectra of several common inorganic scintillators along with the response curves for two widely used PMTs, taken from Ref. [150].

the resulting photon much beyond the visible region, where most of the PMTs and photodiodes have good spectral sensitivity.

The Tl activator in alkali halides reduces the self absorption and enhances the probability of visible photon emission. The activator creates special site within the lattice almost in the middle of the band-gap of the pure crystal as shown in the Fig. 2.12. As a result, the electron de-excitation takes place now through these new energy states within the forbidden gap. This transition results in a visible photon emission and serve as the basis of the scintillation process. The energy structure of the activator in the host crystalline lattice determines the emission spectrum of the scintillator. The emission spectrum of the photons with characteristic time constant determines the over all behavior of the detector. Majority of the inorganic scintillators have more than one decay time constants. The scintillation light is fully utilized if the emission spectrum overlaps with the maximum sensitivity region of the absorption spectra of the light collection devices. Fig. 2.13 shows the emission spectra of several common inorganic scintillators along with the response curves for two widely used PMTs. It can be seen from the Fig. 2.13 that in the case of CsI(Tl) the overlap between emission spectrum

Table 2.2: Characteristic properties of some inorganic scintillators from Ref. [150].

Scintillator	Density (gm/cm^3)	Refractive index	Decay Time μs	λ_{max} nm	Photons /MeV e$^-$s	Hygroscopic
NaI(Tl)	3.67	1.85	0.23	415	38000	Yes
CsI(Tl)	4.51	1.80	5 − 7 [1]	540	65000	Slightly
BGO	7.13	2.15	0.30	480	8200	No
BaF$_2$ Fast	4.89	1.58	0.0006	220	1400	No
BaF$_2$ Slow	4.89	1.5	0.63	310	9500	No

[1]CsI(Tl) has two decay time constants. Shown above is slow and fast=0.4 − 0.7 μs.

and spectral sensitivity of the PMTs is quite small. Efficient light collection for CsI(Tl) can be obtained if it is coupled with a photodiode, which makes it suitable to be used in a compact geometry. Since the PMT itself amplify the signal whereas in case of photodiode there is no signal amplification, but the superior spectral sensitivity with photodiode results in similar energy resolution of CsI(Tl) scintillator either coupled with PMT or photodiode.

Various aspects of commonly used inorganic scintillators such as density, refractive index, decay time constants, peak emission wave length (λ_{max}), number of photons emitted due to 1 MeV energy deposited by fast electrons, and their hygroscopic nature, are listed in the Table 2.2 (from Ref. [150]). The characteristics of the CsI(Tl)-Si(PIN) detector will be discussed in detail later in this chapter. In the subsequent sections, basic characteristics of BGO and BaF$_2$ detectors are outlined.

2.3.3.1 Bismuth Germanate (BGO) detectors

The major advantage of the Bi$_4$Ge$_3$O$_{12}$ (commonly known as BGO) is its high density (7.13 gm/cm^3) and the large atomic number (83) of the bismuth component which results in largest probability per unit volume of any commonly available scintillation material for photo-electric absorption of γ rays. Unfortunately, the light yield from

BGO is relatively low (10-20% of that of NaI(Tl)) and the refractive index is quite high (2.15), which makes inefficient light collection. These undesirable properties result in poor energy resolution. Therefore these detectors are more suitable only when high γ-ray counting efficiency is the primary interest. In the present work these detectors have been used for low energy γ-ray multiplicity measurements so that cross talk between the detectors is negligible (<1% for 662 keV γ rays from ^{137}Cs).

2.3.3.2   Barium Fluoride (BaF$_2$) detectors

The BaF$_2$ is the only inorganic scintillator which has very high atomic number and a very fast component with decay time constant less than 1 ns. These properties make it attractive in the application where both high detection efficiency per unit volume for the γ rays and fast timing response are the primary requirements. It has two decay components, the fast one with decay time 0.6 ns falls in shorter wavelength, whereas the slower one with decay time 630 ns falls in somewhat longer wavelength as shown in the Table 2.2. The total light yield is a small fraction of that of NaI(Tl) which results in poor energy resolution. About 20% of the total scintillation light yield is observed in the fast component. However, it remains important to be used as a start trigger for γ rays in various coincidence experiments. In the present thesis work it has been used to measure the time resolution of the CsI(Tl)-Si(PIN) detector as discussed in the next section.

2.4   CsI(Tl)-Si(PIN) detectors

CsI(Tl)-Si(PIN) detectors have been used in many multi-detector arrays all over the world [157–159] for charged particle measurements. These detectors have also been used in γ-ray measurements [160], and for X-ray imaging in medical applications [161, 162]. This type of detectors have following advantages: (i) CsI(Tl) scintillator coupled to photodiode Si(PIN) makes a compact geometry; (ii) strong dependence of pulse shape
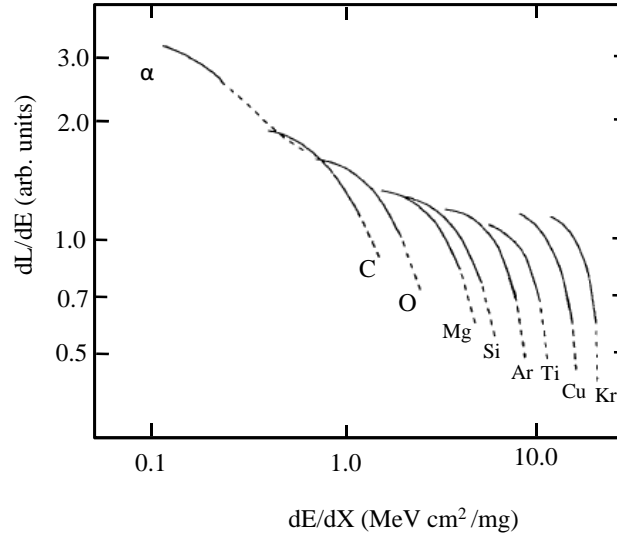
Figure 2.14: Scintillation efficiency dL/dE as a function of the energy loss per unit length dE/dx, from Ref. [163].

on the type of ionizing radiation because of different ratio of fast to slow components of the light output for different type of ionizing radiation; (iii) large size crystal can be grown; (iv) radiation damage is much less and they are cheaper in comparison to the conventionally used silicon detectors.

Light output response of the CsI(Tl) detector for the charged particles up to Z=36 has been studied earlier in the intermediate energy region in detail [163–166]. Investigation of the light output response of CsI(Tl) detectors for fission fragments (FFs) is quite limited. In heavy-ion reactions, separation of fission fragments from projectile like fragments (Z≥3) using conventional methods such as pulse shape discrimination (zero crossover) [167] or ballistic deficit [168] is not feasible. Therefore, these detectors have not been used for the measurement of fission fragments in heavy-ion reactions. But these detectors can be used for the measurement of fission fragments in light charged particles (Z≤2) or neutron induced fission reactions. In particular, CsI(Tl) detectors can be very useful as a FF-tagging device in reactor based neutron induced fission reactions for spectroscopic studies of FFs, where neutron damage to a detector is a serious issue.

It has been reported in the past [163, 165, 166] that the differential scintillation efficiency, dL/dE has a strong dependence on the specific energy loss (dE/dx) for charged particles ($2 \leq Z \leq 36$). It was observed that dL/dE decreases as dE/dx increases and for the same value of dE/dx, the scintillation efficiency is more for particles with large atomic number as shown in the Fig. 2.14 (from Ref. [163]). Since dL/dE depends on dE/dx, it gives rise to a nonlinear relationship between light yield (L) and energy (E) of the particle. This nonlinear behavior is more pronounced at energies below 6 MeV/nucleon. These observations for charged-particles up to Z=36 have been understood in the framework of a model first proposed by Meyer and Murray [169, 170].

The dE/dx behavior of FFs is quite different in comparison to charged particles ($2 \leq Z \leq 36$) because of the dependence of effective charge (Z_{eff}) of the FF on the fragment energy [152, 153]. In order to explore the possibility of using CsI(Tl)-Si(PIN) detector for FFs measurement, we have investigated in the present work the light output response of the detector for fission fragments produced from a ^{252}Cf source. The FFs are produced in a wide range of mass and charge having energies in the range of 0.5 to 1.3 MeV/nucleon in spontaneous fission of ^{252}Cf. The energy dependence of the light output for FFs has been studied by degrading the energies of the FFs in the P-10 gas at different pressures. We have also investigated time response of the detector for γ rays. These CsI(Tl)-Si(PIN) detectors are being used in a charged particle detector array developed at the BARC-TIFR Pelletron/Linac facility, Mumbai [171].

2.4.1 Details of detector setup

The CsI(Tl)-Si(PIN) detectors have been supplied by M/s SCIONIX, Holland. A photograph of two typical CsI(Tl)-Si(PIN) detectors is shown in the Fig. 2.15. The CsI(Tl) crystal has entrance surface area of 25×25 mm^2 and thickness of 10.0 mm. Except the back surface, all other faces are covered with 1.2 μm thick reflecting foil of aluminized mylar. A Si-PIN photodiode manufactured by Hamamatsu Photonics is
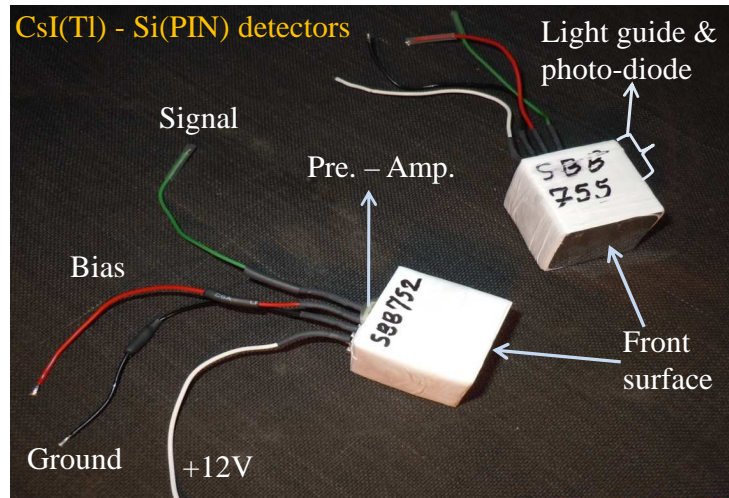
Figure 2.15: A photograph of two typical CsI(Tl)-Si(PIN) detectors.

coupled to the back surface via a $25 \times 25 \times 15$ mm^3 light guide. The photodiode type S3204-08 is 300 μm thick with an active area of 18×18 mm^2. A rectangular collimator of opening area 22×22 mm^2 is placed at the front surface of the crystal to avoid the edge effects. The signal read-out was achieved by a charge sensitive pre-amplifier, attached to the photodiode. The low power dissipation $\sim$120 mW of the pre-amplifier allowed it to be operated in vacuum without special cooling. Signals from pre-amplifier had a DC off-set of 2-3 V, which is eliminated by using a capacitor of 6.0 μF. The required +12 V to the pre-amplifier is supplied using a battery which improves the signal to noise ratio in comparison to supplying the voltage from a NIM module. The gain of the pre-amplifier is 6 mV/MeV for α-particles with output impedance of 50 Ω. Pre-amplifier signals are amplified and shaped using a spectroscopy amplifier (CAEN N968).

The pulse height and energy resolution of the detector are studied as a function of bias voltage applied to the photodiode and shaping time of the spectroscopic amplifier. The leakage current of the photodiode varies in the range of 3-9 nA over the voltage range of 2-100 V. The Figs. 2.16(a)-(d) show the pulse height and energy resolution (FWHM) for α-particles (from ^{241}Am-^{239}Pu source) as a function of (i) bias voltage applied to the photodiode [Figs. 2.16(a) and (b)] (ii) shaping time of spectroscopic
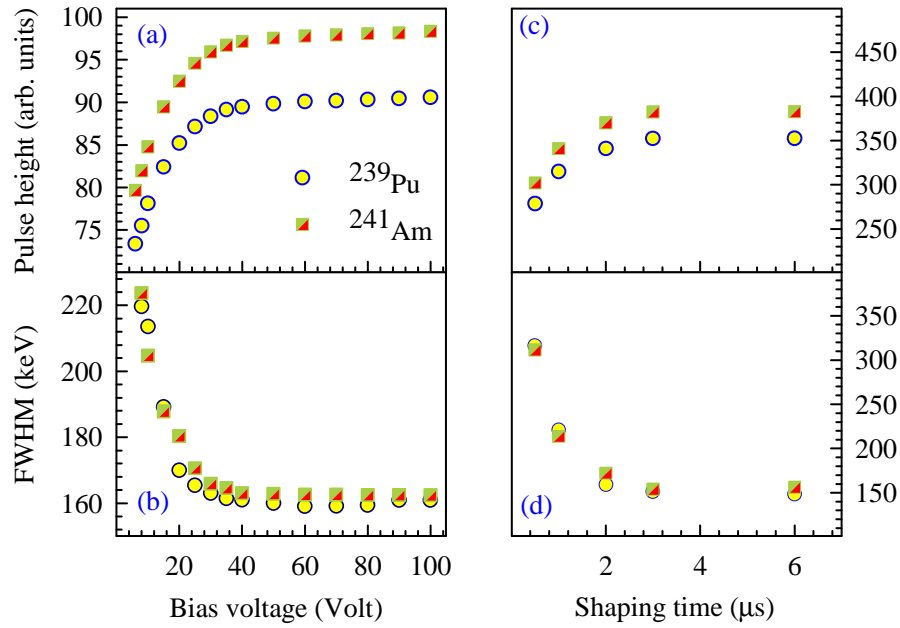
Figure 2.16: Pulse height and FWHM for the α-particles from ^{241}Am-^{239}Pu source as a function of bias voltage applied to the photodiode [in panels (a) and (b)] and shaping time of the spectroscopic amplifier [in panels (c) and (d)]. Circles are for ^{239}Pu and squares are for ^{241}Am.
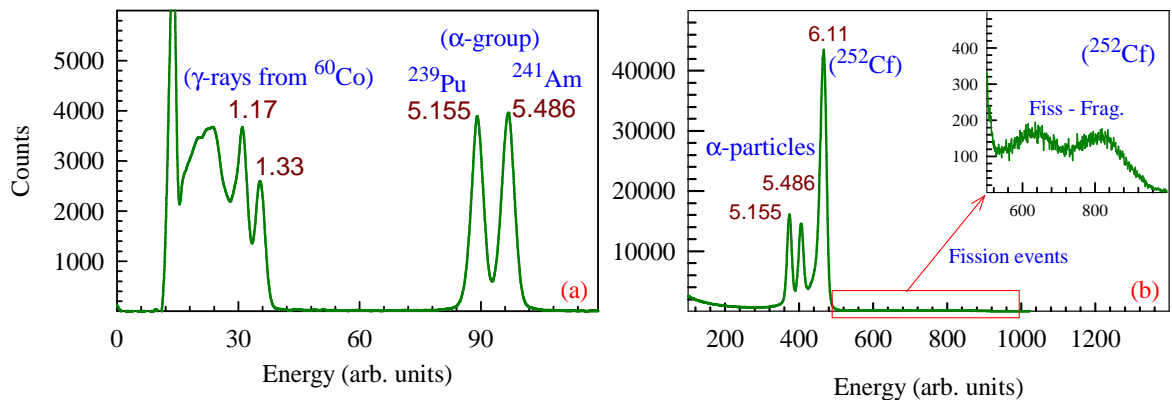
Figure 2.17: (a) Pulse height spectrum for α-particles from ^{241}Am-^{239}Pu and γ rays from ^{60}Co at operating voltage +35 V and shaping time 3 μs. (b) Pulse height spectrum for α-particles (from ^{241}Am-^{239}Pu) and fission fragments (from ^{252}Cf). The low counts due to spontaneous fission events of ^{252}Cf are shown in the inset.
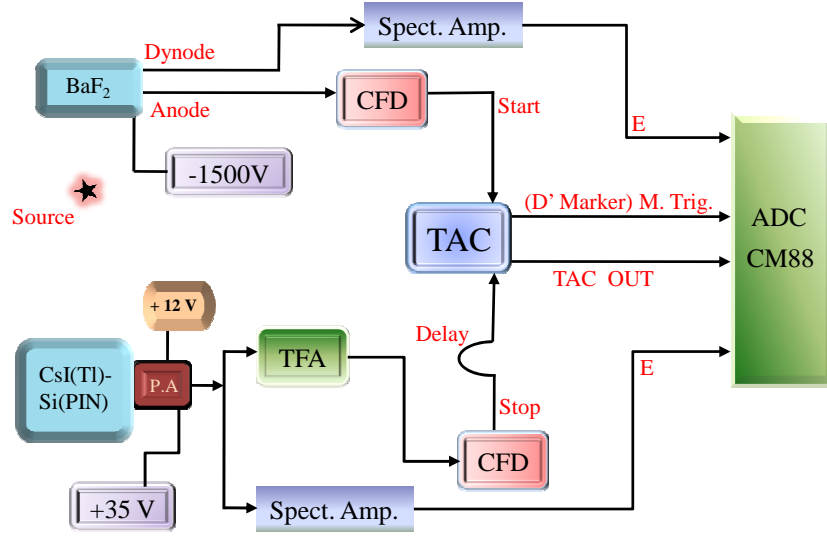
Figure 2.18: A block diagram of the electronics used for γ- γ/FFs coincidence between BaF_2 and CsI(Tl) detectors.

amplifier [Figs. 2.16(c) and (d)]. It is observed that for achieving full light amplification from the crystal, the applied bias voltage and shaping time are around $+35$ V and 3 μs, respectively. A typical energy spectra for α particles (from ^{241}Am-^{239}Pu source) and γ rays (from ^{60}Co) is shown in Fig. 2.17 (a). The broad peak below 1.17 MeV in Fig. 2.17 is due to Compton scattering of γ rays of energies 1.17 and 1.33 MeV. The energy resolution at shaping time of 3 μs and bias voltage $+35$ V is $\sim$3.6% for $\sim$5 MeV α- particles, and $\sim$7.8% for 1.33 MeV γ rays, respectively. Fig. 2.17 (b) shows the energy spectrum for α particles produced from ^{241}Am-^{239}Pu and ^{252}Cf sources. The low counts due to spontaneous fission events of ^{252}Cf are shown in the inset of Fig. 2.17 (b). It is to be noted that pulse heights for high energy FFs is very close to the 6.11 MeV α-particle.

2.4.2   Light output response for fission fragments (FFs)

The light output response of CsI(Tl)-Si(PIN) detector has been investigated for FFs of two different mass and charge groups produced from a ^{252}Cf source. The most probable fragments are ^{104}Mo and ^{144}Ba with corresponding energies of 104 and 80 MeV, respectively [143]. The pulse height spectrum from a ^{252}Cf source has a strong
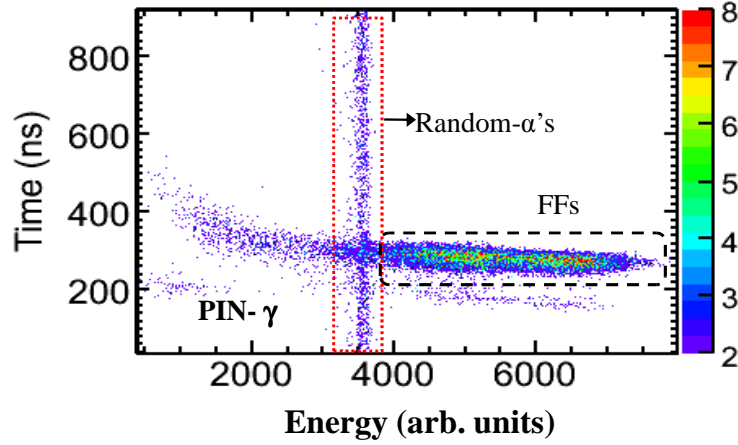
Figure 2.19: A two-dimensional plot of time versus energy of the γ rays, α-particles, and FFs from ^{252}Cf (see text).

peak due to α-particles of energy 6.11 MeV as shown in the Fig. 2.17 (b), that overlaps with FF pulse heights particularly when FF energy is degraded using absorbers. The separation of α-particles from FFs was achieved by employing time-of-flight (TOF) technique, where start signal was taken from a BaF$_2$ detector triggered by prompt γ rays, and the stop signal was from CsI(Tl)-Si(PIN) detector. The CsI(Tl)-Si(PIN) detector and ^{252}Cf source were mounted in a vacuum-tight stainless-steel (SS) chamber, whereas the BaF$_2$ detector was mounted outside but, close to the chamber. Distances of the CsI(Tl)-Si(PIN) and BaF$_2$ detectors from ^{252}Cf source were 28 cm and 2 cm respectively. P-10 gas was used as the energy degrader in the present experiment. The energies were degraded to 0.2 - 0.5 MeV/A for heavy FFs and 0.4 - 0.9 MeV/A for light FFs using P-10 gas at different pressure in the range of 5-50 mbar in steps of 5 mbar. Moreover, the aluminized mylar foil of 1.2 μm attached at the front face of the detector acted as an additional degrader at each gas-pressure.

The electronics configuration used for the TOF study is depicted in Fig. 2.18. Shaping times of the spectroscopic amplifiers for both the detectors were kept at 3 μs. The start signal from BaF$_2$ detector to the time to amplitude converter (TAC) was taken through a constant fraction discriminator (CFD) and stop signal from CsI(Tl)-Si(PIN) detector was taken through a timing filter amplifier (TFA), CFD, and a fixed

delay (25 ns) as shown in Fig. 2.18. The differentiation and integration times of the TFA were kept at 200 and 500 ns, respectively. For above time settings of the TFA, best signal-to-noise ratio was obtained. The range of the TAC was kept at 1 μs and it was calibrated using fixed delays of different magnitudes. Data were collected in event-by-event mode using a CAMAC based multi-parameter data acquisition system.

The FFs and α particles (6.11 MeV) were separated using TOF except for a small overlap as shown in Fig. 2.19. Other than α-particle and FF bands in Fig. 2.19, we also observed a 'PIN-γ' band corresponding to the γ rays reaching directly to the photodiode which are discussed in the next section. Because the start signal to the TAC is generated from γ rays, α particles are emitted randomly in the full range of the TAC. If we collect the data in singles, the ratio of α particles to FFs is observed to be $\simeq 20$, but because of TOF measurement, this ratio reduces to ~ 0.2. The reduction in α-intensity helps in determining the mean energy of the most probable FF after passing through P-10 gas. The small overlap of α particles with FFs was subtracted appropriately at each gas pressure. The pulse height spectra of FFs after subtracting α-contribution are shown in Fig. 2.20(a) for different gas pressures. The change in spectral shape with similar gas pressure is consistent with the earlier reported work [153] where energies of the FFs were measured using a gas ionization chamber.

Energy loss of the most probable light and heavy fragments in P-10 gas and aluminized mylar foil was calculated using the software SRIM [172]. In Fig. 2.20(b), we have shown the measured light yields as a function of calculated incident energy of the FFs after taking into account of the energy loss in gas and aluminized mylar foil. The light yield varies almost linearly as a function of energy. The light yield for heavy FF is observed to be more than that of light FF at a given energy. This difference in light yield is because of the heavier FFs having less dE/dx in CsI material than lighter ones for the same fragment energy [152, 153] as shown in Fig. 2.20(c). The dE/dx of FFs in CsI was calculated using the software SRIM [172] as a function of energy as
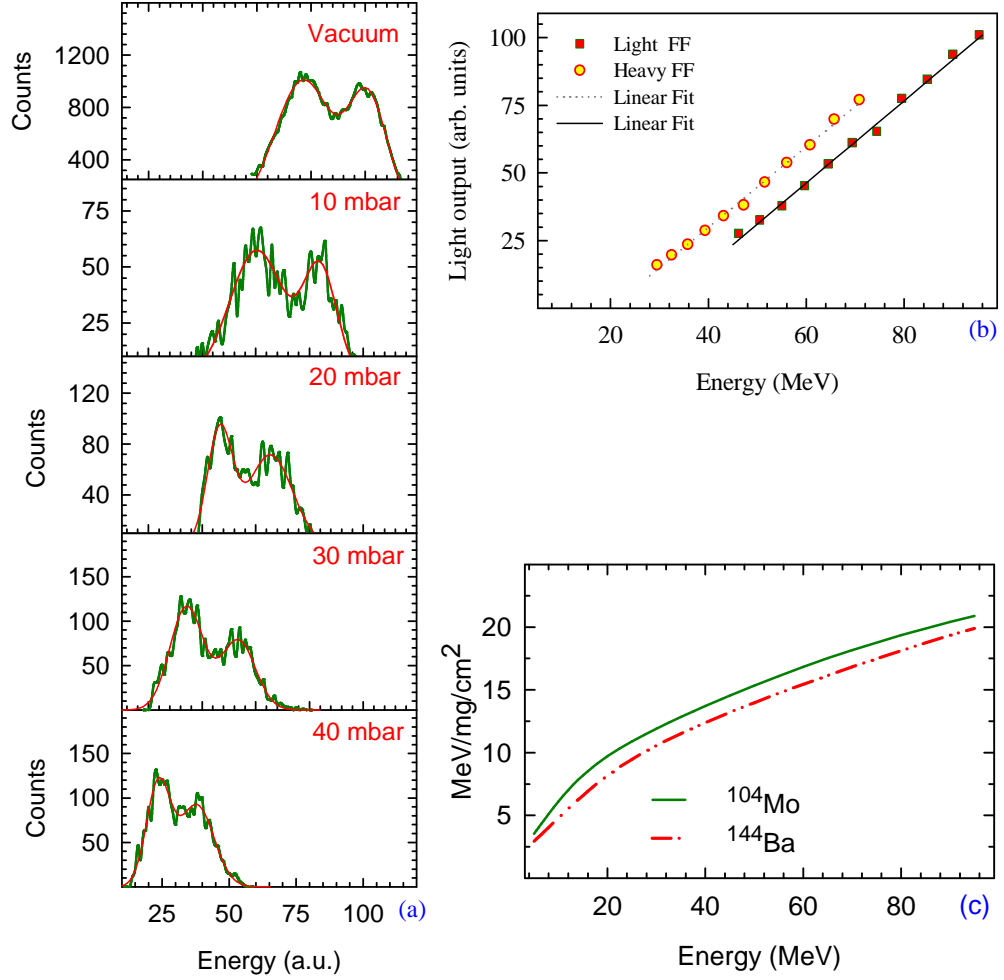
Figure 2.20: (a) Pulse height spectra of ^{252}Cf fission fragments (FFs) after subtracting α-contribution at different gas pressures (see text). Solid line in each panel is a result of two-peak Gaussian fit. (b) Light output of the FFs as a function of their energy deposited in CsI(Tl) crystal. (c) The dE/dx of FFs in CsI calculated as a function of energy using the software SRIM [172] for ^{104}Mo (solid line) and ^{144}Ba (dash-dot line).

shown for ^{104}Mo (light FF) and ^{144}Ba (Heavy FF). The light output response of the FFs in terms of dE/dx is consistent with the behavior previously observed for charged particles (2$\leq$Z$\leq$36) [163, 165]. It may be noted that a constant differential scintillation efficiency (dL/dE) as a function of fragment-energy [Fig. 2.20(b)] is observed for FFs whereas in case of charged particles, dL/dE increases with energy in a wide range of energy from 2.5 to 25.5 MeV/nucleon [163, 165, 166]. This is because the FFs studied in the present work using a ^{252}Cf source have a limited energy range of 0.5 to 1.3 MeV/nucleon. Present results are consistent with the measurement of Fellas *et.*

al [173], where light yield response of CsI(Tl) detector with PMT read-out has been studied for FFs of ^{252}Cf.

Light output response of CsI(Tl)-PMT detector for fission fragments was studied earlier by Fulmer [174], where, the most probable light and heavy fission fragments from thermal neutron induced fission of ^{235}U were magnetically separated. The scintillation light yields in a thin CsI(Tl) crystal (0.003 in.) were determined as a function of range in various gases and metals. The scintillation light yield as a function of energy was derived using energy versus range relationship determined by Schmitt and Leachman [175, 176]. The light yield was reported to be similar for both light and heavy FFs with an approximately linear increase with fragment-energy. However, from dE/dx behavior of the FFs, the scintillation light response for light and heavy FFs is expected to be different.

2.4.3   Time Response for γ rays

The time resolution is one of the most important parameters of any nuclear radiation detector. The factors that contribute to time resolution of any scintillation detector are the decay time constant of the crystal and the signal read-out system. The possible signal read-outs coupled to scintillation crystals are either photo-multiplier tubes (PMTs) or Si-photodiodes (or avalanche photodiode). Because of good signal amplification capability of PMTs, the CsI(Tl)-PMT detector has fast timing response, but it makes the detector bulky and inconvenient to be used in vacuum in high granularity detector arrays. CsI(Tl) detector coupled with Si(PIN) or avalanche photodiode is a suitable choice for the detector arrays because of its compact geometry. The scintillation decay pulse of CsI(Tl) detector can be well represented by a sum of two exponentials with different time constants [177], one fast (τ_f) and other slow (τ_s). τ_f changes with density of ionization of the incident particle and its energy, whereas τ_s is independent of particle type and its energy [177, 178]. The value of τ_s is $\sim$7 μs and τ_f is in the range
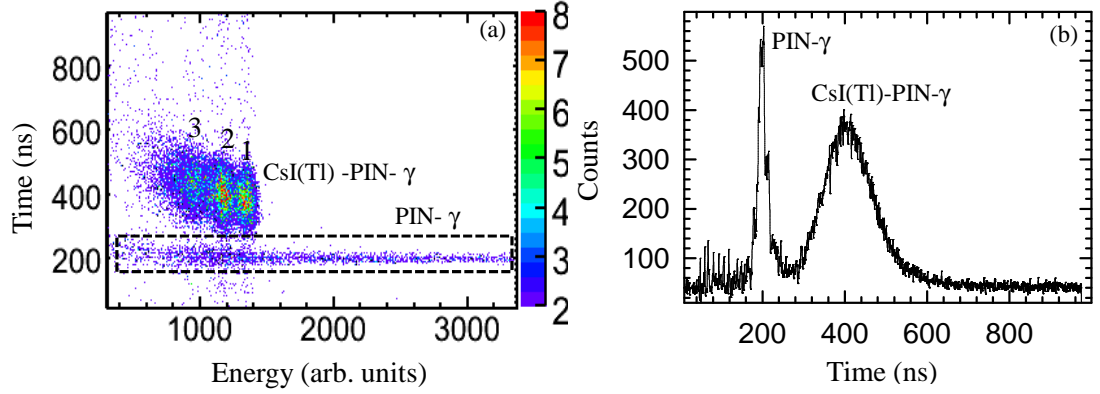
Figure 2.21: (a) A two-dimensional plot of time (from TAC) vs. energy of the γ rays from [60]Co. (b) The time-projection of the two-dimensional plot of panel (a).

of $0.4 - 0.7$ μs and it is a increasing function of particle-energy [177, 178]. The relative resolving time of various particles in CsI(Tl)-Si(PIN) detector is mainly determined by the fast component (τ_f) of the decay time constants. The value of τ_f for 662 keV γ rays is 0.70 ± 0.025 μs [178]. At a given energy, τ_f is largest for γ rays and hence the time resolution for γ rays will be poorest among all other radiation [178].

We have measured the time resolution of the CsI(Tl)-Si(PIN) detector for γ rays by detecting the two prompt γ rays from ^{60}Co in coincidence using a BaF$_2$ detector as start signal and CsI(Tl)-Si(PIN) detector as stop signal. The electronics configuration for this study was same as of Fig. 2.18. Distance of the CsI(Tl)-Si(PIN) detector to source (^{60}Co) was reduced from 28 to 4 cm to increase the coincidence rate. The source-detector (CsI(Tl)) setup was at atmospheric pressure in the covered SS-chamber. Other experimental details were exactly same as used for the investigation of light response of the detector for FFs. A two-dimensional plot of time (from TAC) versus energy of the γ rays (from ^{60}Co) is shown in Fig. 2.21(a). In this figure, two different groups of γ rays are observed. These two γ-groups are identified as (i) the one higher in time correspond to γ rays detected through CsI(Tl) crystal named as 'CsI(Tl)-PIN-γ', and (ii) the one lower in time is due to γ rays reaching directly to the photodiode named as 'PIN-γ'. In the group 'CsI(Tl)-PIN-γ' the sub-groups '1' and '2' correspond to photo-peaks for prompt γ rays of energies 1.33 and 1.17 MeV, respectively from [60]Co

source, whereas the sub-group '3' is due to Compton scattering of both the prompt γ rays. The PIN-γ rays are dominantly Compton scattered through the thin (300 μm) Si(PIN) photodiode which has very less photo-peak efficiency in comparison to the CsI. The pulse height ratio for photodiode signal to BGO+photodiode signal at the same γ-ray energy has been measured [179] to be 28.8 $\pm$ 0.1. Using above information this pulse height ratio for CsI(Tl) crystal has been estimated to be $\sim$7. The high gain of the photodiode makes the pulse heights corresponding to the low energy Compton scattered γ rays to be distributed over the entire energy range as shown in Fig. 2.21(a). In the Fig. 2.21(a) apart from two identified γ-groups, the events due to chance coincidence are also observed in the full time-range of the TAC.

Fig. 2.21(b) shows the time-projection of the time versus energy correlation plot of Fig. 2.21(a). In this time-projection, the peak corresponding to γ rays from CsI(Tl) is broader than the peak for the PIN-γ rays, as expected. The FWHM of the timing peak corresponding to CsI(Tl)-PIN-γ rays can be written in the form as;

$$FWHM^2_{CsI(Tl)-PIN-\gamma} = \Delta t^2_{CsI(Tl)-PIN-\gamma} + \Delta t^2_{BaF_2} + \Delta t^2_{Elect.} \qquad (2.4)$$

where, $\Delta t_{CsI(Tl)-PIN-\gamma}$ is the resolving time of the CsI(Tl)-Si(PIN) detector, Δt_{BaF_2} is the resolving time of the BaF$_2$ detector, and $\Delta t_{Elect.}$ is the electronic time resolution. In a similar way we can write FWHM for the peak corresponding to PIN-γ rays. The resolving time of the BaF$_2$ can be found in literature and its value is $\sim$112 ps [180] for γ rays from ^{60}Co source. The electronic time resolution was measured using a pulse generator, which we obtained as $\sim$3 ns. The FWHM of PIN-γ and CsI(Tl)-PIN-γ peaks shown in Fig. 2.21(b) are 23 $\pm$ 1 ns and 134 $\pm$ 3 ns, respectively. Using Eq.(2.4) the time resolution of the CsI(Tl)-PIN detector for γ rays is determined to be 134 $\pm$ 3 ns. In the present work the time resolution (FWHM) for fission fragments has also been estimated by taking time-projection of time versus energy correlation plot of Fig. 2.19 to be $\sim$25 ns and $\sim$30 ns for light and heavy FFs with average energies of 104 and 80 MeV, respectively. Time resolution for light charged particles would be better than

that for FFs, because for the light charged particles the decay time constant (fast) is smaller and the scintillation light yield is more than the FF at a given energy.

The time resolution of CsI(Tl) detector with PMT read-out for 511 keV γ rays has been reported to be 1.3 ns by Bhattacharjee *et al.* [181]. Harihar *et al.* [167] reported the time resolution to be 14.4 ns for ^{60}Co γ rays and 5.5 ns for FFs from spontaneous fission of ^{252}Cf. The time resolution of CsI(Tl) detector with avalanche photodiode read-out [182] has been observed to be of the order of 40 ns for γ rays. In the present work, the poor signal-to-noise ratio together with large rise time of Si(PIN)-diode [183] makes the time resolution of CsI(Tl) crystal with photodiode read-out to be poorer in comparison to the PMT. It should be noted here that the energy resolution is similar read-out[179], whereas the time resolution differs significantly for CsI(Tl) detector with photodiode and PMT read-outs.

2.4.4   Pulse shape discrimination (PSD)

The versatility of the CsI(Tl) detector is attributed to its unique properties and among many others its intrinsic ability to discriminate different type of charged particles relative to their specific energy loss dE/dx is of special interest. As mentioned earlier, the light output of the CsI(Tl) can be represented as the sum of two exponentials, one fast and the other slow [177]. The light-amplitude ratio of fast to slow components as well as the fast time constant are particle dependent, and therefore, two avenues are possible to discriminate various particles. The technique which utilizes the amplitude ratio of fast to slow components, is based on charge comparison methods [168]. The technique which we have used in the present work utilizes the particle dependent fast component of the decay time constant [177, 178]. In the present case the scintillation light is sensed by a PIN photodiode, which is connected to the input of a charge sensitive pre-amplifier. Since the rise time of such a pre-amplifier is equal to the decay time constant of the scintillation light, the particle type information is contained in
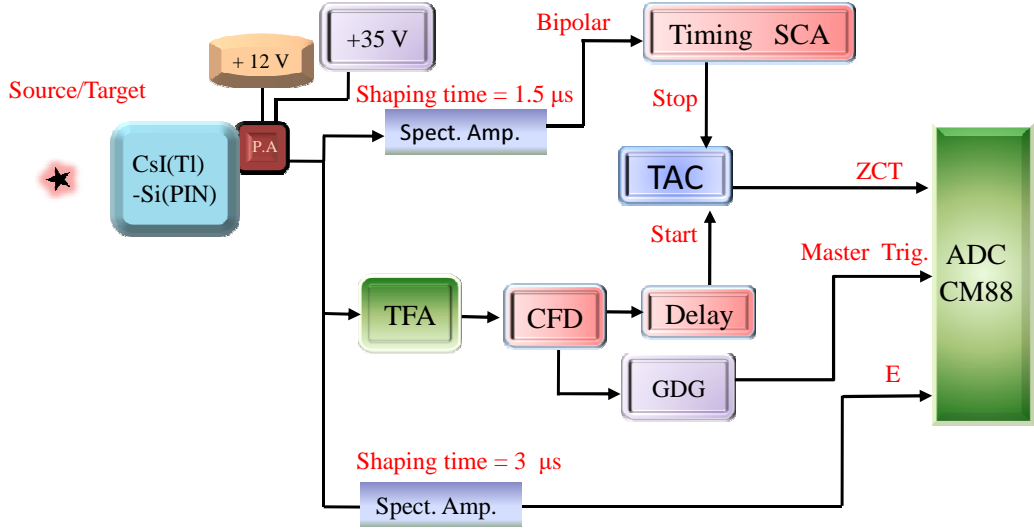
Figure 2.22: A block diagram of the electronics used to obtain pulse shape discrimination with zero crossover (ZCT) technique.

the rise time of the output pulse of the pre-amplifier. In the present technique the particle type information is obtained by the zero crossover time (ZCT) of the output pulse [167]. Since the fast component decreases with increasing dE/dx of the particle, whereas the slow component remains almost constant, therefore the rise time of the pulse and hence ZCT should decrease with increasing dE/dx.

A block diagram of the electronics used to obtain pulse shape discrimination with ZCT technique is shown in the Fig. 2.22. In the present work, we used the timing-SCA module, CANBERRA 2037A to extract the ZCT. Before performing in-beam experiments the PSD was obtained off-line between α particles and γ rays using radioactive sources. A two-dimensional plot of ZCT vs. energy of the particles obtained is shown in the Fig. 2.23(a) for off-line, and in the Fig. 2.23(b) for in-beam from ^{11}B (69 MeV) + ^{232}Th reaction. The in-beam experiment which will be discussed in detail in a later chapter, was performed at 14-MV BARC-TIFR Pelletron facility, Mumbai. In the Figs. 2.23(a) and (b), it is seen that the rise time decrease as the dE/dx increases and for a given particle it increases with the energy. In off-line as well as in-beam PSDs, a very good separation between different particles and γ rays is obtained using the ZCT.
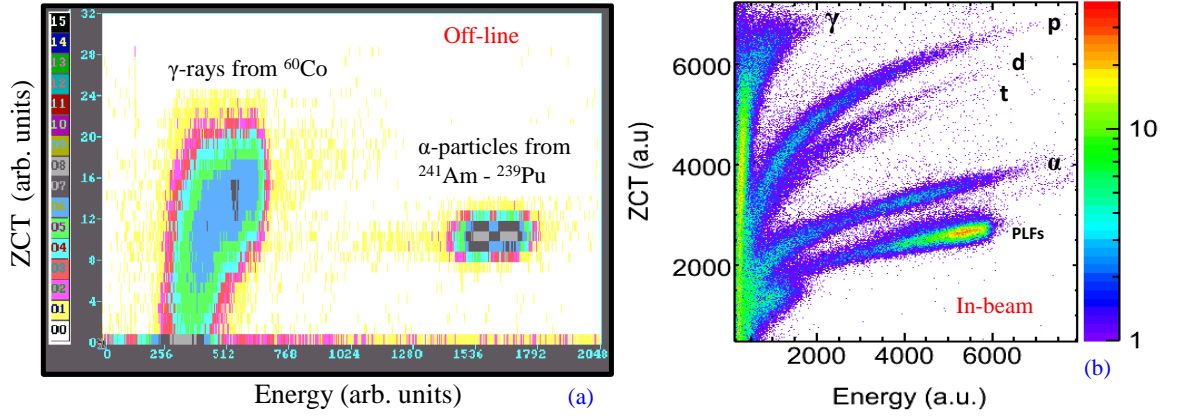
Figure 2.23: Pulse shape discrimination (PSD) using zero crossover time (ZCT). (a) An off-line PSD between α particles and γ rays produced from ^{241}Am-^{239}Pu and ^{60}Co, respectively. (b) An in-beam PSD between various reaction products of ^{11}B (69 MeV)+ ^{232}Th reaction, measured at 14-MV BARC-TIFR Pelletron facility, Mumbai.

2.5   Target preparation

Target preparation is often crucial to the success of an experiment and it is therefore of the utmost importance that the target confirms to the experimental requirements with regard to purity, composition, thickness, etc. Many techniques are used for target preparation such as vacuum evaporation (resistive heating), mechanical rolling, direct glow discharge (electrical discharge), electro-deposition, deposition using an isotope separator, electro-spraying, sputtering, etc. The targets used in the present thesis work along with their relevant information such as isotopic purity, thickness, backing, preparation method, and purpose of use, are listed in the Table 2.3.

2.6   BARC-TIFR Pelletron accelerator facility

The Pelletron accelerator facility at Mumbai, set up as a joint collaborative project between BARC and TIFR, has been serving as a major research facility for heavy-ion accelerator based research in India since its commissioning in December, 1988. The facility is housed at TIFR, Mumbai. For the present accelerator, the maximum terminal voltage is 14 MV. This high electric potential at the terminal is achieved by

Table 2.3: Various targets used in the present thesis work along with their relevant information.

Target	Isotopic purity	Thickness mg/cm^2	Backing	Preparation method	Purpose
^{115}In	95.71%	0.5	No	Vacuum evaporation	NLD study[1]
^{93}Nb	100%	0.6	No	Mechanical rolling	NLD study[1]
^{89}Y	100%	0.7	No	Mechanical rolling	NLD study[1]
^{181}Ta	99.98%	1.5	No	Mechanical rolling	NLD study[1]
^{164}Dy	99.9%	1.1	No	Mechanical rolling	NLD study[1]
^{232}Th	100%	1.5	No	Mechanical rolling	Fission study[2]
^{197}Au	100%	0.4	No	Vacuum evaporation	Det. Calibration[3]
^{209}Bi	100%	0.4	No	Vacuum evaporation	Det. Calibration[3]
^{12}C	98.89%	0.05	^{181}Ta	Direct glow discharge	Det. Calibration[3]
Mylar	100%	0.33	^{181}Ta	Commercially procured	Det. Calibration[3]

[1] For nuclear level-density investigation.

[2] For fission dynamics study.

[3] For energy calibration of CsI(Tl)-Si(PIN) detectors.

means of the chain of steel pellets separated by insulators and hence the name *Pelletron accelerator*. This method leads to more uniform charging compared to moving charging belt and hence less ripple on the HV terminal. A superconducting linear accelerator has also been commissioned in 2002 as a energy booster to the heavy-ion beams produced from Pelletron facility.

Fig. 2.24 shows a schematic layout of the 14UD BARC-TIFR Pelletron accelerator facility, Mumbai. The ion source named 'SNICS' (*source of negative ions from cesium sputtering*), situated at the top of the accelerator tower generates negative ions which are initially accelerated to low energies (150 – 250 keV) in short horizontal section. These low energy singly charge state negative ions are then mass analyzed using a injector magnet before entering to the high voltage vertical accelerator column, where the injected negative ions are accelerated towards the positively charged terminal situated in the middle of the column. Due to this acceleration, negative charged ions gain an energy of V_T MeV, where V_T is the terminal voltage in MV (million volts). Inside the terminal, the ions pass through a thin carbon stripper foil (~ 5 μg/cm^2) or a small volume of a gas, where they strip several electrons resulting in distribution of
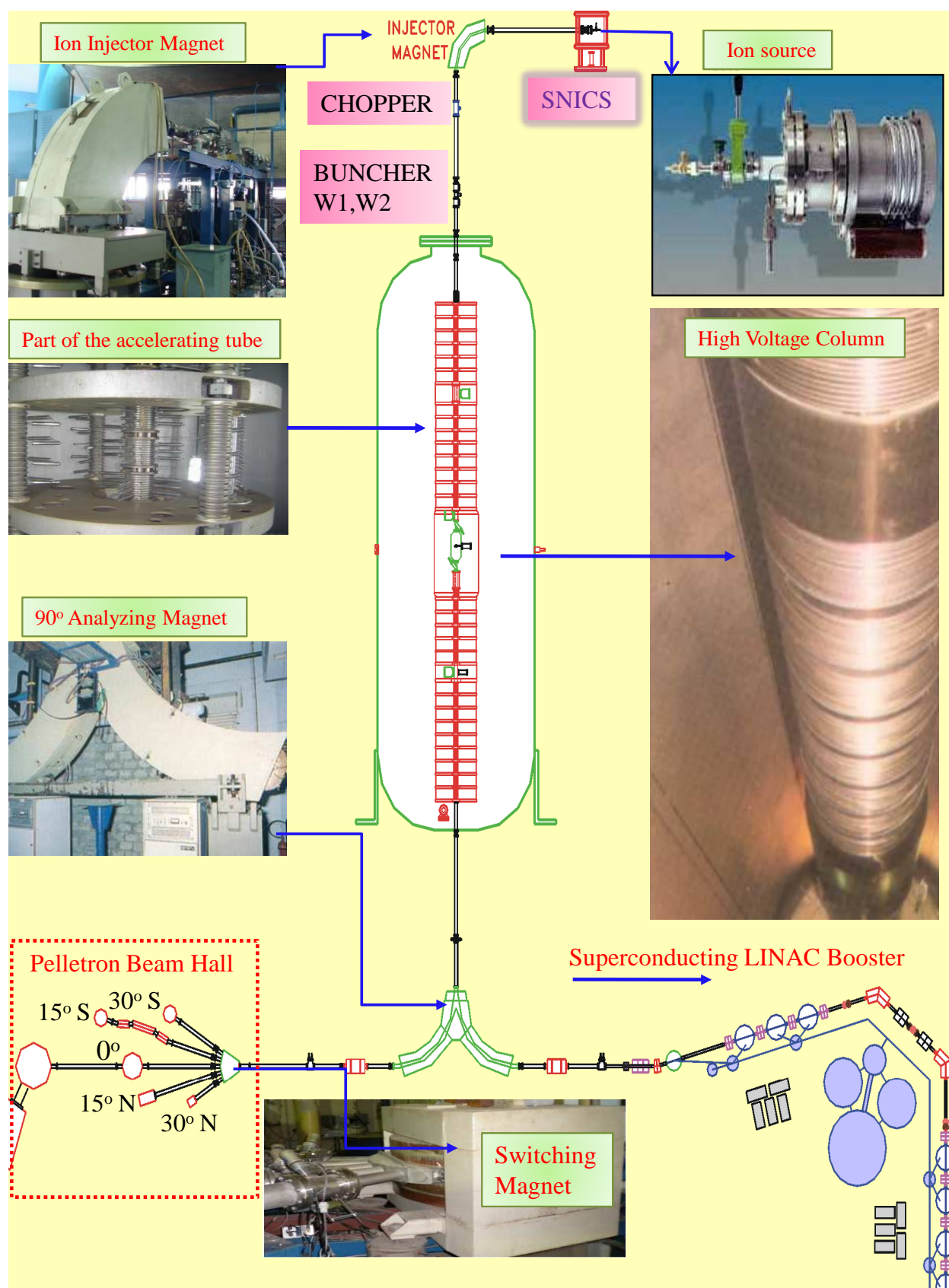
Figure 2.24: A schematic layout of the 14UD BARC-TIFR Pelletron accelerator facility, Mumbai.

positively charged ions. This distribution depends on the type and velocity of the ions. These positively charged ions at the terminal are repelled by the positive voltage at the terminal and are therefore, accelerated to the ground potential. This results in a energy gain of qV_T MeV for a ion with charge state q. Thus, the total energy gain of the ions becomes

$$E = (q + 1) \times V_T \quad \text{MeV.} \tag{2.5}$$

At the end of the accelerating tube, an analyzing magnet is placed which serves the purpose of charge and energy selection of the ions. The energy of the analyzed ions of mass number A and charge state q in this accelerator is given by the relation [184];

$$B = 720.76 \frac{\sqrt{AE}}{q}, \tag{2.6}$$

where B is the magnetic field in Gauss and E is the energy in MeV. This analyzed beam of ions is then transported with the help of switching magnet to any of the beam lines at $0°$, $15°$ N, $15°$ S, $30°$ N, and $30°$ S.

Experiments of the present thesis work were carried out at beam lines of $0°$ and $15°$N. The nuclear level-density investigation were carried out at $15°$N beam-line, where using a very compact scattering chamber the α particles were measured in coincidence with γ-ray multiplicity. The fission dynamics investigation were carried out at $0°$ beam-line, where α particles were measured in coincidence with FFs in a wide angular range using a general purpose scattering chamber which is equipped with two movable arms.

Chapter 3

Nuclear level-density investigation

3.1 Introduction

The study of nuclear level-density (NLD) parameter, 'a' and its dependence on mass and angular momentum is important as it plays a major role in determination of the phase space available for the excited nuclei governing their decay probability in statistical model calculations. The major source of knowledge about level densities at higher excitation energies and spins arises from particle-evaporation spectra in heavy-ion fusion reactions [34, 50, 69–73] analyzed in the framework of the statistical model.

In the present work, we have developed a method for extracting nuclear level-density parameter as a function of angular momentum. Using this method we have obtained results for the inverse level-density parameter ($K = A/a$) as a function of angular momentum for a number of nuclei in shell-closure region of $Z \sim 50$ and mid-shell region of $Z \sim 70$ in the excitation energy range of 30 to 40 MeV. We have used heavy-ion fusion reactions to populate the excited, rotating nuclei and characterized their level-density as a function of angular momentum by measuring α-particle evaporation spectra in coincidence with γ-ray-multiplicity. The reactions are selected to populate residual nuclei with $Z \sim 50$ and 70 after α-particle evaporation corresponding to the shell-closure and mid-shell regions, respectively. The relevant parameters of the fusion reactions are given in Table 3.1. The target-projectile systems se-

lected in the present work correspond to a range of entrance-channel mass-asymmetry, $\alpha = (A_T - A_P) / (A_T + A_P)$. An analysis of the reactions based on Businaro-Gallone critical mass-asymmetry (α_{BG}) for various ℓ-partial waves (Sec. 3.5) reveals that all these reactions will undergo normal compound nuclear formation without a di-nuclear complex formation ($\alpha > \alpha_{BG}$). The bombarding energies are chosen such that all the compound nuclei are formed with ∼60-MeV excitation energy.

The spin-dependent level density makes its most noticeable change in the slope of the high energy tail of the evaporation spectra. This slope is least influenced by the barrier transmission factors. For the present study, we focus on the high energy tail of the α-particle spectra although the spectra are measured over a wider range of energies. By tagging the α-particle energy spectra with the γ-ray-multiplicity fold signal (defined in Sec. 4.2.4), the angular momentum dependence of the level-density parameter has been derived. In the data analysis, each fold value is converted to a corresponding average angular momentum following a procedure that utilizes decay-simulation and detector efficiency factors. The shape of the fold-gated α-particle energy spectra is analyzed in the energy region well above the evaporation barrier. We obtain K values as a function of angular momentum for the residual nuclei by fitting the experimental fold-gated spectra with simulated spectra using the code PACE2 [136].

Selection of high emission-energy region for the analysis leads to a specific excitation energy range in the residual nuclei for which the results obtained are valid [72]. In the present work, this range is from 30 MeV to 40 MeV. Since the multiplicity of α particles and other charged particles are less than unity in the present reactions, it can be safely assumed that α-particle emission leaves residual nuclei with $Z_R = Z_{CN} - 2$ and our results are valid for these $Z (Z_R)$ values.

Table 3.1: The relevant experimental parameters of reactions studied for nuclear level-density investigation (see text).

Index	Reaction	Z_R	N_R	I_R	A_R	α	E_{lab} (MeV)	E_{CN} (MeV)	l_{graz} ($\hbar$)
Shell-closure region:									
a	^{19}F + ^{93}Nb	48	60	0.111	108	0.660	73.5	60.0	29.5
b	^{24}Mg + ^{89}Y	49	60	0.101	109	0.575	100.5	60.6	38.9
c	^{27}Al + ^{89}Y	50	62	0.107	112	0.534	106.0	60.4	38.9
d	^{24}Mg + ^{93}Nb	51	62	0.097	113	0.589	103.3	60.3	39.7
e	^{11}B + ^{115}In	52	70	0.147	122	0.825	58.0	61.0	30.1
f	^{12}C + ^{115}In	53	70	0.138	123	0.811	71.0	61.0	34.7
g	^{16}O + ^{115}In	55	72	0.134	127	0.755	80.0	59.2	35.6
Mid-shell region									
h	^{11}B + ^{164}Dy	69	102	0.192	171	0.874	64.6	58.4	31.9
i	^{12}C + ^{164}Dy	70	102	0.186	172	0.863	73.5	57.1	33.0
j	^{16}O + ^{164}Dy	72	104	0.181	176	0.822	86.0	56.5	32.0
k	^{12}C + ^{181}Ta	77	112	0.185	189	0.875	76.8	57.0	33.0

3.2   Experimental details

The experiments were performed using heavy-ion beams from the BARC-TIFR 14-MV Pelletron accelerator facility at Mumbai. A number of systems were studied as listed in Table 3.1 and the measurements were carried out in two separate experiments. In the first set of experiments, reactions (a) to (d) were studied and in the second, reactions (e) to (k) were studied. The reactions (a) to (g) correspond to the shell-closure region, whereas the reactions (h) to (k) correspond to the mid-shell region. Table 3.1 gives other experimental parameters such as charge (Z_R), neutron number N_R, reduced isospin $I_R = \left(\frac{N-Z}{A}\right)_R$, and mass (A_R) of residual nuclei after α-particle evaporation, entrance-channel mass-asymmetry α, bombarding energy E_{lab}, compound nucleus excitation energy E_{CN}, and grazing angular momentum values l_{graz} for the systems studied in the present work.

3.2.1   Apparatus and their utilization

A compact scattering chamber and a γ-ray-multiplicity setup consisting of fourteen BGO detectors were used for the measurements. A photograph of the experimental setup is shown in the Fig. 3.1, where the inset in the bottom right shows the inside view of the compact scattering chamber. Self supporting thin metallic foils of the targets having thickness in the range of 500-1500 μg/cm^2, were mounted on the target ladder and placed at right angle to the beam. α particles emitted in the reactions were detected by two collimated silicon surface barrier $\triangle E - E$ (25 μm-2 mm) detector telescopes mounted in the median (reaction) plane at back angles. The telescopes were kept at $\theta_{\mathrm{lab}} = 116°$ and 125° for the first set and at $\theta_{\mathrm{lab}} = 125°$ and 153° for the second set. The charged-particle detectors were kept at the backward angles so that they record spectra predominantly from the compound nuclear evaporation. This also helped in reducing the contamination effects due to light mass impurities present in the target material. The telescopes were of equal solid angle of $\sim$5.94 msr. Another
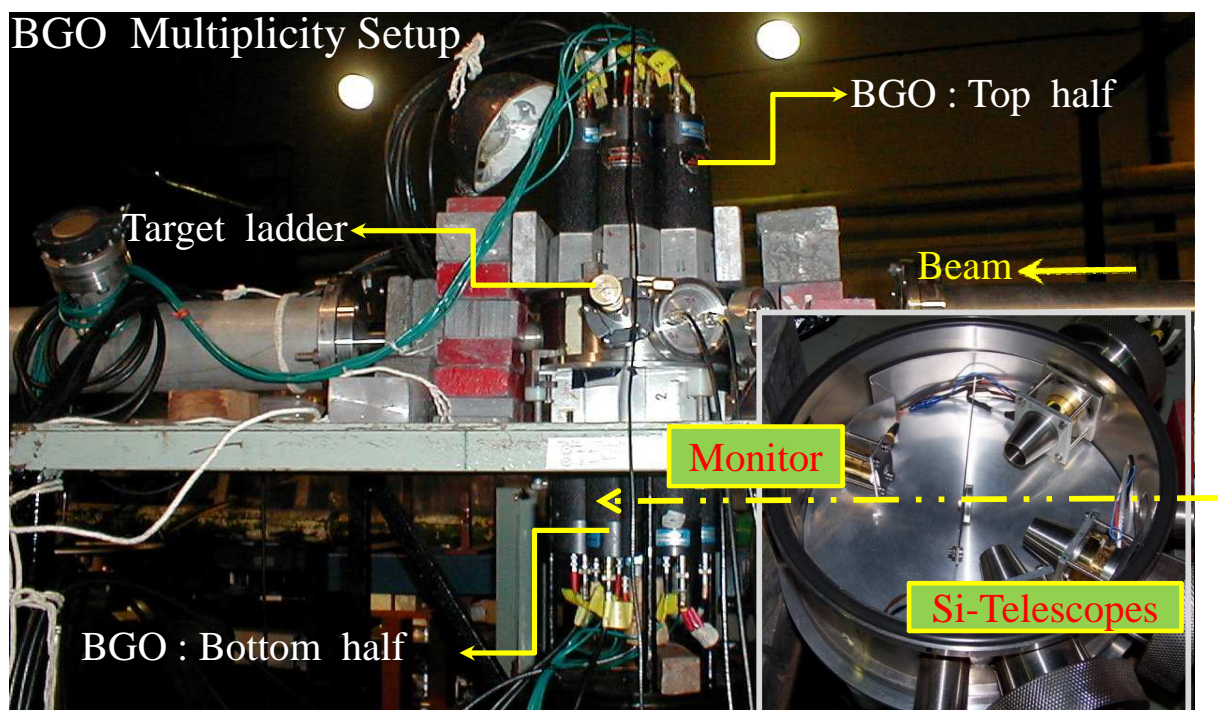
Figure 3.1: A photographs of the experimental setup. The inset in the bottom right shows the inside view of the compact scattering chamber.
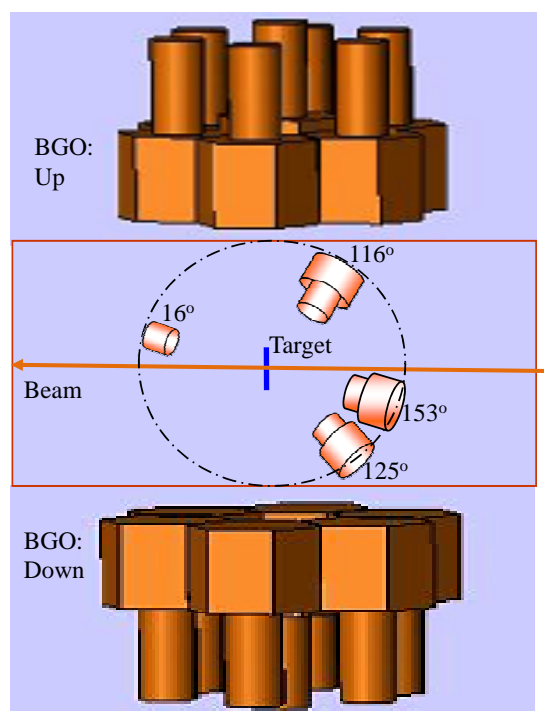
Figure 3.2: Schematic diagram of experimental setup employing fourteen BGO multiplicity filter and the Si-telescopes.

surface-barrier detector having a solid angle of $\sim$0.20 msr was mounted at $\theta_{\text{lab}} = 16°$ for normalization with Rutherford scattering events.

The γ-ray multiplicity array used in the experiments consisted of fourteen bismuth germanate (BGO) detectors each 6.3 cm thick and having a regular hexagonal cross section with a distance of 5.6 cm between the opposite edges. They were mounted on top and bottom of the reaction plane in two close-packed groups of seven each. The two groups were placed at a distance of $\sim$ 2.5 cm on either side of the reaction plane. The middle detector in each group was pulled out to nearly equalize the efficiency of all the detectors. Schematic diagram of experimental setup employing fourteen BGO multiplicity filter and the Si-telescopes is shown in the Fig. 3.2. The energy threshold of the BGO detectors was adjusted to be 150 keV (100 keV for the second set) γ-ray energy. The efficiency of the setup was measured for 662 keV γ rays emitted from a ^{137}Cs source of known strength placed at the target position and the total efficiency was determined to be 51% (55% in the second set). The cross-talk between any two adjacent detectors was also measured using ^{137}Cs, and it was found to be < 1%. The granularity of the BGO multiplicity detector array is appropriate for the present measurements as the average γ-ray multiplicity is around 2-3.

3.2.2 Electronics configuration for coincidence measurements

The linear energy output from any detector was fed to an analog-to-digital converter (ADC) after suitable amplification through a spectroscopy amplifier. The timing or anode output from each BGO detector was sent to a time-to-digital converter (TDC) to measure the prompt γ-ray multiplicity via a combination of timing filter amplifier (TFA), constant fraction discriminator (CFD) and variable delay (DV8000). The common start for the TDC was generated from the delay matched timing signal of the Si-Telescope E-detectors. Schematic layout of the electronics used for charged particle and γ-ray coincidence measurements, is given in Fig. 3.3. The α particles were sep-
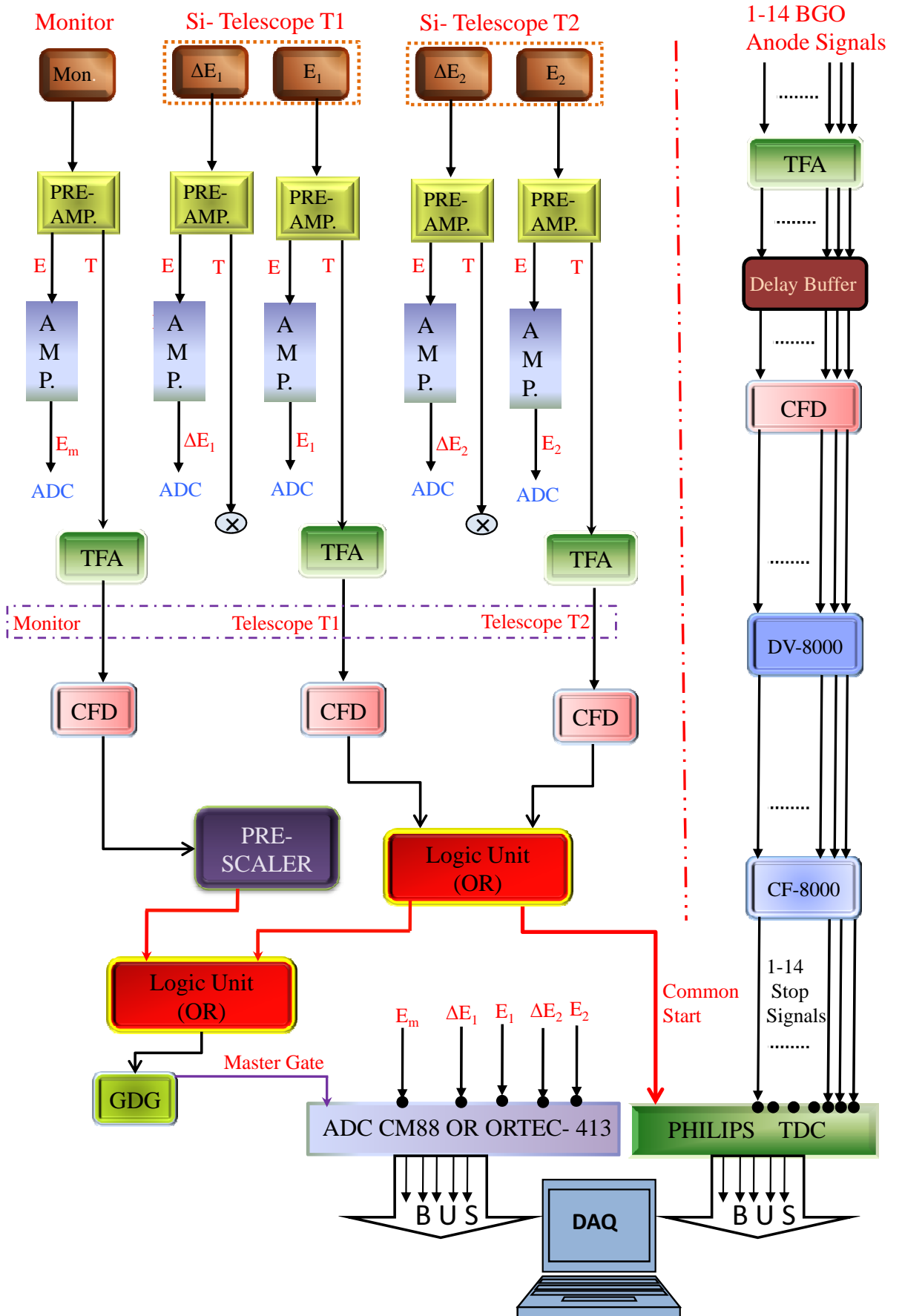
Figure 3.3: Schematic layout of the electronics used for charged particle and γ-ray coincidence measurements.
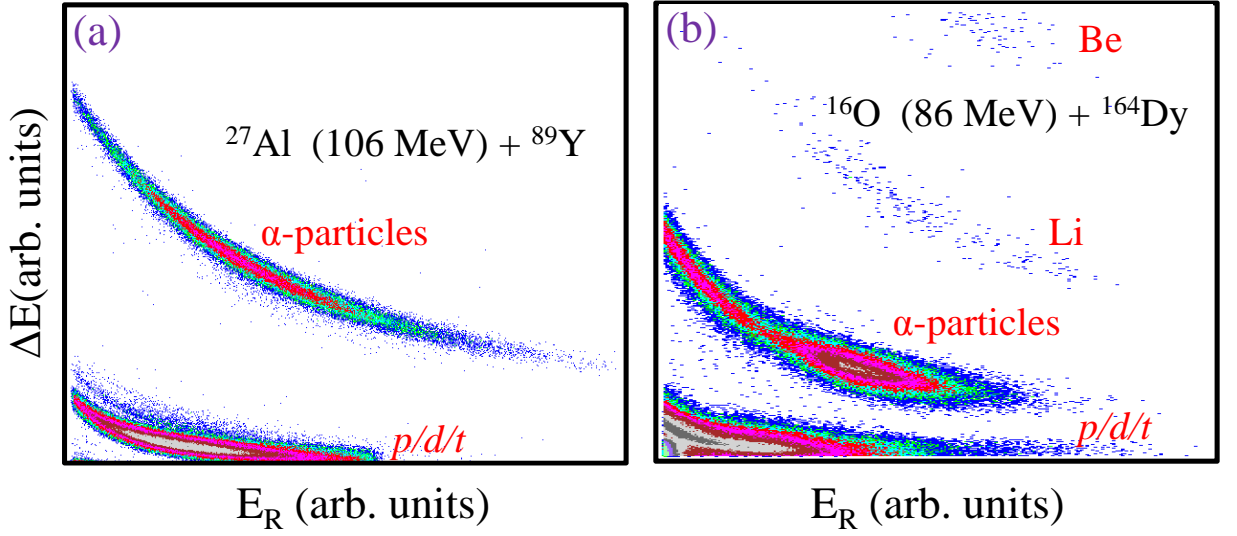
Figure 3.4: Typical two-dimensional spectra of ΔE (25 μm) vs. E (2 mm) at a laboratory angle of 125°, showing different particles produced in the ^{27}Al (108 MeV) + ^{89}Y reaction (shell-closure region) in panel (a) and ^{16}O (86 MeV) + ^{164}Dy (mid-shell region) in panel (b).

arated from other light charged particles and projectile like fragments in the ΔE-E telescopes by the difference in their energy loss in ΔE detectors. Two typical ΔE vs. E spectra from both sets of the experiments are shown in the Figs. 3.4(a) and (b) from reactions ^{27}Al (106 MeV)+ ^{89}Y and ^{16}O (86 MeV)+ ^{164}Dy, respectively. The stability of the amplifier gains corresponding to various Si-detectors was monitored using a precision pulser throughout the measurements. The pulse heights from the ΔE-E detector telescopes and the BGO timing outputs were recorded in a list-mode using CAMAC based multi-parameter data acquisition system.

3.2.3 Detector energy calibration

The Si-telescopes were energy calibrated using α particles from a ^{228,229}Th source and with ^{7}Li ions elastically scattered off a thin ^{197}Au (^{209}Bi in the second set) target. Calibration energies ranged from 6 MeV to 30 MeV. Energy loss of the incident ^{7}Li ions in the target was taken into account in determining the energy calibration. Similarly, energy loss of emitted α particles through the target foil was taken into account in
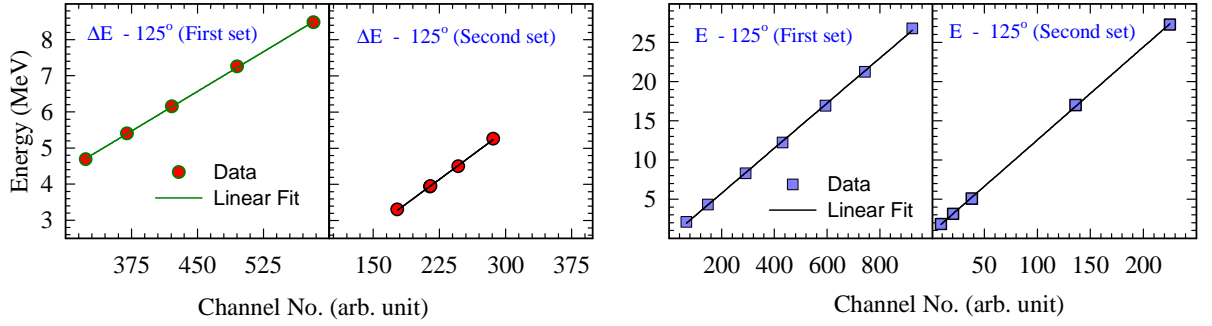
Figure 3.5: Energy calibration plots for typical Si-telescope detectors (ΔE and E) used at an angle of 125° with respect to the beam in two different sets of the experiments.

determining the final energy of the α particles. The typical energy calibration plots for Si-telescope detectors (ΔE and E) used at an angle of 125° with respect to the beam in two different sets of experiments, are shown in the Fig. 3.5.

3.3   Data Analysis

The fold-gated α-particle energy spectra were projected out from the list-mode data after putting suitable two-dimensional gate on the α-particle band and on the γ-ray-multiplicity fold number. Fold is defined as the number of BGO detectors firing simultaneously in an event. Maximum fourteen γ rays were intended to be measured in an event. We got the fold distribution up to fold value of 11 only. The event distribution as a function of γ-ray fold falls off exponentially. Therefore, in a typical event distribution the counts in fold -11 are less than 1% of the total yield.

3.3.1   Background subtraction

Light mass impurities such as carbon and oxygen that are present in the targets created low-energy tails in the energy spectra for two of the light projectiles (^{11}B and ^{12}C). The α particles originating from the reactions with impurity elements appeared in the spectra at low energies, particularly for the low multiplicity folds. As the projectile mass increased from ^{11}B, the background became less severe. For the projectiles heavier

than ^{16}O, there was no appreciable interference of impurity events even for low folds. Every fold-gated spectrum was examined for the presence of this background. The grazing angular momentum populated in the fusion reactions with light impurity elements is much less than that of targets. Therefore, this background decreases rapidly as one moves from low to high γ-ray fold events. This dependence of the background on the fold as well as the α-particle energy is illustrated in a gross manner in the two-dimensional plots as shown in the Fig. 3.6 for all the systems studied. It is seen from Fig. 3.6 that for a given projectile and fold number, the fraction of background in the mass region of $A \sim 180$ is more than that of $A \sim 120$. In the mass region of $A \sim 180$, the α-particle multiplicity (ν_α) is expected to be much less than the lower mass region of $A \sim 120$. Therefore, the background appears to be significant up to fold 3 in this mass region of $A \sim 180$, allowing the analysis to be carried out only for fold 4 and above, where the background contribution is seen to be negligible.

In the shell-closure region, the low-energy component was treated as a background and was removed by following a least-squares fit procedure. In the fits to remove the background, an initial estimation of the exponential fall of the background was made in the energy region of 5 MeV to 10 MeV, where the low energy tail is dominant, using a function $N_1 \exp\left(-E/T_B\right)$ where N_1 is a normalization constant and T_B is a slope parameter. The values of N_1 and T_B thus obtained were used as initial values in the composite function

$$\text{Yield} = N_1 \exp\left(-E/T_B\right) + N_2 E \frac{\exp\left(-E/S_1\right)}{\left[1 + \exp\left(\frac{E_b - E}{S_2}\right)\right]}, \qquad (3.1)$$

where the second term in the right-hand-side with a normalization factor N_2, emission barrier energy factor E_b and slope factors S_1 and S_2 models the shape of the α-particle spectrum in laboratory system. By fitting the spectrum using Eq. (3.1) in the energy interval of 5 MeV to 30 MeV, values of N_1 and T_B were optimized for the whole energy interval. As a typical case for background subtraction, the energy spectra for fold 1 to 3 from ^{11}B$+^{115}$In reaction are shown in top panels of Fig. 3.7. The spectra
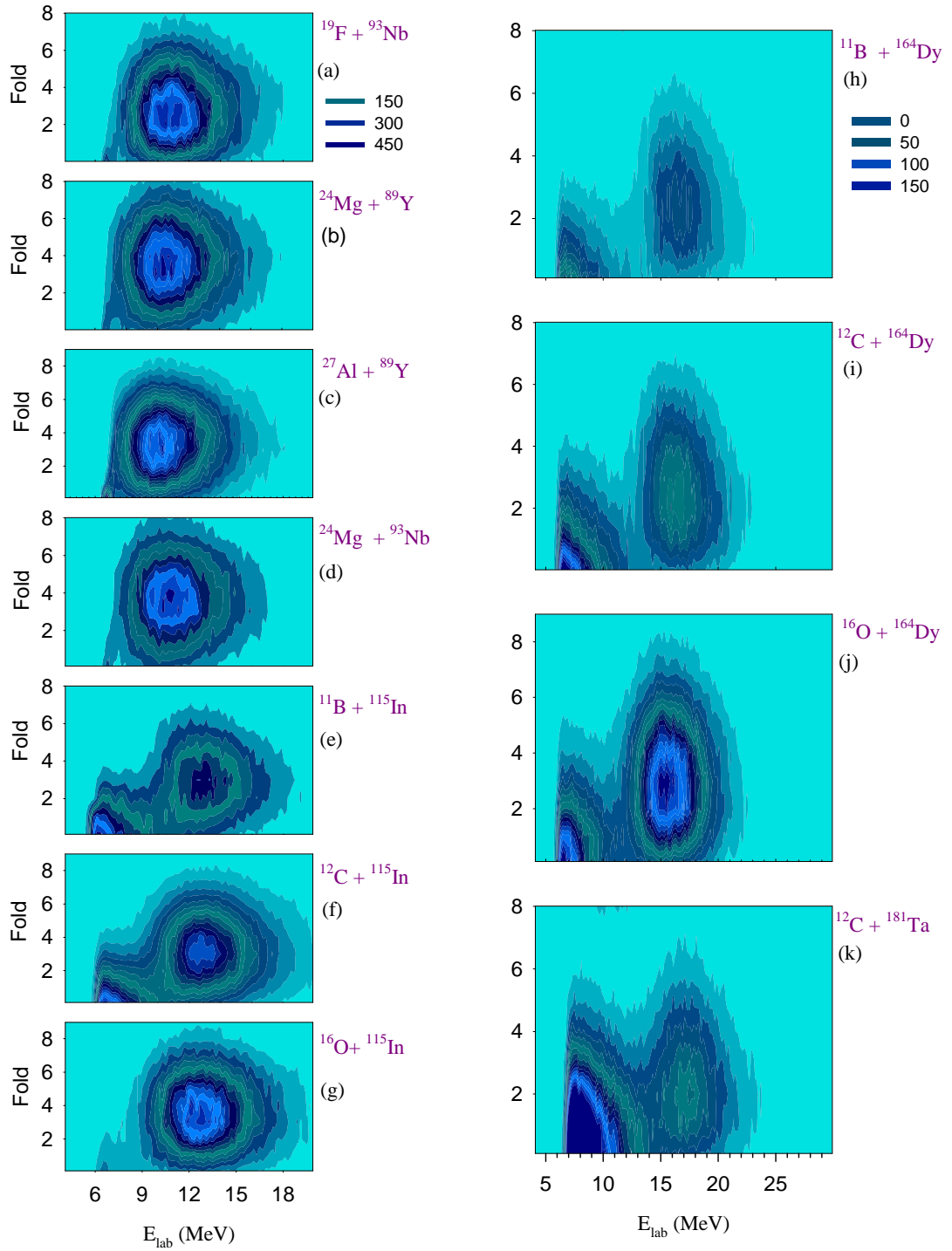
Figure 3.6: Two-dimensional plots of γ-ray fold vs. α-particle energy (laboratory) measured at $\theta_{\mathrm{lab}} = 125°$, in reactions corresponding to shell-closure [panels (a) to (g)] as well as mid-shell [panels (h) to (k)] regions. Along the each panel corresponding reaction is mentioned.
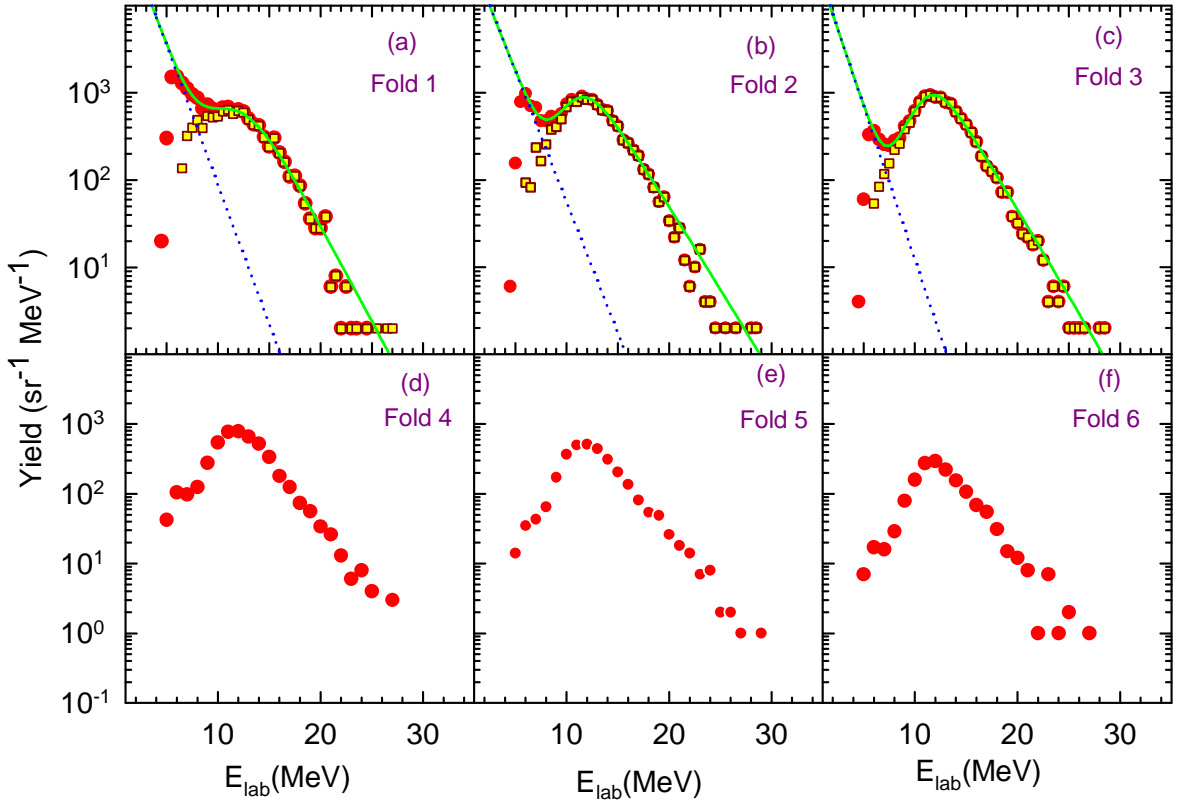
Figure 3.7: (a) - (f) Laboratory α-particle energy spectra measured at $\theta_{\text{lab}} = 153°$ in ^{11}B + ^{115}In reaction for folds 1 to 6 (filled circles). For folds 1 to 3, the solid line is the fit to the spectrum including the low energy part; The dotted line is the fit to the low energy background part of the spectrum and the filled squares represent background subtracted spectra. For fold 4 and above, no background subtraction was done since the data above an energy of 15 MeV are essentially free of background (see text).

before and after background subtraction are shown using filled circles and solid squares, respectively. The dotted line in the figure is the low-energy background part obtained using the optimized parameters N_1 and T_B in the function $N_1 \exp(-E/T_B)$. It was observed that for the fold 1 spectrum the estimated background was less than 0.3% at 15 MeV of α-particle energy and it exponentially reduces at higher energies. The influence of background in determining the slope of the high energy tail (>15 MeV) is negligible. For fold 2 and 3 the influence of the background is further strongly reduced [Figs. 3.7(b)-(c)] and for still higher folds [fold 4 to 6, Figs. 3.7(d)-(f)] the data are essentially free of background above an energy of 15 MeV in the laboratory system. In the shell-closure region, after subtracting the background (for fold 1 to 3), further
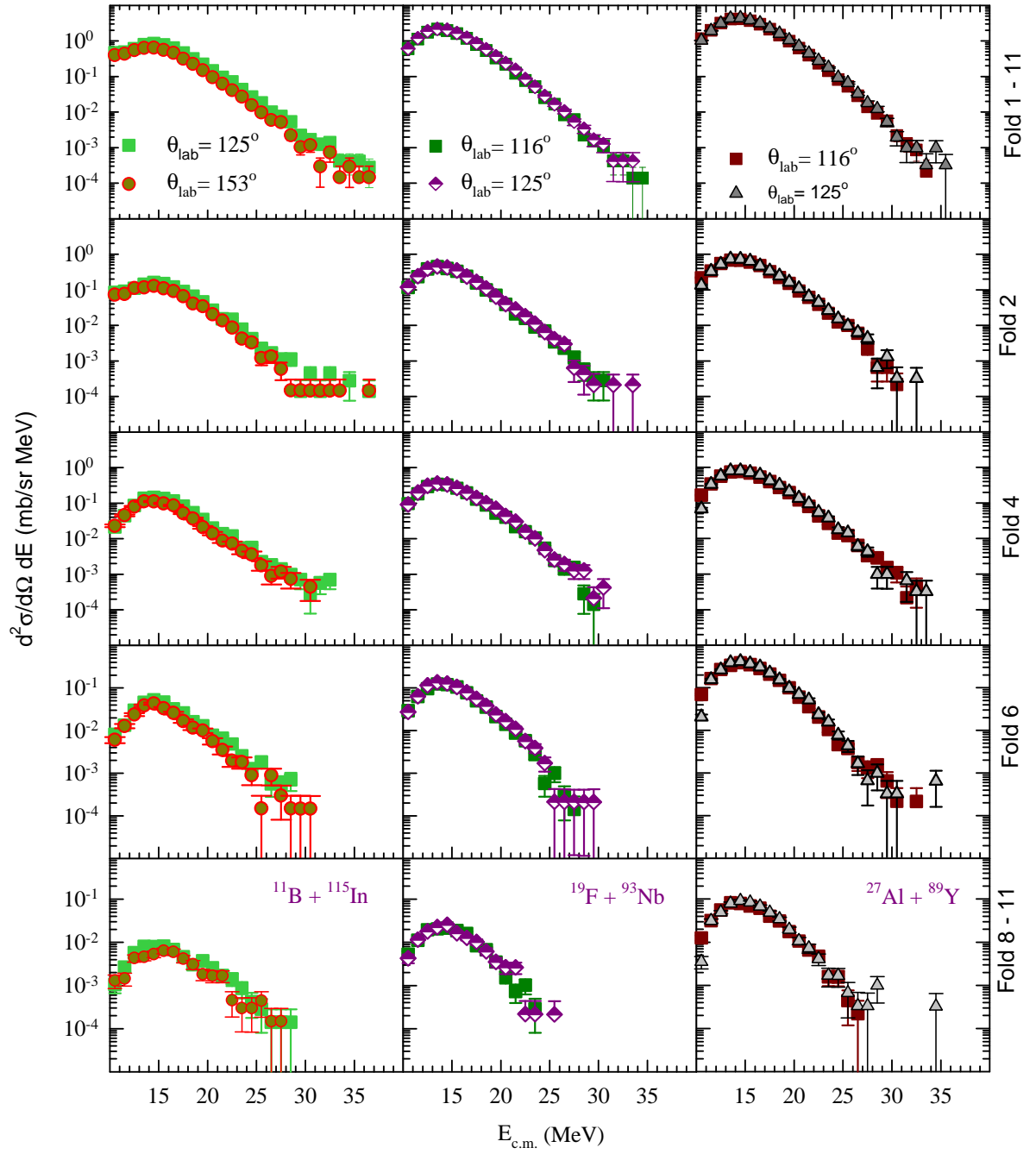
Figure 3.8: Center-of-mass α-particle energy spectra for various folds measured at two laboratory angles in three typical fusion reactions of the shell-closure region: (i) ^{11}B + ^{115}In at θ_{lab} = 125° (solid squares) and 153° (solid circles), (ii) ^{19}F + ^{93}Nb at θ_{lab} = 116° (solid squares) and 125°(diamonds), and (iii) ^{27}Al + ^{89}Y at θ_{lab} = 116° (solid squares) and 125°(triangles).
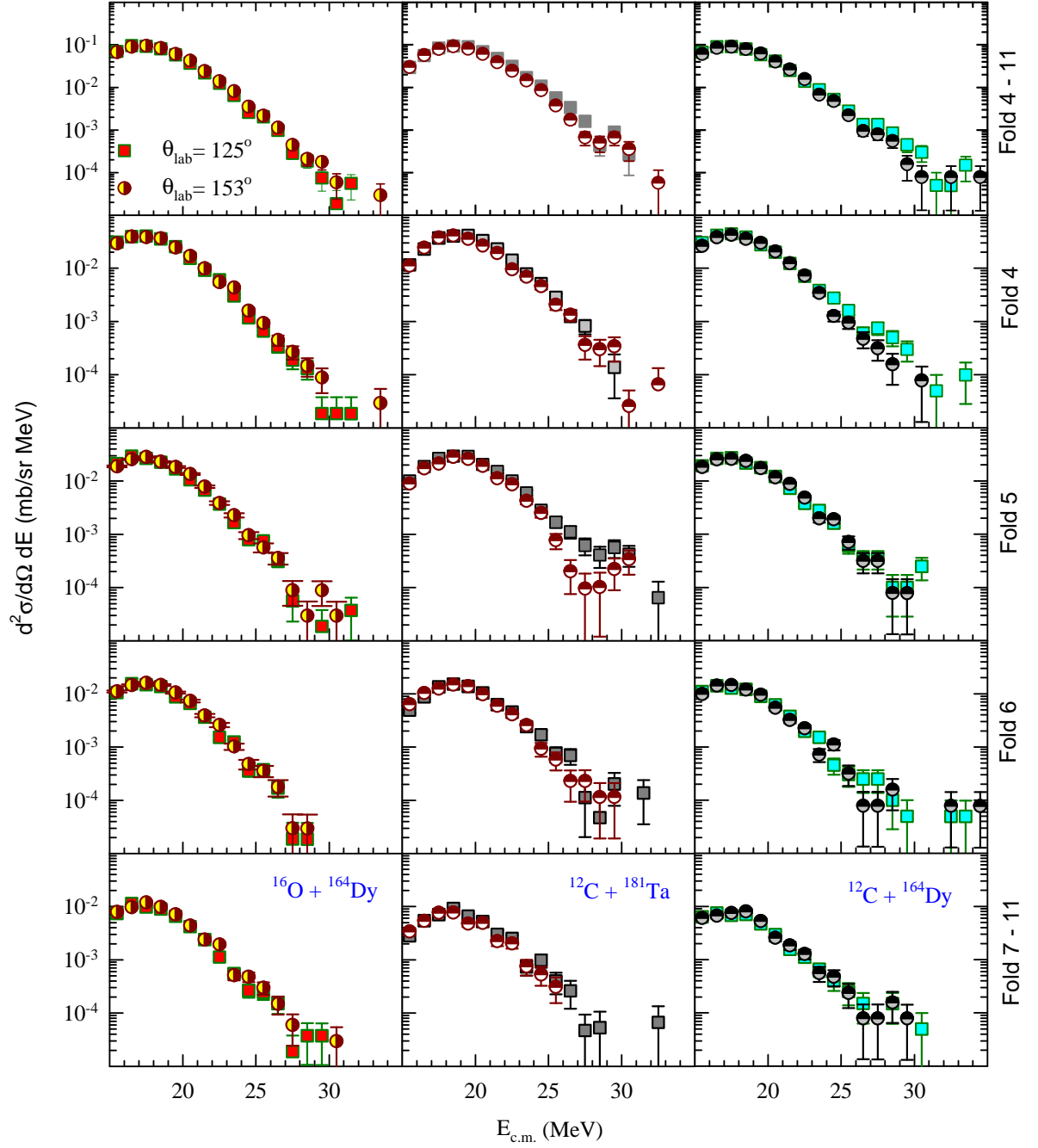
Figure 3.9: Center-of-mass α-particle energy spectra for various folds measured at $\theta_{lab} = 125°$ (solid squares) and 153° (solid circles) in three typical fusion reactions of the mid-shell region; (i) $^{16}O + ^{164}Dy$, (ii) $^{12}C + ^{181}Ta$, and $^{12}C + ^{164}Dy$.
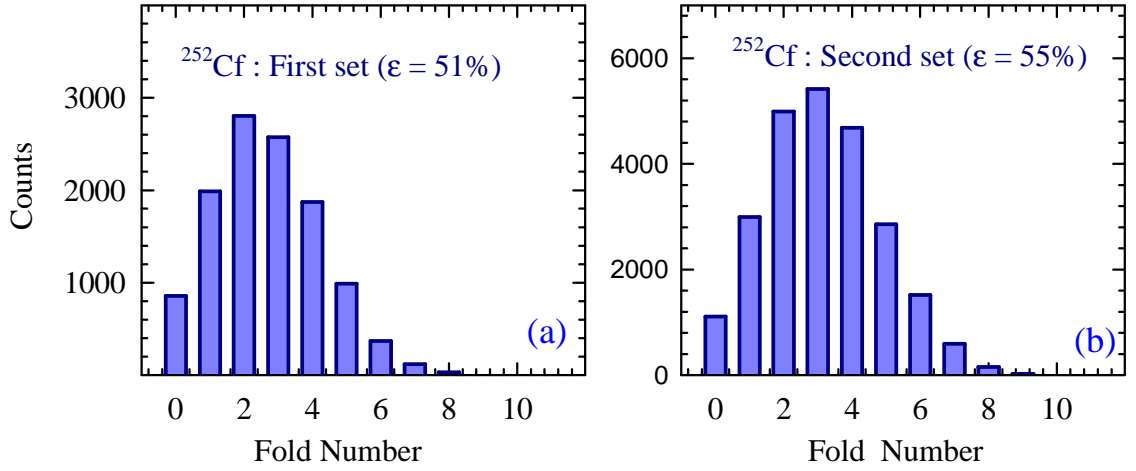
Figure 3.10: Measured γ-ray fold distributions from spontaneous fission of ^{252}Cf for both sets of the experiments in (a) and (b), where ϵ is the total efficiency of the fourteen BGO multiplicity setup.

analysis was carried out only for fold-1 and above.

The laboratory spectra obtained after background subtraction were transformed to compound nucleus center-of-mass (c.m.) system using the standard Jacobian [185]. In the center-of-mass system, the spectra measured at two different laboratory angles overlapped very well for each fold as shown in the Figs. 3.8 and 3.9 for the shell-closure and mid-shell regions, respectively, indicating that the spectra originated in the evaporation process.

3.3.2 Validation of the BGO setup

In the past, γ-ray multiplicity of ^{252}Cf has been measured at different values of energy thresholds of the γ-ray detectors. The average γ-ray multiplicity of ^{252}Cf has been observed to be very sensitive to the energy-threshold values as reflected from the Table 3.2. In order to validate the BGO setup and the conversion procedure from fold to multiplicity used in the present work, γ-ray multiplicity fold distributions from ^{252}Cf spontaneous fission source were measured in each of experiments as shown in the Figs. 3.10(a) and (b). Due to different BGO energy thresholds and hence the different BGO

Table 3.2: Average γ-ray multiplicity of ^{252}Cf reported in literature at various energy threshold values of the γ-ray detectors.

S. No.	$\langle M_\gamma \rangle$	Energy threshold (keV)	γ-ray detectors	Reference
1.	$\sim$10.5	80	NaI(Tl)	Varma *et al.* [145]
2.	$\sim$10.5	80	BGO	Biswas *et al.*[144]
3.	$\sim$10.3	85	NaI(Tl)	Ramamurthy *et al.*[186]
4.	$\sim$9.7	114	NaI(Tl)	Skarsvag *et al.*[187]
5.	$\sim$7.7	140	NaI(Tl)	Verbinski *et al.*[147]
6.	$\sim$7.8	160	BGO	Nayak *et al.*[146]

efficiencies in the first and the second set of the experiments, the relative strengths of the different folds appears to be correspondingly different.

The measured fold distributions were unfolded to get the mean value of corresponding γ-ray multiplicity distribution ($\langle M_\gamma \rangle$) of ^{252}Cf. The average γ-ray multiplicity of ^{252}Cf was found as $\sim$7.8(9.3 in the second set), which is consistent with the earlier reported values as shown in the Table 3.2.

3.3.3 Residue angular momentum and γ-ray multiplicity

The γ-ray fold distributions, measured in coincidence of the α particles in the shell-closure region were corrected for the background, where the background contribution in each fold was estimated from that of α-particle energy spectra. Fig. 3.11 shows the background corrected (only for ^{11}B, ^{12}C, and ^{16}O projectiles) as well as uncorrected fold distributions for 6 out of 12 systems of the shell-closure region. As discussed earlier, no background subtraction was required in the reactions where projectile is heavier than ^{16}O. After background subtraction, the fold distributions in the shell-closure region were analyzed to extract the first two moments of the corresponding γ-ray multiplicity distribution $\left(\langle M_\gamma \rangle , \langle M_\gamma^2 \rangle \right)$ using the procedure given in Ref. [188] that works well for the present type of low-efficiency multiplicity setup and also used in our earlier work
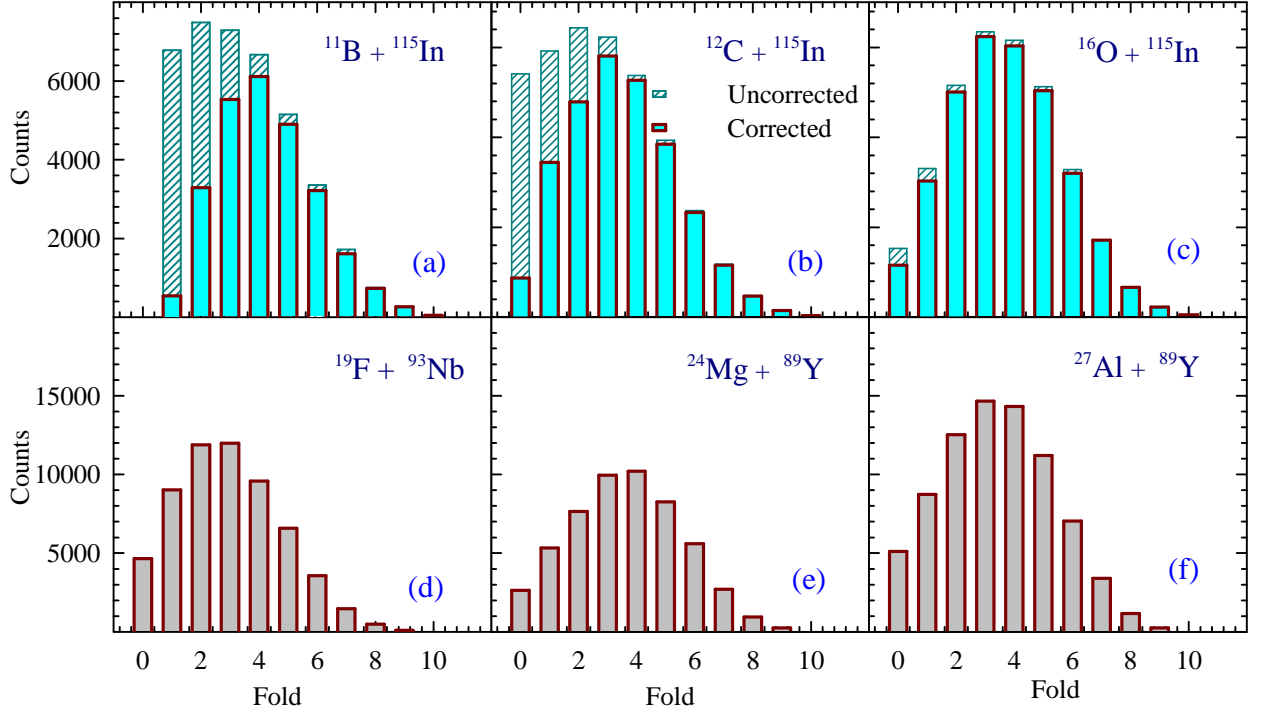
Figure 3.11: Measured γ-ray fold distributions in coincidence with α particles at $\theta_{\text{lab}} = 125°$ for different reactions in the shell-closure region. In panels (a) to (c) the hashed and filled histograms represent the fold distributions before and after background subtraction, respectively. In panels (d) to (f), no background subtraction was done since the α-particle data are essentially free of background in the reactions where projectile is heavier than ^{16}O (see text).

[146]. The compound nucleus angular momentum J_{CN} was assumed to be linearly related with residue γ-ray multiplicity M_γ given as

$$J_{\text{CN}} = a_m M_\gamma + \delta L_\alpha, \tag{3.2}$$

where δL_α is the orbital angular momentum carried away (predominantly) by evaporated α particles. Under such an assumption, following relations hold good;

$$a_m = \sqrt{\frac{\langle J_{\text{CN}}^2 \rangle - \langle J_{\text{CN}} \rangle^2}{\langle M_\gamma^2 \rangle - \langle M_\gamma \rangle^2}}, \tag{3.3}$$

and

$$\langle \delta L_\alpha \rangle = \langle J_{\text{CN}} \rangle - a_m \langle M_\gamma \rangle. \tag{3.4}$$

Table 3.3: Moments of experimental γ-ray multiplicity ($\langle M_\gamma \rangle, \langle M_\gamma^2 \rangle$), compound nuclear angular momentum ($\langle J_{\mathrm{CN}} \rangle, \langle J_{\mathrm{CN}}^2 \rangle$), residue spin ($\langle J_{\mathrm{res}} \rangle$), and related parameters for the shell-closure region.

Index	Reaction	$\langle M_\gamma \rangle$	$\langle M_\gamma^2 \rangle$	$\langle J_{\mathrm{CN}} \rangle$ $(\hbar)$	$\langle J_{\mathrm{CN}}^2 \rangle$ $(\hbar^2)$	$\langle J_{\mathrm{res}} \rangle$ $(\hbar)$	a_m	$\langle \delta L_\alpha \rangle$ $(\hbar)$
a	^{19}F+ ^{93}Nb	8.8	102.9	19.8	444.5	14.2	1.45	6.9
b	^{24}Mg + ^{89}Y	11.3	159.1	25.8	753.2	17.1	1.68	6.8
c	^{27}Al + ^{89}Y	10.6	141.0	25.9	759.1	17.5	1.71	7.7
d	^{24}Mg+ ^{93}Nb	11.4	159.5	26.7	807.2	17.3	1.78	6.4
e	^{11}B + ^{115}In	9.6	115.6	20.3	466.2	14.8	1.52	5.7
f	^{12}C + ^{115}In	10.6	141.6	23.4	619.5	17.0	1.58	6.6
g	^{16}O + ^{115}In	11.6	164.8	24.0	651.3	17.8	1.55	6.0

The a_m and δL_α values were determined as given in Table 3.3 by using the moments $\langle J_{\mathrm{CN}} \rangle$ and $\langle J_{\mathrm{CN}}^2 \rangle$ obtained from the Bass systematics [189] used in the statistical model code PACE2 . The PACE2 code is discussed in detail later in this chapter. The PACE2 code also provides mean values of residual nucleus angular momentum distributions $\langle J_{\mathrm{res}} \rangle$ using its trace-back feature and these values are also shown in Table 3.3 for each system. It is observed that $\langle \delta L_\alpha \rangle$ determined is of similar magnitude as the difference of $\langle J_{\mathrm{CN}} \rangle$ and $\langle J_{\mathrm{res}} \rangle$ calculated from PACE2 , as one would expect. This establishes consistency in the derived average spin values from the γ-ray-multiplicity measurements.

3.3.4 Conversion of fold to average angular momentum

Because of the limited efficiency of γ-ray detection and the uncertainty of angular momentum carried by individual γ-ray, it is not possible to convert each γ-ray fold to spin value on event-by-event basis. Each γ-ray fold corresponds to a window of the angular momentum populated in the residual nuclei. An average angular momentum, $\langle J \rangle$, corresponding to each γ-ray fold was assigned using the procedure as discussed below.
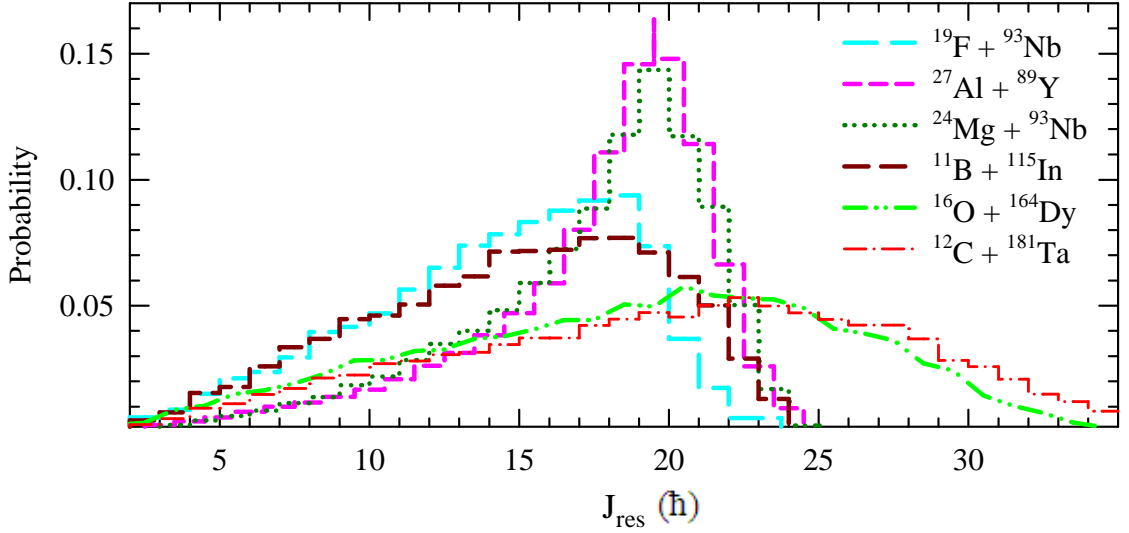
Figure 3.12: Residue angular momentum distribution calculated using the statistical model code PACE2 for some typical reactions of both the mass regions.

For each reaction, the residue angular momentum distribution after α-particle emission (J_{res}) was determined using the trace-back feature of PACE2 as shown in the Fig. 3.12 for some typical reactions of both the mass regions. Despite being similar grazing angular momentum of the compound nuclei for both the mass regions as shown Table 3.1, it is observed from Fig. 3.12 that the residue angular momentum distribution for mass region of $A \sim 180$ are broader and peak at higher angular momenta in comparison to the mass region of $A \sim 120$. The residue angular momentum, J_{res} was converted to a corresponding γ-ray multiplicity distribution, M as a row matrix $\mathcal{A}_M$, where the elements are $M^i = J_{res}^i/a_m, i = 1, N_m$. Here N_m is decided by J_{res}^{max} where J_{res}^{max} is the maximum value of residue spin populated. The parameter a_m was chosen to be 1.6 (1.5 for the second set) which is consistent according to the experimentally estimated values as shown in Table 3.3. The fold distribution F for a given value of multiplicity M, was calculated with a Monte Carlo technique [69, 70] by simulating the history of each γ-ray in the cascade. Fig. 3.13 shows calculated (for total BGO efficiency $\epsilon = 55\%$) fold-distributions for some typical multiplicity values. In the calculation for F all the BGO detectors were assumed to be of equal efficiency. If N_D is the number of
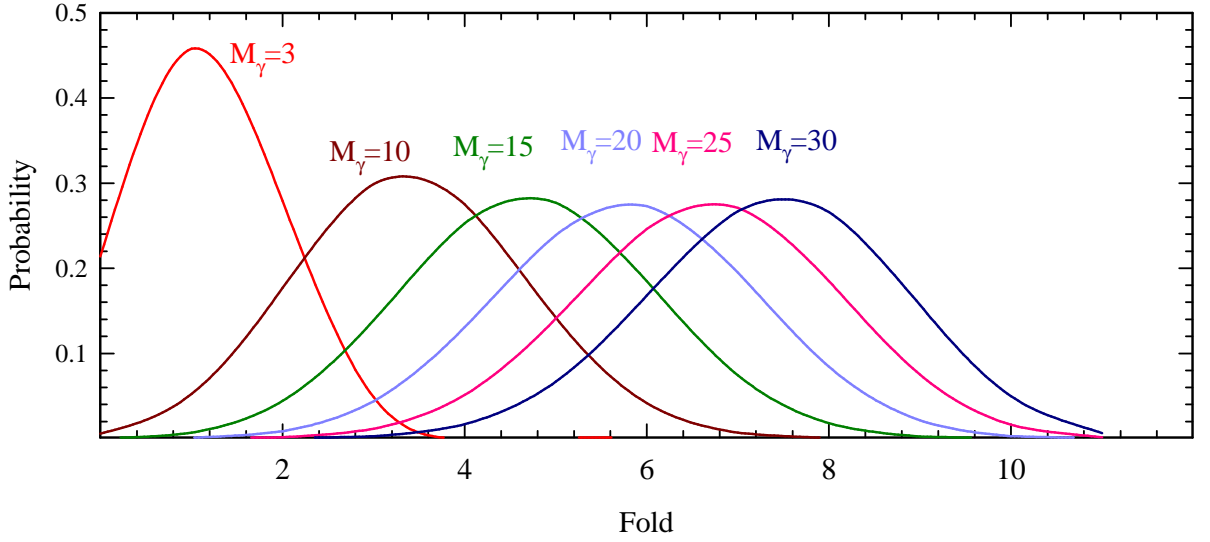
Figure 3.13: Simulated fold distributions of the BGO multiplicity setup with total efficiency of 55% for various lengths of γ-ray cascades (M_γ).

BGO detectors, then there are $(N_D + 1)$ number of firing blocks, B^i $(i = 0, N_D)$, that are assumed to be exposed by a cascade of γ rays of length M. One additional block B° is to take into account of the no firing condition. Elements of fold distribution F are $F^i, i = 0, N_D$. In the algorithm, if i^{th} block is fired by any one γ-ray of the cascade, then the content of B^i is increased by 1 ($\triangle B^i = 1$) for $i = 0, N_D$. If a second γ-ray of the same cascade hits the same detector (registered or not), it cannot hit any other detector and hence it should be lost. The rejection of these multiple hitting γ rays is taken into account by looking for the condition that the total increment $\triangle B^i \geq 1, i = 1, N_D$. If this condition is satisfied by n number of blocks after the full cascade has fired the BGO setup, then the nth element of the fold distribution F would be increased by 1. To obtain the full fold distribution F, the simulation is repeated typically for 10^6 γ-ray cascades of length M. Finally, to write in terms of probability, each element F^i is divided by 10^6. The calculations are carried out for multiplicity values of $M = 1$ to $M = M_{\max}$ where $M_{\max} = J_{\mathrm{res}}^{\max}/a_m$. By combining all the above calculations, a two-dimensional BGO response matrix (multiplicity vs. fold), $\mathcal{B}_{M,F}$ is obtained. Using the matrices $\mathcal{A}_M$ and $\mathcal{B}_{M,F}$ a weighted BGO response matrix, $\mathcal{C}_{M,F} = \mathcal{A}_M.\mathcal{B}_{M,F}$ is
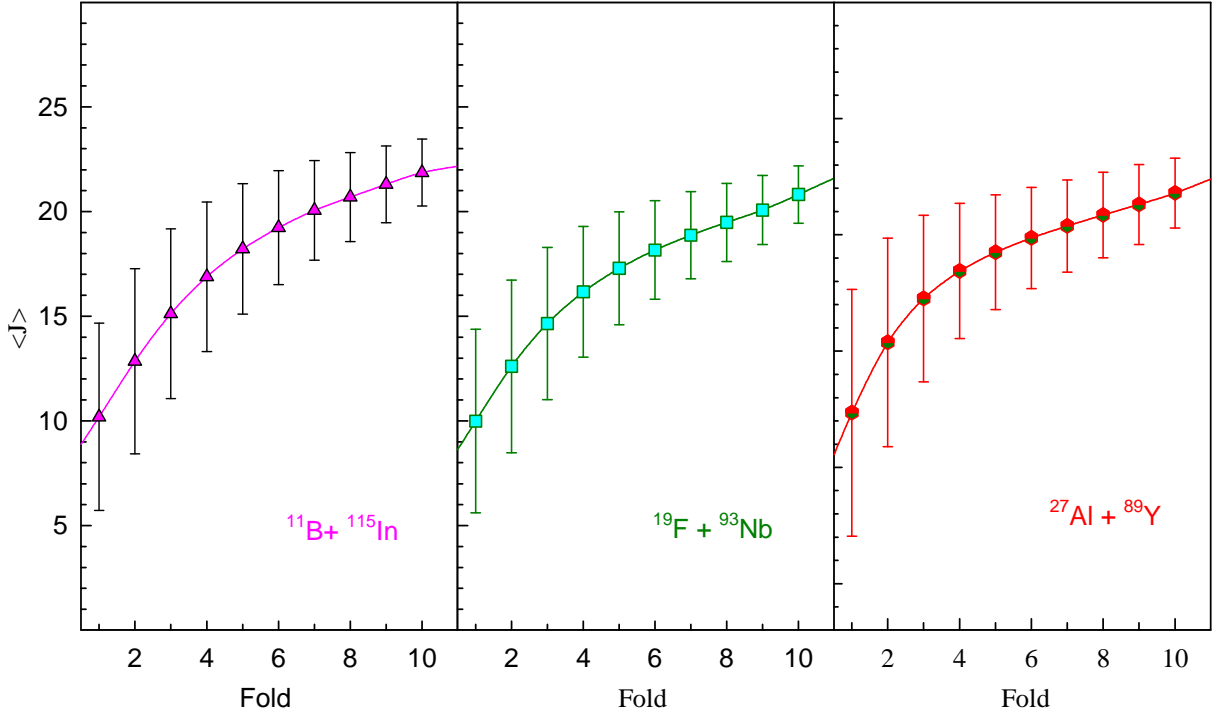
Figure 3.14: The value of average angular momentum $\langle J \rangle$ (in units of $\hbar$) derived as a function of γ-ray fold for three typical reactions of the shell-closure region. The error bars indicate the width δJ (see text).

obtained for a specific residue spin distribution. Finally, by projecting the matrix $\mathcal{C}_{M,F}$ on the fold axis, weighted multiplicity distributions for various folds are obtained. The first moment of the spin distribution (average value of angular momentum) for each fold F is calculated as follows:

$$\langle J \rangle = a_m \frac{\sum_{M=1}^{M_{\max}} M.\mathcal{C}_{M,F}}{\sum_{M=1}^{M_{\max}} \mathcal{C}_{M,F}}. \tag{3.5}$$

In similar fashion the second moment of the distribution $\langle J^2 \rangle$ for each fold is calculated. From here, the width of angular momentum window for each fold is deduced as follows:

$$\delta J = \sqrt{\langle J^2 \rangle - \langle J \rangle^2}. \tag{3.6}$$

The width δJ is large for lower folds and small for higher folds for each reaction. The uncertainty in the assignment of $\langle J \rangle$ varied from $\pm 5\hbar$ to $\pm 2\hbar$ ($\pm 3\hbar$ in the mid-shell region) in going from low folds to high folds.
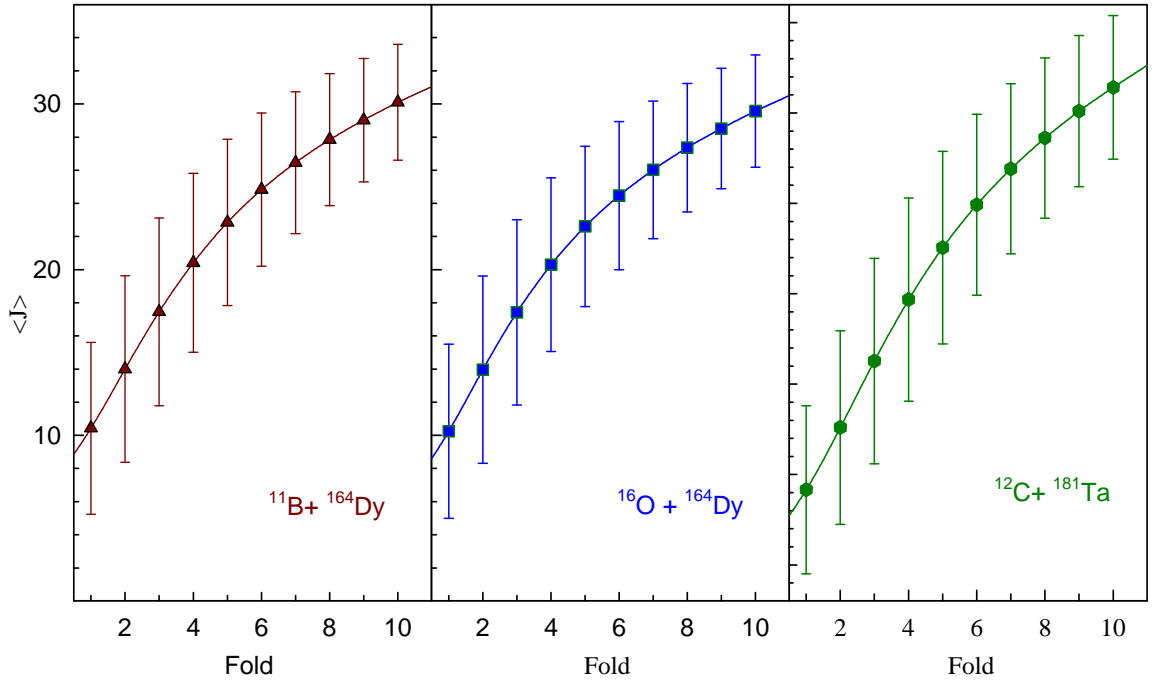
Figure 3.15: The value of average angular momentum $\langle J \rangle$ (in units of $\hbar$) derived as a function of γ-ray fold for three typical reactions of the mid-shell region. The error bars indicate the width δJ (see text).

Figures 3.14 and 3.15 show the values of $\langle J \rangle$ and width δJ as a function of γ-ray fold calculated as above for various systems in the shell-closure and mid-shell regions, respectively. It is seen that in going from fold 1 to 8, the angular momentum is spanned in the range of $10\hbar$ to $25\hbar$ for all the systems of shell-closure region, whereas for the mid-shell region this range is 10 to 30 $\hbar$. The particular non-linear dependence of $\langle J \rangle$ on fold arises due to a combination of the low efficiency of the BGO setup and the shape of the angular momentum distribution in residual nucleus. For a given fold, the assigned average angular momentum in the mid-shell region is larger than that for shell-closure region due to larger residue angular momentum in the mid-shell region in comparison to the shell-closure region [Fig. 3.12].

3.4 Statistical model analysis: Determination of the level-density parameter

The average α-particle spectra obtained from the data at two laboratory angles were compared with the theoretical spectra to derive the level-density parameter. The theoretical spectra were obtained from a statistical model Code PACE2, by taking into account the efficiency of the BGO detector setup and the angular momentum removal by γ rays, as discussed later in this section. The spin-dependent level-density makes its most noticeable change in the slope of the high energy tail of the evaporation particle spectra. This high energy tail of the angular momentum gated α-particle spectra is least-squares fitted with the PACE2 predictions, from where angular momentum dependence of the level-density parameter is determined.

3.4.1 Statistical model calculation using the code PACE2

The statistical model code PACE2 (projection angular momentum coupled evaporation) used in the present work was developed by Gavron [136]. It uses a Monte Carlo procedure to determine the decay sequences using the Hauser-Feshbach formalism [21, 22, 24]. The code does not deal with the CN formation, it begins with an ensemble of compound nuclei having same amount of excitation energy with small spread due to energy loss in the target. The initial angular momentum distribution for the compound nucleus is obtained from the Bass systematics [189] for fusion cross section, where partial fusion cross section at angular momentum ℓ, σ_ℓ, is [4];

$$\sigma_\ell \propto \frac{2\ell + 1}{1 + \exp[(\ell - \ell_{\text{graz}})/\Delta]}, \tag{3.7}$$

where ℓ is the orbital angular momentum in the incident channel which along with the channel spin, gives rise the total angular momentum, J of the CN. In Eq. (3.7), ℓ_{graz} is the grazing angular momentum [see Table 3.1] decided by the fusion cross section, and Δ is the diffuseness parameter which has been chosen to be $\sim 0.5\ \hbar$ in the present
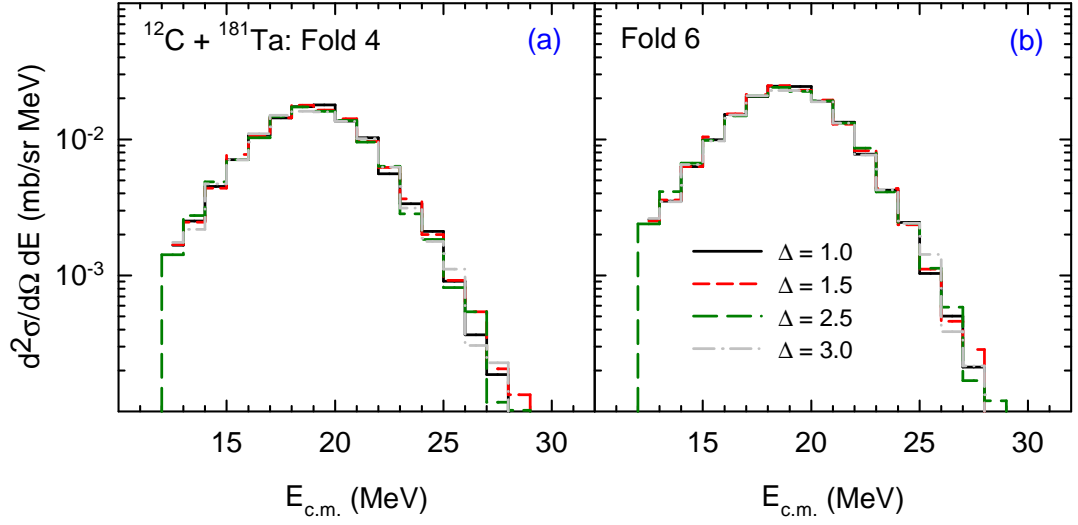
Figure 3.16: PACE2 calculated α-particle spectra for two typical folds 4 and 6 for ^{12}C+^{181}Ta system in panels [(a) and (b)]. Solid, short-dash, medium-dash, and dash-dot histograms are for diffuseness parameter, $\Delta = 1.0$, 1.5, 2.5, and 3.0, respectively.

analysis. We have examined the effect of compound nucleus spin distribution on the slope of high energy part of α-spectrum by varying diffuseness parameter, Δ from 1.0 to 3.0. It is observed that the change in the slope of the PACE2 calculated fold-gated α-particle spectrum is <1% by changing Δ from 1.0 to 3.0, as shown in Fig. 3.16 for two typical folds 4 and 6 in the ^{12}C + ^{181}Ta reaction for inverse level-density parameter $K = 8$.

The level-density $\rho\left(E_X, J\right)$ used in the PACE2 calculations above an excitation energy $E_X \sim 5$ MeV is given by

$$\rho\left(E_X, J\right) = \frac{(2J+1)}{12}\sqrt{a}\left(\frac{\hbar^2}{2\Im}\right)^{3/2}\frac{exp\left(2\sqrt{aU}\right)}{U_{\text{ex}}^2}, \tag{3.8}$$

where, $U_{\text{ex}} = E_X - \Delta P(Z) - \Delta P(N)$ and $U = U_{\text{ex}} - E_{rot}$, where $E_{rot} = \frac{\hbar^2}{2\Im}J(J+1)$ is the rotational energy. $\Delta P(Z)$ and $\Delta P(N)$ are the ground-state pairing energy differences obtained from Gilbert and Cameron's compilation for odd-even mass differences. The moment of inertia $\Im$ was calculated using Sierk rotating liquid drop model [76] and it can be parameterized for the calculation in the spin cut-off parameter as $\sigma^2 = \Im t/\hbar^2$, where t is the thermodynamic temperature. With the spin cut-off parameter, Eq. (3.8)

can be rewritten in the traditional form as in, for example Ref. [48, 61]. At E_X below

~ 5 MeV, Gilbert and Cameron's constant temperature formula [47] was used for the

level-density. We used the following form for level-density parameter a [41], which is

widely used in phenomenological descriptions of nuclear level-density:

$$a = \tilde{a} \left\{ 1 - \frac{\triangle S}{U} \left[1 - exp\left(-\gamma U\right) \right] \right\}, \qquad (3.9)$$

where $\tilde{a}$ is the asymptotic value of the level density parameter and γ is the shell damping

factor for which we have used the value 0.054 MeV^{-1}. The shell correction factor $\triangle S$

was calculated using the Swiatecki and Myers formalism [190], with the convention of

being +ve for the closed shell nuclei. The value of $\tilde{a}$ was externally varied in the code

through the input card. The γ-ray decay intensities were taken from RIPL compilation

[38]. The values of target and projectile spins were also provided in the input. The

other important input parameter in the PACE2 calculation is the transmission coefficient

as a function of energy and orbital angular momentum of the emitted particle. This

is conventionally generated by the optical model potentials (OMPs). In the present

calculations for α-particle emission, the OMP parameters of Igo and Huizenga [191]

were used.

We have thus adopted a widely used set of input parameters for the PACE2 cal-

culations. Our aim in the present work is to compare the shape of the fold-gated as

well as gross (summed over all the folds) experimental α-particle spectra with corre-

sponding spectra from PACE2 calculations at well above the evaporation barrier energy,

and derive the inverse level-density parameter $K = A/\tilde{a}$. By limiting the analysis to

the spectral shape at well above evaporation barrier, the uncertainties associated with

the barrier transmission coefficients are avoided. The normalization of the shape of

the experimental spectra with that predicted by the statistical model calculation, was

done by matching the area under the predicted spectra in the selected energy interval

with that of the experimental spectra in the same energy interval. No attempts were

made to fit the multiplicity of α-particles. The effect of scaling of yrast line on the

level density parameter was separately investigated as discussed later.

3.4.2   PACE2 calculated fold-gated α-particle spectra

The code PACE2 follows the decay of individual compound nucleus using Monte Carlo technique from an initial ensemble until the residual nuclei can no longer decay by particle, γ-ray emission, or fission. All the relevant information of each de-excitation is written in an event-file, which enable a complete traceback determination of the cascade which lead to the final specific nuclei. Thus, one can correlate the types of emitting particles, excitation energy, particle energy, spin, etc. from the event-file.

Fold-gated α-particle energy spectra (in the center-of-mass frame) were calculated within the statistical model code PACE2 using Eq. (3.8) for the E_X and J dependence of nuclear level-density. A fitting procedure was adopted for determining K using the following steps. The program was run typically for 10^6 events for the decay of compound nucleus corresponding to each reaction. From the events file, decay chains were traced in (E_X, J) plane. The distribution of cross-section leading to different J and E_X states after emission of α particles was obtained. From this, a 2D matrix $\mathcal{D}_{E_\alpha^{\mathrm{c.m.}}, J_{res}}$, that corresponds to residue spin distribution for each $E_\alpha^{\mathrm{c.m.}}$ was extracted. The residue spin distribution was then converted to a γ-ray multiplicity distribution using the prescription $M = J_{\mathrm{res}}/a_m$, and thus $\mathcal{D}_{E_\alpha^{\mathrm{c.m.}}, J_{res}}$ was transformed to another 2D matrix $\mathcal{E}_{E_\alpha^{\mathrm{c.m.}}, M}$ ($E_\alpha^{\mathrm{c.m.}}$ vs. γ-ray multiplicity). The parameter a_m was chosen to be 1.6 (1.5 for the second set) as discussed in Sec. 4.3.2. Using the BGO response 2D matrix (multiplicity vs. fold), $\mathcal{B}_{M,F}$ [Sec. 4.4] along with the matrix, $\mathcal{E}_{E_\alpha^{\mathrm{c.m.}}, M}$, a cross-section 2D matrix $\mathcal{F}_{E_\alpha^{\mathrm{c.m.}}, F} = \mathcal{E}_{E_\alpha^{\mathrm{c.m.}}, M}.\mathcal{B}_{M,F}$, was determined. Finally, by projecting the cross-section matrix on the energy axis, the α-particle energy spectra for various folds were arrived at. By summing over all fold-gated spectra, the gross spectrum was obtained.

As mentioned above, in the present analysis the parameter a_m was chosen to be
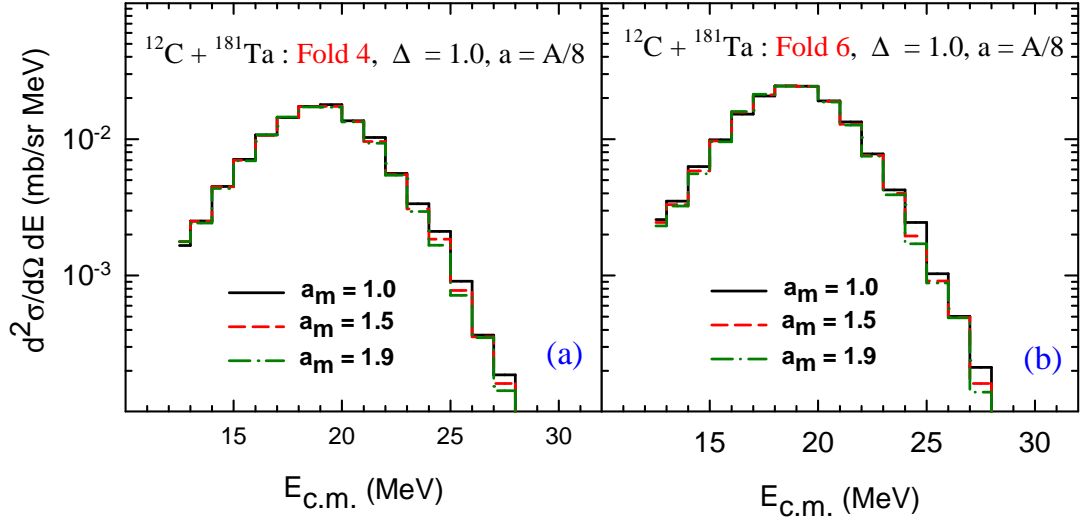
Figure 3.17: PACE2 calculated α-particle spectra for ^{12}C+^{181}Ta system for fold 4 and 6 in panels (a) and (b), respectively. Solid, short-dash, and dash-dot histograms are for parameter, $a_m = 1.0$, 1.5, and 1.9, respectively. The level-density parameter a and diffuseness parameter Δ used in the calculations are, $A/8$ and 1.0, respectively. The plots for a_m= 1.5 and 1.9 are scaled to $a_m = 1.0$, using appropriate scaling factor, SF (see text).

1.6 (1.5 for the second set). We have examined the dependence of slope of α-particle spectrum as a function of the parameter a_m for each fold. It is observed that the slope of the fold-gated spectrum does not change with parameter a_m as shown in the Fig. 3.17, where PACE2 calculations are shown for the ^{12}C + ^{181}Ta system for two typical folds 4 and 6 at various values of a_m. The level-density parameter $\tilde{a}$ and diffuseness parameter Δ, used in the calculations are $A/8$ and 1.0 respectively. The plots for a_m= 1.5 and 1.9 are scaled to $a_m = 1.0$, using appropriate scaling factor, SF. The value of SF for fold 4 is 0.64 for $a_m = 1.5$ and 0.62 for $a_m = 1.9$, whereas for fold 6 it is 1.4 for $a_m = 1.5$ and 2.5 for $a_m = 1.9$. Therefore, by varying parameter a_m, PACE2 calculated α-particle multiplicity changes but the slope of the spectrum remains unchanged.

The structure effect of residual nuclei can affect the γ-ray multiplicity depending on odd or even nature of residual nuclei. In this analysis we are getting an average γ-ray multiplicity and the spin value of residual nuclei. There may be some uncertainty on the absolute value of spin determination. But the results on the dependence of inverse

level-density parameter on average spin of the residue will not be affected.

3.4.3   Least-squares fit method

We have used the least-squares method to analyze the data in order to extract the most probable values and corresponding variance in the parameters being determined. In the present case, the inverse level-density parameter K was varied to fit the energy spectrum. The α-particle energy spectrum is a nonlinear function and, in this case, least-squares solutions are determined by minimizing the statistical variance given by

$$S\left(K\right) = \sum_{i=1}^{N} \frac{\left[Y_i - f\left(K, E_i\right)\right]^2}{\sigma_i^2}, \tag{3.10}$$

where Y_i is the double differential cross section in i^{th} energy bin, $f\left(K, E_i\right)$ is the result of PACE2 calculation for the same energy bin for inverse level-density parameter K after normalization of the spectrum as discussed previously, and σ_i is the statistical error in the measured cross section. The energy region in α-particle spectra to calculate the $S(K)$ value was chosen from 18.5 MeV (21.5 MeV for the higher mass region of $A \sim 180$) to 31.5 MeV for all the systems. By definition, the best-fit parameter $\bar{K}$ occurs when $S\left(K\right)$ is minimum. If the functional form of $f(K, E)$ is correct and the errors, σ_i, in Y_i are normally distributed, then the minimum $S\left(\bar{K}\right)$ obey the chi-square $\chi^2(N-1)$ distribution with $N-1$ degree of freedom, where N is the number of data points considered. We have evaluated $S(K)$ as a function of K using above equation, and in most cases, a parabolic dependence of $S(K)$ on the parameter K was observed. Best-fit parameter $\bar{K}$ was determined from the minimum of the parabola, from which the level-density parameter a can be determined using Eq. (3.9) with $\tilde{a} = A/\bar{K}$. However, because at an excitation energy around 30 to 40 MeV, the multiplying factor in square bracket in Eq. (3.9) is nearly unity for all known values of $\triangle S$, we used the approximation $a = \tilde{a}$ for quoting the results. To define error δK on $\bar{K}$, an interval of 68.3 % confidence level was determined (corresponding to one standard deviation)

using a limit on $S(K)$ defined as [192]

$$S_L = S(\bar{K}) + \frac{S(\bar{K})}{N-1}. \tag{3.11}$$

The error δK is defined as the intercept of the parabola with the limit value S_L. Using the same technique of least-squares, the effect of yrast scaling factor FY was deduced for a selected value of K in the ^{11}B $+^{115}$In reaction as a typical case study.

3.5   Results and discussion

The α-particle evaporation multiplicity ν_α was estimated for the present reactions from the measured evaporation cross sections and Bass fusion cross sections. The values of ν_α calculated using PACE2 code were found to be of similar magnitude. As pointed out earlier, α-particle emission leaves residual nuclei with $Z_R = Z_{\mathrm{CN}} - 2$. A major fraction of the α particles is emitted as first chance emission and the remaining will be by and large after one neutron emission. The residual nucleus excitation energy after first chance α-particle emission is given by

$$E_X = E_{\mathrm{CN}} - S_\alpha - E_\alpha^{\mathrm{c.m.}}, \tag{3.12}$$

where E_{CN}, S_α and $E_\alpha^{\mathrm{c.m.}}$ are the initial excitation energy of the compound nucleus, α-particle separation energy, and kinetic energy of the emitted α-particle, respectively. The approximate range of E_X is between 30 to 40 MeV for α-particle energies selected for the present analysis. The intrinsic excitation energy available for the residual nuclei will be, however, less than E_X by energy locked in the rotational energy of the nuclei, E_{rot}. An estimate of the E_{rot} was made for different angular momentum values using RLDM moment of inertia. Accordingly, for $J = 20\hbar$, the value of E_{rot} are 4.4 MeV and 2.2 MeV in the mass regions of $A \sim 120$ and $A \sim 180$, respectively. Similarly the change in rotational energy in going from $J = 10\hbar$ to $20\hbar$ in ^{122}Te is only 3 MeV. From the above discussion, it can be seen that the net excitation energy of the residual nucleus after α-particle emission is still in a broad range of energies between 30 to 40 MeV and

the residue mass has a small broadening of one or two units. There is no broadening in residue charge due to non selection of the exit channel.

3.5.1   Shell-closure region of $Z \sim 50$

3.5.1.1   Particle spectra and determination of 'gross' K

Using the least-squares method, the experimental gross spectra (summed over all J) measured in the shell-closure region of $Z \sim 50$ were analyzed by comparing with PACE2 predictions. As mentioned earlier, the calculated α-particle yields at the selected high energy region were normalized to the experimental yields while fitting the spectra. The solid circles and histograms shown in Fig. 3.18(a) are experimental and PACE2 calculated gross spectra respectively, after the normalization. The vertical dotted lines in the top panels show the extremes of the energy interval chosen for the fits, and this interval is same for all the fits of the mass region of $A \sim 120$. The insets in the panels show the nearly parabolic variation of $S(K)$ with the parameter K. The minimum of the parabola corresponds to the best-fit value of the inverse level-density parameter K. The reaction index, best-fit K value (with error bar), and experimental as well as calculated (in the parenthesis) multiplicity of α particles, ν_{α} are shown at the bottom of each panel in Fig. 3.18(a).

Fig. 3.18(b) shows the variation of K as a function of Z of the residual nuclei (Z_R) in the shell-closure region of $Z \sim 50$. In this mass region, the 'gross' K values for nuclei studied in the present work lie in the range of 9.0 to 10.5, and are within the liquid drop model estimates [41]. In an earlier work [71, 72], the 'gross' K values for $Z_R = 48$ and 52 were measured in the same excitation energy region. The earlier results had errors of ± 1 unit and may be considered to be consistent with the present measurement within error bars. The data given in Fig. 3.18(b) show that the value of K is strictly not the same for all the systems studied. The average excitation energy of the residual nuclei after α-particle emission is around 35 MeV for the present systems, which according to
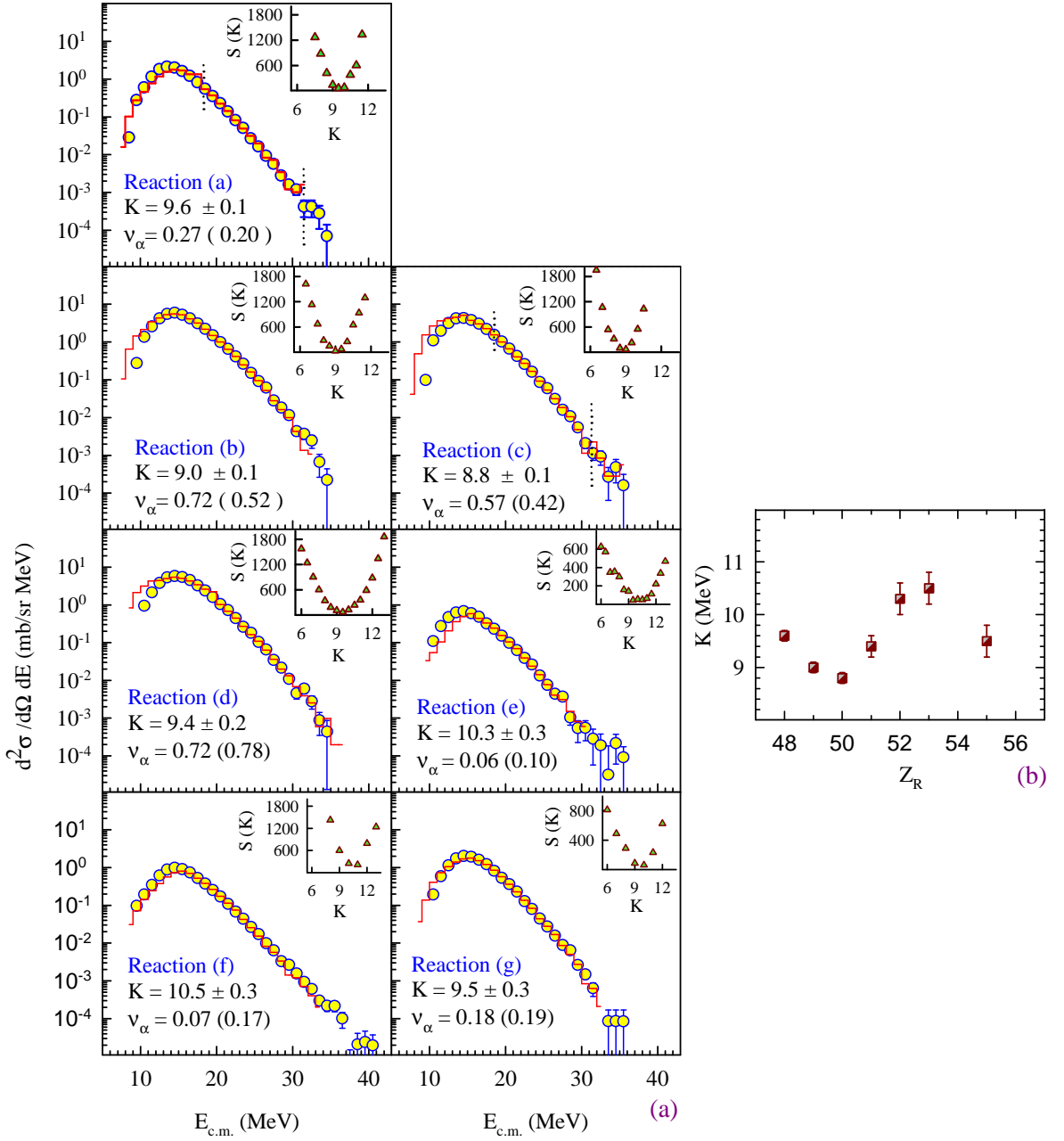
Figure 3.18: (a) Gross α-particle energy spectra (open circles) in center-of-mass system in reactions from (a) to (g) [Table 3.1] and the results of PACE2 statistical model calculation (solid histograms). The vertical dotted lines in the top panels show the extremes of the energy interval chosen for the fits and this interval was same for all the fits. The reaction index, best-fit K value (with error bar), and experimental as well as calculated (in the parenthesis) multiplicity of α particles, ν_α are shown at the bottom of each panel. In the inset, statistical variance $S(K)$ is shown as a function of K from where the best-fit K value was determined as discussed in the text. (b) Inverse level-density parameter K determined from the gross spectra, shown as a function of Z of the residual nuclei in the shell-closure region.
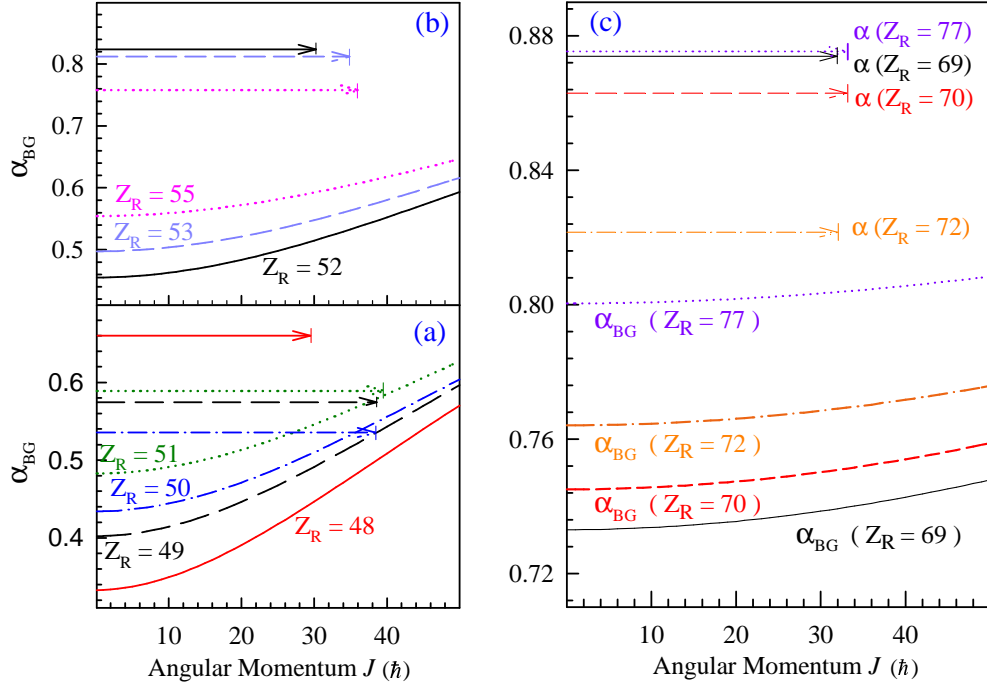
Figure 3.19: α_{BG} as a function of entrance-channel angular momentum J, for systems from a to d [panel (a)], for e to g [panel (b)], and for h to k [panel (c)]. In the figure, the arrows on Y-axis indicate the position of mass-asymmetry parameter, α, for different target-projectile systems which terminate at the corresponding l_{graz} [Table 3.1]. The pattern of the arrow is same as for the corresponding line for α_{BG}. Corresponding to each reaction the value of Z_R is shown along each line.

Ref. [41] is above the energy required for washing out of shell effects. It is seen from Fig. 3.18(b) that the value of K is the lowest for $Z_R = 50$, in contrast with what one might have expected from known behavior of shell effects, by assuming persistence of shell effects even at this excitation energy. Maximum value for K is observed for $Z_R = 52$ and 53. We have no microscopic understanding of these observations but would like to point out that similar differences in level-density parameter in neighboring nuclei have been observed earlier [193] with excitation energy around 60 to 90 MeV.

To understand the role of di-nuclear complex formation during fusion process in producing these apparent differences, we have calculated the Businaro-Gallone critical mass-asymmetry for various ℓ-partial waves in the present reactions of mass regions of $A \sim 120$ as well as that of $A \sim 180$. The effect of entrance-channel mass-asymmetry in

compound nucleus formation has been studied earlier in terms of the mass-asymmetry parameter α with respect to α_{BG} (Businaro-Gallone critical mass-asymmetry) [194]. Fig. 3.19 shows the variation of α_{BG} as a function of angular momentum for all the systems of mass region of $A \sim 120$ [panels (a) and (b)] as well as that of $A \sim 180$ [panel (c)] studied in the present work. It is seen that for all the systems studied, the mass-asymmetry parameter α is on the same side of the α_{BG} line for all angular momentum values (i.e., $\alpha > \alpha_{BG}$ for all J). Therefore, entrance-channel effect with respect to BG point is not expected to play a role for the present systems and all the systems are expected to undergo normal compound nuclear formation without a di-nuclear complex formation. In the work by Liang *et al.* [195] light charged particle emissions from ^{156}Er compound nucleus, populated by ^{12}C + ^{144}Sm and ^{60}Ni +^{96}Zr reactions at same excitation energy, were measured in coincidence with the evaporation residues. The high energy slope of light charged particle spectra for ^{60}Ni -induced reaction was found to be steeper than for the ^{12}C-induced reaction. Similar observation was reported by Govil *et al.* [196] for other systems. However, in these earlier studies, the systems correspond to a large difference in the entrance channel mass-asymmetry, which lie on opposite side of α_{BG}.

3.5.1.2 Angular momentum dependence of K

Figures 3.20–3.23 show the measured α-particle energy spectra for all the systems in the shell-closure region ($Z \sim 50$) for various folds (solid circles) and the corresponding PACE2 best fits (solid histograms) using the same procedure as described earlier. In the insets, the results of least-squares analysis are shown. It is seen that for all cases, a well defined minimum in $S(K)$ is obtained as a function of K. The values of K corresponding to the minimum were taken as the best-fit values. The fold number, the best-fit K value (with error bar), and experimental as well as calculated (in the parenthesis) multiplicity of α particles, ν_α are shown at the bottom of each panel.

Fig. 3.24(a) shows the variation of K with γ-ray fold for all the systems of this
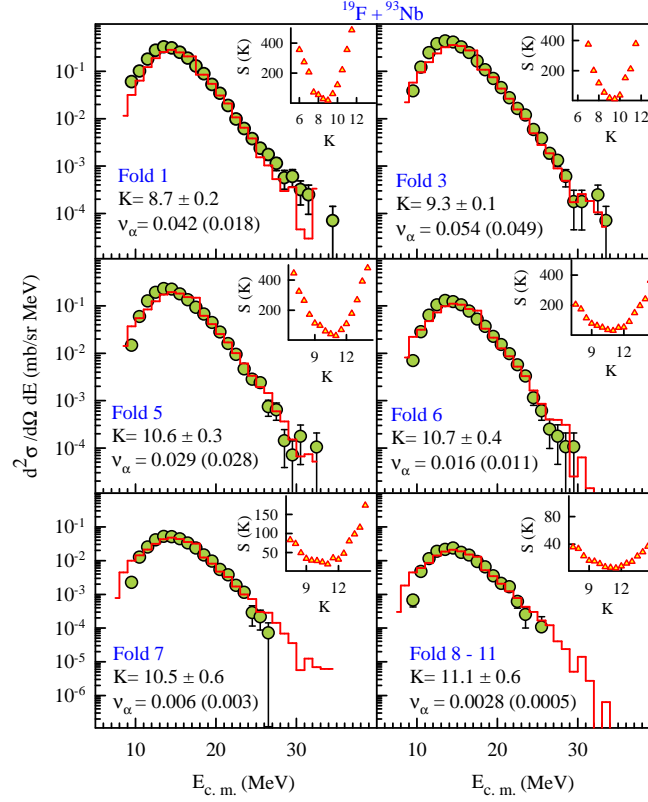
Figure 3.20: Fold-gated α-particle energy spectra in center-of-mass frame in ^{19}F+ ^{93}Nb reaction for various folds (solid circles) along with the results of PACE2 statistical model calculation (solid histograms). The fold number, the K value obtained (with error bar), and experimental as well as calculated (in the parenthesis) multiplicity of α particles, ν_α, are shown at the bottom of each panel. In the inset, statistical variance is shown (triangles) as a function of K from where the best-fit K value was determined as discussed in the text.

mass region of $A \sim 120$. The Z_R values are shown beside each plot. A more physical understanding of the behavior of inverse level-density parameter K as a function of angular momentum may be achieved by plotting the variation of K with $\langle J \rangle$ as shown in the Fig. 3.24(b). The fold to angular momentum conversion was carried out using the similar calculations for all the systems as presented in the Fig. 3.14 for some typical systems in this mass region of $A \sim 120$. In the Figs. 3.24(a) and (b) we also show the 'gross' value of K (average $\pm \delta K$) as a band for comparison. The overall trend does not suggest a constant value for K over the full angular momentum range for all the systems. Some general observations can be made from Fig. 3.24(b) regarding
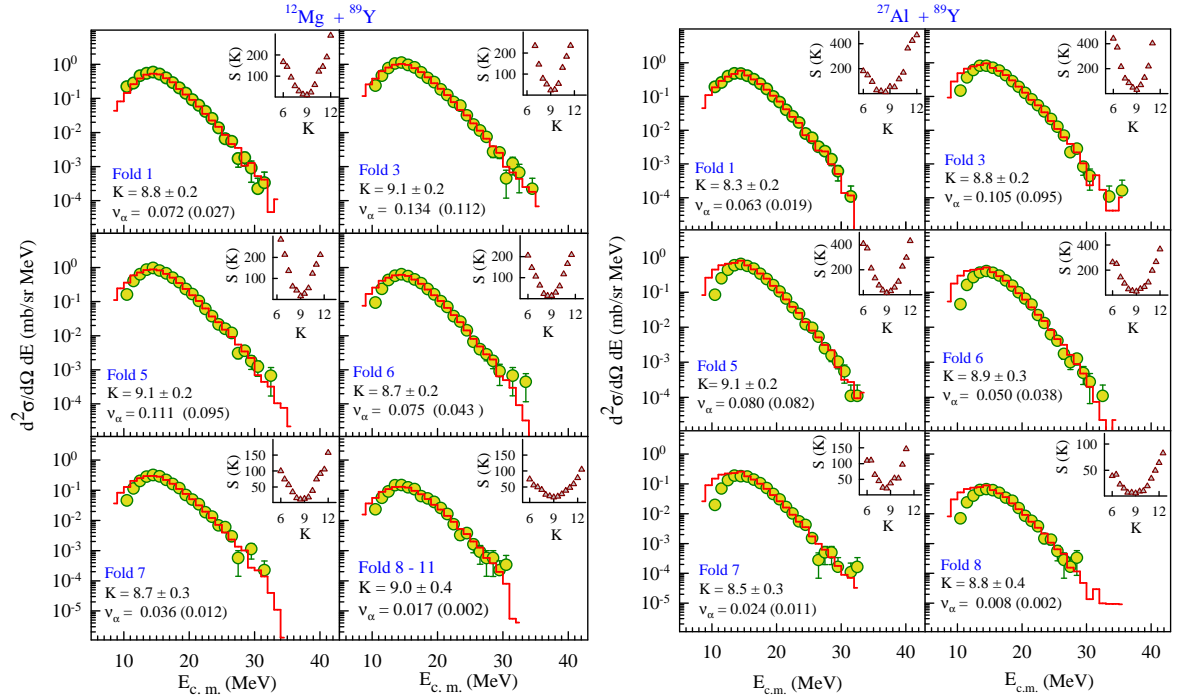
Figure 3.21: Same as in Fig. 3.20 but for the ^{24}Mg+ ^{89}Y and ^{24}Al+ ^{89}Y systems.
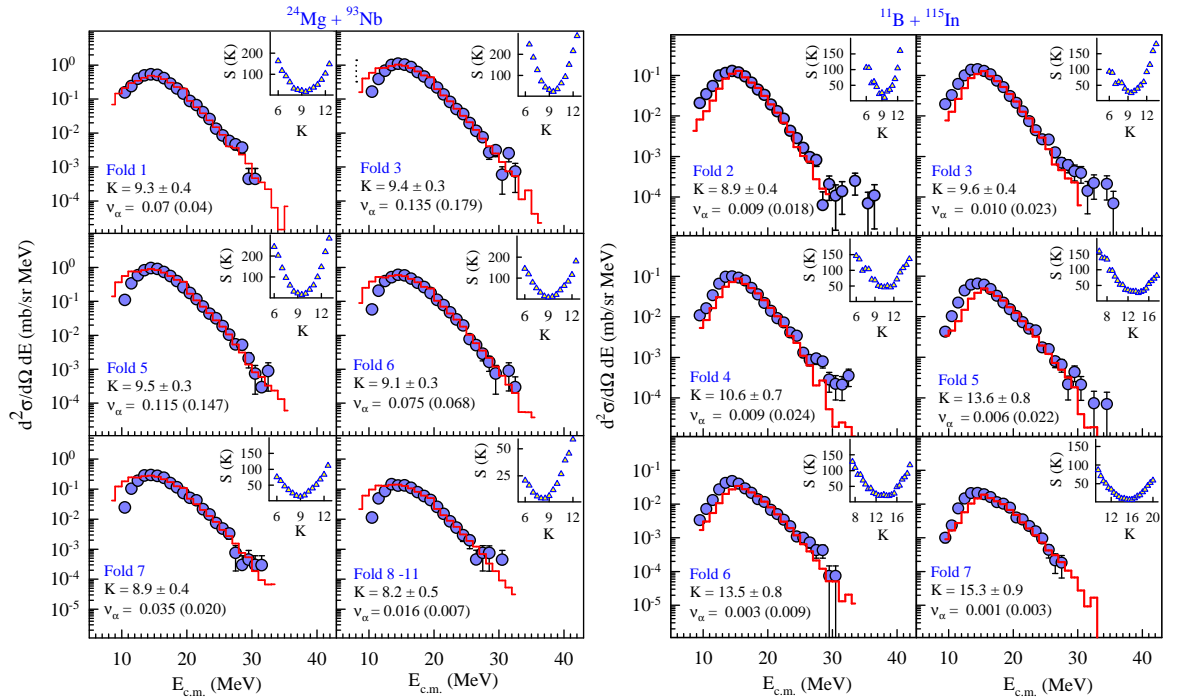
Figure 3.22: Same as in Fig. 3.20 but for the ^{24}Mg+ ^{93}Nb and ^{11}B+ ^{115}In systems.
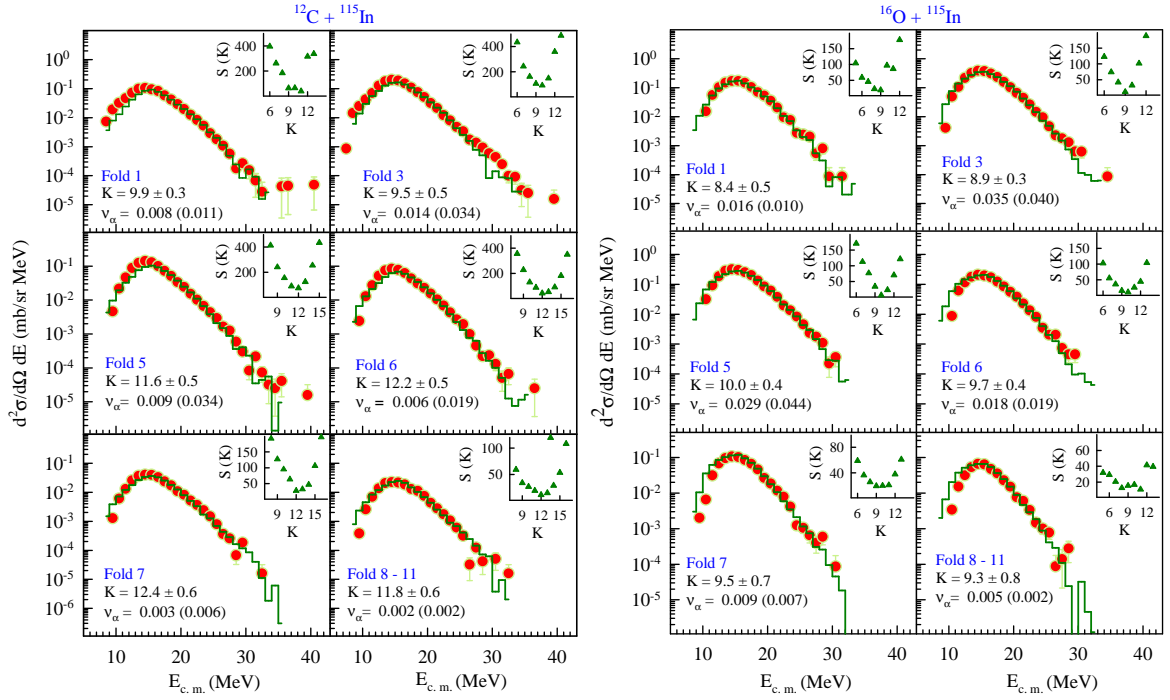
Figure 3.23: Same as in Fig. 3.20 but for the ^{12}C+ ^{115}In and ^{16}O+ ^{115}In systems.

the angular momentum dependence of K for nuclei of different charge Z_R. It is seen that for $Z_R = 49$, 50, and 51 corresponding to very close to the shell-closure, there is a flat behavior for low angular momentum and the results agree with 'gross' K value. However, a downward trend is observed for higher J values. Once the shell region is crossed, for $Z_R = 52$ and 53 a dramatic change in the trend can be observed. In a repeat measurement we have reconfirmed the behavior for the $Z_R = 52$ system where there is a strong increase in K with angular momentum. For this system, the K values are lower than the 'gross' K value in the low-angular-momentum region and are larger for higher values of angular momentum. This trend is continued for $Z_R = 53$ and 48 as well but in a diminished manner. For $Z_R = 55$ the trend is also similar but with a much weaker variation of K with angular momentum.

To explain the slope of the experimental α-particle energy spectra in the high-energy region, one can alternately vary the yrast scaling factor FY by fixing K to a constant value. This was tried out for the $Z_R = 52$ system by fixing K at 9.0 and

Figure 3.24: Inverse level-density parameter K as a function of fold (a) and $\langle J \rangle$ (b) for different Z_R in the shell-closure region. The shaded region in each panel correspond to 'gross' K value.

increasing the yrast scaling factor FY to ~ 2.5 for high folds. From the least-squares fits, it was observed that if K is fixed, the factor FY required to fit the fold-gated spectra for the $Z_R = 52$ system increases as residue angular momentum or the fold number increases. Increase of FY at high spin implies increase of rotational energy from RLDM value at higher spin and this is possible if moment of inertia of the nucleus is reduced from the RLDM value at high spin. The present results are first of its kind as far as we know. The observation of significant variations in K over and above the 'shell corrected' level-density parameter is not fully explained. There are no theoretical
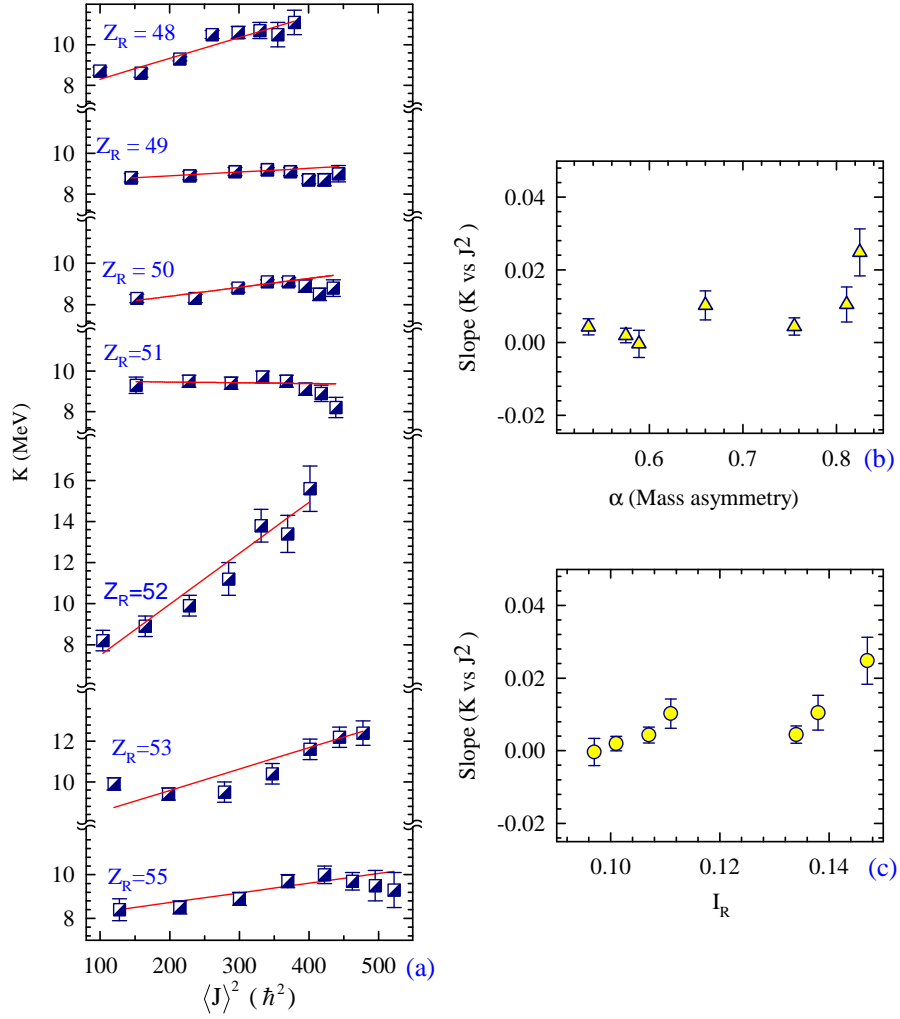
Figure 3.25: (a) Inverse level-density parameter K as a function of $\langle J \rangle^2$ for different Z_R in the shell-closure region. Solid lines are results of linear fits. The slope (K versus $\langle J \rangle^2$) as a function of entrance channel mass asymmetry parameter α in panel (b) and reduced isospin in residue nuclei, I_R [see Table 3.1] in panel (c).

calculations available for a direct comparison with the present results.

A more systematic representation of the behavior of inverse level-density parameter K as function of angular momentum may be achieved by plotting the variation of K with $\langle J \rangle^2$, where a nearly linear dependence is observed over the full angular momentum range as shown in Fig. 3.25(a). The solid lines in the Fig. 3.25(a) are the results of linear fits. The slope of K versus $\langle J \rangle^2$ for each system is shown as a function of entrance channel mass asymmetry α and reduced isospin I_R in Figs. 3.25(b) and

3.25(c), respectively. It is seen that there is an overall increasing trend of the slope of K versus $\langle J \rangle^2$ with either α or I_R.

Recently, microscopic calculation [197] for hot rotating nuclei corresponding to the shell-closure region of $Z = 50$ of the present work shows that the parameter K would increase with angular momentum in all cases. These calculations are not consistent with the present measurements for the trend observed in various compound nuclear reactions. The steep rise of K with angular momentum in ^{11}B, ^{12}C $+^{115}$In reactions is under predicted in these microscopic calculations. In a very recent work by Banerjee *et al.* [198], the neutron evaporation energy spectra have been measured in coincidence with γ rays of different multiplicities for residual nucleus ^{119}Sb in the excitation energy range of 31 - 43 MeV. The residual nucleus ^{119}Sb is very close to the $Z_R = 51$ populated in the ^{24}Mg $+$ ^{93}Nb reaction of the present measurement for which it is observed that parameter K decreases with increasing J at higher values of J. In the work by Banerjee *et al.*, the inverse level-density parameter K for ^{119}Sb is observed to decrease with increasing angular momentum and it is consistent with present measurements.

3.5.2   Mid-shell region of $Z \sim 70$

Similar to the shell-closure region of $Z \sim 50$, in the mid-shell region of $Z \sim 70$ the inverse level-density parameter K is determined by least squares fitting the experimental fold-gated and summed α-particle spectra for fold 4 and above events with corresponding spectra obtained from PACE2 calculations. The calculated α-particle yields in the energy interval of $E_{\text{c.m.}} = 21.5$ to 31.5 MeV, were normalized to the experimental yields while fitting the spectra. No attempts were made to fit the multiplicity of α particles. The measured fold-gated α-particle energy spectra for various γ-ray folds (solid circles) and corresponding PACE2 best fits after the normalization (solid histograms), for all the systems of this mass region of $A \sim 180$, are shown in Figs. 3.26 and 3.27. The insets in the panels show the nearly parabolic variation of $S(K)$ with the parameter

K. The minimum of the parabola corresponds to the best-fit value of the inverse level-density parameter K. The fold number, the best-fit K value (with error bar), and experimental as well as calculated (in parenthesis) α-particle multiplicity, ν_α are shown at the bottom of each panel.

The best-fit inverse level-density parameter K as a function of γ-ray fold and the corresponding average angular momentum $\langle J \rangle$ are shown in Figs. 3.28(a) and (b), respectively. The fold to angular momentum conversion was carried out using the similar calculations for all the systems as presented in the Fig. 3.15 for some typical systems in this mass region of $A \sim 180$. The dotted lines in Fig. 3.28(b) are drawn as guide to eye to show the average behavior. It can be seen in the Figs. 3.28(a) and (b) that within statistical errors the value of K is constant around 8.2 ± 1.1 MeV for each system over the angular momentum range of 15-30$\hbar$. The shaded regions in the Fig. 3.28(a) correspond to this average value of $K = 8.2 \pm 1.1$ MeV. However, the uncertainty, δJ in the value of $\langle J \rangle$ varies from $\pm 5\hbar$ to $\pm 3\hbar$ in this mass region in going from fold 4 to fold 11, but the constant behavior of the parameter K as a function of angular momentum in this mid-shell region, remains unchanged. Similar observation has been reported earlier by Henss *et al.* [77] for ^{64}Ni + ^{92}Zr system, where, the neutron evaporation spectra were measured by selecting only high spin states of average spin 52$\hbar$ in ^{155}Er* nucleus. They obtained a value of level-density parameter $a = $ A/(8.8 $\pm$ 1.3) MeV^{-1} for 52$\hbar$ and for excitation energies between 30 and 36 MeV, which is close to the value of 'a' for low spins and low excitation energy in nuclei of similar mass. In the mass region of $Z \sim 50$ shell closure, we obtained strong dependence of inverse level-density parameter K on angular momentum in the range of 15-30 $\hbar$ in the ^{11}B + ^{115}In system ($Z_R = 52$) where the K value varied from 8.9 $\pm$ 0.4 MeV for low angular momentum to 15.3 $\pm$ 0.9 MeV for high angular momentum. However, in the mid-shell region, the value of K remains nearly constant over an angular momentum range of 15$\hbar$ to 30$\hbar$. There is no microscopic understanding of these observations but the present experimental results will serve as important inputs for carrying out these
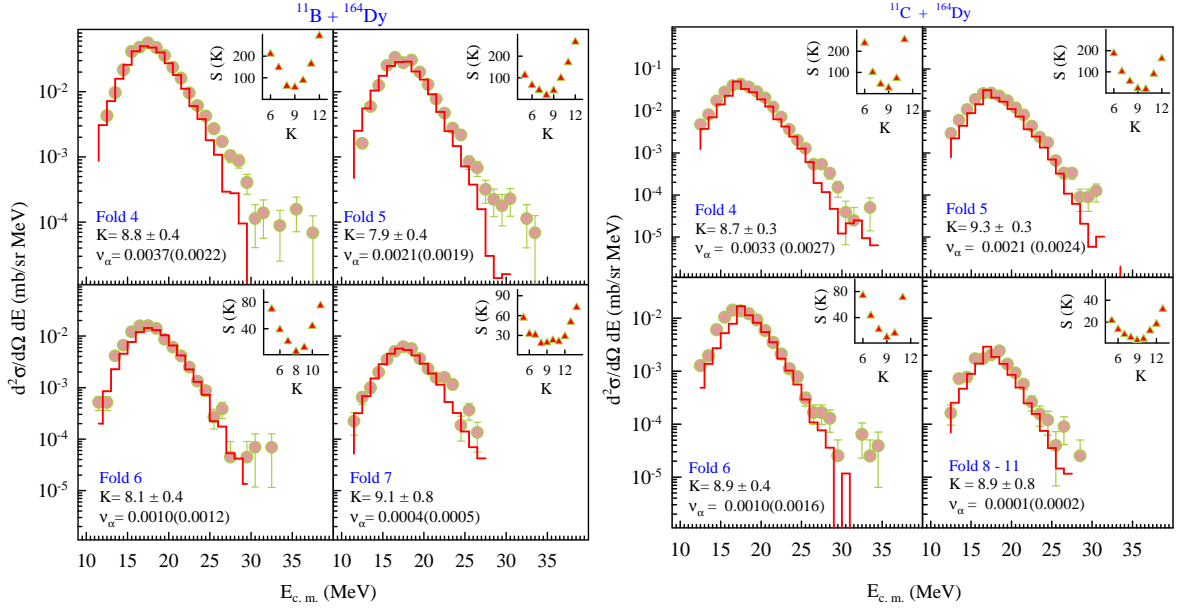
Figure 3.26: Fold-gated α-particle energy spectra in center-of-mass frames in ^{11}B+ ^{164}Dy and ^{12}C + ^{164}Dy reactions for various folds (solid circles) along with the results of PACE2 statistical model calculation (solid histograms). The fold number, best-fit K value (with error bar), and experimental as well as calculated (in the parenthesis) multiplicity of α particles, ν_α are shown at the bottom of each panel. In the inset, statistical variance is shown (triangles) as a function of K from where the best-fit K value was determined as discussed in the text.
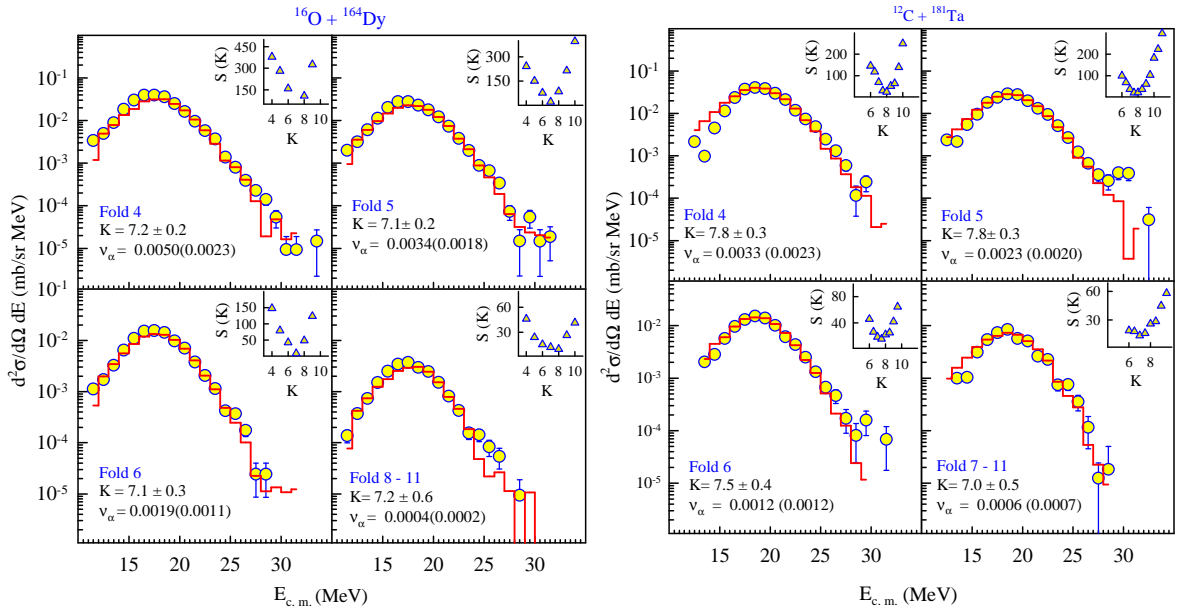
Figure 3.27: Same as in Fig. 3.26 but for the ^{16}O+ ^{164}Dy and ^{12}C + ^{181}Ta systems.
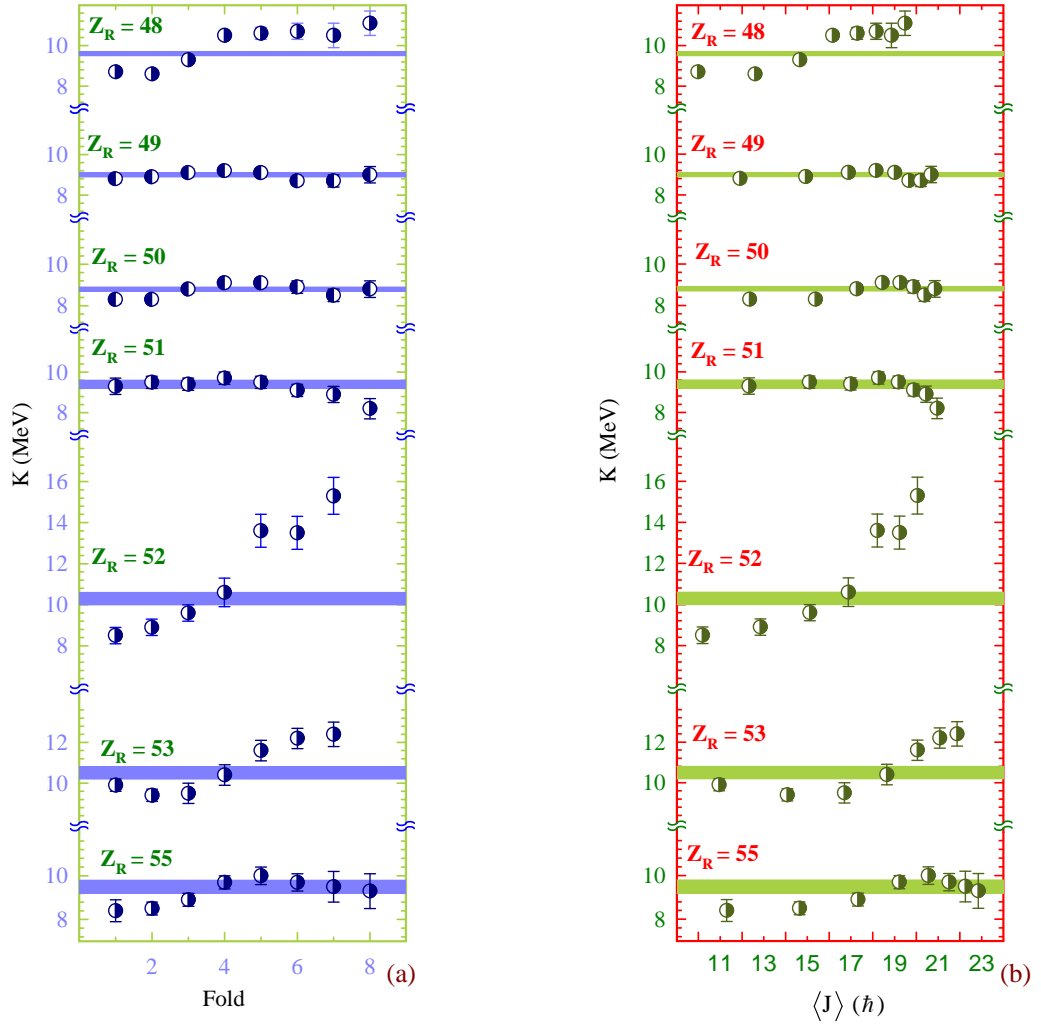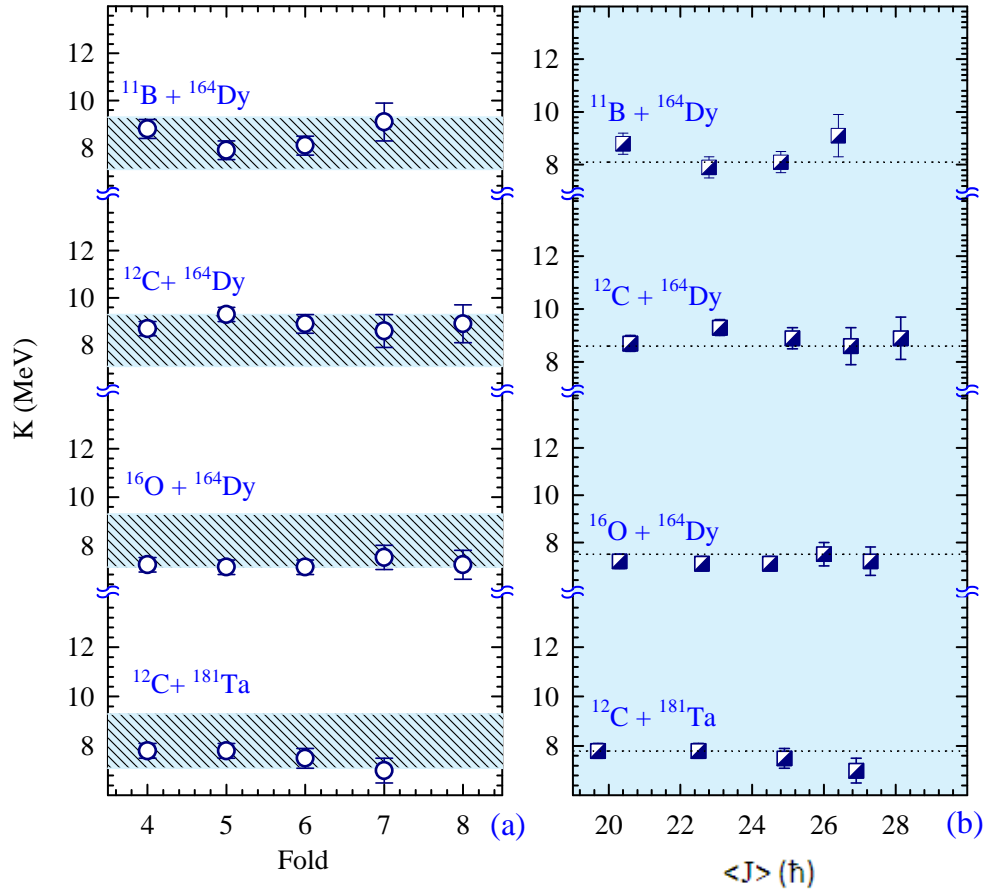
Figure 3.28: Inverse level-density parameter K as a function of fold (a) and $\langle J \rangle$ (b) for different reactions of the mid-shell region. In panel (a), the hashed regions correspond to $K = 8.2 \pm 1.1$ MeV. In panel (b), the dotted lines are shown to guide the eye.

calculations.

In the mid-shell region, the gross energy spectra of α particles summed over all γ-ray folds of 4 and above were also compared with corresponding PACE2 predictions. The gross value of K for the summed spectrum was obtained using again the least-squares fit method for each system. This gross value of K is plotted as a function of charge of residual nuclei as shown in Fig. 3.29 (solid squares). The 'gross' K values for nuclei in this mass of $A \sim 180$ are around 8.2 ± 1.1 MeV, as shown by shaded region in Fig. 3.29. This value is consistent with systematics established for low excitation energy and spin [37]. In Fig. 3.29, we also show (solid circles) the gross values of K (summed over all γ-ray fold events) for mass region of $A \sim 120$ ($Z_R = 48\text{-}55$). It is seen

that the gross value of K for the mass region of $A \sim 180$ is lower than that for mass region of $A \sim 120$. However, it may be noted that in mass region of $A \sim 120$ the gross value of K determined from summed spectra for all γ-ray fold of 4 and above events is expected to be higher than the value corresponding to summed over all γ-ray fold events because of increase of K as a function of angular momentum in the range of $15\hbar$ to $30\hbar$. This will lead to further difference in 'gross' K values for mass regions of $A \sim 120$ and $A \sim 180$ than shown in Fig. 3.29.

As discussed earlier, the high-energy slope of light charged particle spectrum is affected by entrance channel mass asymmetry [195, 196]. The entrance channel mass-asymmetry parameter α for mass region of $A \sim 180$ is larger than that of $A \sim 120$ [Table 3.1]. It is seen from Fig. 3.19 that similar to the mass region of $A \sim 120$, in the mass region of $A \sim 180$ also the value of mass asymmetry parameter α is higher than α_{BG} for all angular momentum values (i.e., $\alpha > \alpha_{BG}$ for all J). Therefore, the entrance channel effect with respect to BG point is not expected to play a role for the present systems. Lower value of K for mass region of $A \sim 180$ than that of $A \sim 120$, can not be due to entrance channel effect. It can be seen that the value of K is higher at $Z = 48\text{-}55$ (shell closure region) than at $Z \sim 70\text{-}77$ (mid-shell region). The present results on the value of K seen over the entire range of $Z = 48$ to 77 imply the role of shell closure in the enhancement of K in $Z = 50$ region.

In our analysis for the inverse level-density parameter K, we relied on Bethe's Fermi-gas formula for the level densities [Eq. (3.8)]. The spin cut-off parameter for angular momentum distribution of levels was included in the formula. A recent theoretical analysis of excitation energy and angular momentum dependence of level densities using microscopic SPA+RPA approach [58] showed that in mid-mass nuclei the spin cut-off approximation in Bethe's formula works well for $J \leq 35\hbar$ at excitation energy $E_X = 30$ MeV. It was found that with an appropriate E_X dependent value of spin cut-off parameter, Bethe's formula almost reproduces SPA and SPA + RPA results
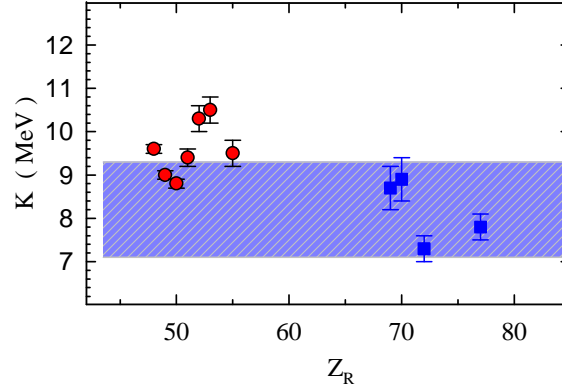
Figure 3.29: Inverse level-density parameter K determined from the summed spectra (fold 4 and above) as a function of Z of residual nuclei. Circles are from the shell-closure region and squares are from the mid-shell region. The hashed region corresponds to K = 8.2 ± 1.1 MeV.

at different excitation energies below a certain J value. Since the residual nucleus excitation energies of interest in the present work are around ~ 35 MeV and angular momentum values are below $35\hbar$, it may be stated that Bethe's formula adequately accounts for the angular momentum distribution of the levels. The correspondence between the values of K used in Bethe's formula and values of K calculated using SPA has been discussed in Ref. [57] for various temperature and angular momentum domains. According to [57], instead of full SPA calculation for the level-density, it should be enough to use Bethe's formula with K calculated using SPA. In a similar view point, the experimentally determined K values using the Bethe's formula in a statistical model code should show correspondence with K values calculated using the SPA [72]. It would be interesting to obtain microscopic calculations of K for various angular momentum domains and compare with the present results.

The authors of Ref. [60] pointed out that they are the first ones to calculate the level-density parameter $a(E)$ and the spin cut-off parameter for a large number of nuclei using a realistic microscopic approach. The calculations were carried out at excitation energies of neutron resonance reactions. As expected from their microscopic theory, the spin cut-off parameter showed structures that reflect the angular momentum of the

shell model orbitals near the Fermi energy. The results from present experiment will provide a testing ground for the microscopic model calculations at moderate excitation energies and angular momenta.

Chapter 4

Measurements of α-particle multiplicities in heavy-ion fission reactions

4.1 Introduction

In heavy-ion induced fusion-fission reactions, neutron and charged-particle (mainly proton and α-particle) emission takes place from various stages, namely from the fissioning compound nucleus (prescission) and from the accelerated fission fragments (postscission) [96, 97]. Prescission neutron and charged particle emission spectra and multiplicities provide important information on the statistical and dynamical aspects of the fusion-fission process [96, 97]. In the case of α-particle emission, it is observed that particles are also emitted very near the neck region in the fission process just before scission, akin to the ternary fission events in low energy fission [129–133]. This part of prescission α-particles emitted near the neck region is termed as near scission emission (NSE). Moving-source analysis is employed in heavy-ion-induced fission to disentangle the contributions of different sources to the inclusive α-particle multiplicity. Although there have been many studies on prescission α-particle emission in many heavy-ion induced fusion-fission reactions [96–98, 129–132], a global systematics is yet to be developed. Similarly, there are no systematic studies so far for the NSE over a large fissility (x) range in heavy-ion induced fusion-fission reactions.

In addition, at beam energies near the Coulomb barrier, the transfer induced fission cross section becomes significant [199–201]. In the case of α-cluster projectiles (such as ^{6,7}Li, ^{6}He, and ^{12}C), a portion of coincident α particles may also originate from transfer-induced fission events. In such cases, the projectile like fragment (PLF) can be an α-particle itself or it can decay subsequently to an α-particle. The α particles produced from transfer events exhibit a bell-shaped angular distribution having a maximum near the grazing angle. Thus, depending on entrance channel parameters of the heavy-ion reaction, the transfer processes can also contribute to the inclusive α-particle multiplicity, adding to the complexity of the analysis of experimental data.

In the present work, we have carried out measurements of α-particle energy spectra in coincidence with fission fragments for ^{11}B (62 MeV) + ^{232}Th ($Z^2/A = 37.14$) and ^{12}C (69 MeV) + ^{232}Th ($Z^2/A = 37.77$) systems in a wide range of relative angles between fission fragments and α particles. The α-particle multiplicity spectra for each system at various relative angles have been fitted simultaneously with the moving-source model calculations to extract the components of multiplicity corresponding to different emission stages of the fusion-fission process. The obtained results for both the systems are compared with each other. In case of ^{12}C induced fission, significantly large value of α_{nse} is observed as compared with ^{11}B + ^{232}Th system, indicating that due to α-cluster structure of ^{12}C there may be an admixture of some other source of α-particle emission to the NSE component in the ^{12}C + ^{232}Th reaction apart from earlier mentioned four conventional sources involved in the fusion-fission process.

The data obtained for ^{11}B + ^{232}Th system are first analyzed along with data from literature over a wide range of excitation energy and fissility of the compound system to develop systematic features of pre- and near-scission emission as a function of α-particle emission Q-value and Z^2/A of compound systems. The anomalously large value of α_{nse} in case of ^{12}C + ^{232}Th reaction is then compared with above mentioned systematics, providing a strong clue to understand the ^{12}C + ^{232}Th reaction data.
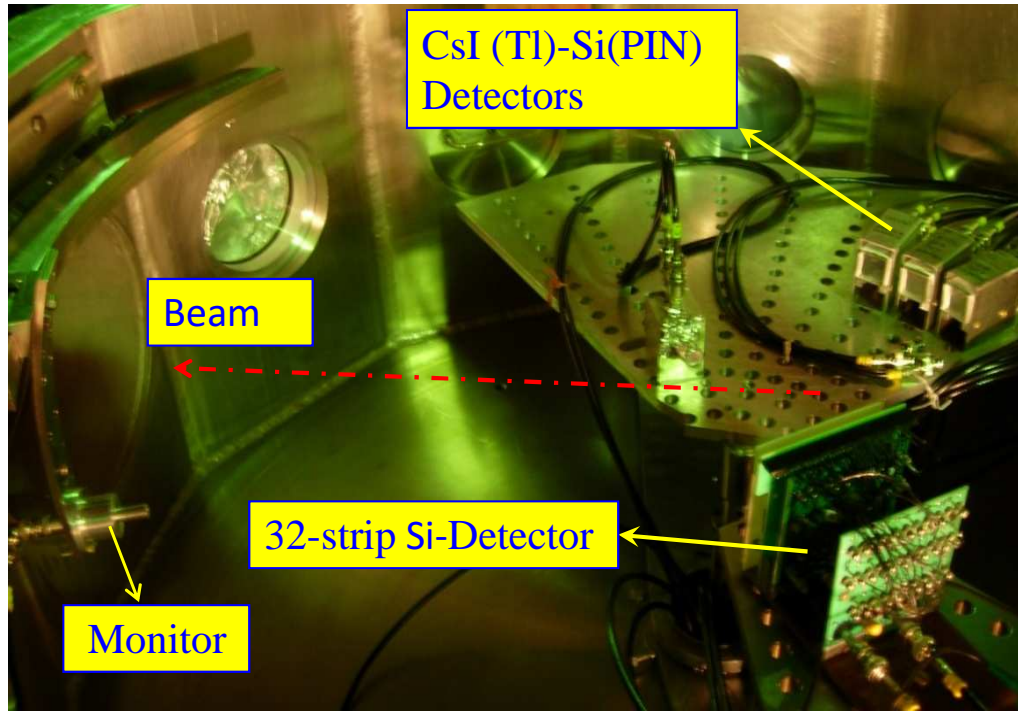
Figure 4.1: A photograph of the first experimental setup where a 32-strip Si-detector was used for fission fragment detection.

4.2   Experimental details

Experiments were performed using ^{11}B (62 MeV) and ^{12}C (69 MeV) beams from the BARC-TIFR 14-MV Pelletron accelerator facility at Mumbai. A self-supporting thin metallic foil of ^{232}Th with thickness 1.6 mg/cm^2 was used as a target. Measurements were carried out in two separate experiments. In the first experiment, the fission fragments were detected using a position sensitive 32-strip silicon detector (SSD) having delay line read-out [202] with an angular opening of ~32° and centered at 150° with respect to the beam direction. In the second experiment, a position sensitive gridded gas ionization chamber consisting of ΔE_{gas} and E_{gas} elements [156] was used to detect the fission fragments. The detector was centered at 145° with respect to beam direction and covered an angular opening of 30°. In both the experiments, α particles were detected by three collimated CsI(Tl)-Si(PIN) detectors [142] with an angular opening of ±3.5°. Photographs of experimental setups for the first and second set of
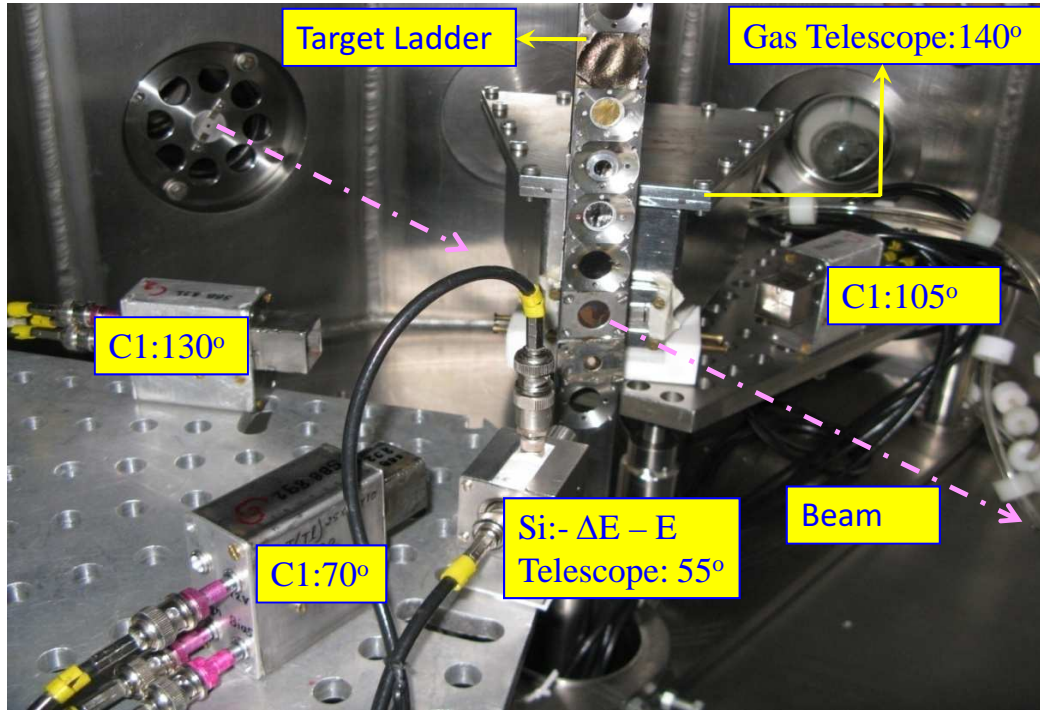
Figure 4.2: A photographs of the second experimental setup where a position sensitive gas ionization telescope was used for fission fragment detection.

the experiments are shown in the Figs. 4.1 and 4.2, respectively.

4.2.1 CsI(Tl) detector response and energy calibration

The charged particle measurement for ^{11}B + ^{232}Th system was carried out in the first as well as the second set of the experiments, whereas for ^{12}C + ^{232}Th systems it was only the second set. In the first set of experiments, the CsI(Tl) detectors were placed at the back angles in the range of 115° to 155° on either side of the beam direction. In the second set of the experiments, the CsI(Tl) detectors were placed at angles of 70°, 105°, and 130° with respect to the beam direction in case of ^{11}B + ^{232}Th reactions, whereas in the case of ^{12}C + ^{232}Th reaction these angles were 75°, 100°, and 135°. The particle identification in CsI(Tl) detectors was achieved using a pulse shape discrimination (zero crossover) technique. The γ rays, light charged particles (p, d, t, and α), and PLFs were well separated in the two-dimensional plot of zero crossover (ZCT) versus pulse height
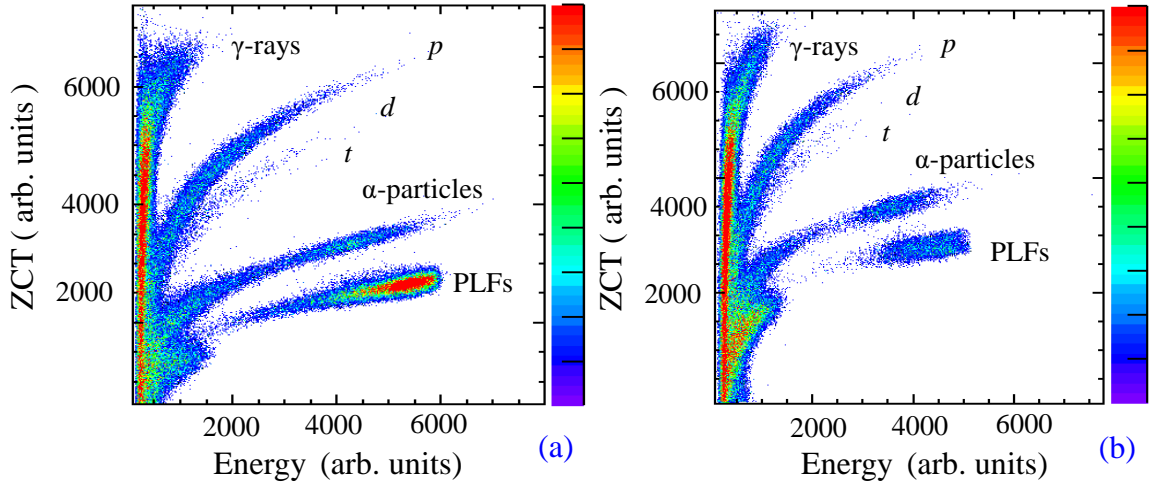
Figure 4.3: Typical two-dimensional plots of zero crossover (ZCT) versus energy from CsI(Tl) detectors at laboratory angles of 100° (in panel (a)) and 135° (in panel (b)) for different particles produced in ^{11}B + ^{232}Th reaction.

as shown in Figs. 4.3(a) and (b) typically at two laboratory angles of 100° and 135°, respectively for ^{11}B + ^{232}Th system. The energy threshold for α-particle identification was ∼9.5 MeV (and ∼5 MeV in second experiment). The higher threshold in the first experiment is due to a 14.9-μm aluminum foil used to stop the fission fragments.

The CsI(Tl) detectors were energy calibrated for α-particles using ^{228,229}Th source and in-beam energy calibration runs. In the first experiment, the in-beam calibration made use of the discrete α-particle peaks corresponding to ^{15}N* states from the reactions ^{12}C $(^7$Li, α) ^{15}N* at a ^{7}Li beam-energy of 15 MeV. In the second experiment the discrete states of ^{20}Ne* from the ^{12}C $(^{12}$C, α) ^{20}Ne* reaction at ^{12}C beam energies of 25 and 40 MeV, were used. In the present work, however, we did not analyze the proton spectra, but the CsI(Tl) detectors were energy calibrated for protons also. For this purpose, elastically scattered protons from thin ^{12}C, ^{197}Au, and ^{232}Th targets and recoil protons from the ^{12}C beam-bombardment on mylar, were used. The measured light yield as a function of energy of α particles and protons are shown in Figs. 4.4(a) and (b), respectively for three CsI(Tl)-detectors; C1, C2, and C3 having different electronic gain settings. The light yield varies almost linearly for protons, whereas for α
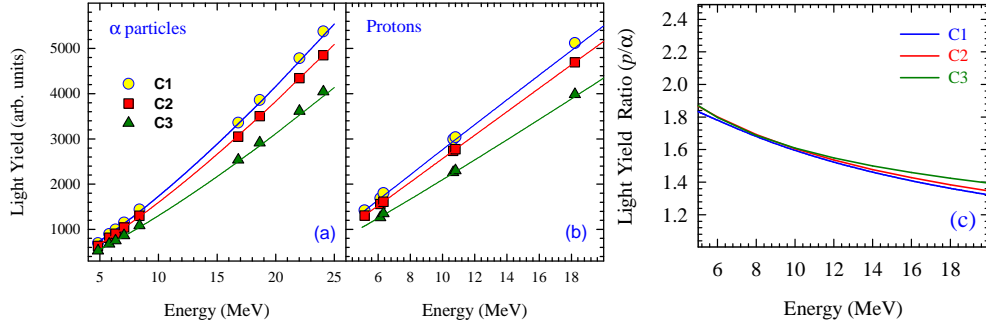
Figure 4.4: The light yield measured in the second set of the experiments as a function of energy of α particles (a) and protons (b) for three CsI(Tl)-detectors, C1, C2, and C3 having different electronic gain settings. (c) The light output ratio of proton to α-particle as a function of their energy deposited in the CsI(Tl) crystal.

particles, it is nonlinear. The Z and E dependent light yield shown in Figs. 4.4(a) and (b) was fitted with the following functional form;

$$L(Z, E) = a_e Z^b E^c + d_o, \tag{4.1}$$

where the constant a_e and d_o are related to electronics gain settings, while 'b' and 'c' depend on particle type and their response within the crystal, respectively. The value of the constant 'c' obtained for α-particle and proton are 1.3 and 1.0, respectively. The value of the constant 'c' was observed to be independent of the value of 'b'. By varying the constant 'b', the parameter a_e varies accordingly but the value of 'c' remains constant which is consistent with the earlier reported results [164]. In Figs. 4.4(a) and (b) solid lines show the fit to the light output data using the Eq. (4.1). The ratio of light output for proton to α-particle was obtained as a function of their energy, as shown in Fig. 4.4 (c). For a given energy deposited in the CsI(Tl) crystal, the light yield for proton is more than the α-particle and this difference decreases with increasing energy. The differences in light yield [4.4(a) and (b)] as well as the rise time [Fig. 4.3(a) and (b)] for α-particle and proton are attributed to their specific energy loss behavior (-dE/dx) in the crystal [142] as discussed in the chapter-2.

Table 4.1: Main features of the Si-strip detector [202].

Parameter	Value
Sensitive area	60×60 mm^2
Thickness	300 μm
Number of strips	32
Strip width	1778 μm
Inter-strip distance	100 μm
Working voltage	10 – 300 V
Breakdown voltage	>300 V
Thickness of upper dead layer	5 μm
Thickness of lower dead layer	5 μm

4.2.2 Measurement of FF: 32-strip Si-detector

In the first set of the experiments [Fig. 4.1], a position sensitive 32-strip silicon detector (SSD) with delay line read-out [202] was used for the fission fragment detection. The detector was centered at 150° with respect to the beam direction and covered an angular opening of ∼32°. The Si-strip detector was fabricated at Bharat Electronics Laboratory, Bengaluru, India in collaboration with Electronics Division of BARC, Mumbai, India using an n-Si substratum with resistivity of 25 kΩ cm. The p$^+$ n$^-$ junctions were made with implanted boron using planar technology. The major specifications of the detector are shown in the Table 4.1. However, the active area of the detector was 60×60 mm^2, but during the experiment it was masked to 48×42 mm^2.

The position information is obtained by using the delay line method. Unlike coupling the detector strip and delay-line tap directly, a two-stage AC coupled common source FET amplifier is used in between each detector strip and delay-line tap. The delay-line circuit is essentially a low-pass filter made from LC cells. In the present circuit the value of inductor (L) is 36 μH and capacitance (C) is 4.7 pF. Thus, the
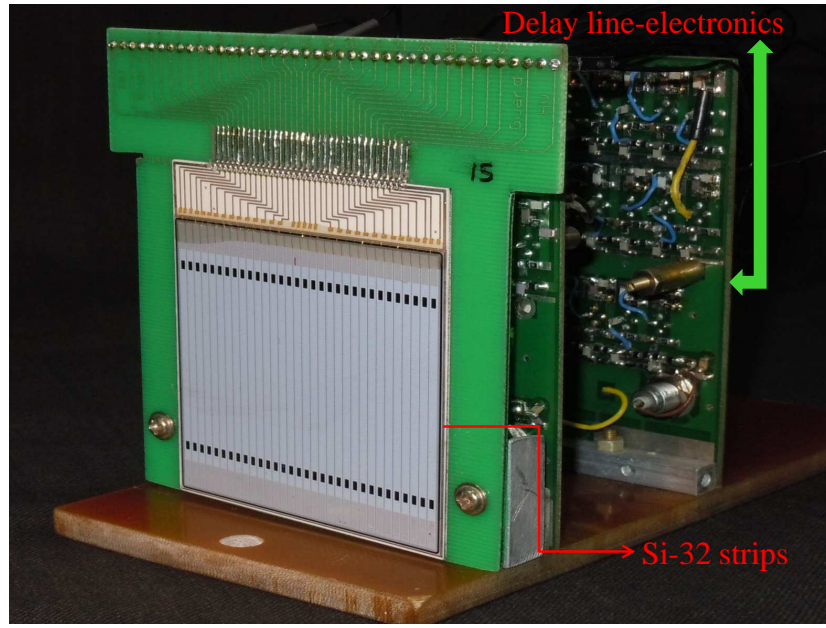
Figure 4.5: A photograph of the 32-strip Si-detector used in the first set of the experiments for fission fragment detection.

calculated value of characteristic impedance ($Z_o = \sqrt{L/C}$) is ~2.7 kΩ and per cell delay ($\tau_d = \sqrt{L \times C}$) comes to be ~13 ns. Each tap of delay-line is made up of two cells (interleaving one cell in between). Thus, calculated value of per tap delay becomes ~26 ns but we get practical value ~30 ns due to stray capacitance of the tracks of printed circuit board (PCB). In total 16 such amplifiers and above mentioned LC delay-line circuit were assembled on a small printed circuit board which was mounted on the rear side of 32-strip Si-detector. Surface mounted devices (SMD) resistors, capacitors and inductors were used to reduce the size of the PCB. The gain of each amplifier was adjusted in the range of 2 - 5 by changing the value of bypass capacitance in the source FET circuit, thus, compensating against higher attenuation suffered by the position signal of the strip facing higher delay. In this way, we have made the amplitude of position signal of all strips almost equal and thereby, achieving reduction in the broadening of position signal peaks. A photograph of the detector along with the delay line electronics is depicted in the Fig. 4.5. The 32-strip silicon detector is seen in the front and the PCB consisting of two sets of 16-tap delay-line and 16 units
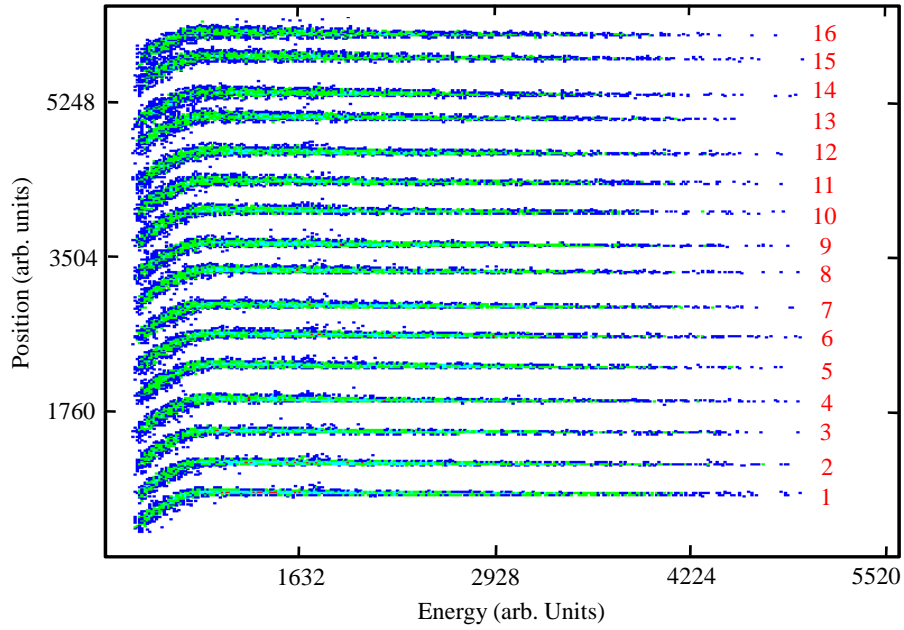
Figure 4.6: A typical two-dimensional fission fragment position versus energy spectrum in ^{11}B + ^{232}Th reaction obtained from one set of 16 strips. In the right-hand-side, strip positions are marked, where '1' and '16' correspond to the central region and the extreme right-end of the detector.

of two-stage FET amplifiers are mounted behind the detector.

Two time-to-amplitude converters (TACs) were used to generate the position signals where start signal was derived from common electrode (cathode) of detector and the stop signals were derived from position (anode-strip) side after delay line read-out through all 32 strips. The common energy signal after energy pre-amplifier was shaped through a shaping amplifier. A typical two-dimensional position versus energy spectrum obtained from one set of 16 strips in ^{11}B + ^{232}Th reaction, is shown in the Fig. 4.6. In the right-hand-side of the Fig. 4.6, strip positions are marked, where '1' and '16' correspond to the central region and the extreme right-end of the detector. The higher strip position correspond to the large angle with respect to the beam direction.
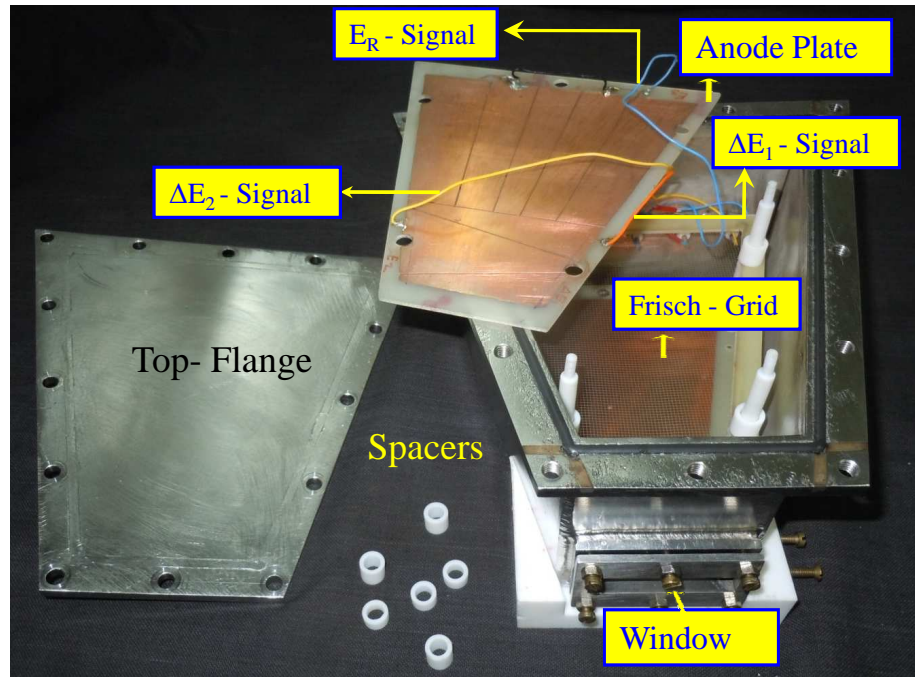
Figure 4.7: A photograph the position sensitive gas ionization telescope used in the second set of the experiments for fission fragment detection.

4.2.3 Measurement of FF: Position sensitive gas ionization chamber

In the second experiment, a position sensitive gridded gas ionization chamber consisting of ΔE_{gas} and E_{gas} elements [156] was used to detect the fission fragments. The detector was centered at 145° with respect to beam direction and covered an angular opening of 30°. A photograph of this position sensitive gas telescope is depicted in the Fig. 4.7. Basic characteristics of the detector are discussed earlier in the chapter-2.

The detector was filled with P-10 (90% Ar + 10% CH$_4$ mixture) gas and kept at a constant pressure of 150 mbar in a gas-flow mode thought out the experiments. The cathode was kept at -100 V and positive voltages applied to the grid (+125 V) and anode (+250 V). The ΔE anode segment is further splitted into two segments as shown in the Fig. 4.7, in such a way that the average dE/dx is almost equal in both the regions for the FFs entering the central line of the detector. FFs, passing at any other angle will lose energies proportional to the path lengths in ΔE_1 and ΔE_2 regions. A
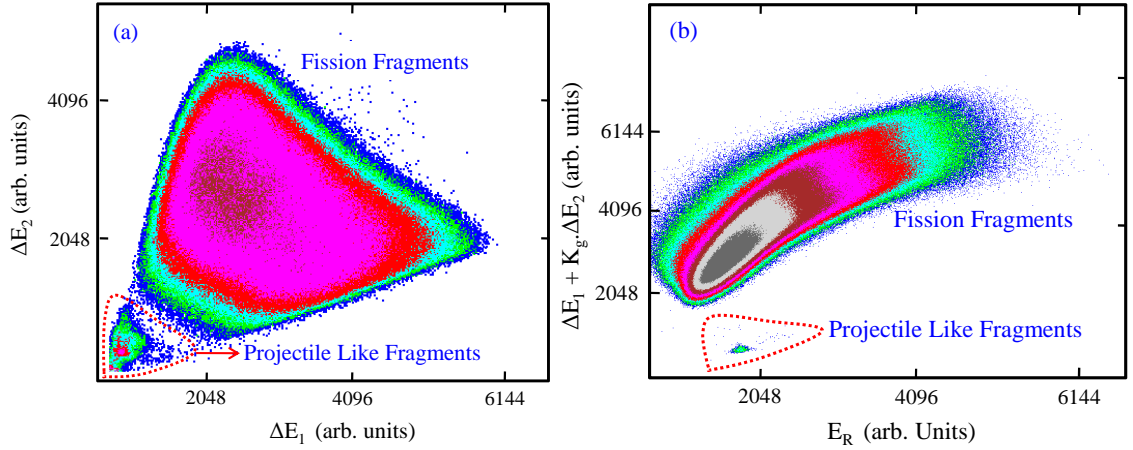
Figure 4.8: Two-dimensional plots of ΔE_1 vs. ΔE_2 [in panel (a)] and $\Delta E_1 + K_g.\Delta E_2$ vs. residual energy loss E_R [in panel (b)] of the fission fragments produced in ^{12}C + ^{232}Th reaction. K_g is the gain matching factor between ΔE_1 and ΔE_2 (see text).

typical ΔE_2 vs. ΔE_1 plot is shown in the Fig. 4.8(a), where FFs are clearly separated from projectile like fragments (PLFs) produced in ^{12}C + ^{232}Th reaction. The Fig. 4.8 (b) shows the ($\Delta E_1 + K_g \Delta E_2$) vs. E_R plot, where E_R is the residual energy deposited by the FFs in the E-segment of the anode. K_g is a ratio of electronic gains of ΔE_1 to ΔE_2, and was measured to be 2.2 using the pulse generator. The position information was obtained using the charge division method. Position parameter is defined as;

$$x = \frac{\Delta E_1 - K_g \Delta E_2}{\Delta E_1 + K_g \Delta E_2}. \tag{4.2}$$

A typical position spectrum obtained from the gas ionization telescope in ^{12}C + ^{232}Th reaction, is shown in the Fig. 4.9. The total width of the position spectrum corresponds to the detector angle opening of 30°. Thus, gas ionization chamber in the ΔE vs. E arrangement, provides angle information of the FFs with respect to the beam direction as well as a clear disentangling between FFs and the PLFs.

4.2.4   Electronics configuration for coincidence measurements

The linear energy outputs from all the detectors were fed to analog-to-digital converters (ADCs) after suitable amplification through spectroscopy amplifiers. The ZCT outputs
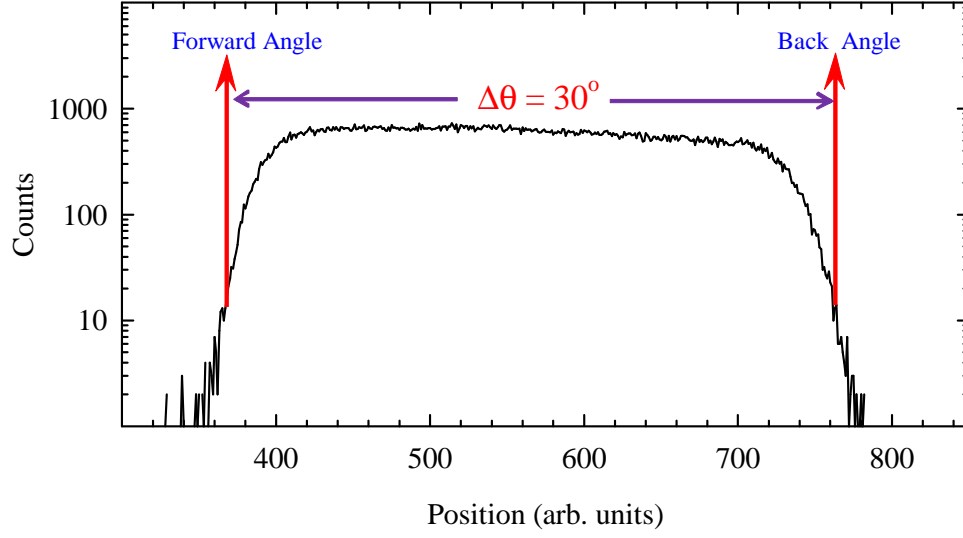
Figure 4.9: A typical fission fragment position spectrum obtained from the gas ionization telescope in ^{12}C + ^{232}Th reaction. The forward and back angles are with respect to the beam direction.

from the CsI(Tl) detectors and the two position TAC-outputs from the 32-strip detector were also fed to the ADCs. The event trigger for data collection was generated with the fission events from the FF-detector via a combination of timing filter amplifier (TFA), constant fraction discriminator (CFD). In case of the gas detector, the timing signal was obtained from the cathode. Schematic layout of the electronics used for charged particle and fission fragment coincidence measurements is given in Fig. 4.10. The 'PSD BLOCKS' in the Fig. 4.10 refer to the electronics configuration of pulse shape discrimination which has been discussed in detail in the chapter-2.

The time correlations between light particles and FFs were recorded through time-to-amplitude converters (TACs). The coincidence TAC spectra between α particles and FFs obtained in the first set of experiments (for ^{11}B + ^{232}Th system) and in the second set (for ^{12}C + ^{232}Th system) are shown in the Figs. 4.11(a) and (b), respectively. The coincidence TAC-spectrum is quite sharp in case of the 32-strip Si-detector (width ∼70 ns), whereas for the gas detector it is comparatively broader (width ∼120 ns). This difference in the widths of TAC spectra obtained from 32-strip Si-detector and the gas detectors is attributed to the larger rise time of the gas detector pulse than that
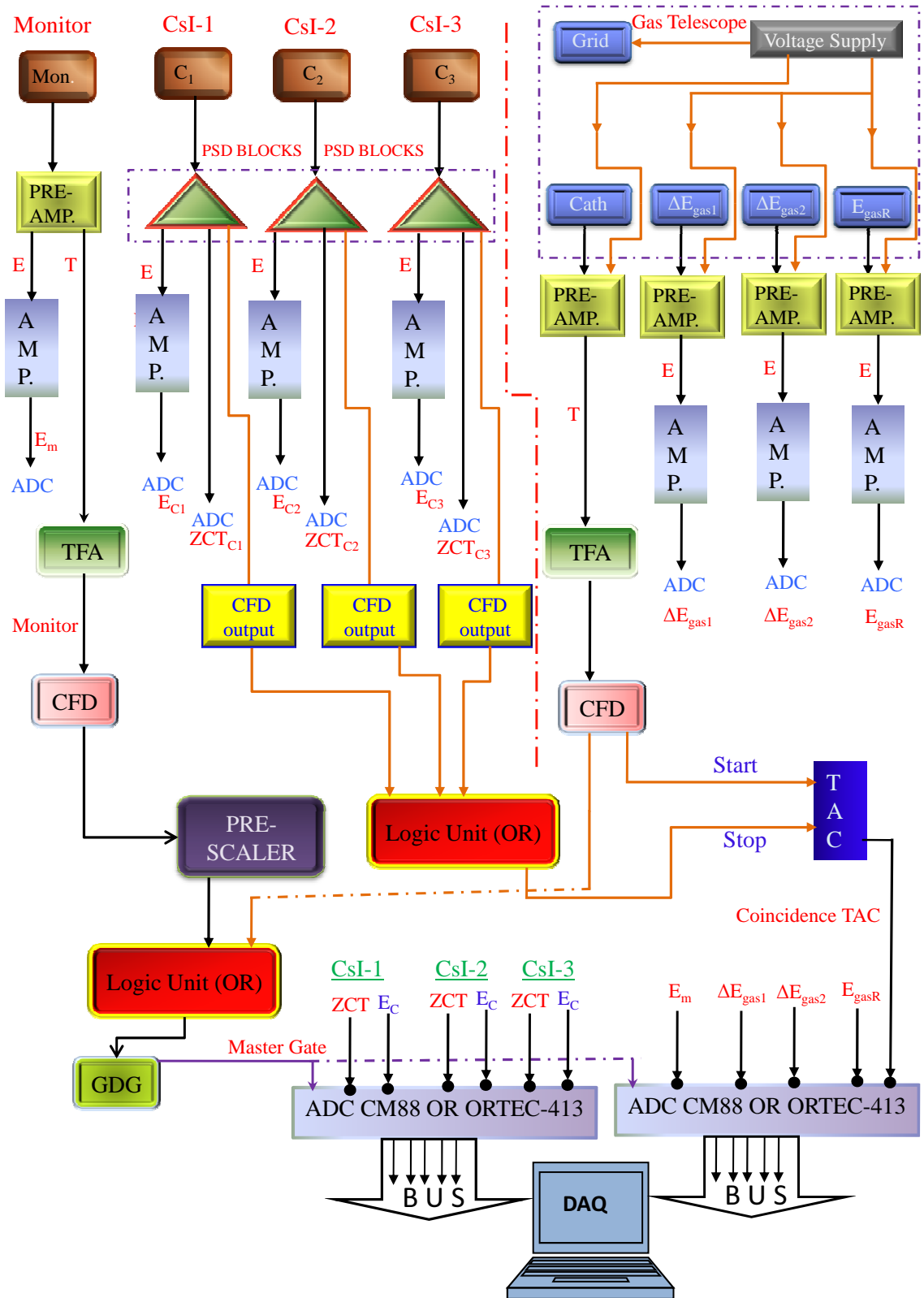
Figure 4.10: Schematic layout of the electronics used for charged particle and fission fragment coincidence measurements. The 'PSD-BLOCKS' refer to the electronics configuration of pulse shape discrimination which has been discussed in detail in the chapter-2.
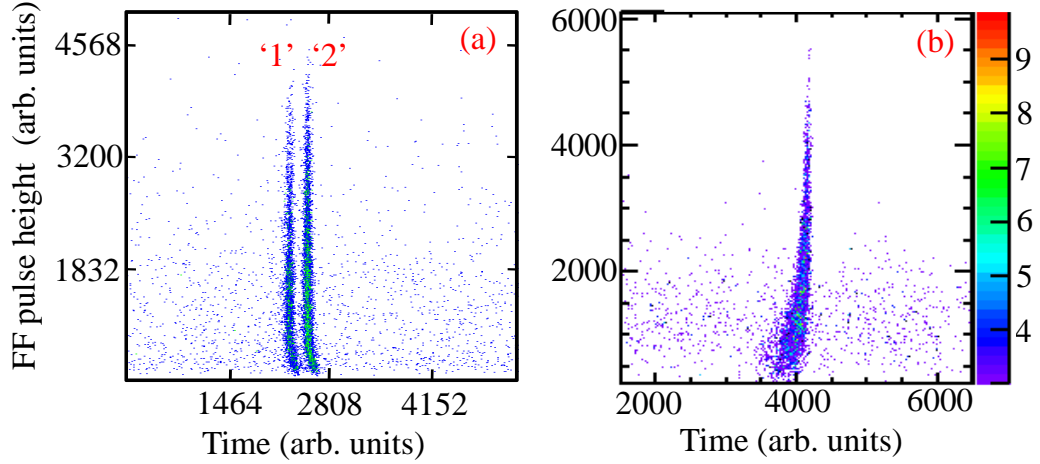
Figure 4.11: Fission fragment (FF) pulse-height versus the time correlation between α particles and FFs from 32-strip Si-detector in ^{11}B + ^{232}Th reaction (a) and gas ionization chamber in ^{12}C + ^{232}Th reaction (b). In panel (a), the two bands named as '1' and '2', correspond to the two sets of 16 strips having certain time-delay [Sec. 4.2.2].

of Si-detector. The coincidence TACs were used to correct for random coincidences. The stability of the amplifier gains corresponding to various detectors was monitored using a precision pulser throughout the measurements. The data were recorded in a list-mode using CAMAC based multi-parameter data acquisition system.

4.3   Data Analysis: Moving-source fit

The angular opening of the fission detector in both the experiments was divided into four equal parts. Thus, in case of ^{11}B + ^{232}Th reaction, a total number of 24 combinations of α-particle spectra each having different relative angles with respect to the beam (θ_α) and fission fragments ($\theta_{\alpha fd}$), were obtained from the combined geometry of both the experiments. Whereas for ^{12}C + ^{232}Th system, a total number of 12 combinations of α-particle spectra were obtained from the second set of the experimental geometry.

The inclusive α-particle coincidence spectra were projected out from the list-mode data by imposing separate gate conditions: (i) prompt coincidence TAC, (ii) the se-

Figure 4.12: The α-particle multiplicity spectra in ^{11}B + ^{232}Th reaction along with fits of moving-source model for different combination of laboratory angles of CsI(Tl) detectors with respect to beam direction, θ_α and detected fission fragments, $\theta_{\alpha fd}$. The dotted, long-dashed, short-dashed, and dash-dot curves are contributions from compound nucleus, detected fission fragment, complementary fission fragment, and near scission emission, respectively. The solid curve indicates the total contribution from four sources.

Figure 4.13: The α-particle multiplicity spectra in ^{12}C + ^{232}Th reaction along with fits of moving-source model for different combination of laboratory angles of CsI(Tl) detectors with respect to beam direction, θ_α and detected fission fragments, $\theta_{\alpha fd}$. The dotted, long-dashed, short-dashed, and dash-dot curves are contributions from compound nucleus, detected fission fragment, complementary fission fragment, and near scission emission, respectively. The solid curve indicates the total contribution from four sources.

Figure 4.14: Schematic velocity diagram for α-particle emission from different sources such as compound nucleus, fission fragments (FE), and near-scission emission (NSE). The circles represent the most-probable velocities of α particles emitted from compound nucleus (dash-dot), from detected fragment (dotted), and complementary fragment (dashed). The NSE is perpendicular to the scission axis defined by the detected fragment direction.

lection of the fission - fragment angle with respect to the beam, (iii) an appropriate two-dimensional banana-gate to select the fission events; from FF energy versus coincidence TAC in the first set of the experiments and from ΔE vs. E-plot in the second set of the experiments, and (iv) an appropriate two-dimensional banana-gate to select the only α particles from ZCT versus energy plots for each charged particle detector. After correcting for random coincidence, the normalized α-particle multiplicity spectra were obtained by dividing the coincidence spectra with total number of fission single events. Figs. 4.12 and 4.13 show typical normalized α-particle multiplicity spectra for ^{11}B + ^{232}Th and ^{12}C + ^{232}Th systems, respectively.

The inclusive coincidence α-particle spectra shown in the Figs. 4.12 and 4.13 includes contributions from the compound system (prescission), the accelerated fission fragments (postscission), and the near scission emission (NSE). The Procedure to disentangle the inclusive spectrum into prescission, postscission and near-scission components, relies upon the energy and angular distributions of the α particles. The prescis-

sion and postscission particles are emitted isotropically in their respective rest frames, in the laboratory frames they are focused in the moving direction of the corresponding source; termed as the kinematic focusing. The near-scission emission of α particles takes place perpendicular to the scission axis. However, the kinematic focusing is more effective for lighter particles, but in case of α particles, the significant difference between the emission barriers for various emitting sources makes more effective the disentangling of the inclusive spectrum into prescission, postscission and near-scission components. For each system, multiplicity spectra are fitted simultaneously by the moving-source model including four different sources namely the compound nucleus, the two complementary fission fragments, and the NSE.

4.3.1 Prescission and postscission components

The α-particles are assumed to be emitted isotropically in the rest frames of prescission and postscission sources. In the moving-source analysis, symmetric mass division is assumed for the fragments and mean values of fragment mass and charge have been used. The α-particle energy spectra in the rest frames for prescission and postscission sources are calculated using the constant-temperature level-density formula with the expression [96, 203];

$$n(\epsilon) = N\alpha_p \epsilon \sigma(\epsilon) \exp\left(\frac{-\epsilon}{T}\right), \tag{4.3}$$

where α_p and ϵ are the multiplicity and energy of the emitted α-particles in the rest frame, T is the temperature of the source, $\sigma(\epsilon)$ is the inverse reaction cross section and N is a normalization constant, which was obtained using the condition;

$$\int_0^\infty n(\epsilon)\mathrm{d}\epsilon = 1. \tag{4.4}$$

The integration in the Eq. (4.4) was performed using the numerical recipe. The inverse reaction cross section $\sigma(\epsilon)$ is calculated using the Wong's expression [204];

$$\sigma(\epsilon) = \frac{\hbar\omega R_0^2}{2\epsilon} \ln\left(1 + \exp\left[\frac{2\pi}{\hbar\omega}(\epsilon - V_B)\right]\right), \tag{4.5}$$

where $\hbar\omega$ is the curvature of fusion barrier for angular momentum $\ell = 0$. The values of $\hbar\omega$ for prescission and postscission sources are determined from the fits to the fusion excitation functions for ^{4}He + ^{237}Np [205] and ^{4}He + ^{59}Co [206], respectively with the predictions of the one-dimensional barrier penetration model code CCFUS [16]. Thus, $\hbar\omega_{\text{pre}}$ and $\hbar\omega_{\text{post}}$ values used in the moving-source model for prescission and postscission sources are 4.8 and 4.0 MeV, respectively. The V_B is the emission barrier height of the α-particles and is calculated using the expression [134];

$$V_B = \frac{1.44 Z_P(Z_S - Z_P)}{r_0 \left[A_P^{1/3} + (A_S - A_P)^{1/3} \right] + \delta} \text{MeV}, \tag{4.6}$$

where A_P, Z_P and A_S, Z_S are the mass and charge of the α-particle and emitting source, respectively. The value of r_0 is taken to be 1.45 fm [96]. δ is a factor which takes into account for the reduction in emission barrier due to deformation effects and it is taken to be 2.0 fm for compound nucleus [134] and 0.4 fm for fission fragment [98, 207]. Thus, the effective emission barrier heights (V_B) calculated for the compound nucleus and fission fragment are 20.2 and 13.4 MeV for ^{11}B + ^{232}Th system and 20.3 and 13.5 MeV for ^{12}C + ^{232}Th system, respectively. The temperatures T_{pre} and T_{post} are calculated using the relation $T = \sqrt{E^*/a}$, where E^* is the intrinsic excitation energy of the source. The excitation energies for fission fragments are calculated using the relation:

$$E_f^* = E_{\text{CN}} + Q_f - TKE - E_{\text{part.}}^{\text{pre}}, \tag{4.7}$$

where, E_{CN} is the excitation energy of the compound nuclei and its value for ^{11}B + ^{232}Th and ^{12}C + ^{232}Th systems are 45.5 and 42.8 MeV respectively. In Eq. (4.7), the Q_f and TKE are the Q-value for the fission process and average total kinetic energy of the fission fragments. The values of Q_f are calculated from experimental masses assuming symmetric fission. The TKE values are calculated using the Viola's systematics [105]. In Eq. (4.7), $E_{\text{part.}}^{\text{pre}}$ is the CN excitation energy loss due to prescission particle emission; it is a sum of kinetic energy and binding energy of the prescission particle (dominantly neutron) emission. The average kinetic energy of the neutron was assumed to be 2.5

MeV. The prescission neutron multiplicity ν, was estimated from the systematics. The level-density parameter 'a' is taken as $A/11$ for compound nucleus and $A/7$ for fission fragments [96]. T_{pre} is scaled down by a factor of $11/12$ to account for multi-step evaporation [96, 208, 209]. Thus, T_{pre} and T_{post} values are calculated to be 1.2 and 1.25 MeV for ^{11}B $+$ ^{232}Th system and 1.18 and 1.25 MeV for ^{12}C $+$ ^{232}Th system, respectively.

4.3.2   Near-scission component

Near scission emission takes place dominantly perpendicular to the scission axis [77] and peaks at an energy in-between the compound nucleus emission and fragment emission peaks. The energy and angular distributions for NSE are assumed to be Gaussian in the rest frame as given by the expression [96];

$$n(\epsilon, \theta) = N_{\mathrm{nse}} \alpha_{\mathrm{nse}} \exp \left[\frac{-(\epsilon - \epsilon_p)^2}{2\sigma_\epsilon^2} \right] \exp \left[\frac{-(90° - \theta)^2}{2\sigma_\theta^2} \right], \qquad (4.8)$$

where ϵ, α_{nse}, ϵ_p, θ, σ_ϵ, and σ_θ are the α-particle multiplicity of near scission emission, peak (or mean) energy, relative angle of α-particles with respect to the scission axis, standard deviations of the energy, and the angular distributions, respectively, in the rest frame. The N_{nse} is the normalization constant.

The α-particle spectra calculated in rest frames of four sources are converted to laboratory frames using the appropriate Jacobians and finally summed up to fit the measured spectra. In the moving-source fit, the parameters T_{pre}, T_{post}, V_B^{pre}, and V_B^{post} are not varied whereas the prescission and postscission multiplicities (α_{pre} and α_{post}) and parameters related to NSE, are kept as free parameters. The mean fragment velocities are determined using Viola's systematics [105] for the total kinetic energy released in fission process.
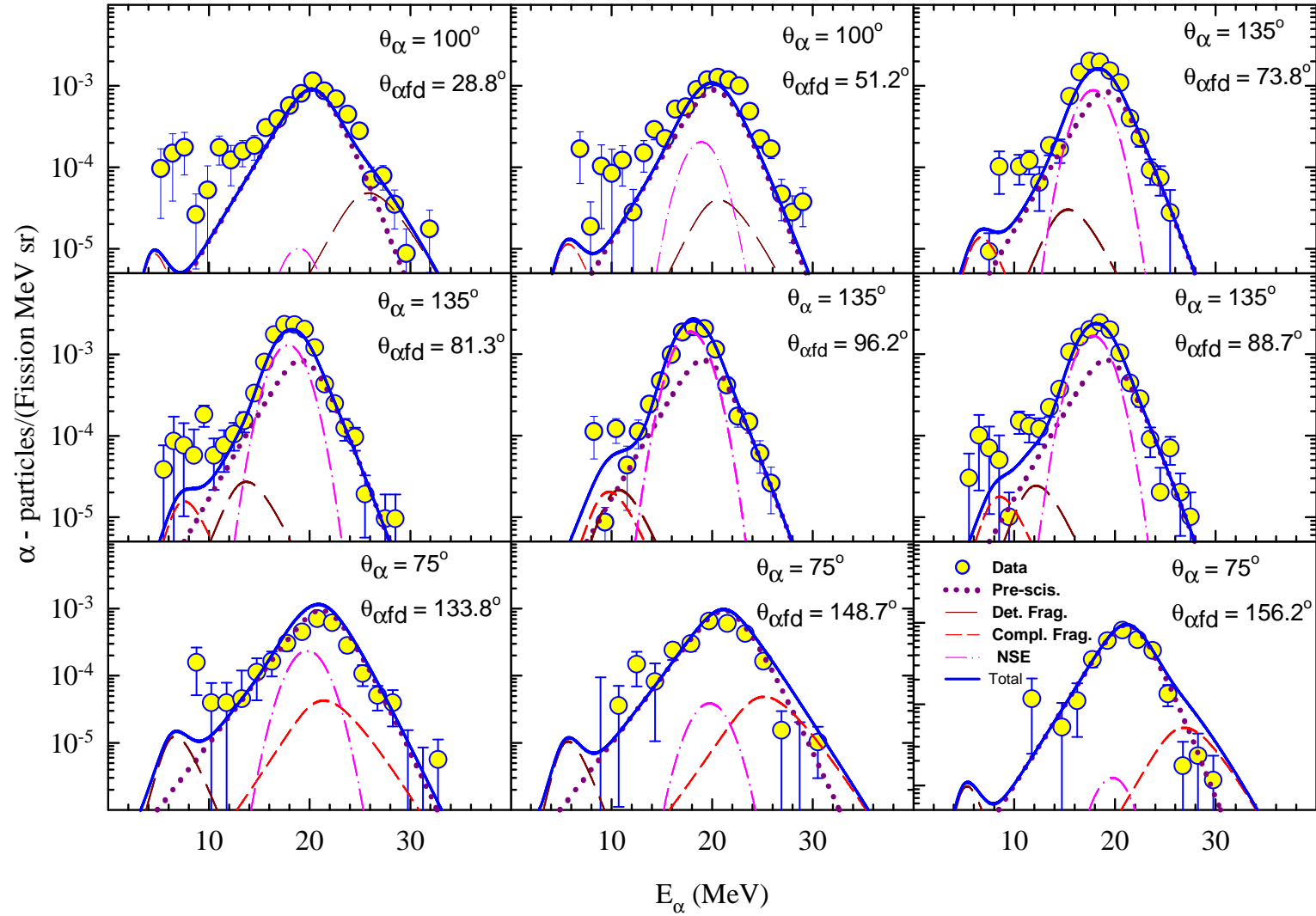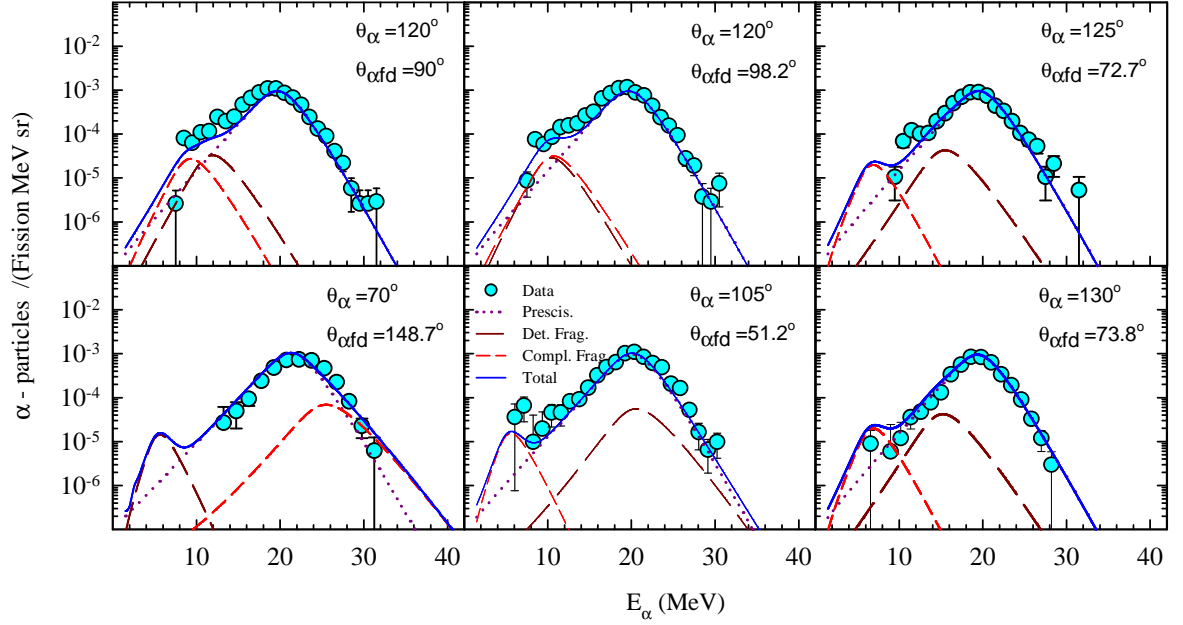
Figure 4.15: The α-particle multiplicity spectra in ^{11}B + ^{232}Th reaction along with fits of moving-source model for different combination of laboratory angles of CsI(Tl) detectors with respect to beam direction, θ_α and detected fission fragments, $\theta_{\alpha fd}$. The dotted, long-dashed, and short-dashed, are contributions from compound nucleus, detected fission fragment, and complementary fission fragment, respectively. The solid curve indicates the total contribution from three sources.

4.4   Results and discussion

For ^{11}B + ^{232}Th system, the fitted spectra for the individual source and after summing are shown in Fig. 4.12. The values of the parameters corresponding to the best fit are found to be $\alpha_{\text{pre}} = (5.2 \pm 0.1) \times 10^{-3}$, $\alpha_{\text{post}} = (0.17 \pm 0.02) \times 10^{-3}$, $\alpha_{\text{nse}} = (0.5 \pm 0.05) \times 10^{-3}$, $\epsilon_p = 19.3 \pm 0.3$ MeV, $\sigma_\epsilon = 3.4 \pm 0.2$ MeV, and $\sigma_\theta = 11.5° \pm 1.6°$ having a minimum χ^2/(degree of freedom) value of 5.07. Fits, for ^{11}B + ^{232}Th system are also obtained by excluding the NSE component in the moving-source model, the fitted spectra for the individual source and after summing are shown in Fig. 4.15 for typically 6 of 24 combinations of θ_α and $\theta_{\alpha fd}$. The best-fitted values are $\alpha_{\text{pre}} = (5.8 \pm 0.1) \times 10^{-3}$ and $\alpha_{\text{post}} = (0.16 \pm 0.02) \times 10^{-3}$, corresponding to minimum χ^2/(degree of freedom) value of 6.1. Here the errors quoted in the extracted parameters include only statistical uncertainties. It is seen that fitting quality of the spectra improves

Table 4.2: α-particle multiplicities corresponding to different emission stages for both the systems. The temperatures, emission barriers, and parameters related to near-scission emission are also given.

Parameter	^{11}B + ^{232}Th	^{12}C + ^{232}Th.
E_{CN} (MeV)	45.5	42.8
T_{pre} (MeV)	1.2	1.18
T_{post} (MeV)	1.25	1.25
V_B^{pre} (MeV)	20.2	20.3
V_B^{post} (MeV)	13.4	13.5
α_{pre}	$(5.2 \pm 0.1) \times 10^{-3}$	$(5.4 \pm 0.2) \times 10^{-3}$
α_{post}	$(0.17 \pm 0.02) \times 10^{-3}$	$(0.13 \pm 0.04) \times 10^{-3}$
α_{nse}	$(0.5 \pm 0.05) \times 10^{-3}$	$(3.1 \pm 0.2) \times 10^{-3}$
ϵ_p (MeV)	19.3 ± 0.3	19.25 ± 0.10
σ_ϵ (MeV)	3.4 ± 0.2	1.66 ± 0.10
σ_θ	$11.5° \pm 1.6°$	$17.9° \pm 1.1°$

particularly for $\theta_{\alpha fd} \sim 90°$ if the NSE component is included in the moving-source model. It should be noted here that in contrast to the works by Wilczynska *et al.* [132] for ^{40}Ar + ^{232}Th and Lindl *et al.* for ^{37}Cl + ^{124}Sn and ^{28}Si + ^{141}Pr systems [129], in the ^{11}B + ^{232}Th reaction the small value of α_{nse} and closeness of peak energies of prescission and near-scission emission do not make the spectral shapes of $\theta_{\alpha fd} \sim 90°$ differ very much from those which are away from $\theta_{\alpha fd} = 90°$.

For ^{12}C + ^{232}Th system, the fitted spectra for the individual source and after summing are shown in Fig. 4.13 for 9 out 12 combinations of θ_α and $\theta_{\alpha fd}$. The best fitted values of the parameters are found to be $\alpha_{\mathrm{pre}} = (5.4 \pm 0.2) \times 10^{-3}$, $\alpha_{\mathrm{post}} = (0.13 \pm 0.04) \times 10^{-3}$, $\alpha_{\mathrm{nse}} = (3.1 \pm 0.2) \times 10^{-3}$, $\epsilon_p = 19.25 \pm 0.10$ MeV, $\sigma_\epsilon = 1.66 \pm 0.10$ MeV, and $\sigma_\theta = 17.9° \pm 1.1°$ corresponding to a minimum $\chi^2/(\text{degree of freedom})$ value of 3.71. The results obtained from four-source analysis for ^{11}B + ^{232}Th and ^{12}C + ^{232}Th systems are shown in the Table 4.2. The α_{pre} and α_{post} values for both the systems are similar, whereas the NSE multiplicity for ^{12}C + ^{232}Th system is significantly larger than

^{11}B + ^{232}Th system having similar fissility, excitation energy, and angular momentum. Extracted standard deviations for energy and angular distributions of the near-scission emission (σ_ϵ and σ_θ) are also observed to be significantly different for both the systems. These observations indicate that due to α-cluster structure of ^{12}C there is an admixture of some other source of α-particle emission to the NSE component in the ^{12}C + ^{232}Th reaction apart from earlier mentioned four conventional sources involved in the fusion-fission process.

In the next chapter, an attempt made to reproduce the prescission multiplicities using the statistical model codes, will be discussed. Further, the prescission and near-scission data from ^{11}B + ^{232}Th system has been analyzed along with the literature data to develop certain global features of the prescission and near-scission emission characteristics. The anomalous results obtained above for ^{12}C + ^{232}Th reaction are then compared with systematics which provide more strong clue to understand these puzzling results.

Chapter 5

Systematics of prescission and near-scission α-particle multiplicities

5.1 Statistical model calculations for prescission α-particle multiplicity

In the past, statistical model calculations with the inclusion of fission delay have been carried out to reproduce measured values of prescission neutron (ν_{pre}) and α-particle (α_{pre}) multiplicities for various systems. In order to quantitatively understand the α_{pre} values determined for the ^{11}B + ^{232}Th and ^{12}C + ^{232}Th systems, we have used the statistical model code JOANNE2 [110] which incorporates the deformation-dependent particle binding energies and transmission coefficients. Prescission emission is assumed to take place from two stages in the deformation space corresponding to mean pre-saddle deformation (Z_{tr}) and mean saddle-to-scission deformation (Z_{ssc}). The JOANNE2 code allows only particle emission from nearly spherical systems for mean pre-saddle time (τ_{tr}) and then allows fission decay to compete with particle emission for mean saddle-to-scission time (τ_{ssc}). It is seen for the present systems that for a fixed fission delay the particle multiplicities are insensitive to Z_{tr}, but very much sensitive to Z_{ssc}. Fig. 5.1 shows the deformation energy diagram for ^{11}B + ^{232}Th system in terms of the simplified rotating liquid drop model incorporated in the code JOANNE2. The deforma-
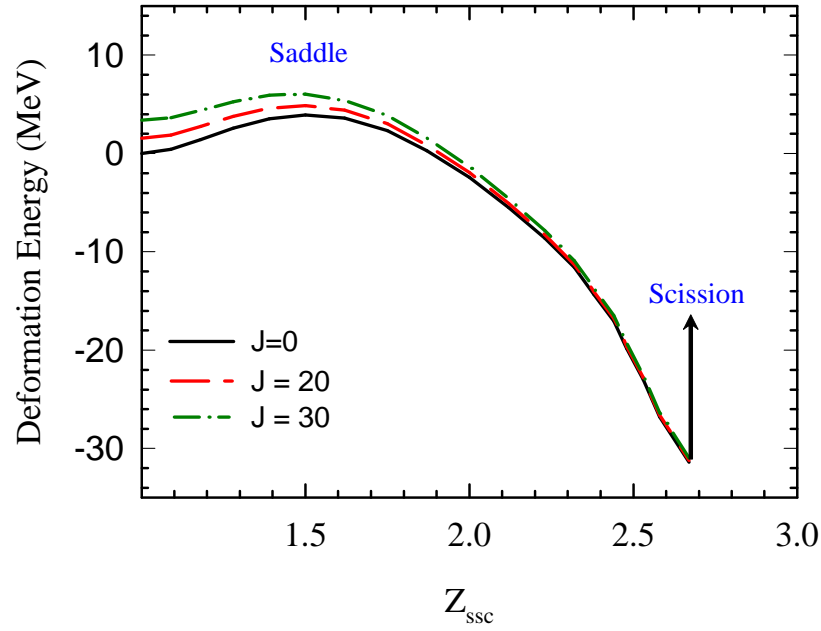
Figure 5.1: Deformation energy plot for ^{11}B + ^{232}Th system at compound nucleus angular momentum, $J = 0$, 20, and 30 $\hbar$.

tion energy curve for ^{12}C + ^{232}Th system is observed to be similar to that of ^{11}B + ^{232}Th system. It can be seen from Fig. 5.1 that the saddle-to-scission emission can be considered with Z_{SSC} values in the range of 1.5 to 2.7 for both the systems.

It is seen that due to deformation the mean kinetic energies of the prescission particles change in a dramatic manner [110]. Fig. 5.2(a) (from Ref. [110]), shows the change in mean kinetic energies of neutrons, protons, and α particles as a function of elongation Z_{axis} (in units of diameter of the spherical system) relative to the emission from spherical nuclei for ^{195}Pb with J=0 and excitation energy of 50 MeV. The small changes in the mean neutron energy is due to the dependence of the deformation energy on Z_{axis}. The initial decrease in the mean kinetic energies of the light charged particles is mainly due to the change in transmission coefficients due to deformation (lowering of the emission barriers). The increase above $Z_{axis} \sim 2.2$ is due to the rapid rise in the thermal excitation energy as the scission point is approached. Reduction in effective emission barriers of proton and α-particle should give rise an enhancement in the charged particle emission relative to the neutron. But, at the same time charged
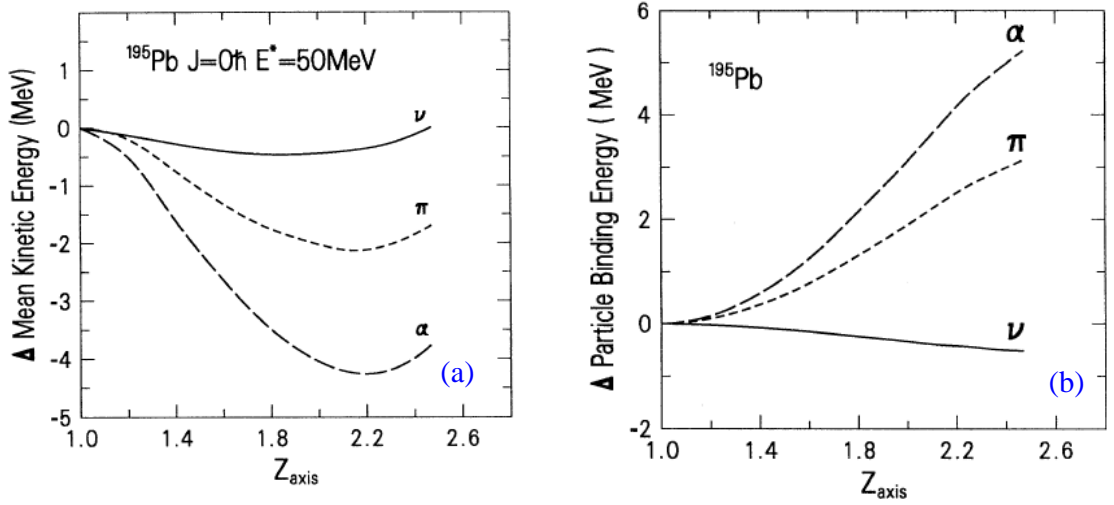
Figure 5.2: Change in mean kinetic energies [in panel (a)] and binding energies [in panel (b)] of neutrons, protons, and α particles as a function of elongation Z_{axis} (in units of diameter of the spherical system) relative to the emission from spherical nuclei for ^{195}Pb with $J=0$ and excitation energy of 50 MeV, from Ref. [110]

particle binding energies are altered quite significantly as a function of deformation as shown in the Fig. 5.2(b) (from Ref. [110]). The neutron binding energies decreases slightly whereas the proton and α-particle binding energies increase dramatically with deformation [110]. Such behavior is expected, since for a fixed deformation the removal of charge causes a rapid increase in the nuclear deformation energy, while removal of neutron causes a slight decrease. Thus, the increase in the binding energy of charged particles causes a suppression of the proton and α-particle emission which otherwise could have been more due to lower emission barriers.

JOANNE2 calculations are carried out by varying either Z_{ssc} or τ_{ssc} to examine its effect on ν_{pre} and α_{pre}. The value of Z_{tr} is fixed at 1.28 for both the systems. The value of τ_{tr} is fixed at 20 zs (1 zs = 10^{-21} s) from the systematics available in the literature [88]. In the first case, the ν_{pre} and α_{pre} values are calculated as a function of Z_{ssc} at a fixed value of $\tau_{ssc} = 100$ zs. The level-density parameters for spherical compound nucleus a_n and for the saddle-to-scission stage a_{ssc} at each Z_{ssc}, are calculated within the code using the formalism of Toke and Swiatecki [210]. For both the systems, it is
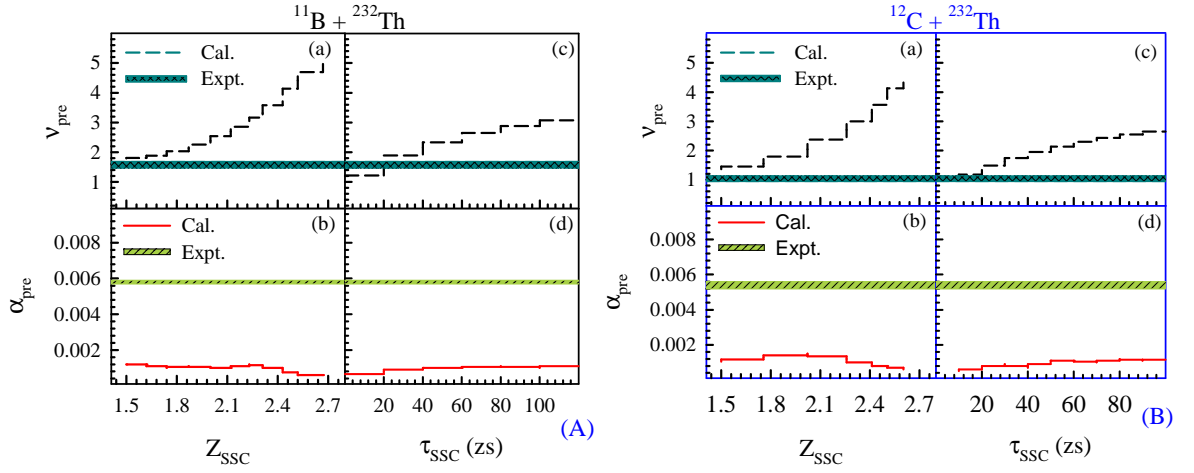
Figure 5.3: The ν_{pre} and α_{pre} calculated using the code JOANNE2 as a function of Z_{SSC} [panels (a) and (b)] and τ_{SSC} [panels (c) and(d)] for the ^{11}B $+^{232}$Th and ^{12}C $+$ ^{232}Th systems [in (A) and (B)]. The shaded regions in all the panels represent the corresponding experimental values of ν_{pre} and α_{pre}. The experimental ν_{pre} values are taken from literature (see text).

seen that ν_{pre} increases strongly with Z_{ssc} whereas α_{pre} increases mildly up to a certain value of Z_{ssc} and then decreases as shown in the panels (a) and (b) of Figs. 5.3(A) and 5.3(B) for the ^{11}B $+$ ^{232}Th and ^{12}C $+$ ^{232}Th systems. In the second case the ν_{pre} and α_{pre} values are calculated as a function of τ_{ssc} at a fixed value of $Z_{ssc} = 2.23$ where α_{pre} is maximum [panel (b) of Figs. 5.3(A) and (B)]. The calculated ν_{pre} shows a strong increase with τ_{ssc} whereas the α_{pre} increases very little initially and saturates at τ_{ssc} $\sim$50 zs as shown in in the panels (c) and (d) of Figs. 5.3(A) and 5.3(B). The shaded regions in all the panels of Fig. 5.3 represent the corresponding experimental values. The experimental ν_{pre} in in the panels (a) and (c) of Figs. 5.3(A) and 5.3(B) have been obtained after scaling the experimental data of Ref. [88] at different excitation energies to corresponding to the present ones in ^{11}B $+$ ^{232}Th and ^{12}C $+$ ^{232}Th reactions. As seen from panels (a) and (c) of Figs. 5.3(A) and 5.3(B), the experimental ν_{pre} is reproduced with statistical model calculation using the code JOANNE2 for a suitable set of input parameters but the experimental α_{pre} can not be reproduced by any choice of the input parameters [panels (b) and (d) of Figs. 5.3(A) and 5.3(B)]. Statistical model calculations using the code PACE2 [136] including fission delay are also carried
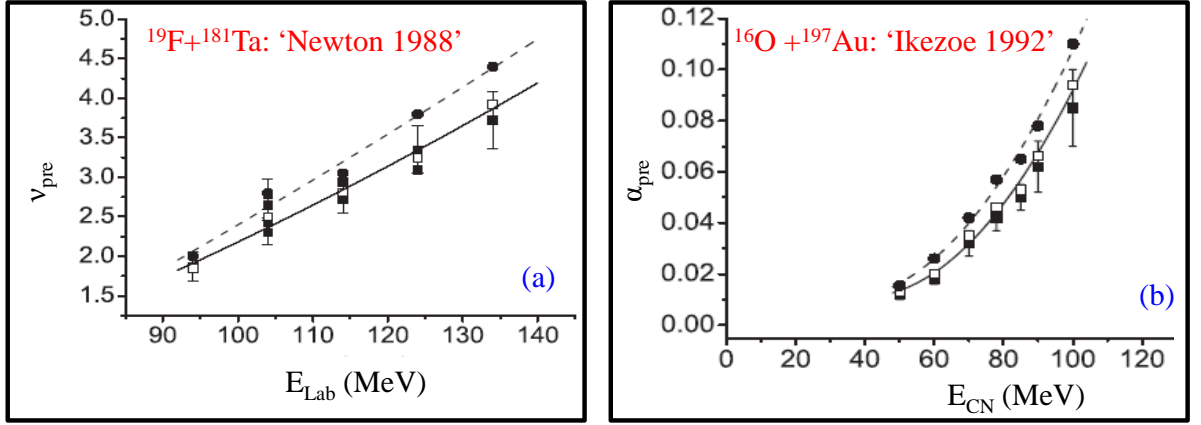
Figure 5.4: Experimental prescission neutron [ν_{pre} in (a)] and α-particle [α_{pre} in (b)] multiplicities as a function of beam/excitation energies from Ref. [128]. The filled squares show experimental data for ν_{pre} and α_{pre} from Refs. [212] and [98], respectively. Filled circles and open squares represent theoretical calculations based on one- and three-dimensional Langevin approaches [128], respectively.

out and results are similar to that obtained with JOANNE2. Similar difficulty of not reproducing simultaneously experimental ν_{pre} and α_{pre} by a statistical model code has been reported earlier also for ^{28}Si + ^{232}Th system [211].

5.2   Systematics of prescission α-particle multiplicity

The α_{pre} values measured earlier in many heavy-ion induced fusion-fission reactions are observed to increase non linearly with excitation energy of the compound nucleus (E_{CN}) [98], whereas the prescission neutron multiplicity, ν_{pre} varies almost linearly as a function of excitation energy [88, 212]. Figs. 5.4(a) and (b) show experimental prescission neutron (from Ref. [212]) and α-particle (from Ref. [98]) multiplicities as a function of beam/excitation energies for two typical target-projectile systems. In the Figs. 5.4(a) and (b), filled circles and open squares represent theoretical calculations based on one- and three-dimensional Langevin approaches [128], respectively. Thus, Langevin calculations are consistent with experimental observations for ν_{pre} and α_{pre}. In order to further verify these apparent differences in the behavior of ν_{pre} and α_{pre} as a
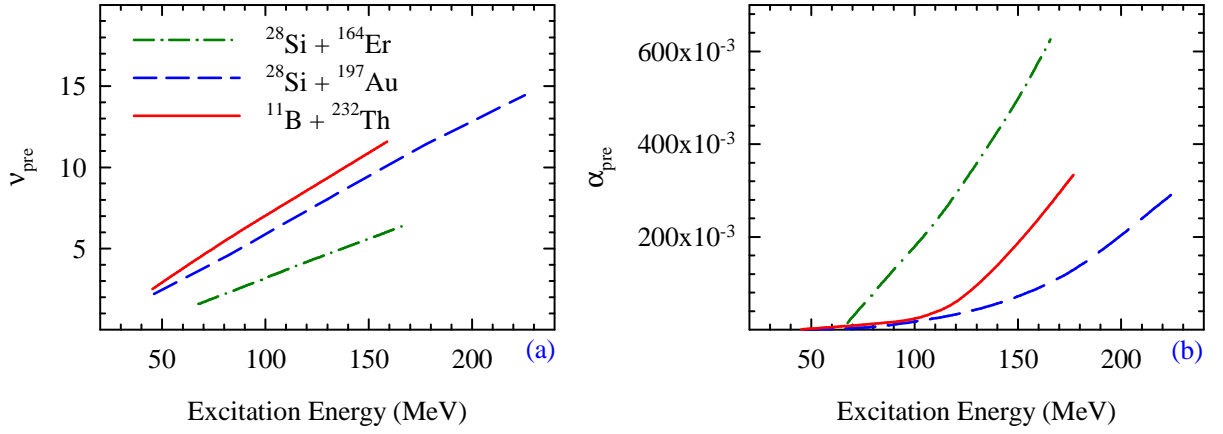
Figure 5.5: JOANNE2 [110] calculated prescission neutron (ν_{pre} in (a)) and α-particle (α_{pre} in (b)) multiplicities as a function of excitation energy.

function of E_{CN}, statistical model calculations were carried out using the code JOANNE2 for many target-projectile systems. Figs. 5.5(a) and (b) show JOANNE2 calculated prescission neutron (ν_{pre}) and α-particle multiplicities as a function of excitation energy at $\tau_{tr} = 20$ zs and $\tau_{ssc} = 60$ zs for three typical reactions. It is seen from Figs. 5.5(a) and (b) that with increasing compound nuclear mass, ν_{pre} dominates over α_{pre} and at a given excitation energy ν_{pre} is larger for heavier system. This behavior of ν_{pre} is attributed to the larger N/Z ratio with increasing compound nuclear mass which makes the neutron emission favorable over charged particle emission. The α_{pre} values are order of magnitude smaller than the ν_{pre}. It is seen from Fig. 5.5 (b) that the order of non-linearity of α_{pre} with excitation energy increases as the mass of the compound nuclear system increases. This dramatically different behavior of prescission α-particle emission in comparison to neutron, may be due to: (i) significantly lower decay width for α-particle emission and (ii) with increasing compound nuclear mass the fission decay width increases which further suppress the prescission α-particle emission.

According to statistical theory, for a given particle type the particle emission width is proportional to level-density of residual nucleus, $\rho(U)$, where U is the excitation energy of the residue. $U = E_{\text{CN}} + Q_p - E_k$, where Q_p and E_k are the particle emission Q-value and emitted particle kinetic energy. Thus, for a given E_{CN} and particle type, the
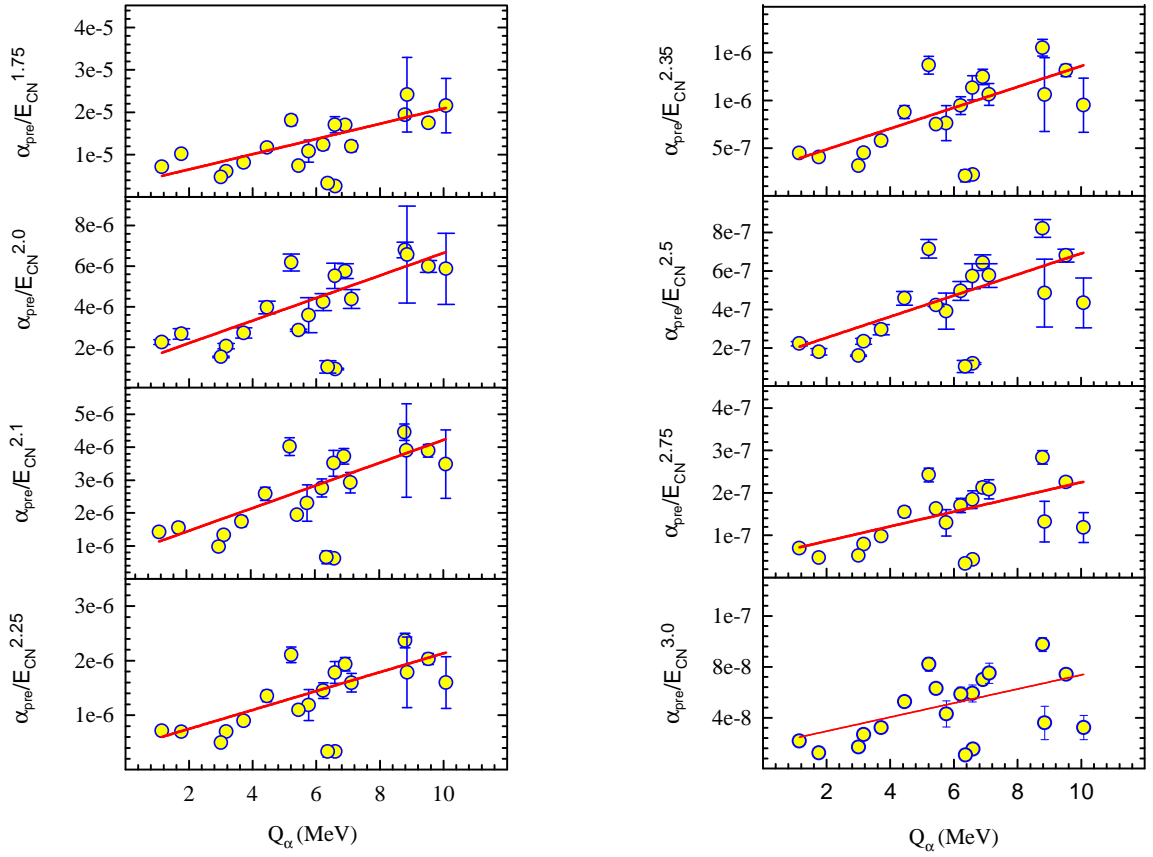
Figure 5.6: Experimental values of α_{pre} normalized with E_{CN}^n for all available data for various systems as a function of α-particle emission Q-value (Q_α) at various values of normalization factor 'n'. Different lines in each curve represent the linear fits.

particle emission width should increase with Q_p. In order to investigate the nonlinear behavior of the α_{pre} as a function of U for a variety of compound nuclear systems, the α-particle emission Q-value (Q_α) seems to be a crucial parameter. It is seen from JOANNE2 calculations that the α_{pre} increases non linearly with excitation energy as $E_{\text{CN}}^{1.5}$ to $E_{\text{CN}}^{3.5}$ in going from compound nuclear mass number 150 to 270. Therefore, with a proper scaling of α_{pre} by a certain power of E_{CN}, it is possible to obtain a systematic behavior with respect to α-particle emission Q-value for different target-projectile systems leading to a wide variety of compound nuclei.

The experimental values of α_{pre} normalized with E_{CN}^n for all available data for various systems are plotted as a function of α-particle emission Q-value (Q_α) at different values of n in the range of 1.0 to 3.5 as shown in the Fig. 5.6 for some typical values
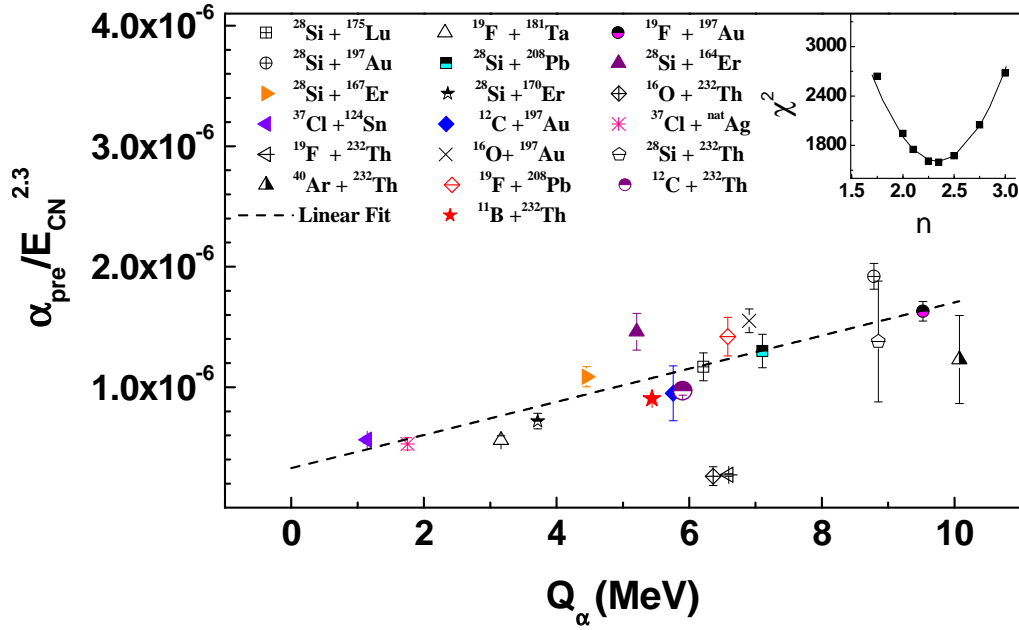
Figure 5.7: The α_{pre} normalized with $E_{\mathrm{CN}}^{2.3}$ (E_{CN} is the compound nucleus excitation energy) as a function of α-particle emission Q-value (Q_α) for ^{11}B, ^{12}C + ^{232}Th systems and the available data from literature for following systems: ^{28}Si + ^{175}Lu [96], ^{28}Si + ^{164,167,170}Er [97], ^{37}Cl + ^{124}Sn [129], ^{37}Cl + ^{nat}Ag [131], ^{40}Ar + ^{232}Th [132], ^{19}F + ^{232}Th [203], and ^{28}Si + ^{232}Th [211]. Data for ^{28}Si + ^{197}Au, ^{28}Si + ^{208}Pb, ^{19}F + ^{197}Au, ^{19}F + ^{208}Pb, ^{16}O + ^{197}Au, and ^{19}F + ^{197}Ta are from Ref. [98] and for ^{16}O + ^{232}Th and ^{12}C + ^{197}Au are from Ref. [130]. The dashed line is a linear fit to the data. The inset shows the parabolic variation of χ^2 with the excitation energy normalization factor n (see text).

of n. For each value of n, the normalized α_{pre} shows a linearly increasing trend with Q_α. In order to determine the best power dependence of α_{pre} on E_{CN}, the χ^2 value is determined for each n, by comparing the data for normalized α_{pre} as a function of Q_α with the best linear-fit to the data. The variation of χ^2 with n is obtained to be parabolic from where the best fit value of n is obtained as 2.3 ± 0.1 (as shown in the inset of Fig. 5.7). Therefore, in order to compare the α_{pre} values for various systems we have normalized the available data on α_{pre} with $E_{\mathrm{CN}}^{2.3}$. The spread in α_{pre} data after normalizing with $E_{\mathrm{CN}}^{2.3}$ for a given system is observed to be within the error bars in cases where, α_{pre} data are available as a function of E_{CN} [97, 98, 129, 203]. In these cases a weighted average of the normalized α_{pre} values of a given system is taken to investigate the dependence of α_{pre} on Q_α. Figure 5.7 shows the present results for

^{11}B, ^{12}C + ^{232}Th systems and the available data of $\alpha_{\text{pre}}/E_{\text{CN}}^{2.3}$ as a function of Q_α) for various systems. It is observed that the normalized α_{pre} shows a correlation with Q_α and increases linearly. It is interesting to note that the ν_{pre} values show a systematic behavior in terms of fissility after normalizing with E_{CN} [88], whereas α_{pre} shows a systematic behavior in terms of Q_α after normalizing with $E_{\text{CN}}^{2.3}$. However, it would be more relevant to analyze ν_{pre} also in terms of neutron emission Q-value because the same fissility can be achieved for compound nuclei having widely different Q-values for a given particle emission.

5.3 Systematics of near-scission multiplicity

For ^{12}C + ^{232}Th system the value of α_{nse} appears anomalously enhanced in comparison to the ^{11}B + ^{232}Th system. Due to α-cluster structure of ^{12}C, in addition to the four conventional sources, there may be an extra source of α-particle emission in ^{12}C + ^{232}Th reaction. Therefore, the α_{nse} determined in the ^{11}B + ^{232}Th reaction is first analyzed with all available data from low energy as well as the heavy-ion fission. It is seen that the value of α_{nse} in the ^{11}B + ^{232}Th reaction at $E_{\text{CN}} = 45.5$ MeV is significantly lower than the systematics with respect to Z^2/A and Q_α for low-excitation-energy fission as shown in the Fig. 5.8(a) and (b), respectively. The linear increase of α_{nse} with Z^2/A in low excitation energy fission is consistent with liquid drop model calculations for dynamical emission of α-particles near the scission configuration as the gain in potential energy from saddle-to-scission increases with Z^2/A [78, 112]. Since the Q_α also increases with Z^2/A, the α_{nse} values in low excitation energy fission appears to be increasing with Q_α. The α_{nse} determined in the ^{11}B + ^{232}Th reaction is compared with heavy-ion data available in literature as shown in the Fig. 5.9. It is seen that the α_{nse} from heavy-ion fission data does not exhibit any systematic behavior. In heavy-ion induced fusion-fission reactions it has been observed that α_{nse} increases quite significantly with excitation energy [97, 130] in contrast to low excitation energy
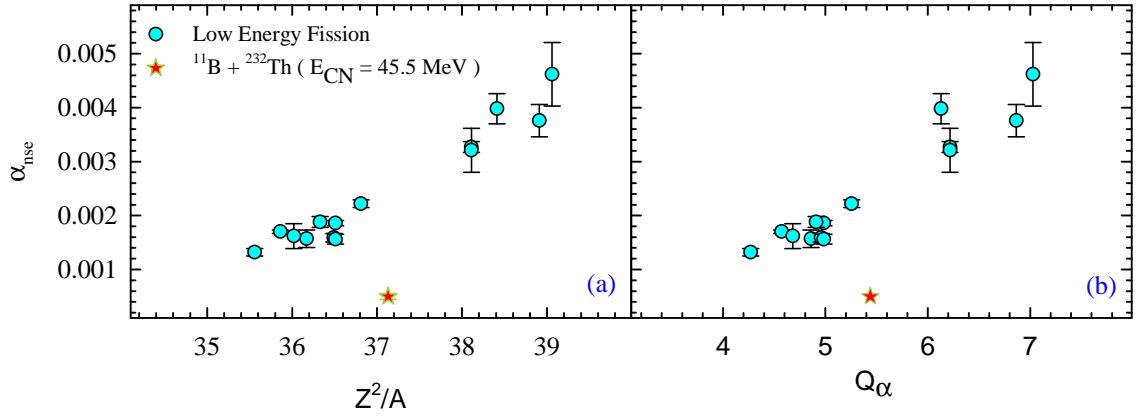
Figure 5.8: Near-scission α-particle multiplicity as a function of Z^2/A (a) and Q_α (b) from low energy fission and ^{11}B + ^{232}Th reaction.

fission where dependence of the α_{nse} on excitation energy in the range of 8 to 20 MeV is quite weak [78]. The peak energy for NSE α-particles (ϵ_p) in low energy fission is constant within 15 to 16 MeV whereas in heavy-ion-induced fission it is scattered from 12.5 to 19.5 MeV for different systems [96, 97, 129–132] as shown in the Fig. 5.10. These comparisons about the features of NSE indicate that the near-scission emission mechanism in heavy-ion-induced fission differs from low-excitation-energy fission.

In order to understand the near scission emission mechanism in heavy-ion fusion-fission process, the ratio of α_{nse} to total pre-scission α-particle multiplicity ($\alpha_{\text{pre}}+\alpha_{\text{nse}}$) is calculated for the ^{11}B + ^{232}Th system and other heavy-ion data from literature. The fractional α_{nse} for the ^{11}B + ^{232}Th system is determined to be $(8.6 \pm 0.2)\%$. The fractional α_{nse} for all available systems is plotted as a function of Z^2/A as shown in Fig. 5.11 where vertical spread in some cases corresponds to different excitation energies of a given system. It is seen that fractional α_{nse} is nearly same at around 10% of the total prescission multiplicity over a wide range of Z^2/A and excitation energy, as indicated with dashed lines in Fig. 5.11. The results for ^{16}O + ^{232}Th on α_{nse} as well as α_{pre} (as seen in the Fig. 5.7) are quite off from the average behavior, and may be due to inaccurate determination of the different components of the α-particle multiplicity. The insensitivity of α_{nse} with Z^2/A has been seen earlier also by Sowinski *et al.* [130] for two
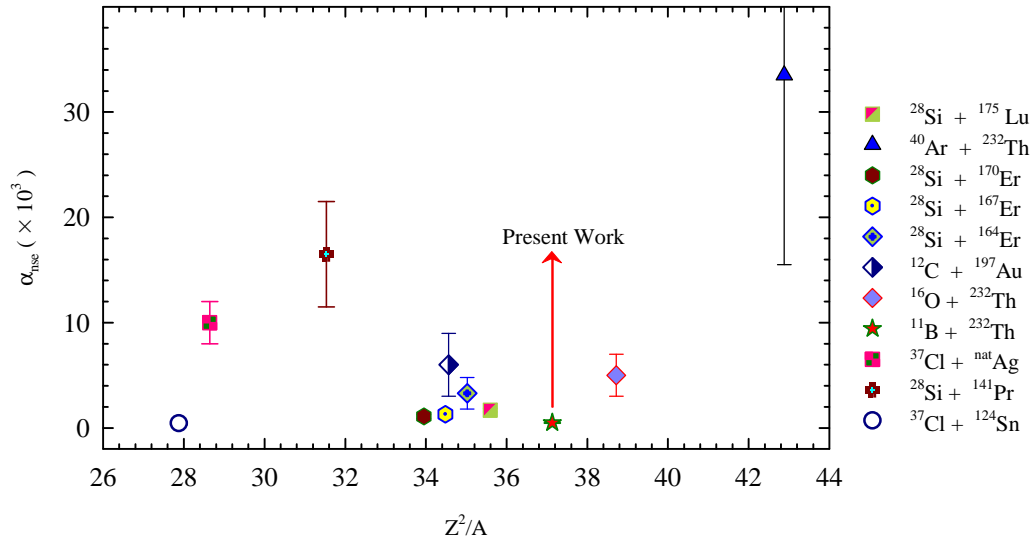
Figure 5.9: Near-scission multiplicity from ^{11}B + ^{232}Th and other heavy-ion data from literature as a function of Z^2/A (a). The different data points are for following systems: ^{28}Si + ^{175}Lu [96], ^{28}Si + ^{164,167,170}Er at beam energy of 155 MeV [97], ^{37}Cl + ^{nat}Ag [131], and ^{40}Ar + ^{232}Th [132]. Data for ^{37}Cl + ^{124}Sn and ^{28}Si + ^{141}Pr are from Ref. [129] and for ^{16}O + ^{232}Th and ^{12}C + ^{197}Au are from Ref. [130].
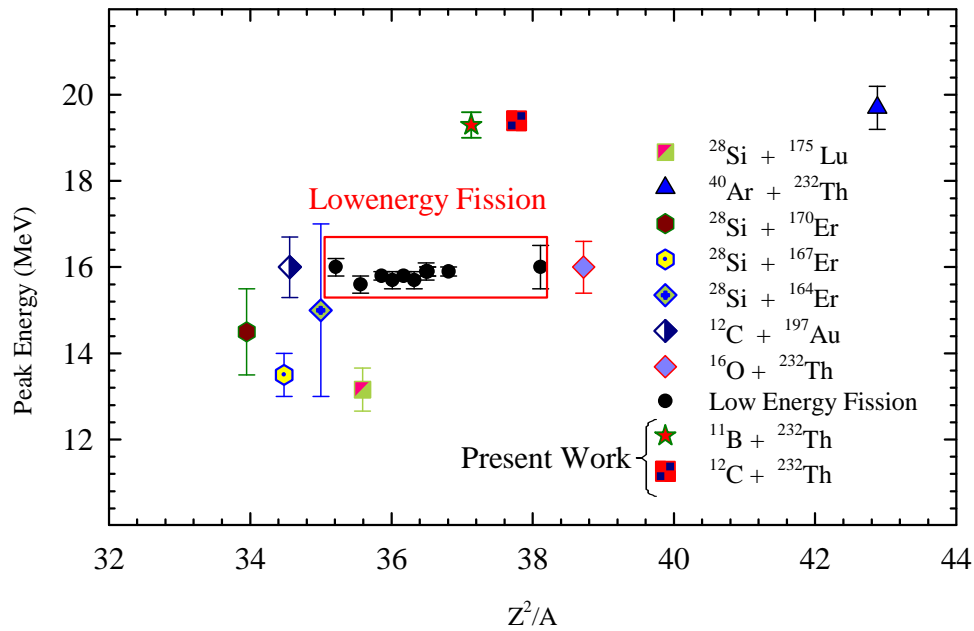
Figure 5.10: Near-scission peak energy in the present reactions and all available data from literature as a function of Z^2/A (a). The different data points are from the same references as in the Fig. 5.9.
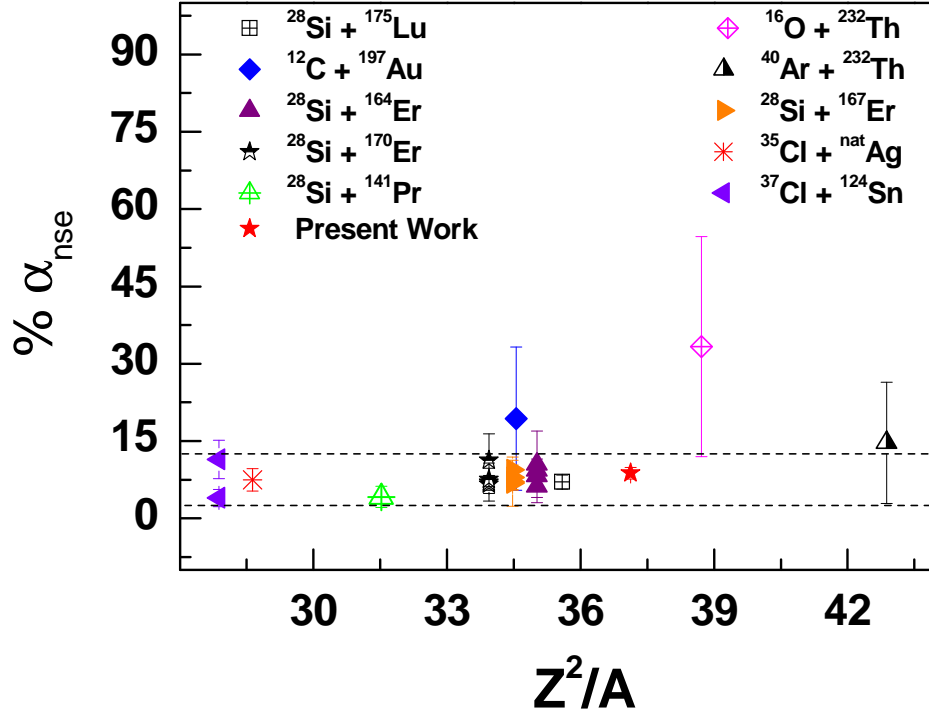
Figure 5.11: The % α_{nse} as a function of Z^2/A of the fissioning system. The different data points are for following systems: ^{28}Si + ^{175}Lu [96], ^{28}Si + ^{164,167,170}Er [97], ^{37}Cl + ^{nat}Ag [131], and ^{40}Ar + ^{232}Th [132]. Data for ^{37}Cl + ^{124}Sn and ^{28}Si + ^{141}Pr are from Ref. [129] and for ^{16}O + ^{232}Th and ^{12}C + ^{197}Au are from Ref. [130]. The vertical spread in some cases corresponds to different excitation energies of a given system. The dashed lines are shown to guide the eye.

projectile-target systems having widely different Z^2/A values. These features of α_{nse} in heavy-ion fission indicate that α-particles emitted from neck region near the scission point are due to statistical emission process in contrast to low energy fission where it is a pure dynamical process. It seems that as the available excitation energy increases, statistical emission dominates over dynamical emission. This indicates that the neck collapse is faster in the case of low-energy or spontaneous fission case [111] whereas at higher excitation energies, it is a slow process. It may, therefore, be inferred that the scission (or neck rupture) process exhibits a change over from a super-fluid to viscous nature as the excitation energy is increased. In literature it has been conclusively established that the α_{nse} in thermal or 1-MeV neutron induced fission (corresponding E_{CN} = 6 - 8 MeV) is less than in spontaneous fission of the same fissioning nuclei

[122–124] which is also in favor of the above arguments.

It should be noted here that in spontaneous and thermal neutron induced fission, a considerable amount of energy dissipation during the descent from saddle-to-scission has been observed. In particular, the neutrons and γ rays emitted from the fragments provide the clear signature of the energy dissipation in low-excitation-energy fission. It seems that in saddle-to-scission region the two-body viscosity is prevailed even at low excitation energies and during the scission process it is the one-body viscosity.

5.4   Anomalous behavior in ^{12}C + ^{232}Th reaction

The α_{pre} value determined in the ^{12}C + ^{232}Th reaction is consistent with the developed heavy-ion systematics [Fig. 5.7], where it is established that α_{pre} values when normalized to $E_{\mathrm{CN}}^{2.3}$ show a linearly increasing trend with α-particle emission Q-value [139]. The NSE multiplicity for the ^{12}C + ^{232}Th system is significantly larger than ^{11}B + ^{232}Th system having similar fissility, excitation energy, and angular momentum for which α_{nse} is $(0.5 \pm 0.05) \times 10^{-3}$ [139]. The fraction of NSE multiplicity (α_{nse}) to total prescission α-particle multiplicity ($\alpha_{\mathrm{pre}} + \alpha_{\mathrm{nse}}$) for the ^{12}C + ^{232}Th system is $\sim 36\%$ which is also significantly off from the systematics [Fig. 5.11], where it is nearly same at around 10% for a variety of compound nuclear systems. In the systematics, it is also seen that ^{12}C + ^{197}Au and ^{16}O + ^{232}Th reactions show somewhat larger average α_{nse}. These observations provide a strong indicator that due to α-cluster structure of ^{12}C there is an admixture of some other source of α-particle emission to the NSE component in the ^{12}C + ^{232}Th reaction apart from earlier mentioned four conventional sources involved in the fusion-fission process.

In order to understand the anomalous behavior in ^{12}C + ^{232}Th reaction, we examine first the two-dimensional particle identification plot of zero crossover versus pulse height from a CsI(Tl) detector at a laboratory angle of $\theta_{\alpha} = 135°$ as shown in Fig. 5.12. Unlike ^{11}B + ^{232}Th reaction, in case of ^{12}C + ^{232}Th reaction, a high energy component
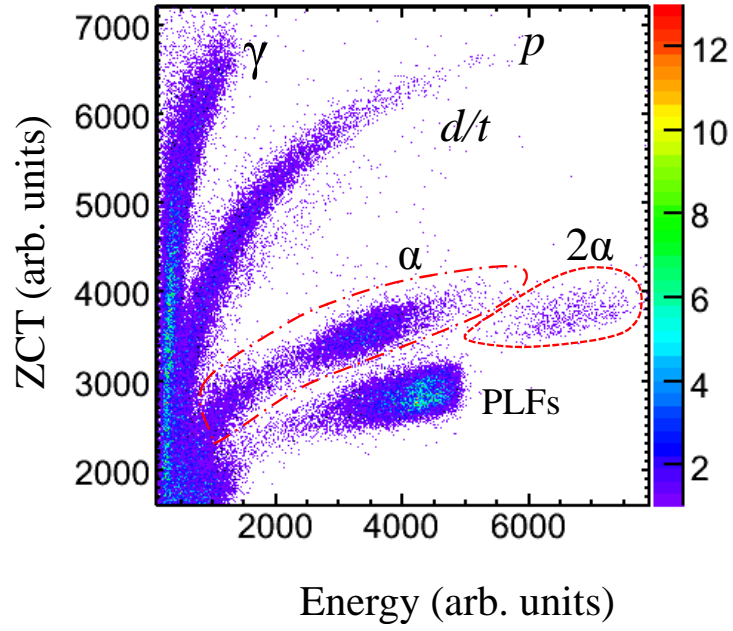
Figure 5.12: A two-dimensional plot of zero crossover (ZCT) versus energy from a CsI(Tl) detector at a laboratory angle of 135° for different particles produced in the ^{12}C (69 MeV) + ^{232}Th reaction.

of varying intensity depending on θ_α is observed along the α-particle band as depicted in the Fig. 5.12. As discussed in the chapter-2, in the case of CsI(Tl) detectors, the rise time for a given particle increases with particle energy [142]. In the present measurement the high energy component is observed to have rise time similar to that for lower energy α particles, suggesting that it is due to the summed energy of two lower energy α particles entering the detector simultaneously.

5.4.1 Source of excess α-particles in ^{12}C + ^{232}Th

The enhanced α_{nse} value in the ^{12}C + ^{232}Th reaction indicates that excess α particles of energies of around 20 MeV are emitted dominantly perpendicular to the detected FF and at backward angles with respect to the beam direction. The observation of the 2α-events as shown in Fig. 5.12, suggests that due to the α-cluster structure of ^{12}C, excess α particles may originate from ^{8}Be breakup following α-transfer induced fission coincidence events as demonstrated in the Fig. 5.13. The folding angle between the
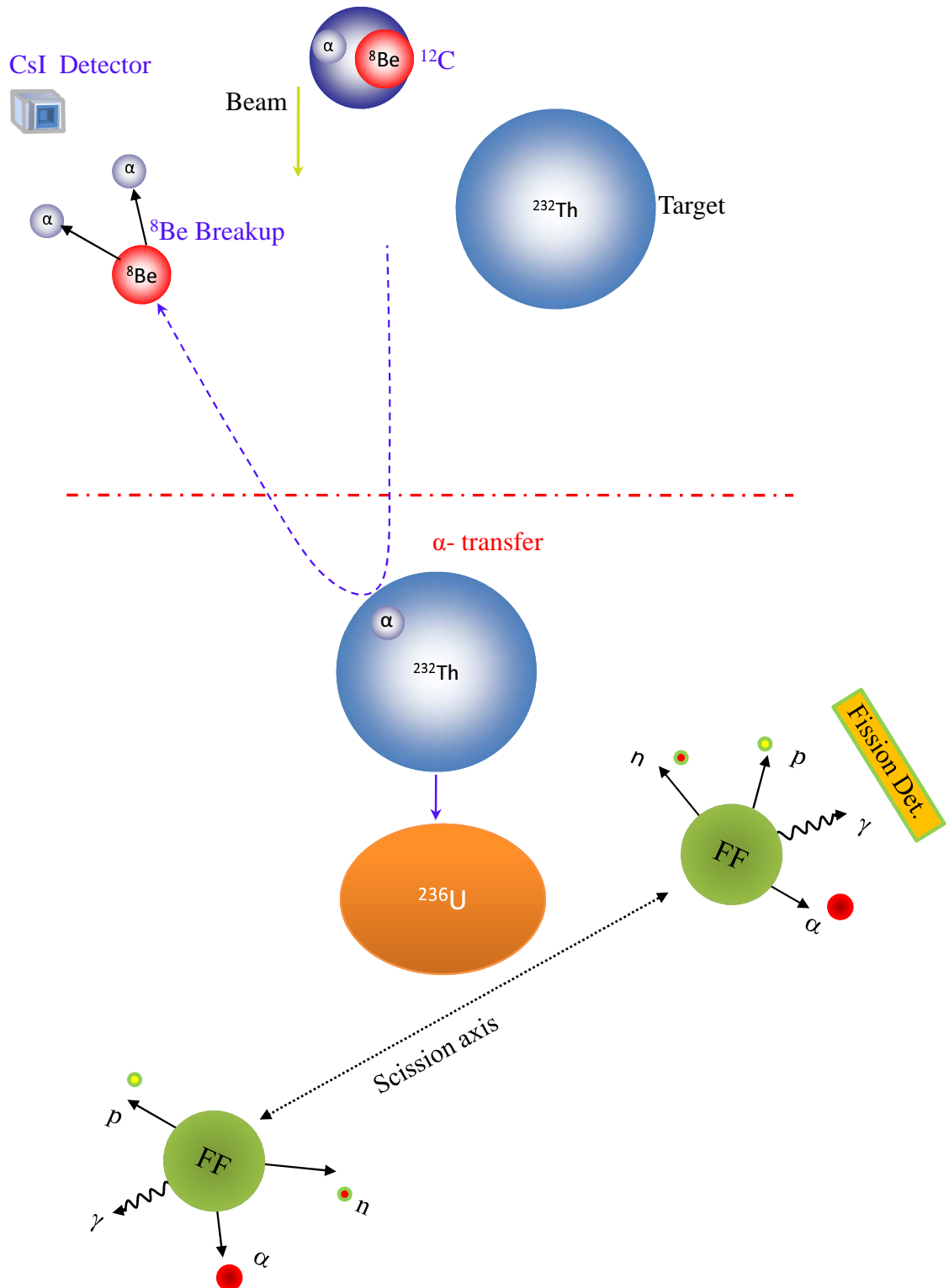
Figure 5.13: Schematic representation of the α-particle emission due transfer-breakup process in ^{12}C + ^{232}Th reaction.
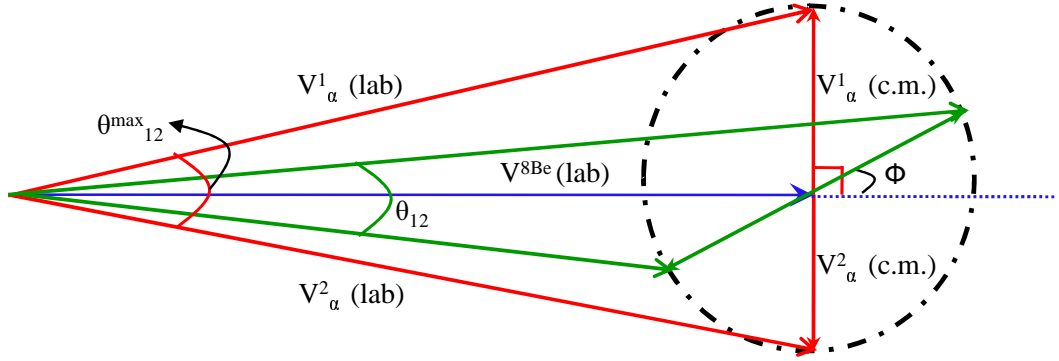
Figure 5.14: Schematic velocity-vector representation of ^{8}Be breakup into two α particles for two center-of-mass angle ϕ of one of the breakup α particles. The θ_{12} is the folding angle between the α particles at a center-of-mass angle ϕ. The θ_{12}^{max} is the maximum folding angle which corresponds to $\phi = 90°$.

two α particles produced from ^{8}Be breakup will depend on their relative energy (E_{rel}) and kinetic energies [213, 214]:

$$\cos\theta_{12} = \frac{E_{\alpha 1} + E_{\alpha 2} - 2E_{rel}}{2\sqrt{E_{\alpha 1}E_{\alpha 2}}}, \qquad (5.1)$$

where $E_{\alpha 1}$ and $E_{\alpha 2}$ are the kinetic energies of the α particles produced from ^{8}Be breakup. E_{rel} is calculated using the relation $E_{rel} = E^* + Q_{BU}$, where E^* is the excitation energy of the state from where breakup occurs and Q_{BU} is the breakup Q-value which is 92 keV [214]. For a given velocity of ^{8}Be (V_{Be}) in the laboratory frame, a schematic vector representation of ^{8}Be breakup into two α particles for two typical center-of-mass angle, ϕ of one of the two breakup α particles is shown in the Fig. 5.14, where θ_{12} is the folding angle between the α particles at an angle ϕ. For kinetic energy of ^{8}Be, $E_{Be} = 38$ MeV, the kinetic energies ($E_{\alpha 1}$ and $E_{\alpha 2}$) and folding angle, θ_{12} of the α particles produced from ^{8}Be breakup as a function of angle ϕ are shown in the Figs. 5.15(a) and (b), respectively at various relative energies, E_{rel}; 92, 200, and 500 keV. At $\phi = 90°$ which corresponds to a maximum folding angle (θ_{12}^{max}), $E_{\alpha 1} = E_{\alpha 2} = (E_{Be} + E_{rel})/2$ and at any angle ϕ, $E_{\alpha 1} + E_{\alpha 2} = E_{Be} + E_{rel}$ as shown in the Fig. 5.15(a). For a given value of E_{Be}, θ_{12} varies from $0°$ to the θ_{12}^{max} depending on E_{rel}. With increasing E_{rel}, the θ_{12}^{max} increases correspondingly as shown in the Fig. 5.15 (b). For instance, for $E_{Be} = 38$ MeV, θ_{12}^{max} varies from $5.5°$ to $12.8°$ in going from $E_{rel} = 92$
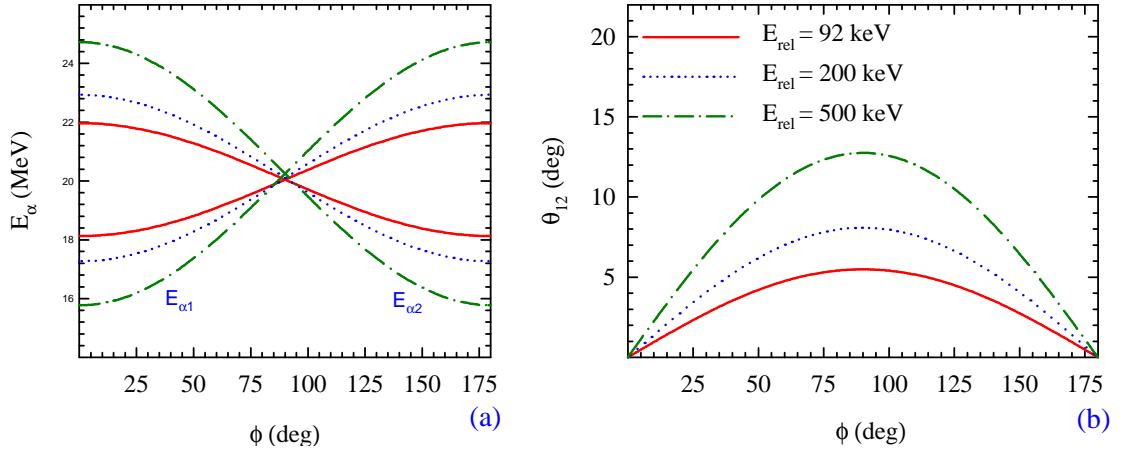
Figure 5.15: Kinetic energies (a) and folding angle, θ_{12} (b) of the α particles produced from ^{8}Be Breakup as a function of center-of-mass angle (ϕ) of one of the two breakup α particles at various relative energies, $E_{\rm rel}$; 92 keV (solid lines), 200 keV(dotted lines), and 500 keV(dash-dot lines).

keV to 500 keV. Therefore, in some of the coincidence events the angular acceptance of each CsI detector ($\pm 3.5°$) allows both the α particles produced from ^{8}Be breakup to reach the detector simultaneously. The high-energy 2α-events shown in Fig. 5.12 correspond to these smaller folding angle events.

5.4.2 2α-particle multiplicity spectra

In order to understand the role of ^{8}Be breakup in the fission observables, the normalized 2α-particle multiplicity spectra in the ^{12}C + ^{232}Th reaction are obtained at first by dividing the 2α-particle coincidence spectra by the total number of fission single events. The normalized 2α-particle multiplicity spectra are shown in Fig. 5.16(a) at three laboratory angles (θ_α). In Fig. 5.16(b), the energy-integrated 2α-yield is shown as a function of θ_α. Earlier, angular distributions of Be transfer products produced in the ^{12}C + ^{232}Th reaction have been measured at the same beam energy as in the present one [5]. Since the angular distribution of Be transfer products peaks around the grazing angle ($\sim 120°$) [5], the angular distribution of 2α-yield is also expected to dominate at similar backward angles. The 2α-yield angular distribution observed in
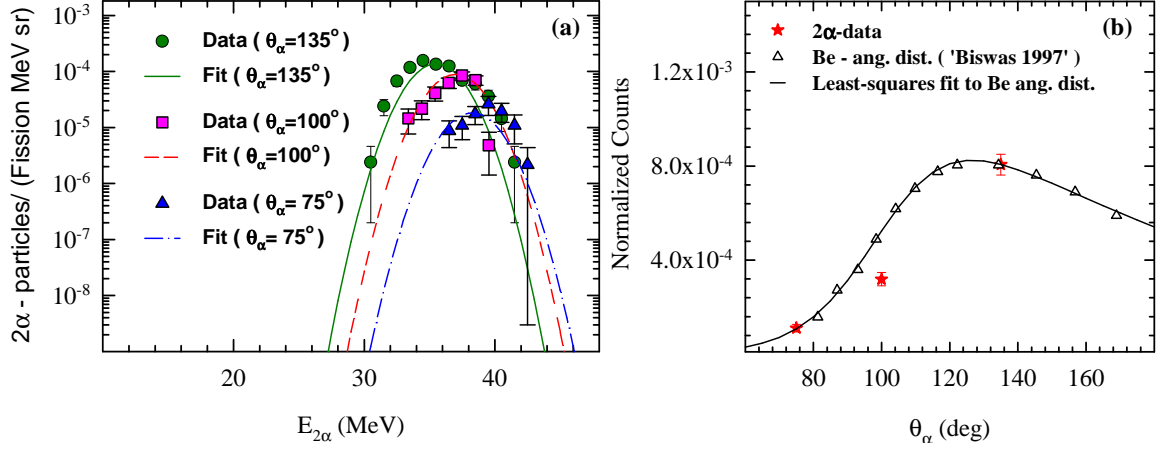
Figure 5.16: (a) The 2α-particle multiplicity spectra produced from ^{8}Be breakup at three laboratory angles (θ_α), where different lines are the moving-source fits. (b) The energy-integrated 2α-particle yield as a function of θ_α (star) and (b) the experimental data (triangle from Ref. [5]) and least-squares fit (solid line) of the Be angular distribution after normalizing with the 2α-particle yield at $\theta_\alpha = 135°$ (see text).

the present work is consistent with that for Be as seen in Fig. 5.16(b), where the Be angular distribution (from Ref. [5]) is plotted after normalizing at $\theta_\alpha = 135°$.

These 2α-particle multiplicity spectra shown in Fig. 5.16(a), are fitted simultaneously with the moving-source calculation using the ^{8}Be breakup as a source of 2α-particle emission. For simplicity, the 2α particles are assumed to be moving together along the direction of ^{8}Be, so that the angular distribution of the 2α particles follows to that of ^{8}Be. The following expression for the energy and angular distributions of the 2α particles is used in the rest frame;

$$n(\epsilon^{2\alpha}, \theta') \sim \alpha_{\text{br}}^{2\alpha} W_{\text{c.m.}}(\theta) \exp\left[\frac{-(\epsilon^{2\alpha} - \epsilon_{\text{br}}^{2\alpha})^2}{2\sigma_{\text{br}}^{2\alpha^2}}\right], \tag{5.2}$$

where $\epsilon^{2\alpha}$, $\alpha_{\text{br}}^{2\alpha}$, $\epsilon_{\text{br}}^{2\alpha}$, and $\sigma_{\text{br}}^{2\alpha}$ are the 2α-particle summed energy, multiplicity, summed peak energy, and standard deviation of the summed energy distribution, respectively, in the rest frame. $W_{\text{c.m.}}(\theta')$ is the angular distribution of ^{8}Be in the rest frame which is calculated using the relation, $W_{\text{c.m.}}(\theta') = G(x, \theta_L)W_L(\theta_L)$, where $G(x, \theta_L)$ is the Jacobian and x is the ratio of velocities of the compound nucleus to that of ^{8}Be in the center-of-mass frame. $W_L(\theta_L)$ is the angular distribution of ^{8}Be in the laboratory frame

at an angle of θ_L with respect to the beam direction. In the moving-source analysis, $W_L(\theta_L)$ is obtained by using the parameters from least-squares fitting of experimental angular distribution of Be with following functional form;

$$W(\theta_L) = \frac{\exp\left(-P1/\theta_L\right)}{1 + \exp\left[\frac{P2-\theta_L}{P3}\right]}, \tag{5.3}$$

where, $P1$, $P2$, and $P3$ are the constants. The least-squares fitted angular distribution of Be is shown in Fig. 5.16(b). The 2α-particle spectra calculated in the rest frame are converted to the laboratory frame using the appropriate Jacobian to fit the measured spectra. The fitted spectra at different laboratory angles are shown in Fig. 5.16(a). The best-fit values of the parameters are found to be $\alpha_{\mathrm{br}}^{2\alpha} = (2.6 \pm 0.3) \times 10^{-4}$, $\epsilon_{\mathrm{br}}^{2\alpha} = 37.6 \pm 0.2$ MeV, and $(\sigma_{\mathrm{br}}^{2\alpha}) = 1.6 \pm 0.2$ MeV, corresponding to a minimum $\chi^2/$(degree of freedom) value of 4.1. The value of $\epsilon_{\mathrm{br}}^{2\alpha}$ extracted from the analysis is close to the calculated center-of-mass kinetic energy of ^{8}Be from kinematics including optimum Q-value (Q_{opt}) [5].

5.4.3 Reanalysis of α-particle multiplicity spectra, including transfer-breakup source

With the above values for the ^{8}Be breakup process, we carried out a reanalysis of the α-particle multiplicity spectra including five sources in the moving-source model: the compound nucleus, both fission fragments, the NSE, and the ^{8}Be breakup. When only one of the two α particles produced from the ^{8}Be breakup enters the CsI detector, its kinetic energy, E_α overlaps with that of α particles produced from pre-, post-, and near-scission emission. For simplicity in the moving-source fit, E_{rel} is neglected so that at a given θ_α, $E_\alpha = \frac{1}{2}E_{\mathrm{Be}}$. The energy and angular distributions of one of the two breakup α particles are calculated in the rest frame of the compound nucleus by using the corresponding expression of Eq. (5.2). In the moving-source fit, except for the parameters T_{pre}, T_{post}, V_B^{pre}, and V_B^{post}, which are set to old values, all other parameters are kept as free parameters. The fitted spectra for the individual source and after
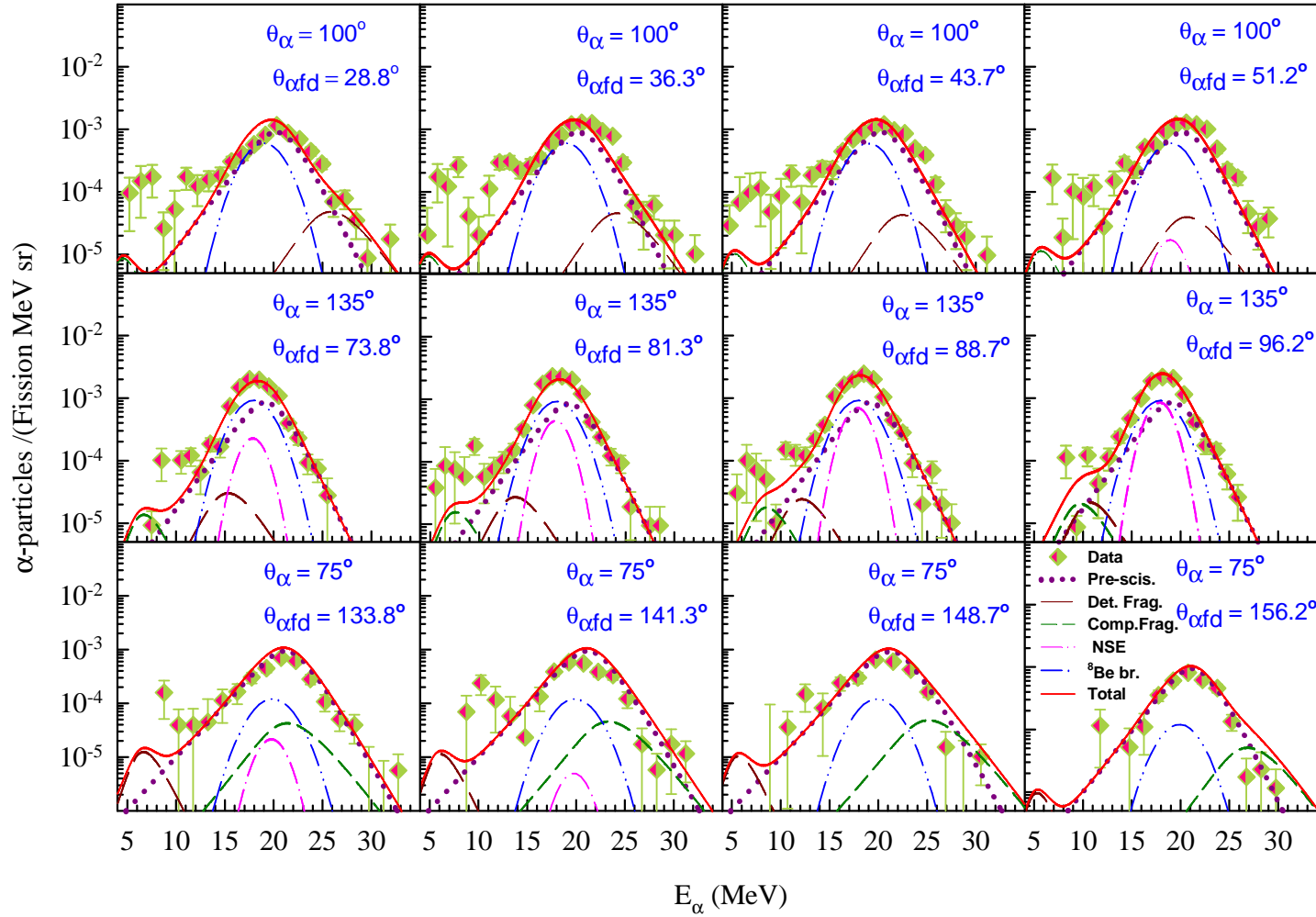
Figure 5.17: The α-particle multiplicity spectra in ^{12}C + ^{232}Th reaction along with fits of moving-source model for different combination of laboratory angles of CsI(Tl) detectors with respect to the beam direction, θ_α and detected fission fragments, $\theta_{\alpha fd}$. The dotted, long-dashed, short-dashed, dash-dot, and dash-dot-dot curves are contributions from compound nucleus, detected fission fragment, complementary fission fragment, near-scission emission, and ^{8}Be breakup, respectively. The solid curve indicates the total contribution from all five sources.

summing are shown in Fig. 5.17. The best-fit values of the parameters are now obtained as $\alpha_{\rm pre} = (5.4 \pm 0.2) \times 10^{-3}$, $\alpha_{\rm post} = (0.13 \pm 0.04) \times 10^{-3}$, $\alpha_{\rm nse} = (0.88 \pm 0.20) \times 10^{-3}$, $\epsilon_p = 19.25 \pm 0.10$ MeV, $\sigma_\epsilon = 1.34 \pm 0.20$ MeV, $\sigma_\theta = 13.5° \pm 3.0°$, $\alpha_{\rm br} = (2.1 \pm 0.1) \times 10^{-3}$, $\epsilon_{\rm br} = 19.4 \pm 0.2$ MeV, and $\sigma_{\rm br} = 1.95 \pm 0.20$ MeV, corresponding to a minimum $\chi^2/$(degree of freedom) value of 3.8. The errors quoted in the extracted parameters include only statistical uncertainties. Thus, by including ^{8}Be as a source in the moving-source analysis, only the value of $\alpha_{\rm nse}$ has changed significantly, whereas other values are nearly unchanged from the earlier four-source analysis. The fraction of NSE multiplicity ($\alpha_{\rm nse}$) to total prescission α-particle multiplicity ($\alpha_{\rm pre} + \alpha_{\rm nse}$) is reduced from $(36.4 \pm 3.2)\%$ to $(14.0 \pm 3.8)\%$ and follows the heavy-ion systematics [139]. The peak energy ($\epsilon_{\rm br}$) extracted from the analysis is also nearly one-half of the value of $\epsilon_{\rm br}^{2\alpha}$.

5.4.4 Monte Carlo calculation of the 2α-yield

It is to be noted here that the fraction of 2α-events is observed to be $\sim$12% of single α-particle events generated from ^{8}Be breakup in coincidence with fission fragments. A Monte Carlo calculation is carried out for the present experimental geometry, where 10^5 ^{8}Be nuclei are distributed in the reaction plane according to the measured angular distribution of Be (from Ref. [5]) and a $\pm 3.5°$ azimuthal random spread is allowed. It is seen that for ^{8}Be center-of-mass kinetic energy $E_{\rm Be}^{c.m.} = 38$ MeV and $E_{\rm rel} = 92$ keV, the fraction of 2α-events is 27.2% of single α-particle events. A larger calculated fraction of 2α-events in comparison to the measured value indicates the involvement of higher values of $E_{\rm rel}$ in the reaction, as pointed out earlier also in related works [213, 214]. In those works, it is shown that the $E_{\rm rel}$ spectra have peaks at 92 keV with about half of all the ^{8}Be breakup yield, and a broad continuum in the higher $E_{\rm rel}$ region with the remainder of the breakup yield. The sharp increase of folding angle with $E_{\rm rel}$ as mentioned earlier would result in lowering of the measured fraction of 2α-events if higher values of $E_{\rm rel}$ are involved in the reaction.

Chapter 6

Summary, conclusions and future outlook

The statistical and dynamical aspects of the excited nuclei in the two dimensional space of excitation energy (E_X) and angular momentum (J) play a key role in understanding a wide range of nuclear phenomena. The heavy-ion collisions bring in high E_X and J values to the system and enable to study the excited nuclei of a variety of choices in a wide range of E_X and J by varying the Z and A of the projectile and target nuclei. In particular, the fusion reaction leads to compound nucleus formation where complete amalgamation of projectile and target takes place. In the first part of the present thesis, the statistical aspects in the decay of medium heavy compound nuclei $(Z \sim 50$ - $70)$, in particular the spin dependence of the nuclear level-density has been investigated. The second part of the thesis addresses the dynamical aspects involved in the nuclear fission decay. Summary, conclusions, and future outlook for the present thesis work are discussed in the following sections.

6.1   Summary and conclusions

With the motivation of investigating the spin dependence of the nuclear level-density parameter 'a', a series of experiments have been performed where we have measured the γ-ray-multiplicity-fold gated α-particle energy spectra in heavy-ion fusion reactions

which populate residual nuclei in the shell-closure region of $Z \sim 50$ and mid-shell region of $Z \sim 70$ at an excitation energy range of 30 to 40 MeV. The target-projectile systems selected in the present work correspond to a range of entrance-channel mass-asymmetry, $\alpha = (A_T - A_P) / (A_T + A_P)$ spanning both sides of the Businaro-Gallone critical mass-asymmetry (α_{BG}). The results do not indicate any effect of α_{BG} on the level-density parameter in the compound nuclear reactions.

Despite placing the charged particle detectors at the back angles with respect to the beam direction, the light mass impurities (carbon and oxygen) that are present in the targets contribute to the low energy tails in the energy spectra for mainly two of the light projectiles (^{11}B and ^{12}C). The α particles originating from the reactions with impurity elements appeared in the spectra at low energies, particularly for the low multiplicity folds. This low energy component was treated as a background and was removed in the shell-closure region of $Z \sim 50$ by following a least squares fit procedure. In the mid-shell region of $Z \sim 70$ and $A \sim 180$, the background dominated for low γ-ray folds (up to fold 3). Therefore, in the mass region of $A \sim 180$, analysis has been carried out only for fold 4 and above events, where the background contribution was seen to be negligible.

Fold to multiplicity conversion procedure was validated by measuring spontaneous fission γ-ray multiplicity of ^{252}Cf. The average γ-ray multiplicities of ^{252}Cf for BGO energy thresholds of 100 keV and 150 keV were found to be $\sim$7.8 and 9.3, respectively, which are consistent with the earlier reported values [144–147, 186, 187]. The first two moments of the multiplicity distributions in the reactions for the shell-closure region of $Z \sim 50$ were also determined. By comparing the moments of multiplicity distribution with those of initial compound nucleus spin distributions, the factor a_m used for conversion of γ-ray multiplicity to the compound nuclear angular momentum was determined to be around 1.5. Later on, the insensitivity of the slope of the high energy part of α particle spectra with the factor a_m was confirmed. This ruled out any

possibility of uncertainty due to the factor a_m in the the inverse level-density parameter $K = A/a$ determined from the slope of the high energy part of α particle spectra. In the analysis, each γ-ray multiplicity fold was converted to a corresponding average angular momentum in the residual nuclei following a procedure that utilizes the decay simulations and detector efficiency factors. The uncertainty of the assigned average angular momentum varied from ± 5 to $\pm 3\hbar$ in going from low folds to high folds.

The aim in the present work was to compare the shape of the fold-gated as well as gross (summed over all J) experimental α-particle spectra at well above the evaporation barrier energy with corresponding spectra from statistical model calculations using the code PACE2 and derive the inverse level density parameter K. By limiting the analysis of the energy spectra at well above the evaporation barrier, the uncertainties associated with the barrier transmission coefficients were avoided. Within the code PACE2 , the phenomenological back-shifted Fermi-gas description of the nuclear level density was used. Ignatyuk's prescription for level-density parameter 'a' [41] was employed which takes into account the excitation energy dependent shell effects. The asymptotic value of the parameter 'a' was externally varied in the code through the input card. The normalization of the shape of the experimental spectra with that of the predicted one by statistical model calculation, was done by matching the area under the predicted spectra in the selected energy interval with that of the experimental spectra in the same energy interval. No attempts were made to fit the multiplicity of α particles.

In the shell closure region of $Z = 50$, the 'gross' K value (summed over all J) was seen to be in the range 9.0 - 10.5 MeV, which is within liquid drop model estimate [137]. It was observed that the 'gross' K value is the lowest for $Z_R = 50$, in contrast with what one would expect from known behavior of shell effects, by assuming persistence of shell effects even at this excitation energy. Maximum value of 'gross' K was observed for $Z_R = 52$ and 53. We have no microscopic understanding of these observations but would like to point out that similar differences in level-density parameter in neighboring

nuclei have been observed earlier [193] at excitation energy around 60 to 90 MeV . The variation of K as a function of angular momentum in the range of 5 to $30\hbar$ for the shell-closure region showed several interesting features not accounted by the shell and angular momentum corrected values of K used in PACE2 calculations [137]. The overall trend in the shell-closure region did not suggest a constant value for K over the full angular momentum range. Below about 15 $\hbar$ of angular momentum, the K values were similar to the corresponding 'gross' K values for all the systems. For $Z_R = 49$, 50 and 51, a flat behavior for low angular momentum and then a downward trend for higher J values was observed. Once the shell closure $Z_R = 50$ was crossed, for $Z_R = 52$ and 53 a dramatic change in the trend could be observed. In a repeat measurement we have re-confirmed the behavior for the $Z_R = 52$ system where there is a strong increase in K with angular momentum. This trend continued for $Z_R = 53$ as well, but in a diminished manner. For $Z_R = 55$ and 48, the trend was also similar but with a much weaker increase of K with angular momentum. In contrast to the shell closure region of $Z = 50$, in the mid-shell region of $Z \sim 70$ the average value of K is 8.2 ± 1.1 MeV [138], and remains essentially constant around the average value in the angular momentum range of 15 to $30\hbar$ [138]. It is seen that the gross value of K for the mid-shell region of $Z \sim 70$ and $A \sim 180$ is lower than that for the shell-closure region of $Z \sim 50$ and $A \sim 120$.

The present results are first of its kind for nuclei in the shell-closure region and in the mid-shell region, which point out certain effects not accounted for in the phenomenological prescriptions of NLD. These results would serve as important inputs for microscopic theories to understand the statistical properties of nuclei in different mass regions.

In case of heavy compound nuclear systems ($Z \gtrsim 80$ and $A \gtrsim 200$) populated in heavy-ion reactions, fission competes with particle emission and the dynamical effects become important along with the statistical ones. The dynamical effects during the

nuclear fission manifest in terms of the nuclear viscosity which lead to the energy dissipation from collective motion to the internal degrees of freedom. Despite substantial efforts, both experimentally and theoretically, the precise nature and magnitude of nuclear viscosity remains one of the major problems as yet unsolved in nuclear physics. The FFs kinetic energies, prescission yields of neutrons, charged particles [96–98], GDR γ rays [99] from the compound system before fission have been used as probes to gain insight about the the precise nature and magnitude of nuclear viscosity.

Employing above probes the effect of nuclear viscosity inside and out side the saddle has been understood to a good extent. However, at the time of scission, the actual snapping up of the neck joining the two nascent fission fragments is still not clearly understood. Moreover, the probes mentioned above are not suitable in a wide energy regime from spontaneous fission to the heavy-ion fission. A suitable probe sensitive to scission point needs to be employed to address the above questions. Ternary fission (or near scission emission) presents a good choice for studying the nuclear viscosity in the wide energy regime. Using the NSE as a probe, the scission point characteristics such as the kinetic energy of the FFs, neck radius, FF separation, etc. can be determined. The kinetic energy at scission point carries important information about the transition from saddle to scission and energy dissipation during this transition. Thus, the NSE can provide the information about the nuclear viscosity not only during the scission process but also during the descent from saddle to scission.

With these motivations, measurements were carried out for α-particle energy spectra in coincidence with fission fragments for the systems of ^{11}B (62 MeV) + ^{232}Th (Z^2/A = 37.14) and ^{12}C (69 MeV) + ^{232}Th (Z^2/A = 37.77) in a wide range of relative angles with respect to FF emission direction. These measurements have been described in the second part of the present thesis. The measured energy spectra were fitted with moving source model calculations to extract the α-particle multiplicities corresponding to different emission stages of the fusion-fission process. The results in ^{11}B+ ^{232}Th reaction

have been analyzed along with data from literature over a wide range of excitation energy (E_{CN}) and fissility (x) of the compound system to develop the systematic features of prefission and near-scission emission as a function of α-particle emission Q-value and Z^2/A of the compound system.

The fraction of near-scission multiplicity (α_{nse}) is observed to be nearly same at around 10% of the total prescission multiplicity ($\alpha_{pre} + \alpha_{nse}$) for various systems over a wide range of Z^2/A and excitation energy suggesting that the near scission emission of α-particles is a statistical process in heavy-ion induced fission reactions [139]. It is seen that prescission α-particle multiplicity (α_{pre}) normalized to $E_{CN}^{2.3}$ shows a systematic linearly increasing trend with α-particle emission Q-value [139, 141]. The above observations indicate that the α-particle emission from the neck is a statistical decay process at higher excitation energies, in contrast to low energy and spontaneous fission where the neck-emission is a dynamical or fast process. Therefore, it can be inferred that nuclear collective motion during scission exhibits a change over from super-fluid to viscous nature with increasing excitation energy. Existence of superfluidity within the nuclear medium has been a longstanding puzzle.

In case of ^{12}C (69 MeV) + ^{232}Th reaction, the near-scission multiplicity is observed to be anomalously enhanced in comparison to the heavy-ion systematics, indicating the presence of another source of α-particle emission in the ^{12}C + ^{232}Th reaction in addition to pre-, post-, and near-scission emission stages [140]. In the two-dimensional particle identification plot, a high energy component corresponding to the summed energy of two α particles is observed. The observation of these 2α-events suggests that due to the α-cluster structure of ^{12}C, there is a significant component of ^{8}Be breakup followed by α-transfer induced fission events. Since the α-transfer grazing angle for ^{12}C (69 MeV) + ^{232}Th system is at $\sim$120° [5], the intensity of these 2α-events dominates at the backward angles with respect to the beam direction. The analysis of ^{8}Be breakup explains very well the 2α-particle multiplicity spectra at different laboratory angles.

For the first time, a new component corresponding to transfer-breakup process has been considered in the moving source model to disentangle the different contributions to the inclusive α-particle multiplicity. Reanalysis of the α-particle multiplicity spectra including five sources in the moving source model: the compound nucleus, both the fission fragments, the NSE, and ^{8}Be breakup was carried out. The results obtained for pre- and near-scission multiplicities follow the recently developed heavy-ion systematics very well. The present results clearly indicate an extra source of α-particle emission in heavy-ion fusion-fission reactions due to α-clustering in projectile nuclei [140].

The CsI(Tl)-Si(PIN) detectors, used for charged particle measurements in the second part of the thesis work, were characterized on various aspects [142]. Pulse height response of the detectors was investigated for fission fragments (FFs) produced in spontaneous fission of ^{252}Cf. The scintillation light yield is observed to increase linearly as a function of energy for both the light and heavy FFs. At a given energy the light yield for heavier fragments is observed to be more than that of lighter ones. This indicates that the scintillation light yield for fission fragments follow the similar dependence on $\mathrm{d}E/\mathrm{d}x$ as of light charged particles and heavy-ions. The time resolution of the CsI(Tl)-Si(PIN) has been determined to be 134 ± 3 ns using γ-γ coincidence method.

6.2   Future outlook

In the first part of the thesis, we obtained quite interesting results on spin dependence of the inverse level-density parameter K in the shell-closure region of $Z \sim 50$ and mid-shell region of $Z \sim 70$ in the excitation energy range of 30 to 40 MeV. In order to understand the anomalous results of the shell-closure region of $Z \sim 50$, further refined measurements and at the same time microscopic calculations are worth to attempt.

☐   In the present work, the parameter K is determined for the residual nuclei after α-particle emission. As pointed out earlier, α-particle emission leaves residual

nuclei with $Z_R = Z_{CN} - 2$. Although, a major fraction of the α particles is emitted as a first chance emission, still some uncertainty remains in the mass of the residual nucleus. If coincidence measurements of α-particles and γ rays are performed with the tagging of the evaporation residues (ERs) of well defined mass and charge, issues related to the background and mass of the residual nucleus for which the parameter K is determined, will be better resolved.

☐ In the present study, the parameter K is determined by selecting one exit channel of the compound nuclear decay, the α-particle emission. It is worth to investigate spin dependence of the parameter K through other exit channels such as the proton and neutron emission.

☐ In the present study different final nuclei are produced using quite different reactions (in particular with different mass asymmetries). Though, the analysis of the reactions based on Businaro-Gallone critical mass-asymmetry reveals that all these reactions undergo normal compound nuclear formation without a dinuclear complex formation. The BG analysis only serves as a guideline and is not a substitute to rule out the possible entrance channel effects. It would be helpful for the understanding if one and the same compound nucleus had been produced using different reactions (with different mass asymmetries), or if all compound nuclei had been produced by reactions with similar projectiles (and similar mass asymmetry), or best of all above to disentangle two effects, namely possible entrance-channel (reaction) effects on the α-particle spectra and structure (level-density) effects.

☐ Due to limited efficiency of γ-ray detection and the uncertainty of angular momentum carried by individual γ-ray, it was not possible to convert γ-ray fold to spin value on event-by-event basis. Each γ-ray fold corresponds to a window of the angular momentum populated in the residual nuclei. It would be helpful to carry out these measurements with a larger γ-array with higher detection

efficiency to reduce the width of the assigned spin values to different γ-ray folds.

☐   If we closely examine the trends of the parameter K with the spin in those cases of the shell-closure region of $Z \sim 50$ where strong variations are observed, it seems that K increases with spin up to a certain spin value and then drops down. It would be interesting to investigate the parameter K in higher spin domains in the reactions for which the dropping region of the K was not feasible due to small value of the maximum angular momentum of the residual nuclei.

☐   From theoretical point of view, present study serves to provide important inputs for microscopic theories to understand the statistical properties of nuclei in different mass regions. It would be interesting to carry out calculations to reproduce the parameter K determined around the shell-closure and in the mid-shell regions. Recently, for the shell-closure region of $Z = 50$ of the present work, microscopic calculations were carried out [197] which show that the parameter K increases with angular momentum in all cases. These calculations are not fully consistent with the present measurements and detailed microscopic calculations will be useful to understand the dependence of K on angular momentum.

In the second part of the thesis, we have developed for the first time the systematics for pre- and near-scission emission α-particle multiplicities in heavy-ion fission. In case of ^{12}C (69 MeV) + ^{232}Th reaction, the near-scission multiplicity was observed to be anomalously enhanced in comparison to the heavy-ion systematics, which has been understood by incorporating ^{8}Be breakup followed by α-transfer induced fission events. Present study invites further measurements as well as theoretical calculations as discussed below;

☐   In case of near-scission systematics, since the available data are limited, it is desirable to measure the near-scission multiplicity for many other systems covering a wide range of fissility and excitation energy (E_X).

☐   In the low excitation energy region, though the E_X dependence is fairly weak, but at the same time it is also seen that the ternary yield in thermal or 1-MeV neutron induced fission (corresponding E_{CN} = 6 - 8 MeV) is less than in spontaneous fission of the same fissioning nucleus [122–124]. This behavior suggests that there might be a minimum in the α-particle yield if measured at various energies in the interval of 1 to 20 MeV. This expectation is consistent with our conclusions that with increasing E_X ternary α-particle emission is governed by the statistical process, as opposed to the spontaneous fission case in which α-particle emission takes place by dynamical process. This change over from dynamical emission to statistical process needs to be investigated in a systematic manner. Therefore, it is desirable to carry out measurement for the ternary yields in the energy interval of 1 to 20 MeV.

☐   The peak energy for NSE α particles (ϵ_p) in low energy fission is constant within 15 to 16 MeV whereas in heavy-ion induced fission it is scattered from 12.5 to 19.5 MeV for different systems [96, 97, 129–132]. For low energy fission, inverse trajectory calculations [114–117] have been carried out to reproduce the observed peak energies, where in the initial conditions of three charges (positions and momenta) were considered without paying any attention to the neck rupture process. The available data on peak energy in heavy-ion fission systems are quite scattered and seems to fall into two groups. It would be interesting to carry out inverse trajectory calculations incorporating the neck rupture process in heavy-ion fission to reproduce the peak energies.

☐   For ^{12}C (69 MeV) + ^{232}Th system, the α-transfer grazing angle is at ∼120° with respect to the beam direction which is close to perpendicular to the scission axis in the present experimental geometry, therefore, NSE α particles had a strong overlap with the ones produced from ^{8}Be breakup, enhancing the near scission multiplicity. It is worth to carry out these measurements at various beam

energies. With increasing beam energies of ^{12}C, the corresponding α-transfer grazing angle will shift at forward angles with respect to the beam direction. Moreover, it would be of further interest to carry out the measurements using ^{13}C projectile where α-transfer will result in ^{9}Be having high threshold for breakup.

References

[1] J. Toke and W. U. Schroder, Ann. Rev. Nucl. Science **42**, 401 (1992).

[2] G. R. Satchler, M. A. Nagarajan, J. S. Lilley, and I. J. Thompson, Anns. Phys. **178**, 110 (1987).

[3] J. de Boer, G. Dannhäuser, H. Massmann, F. Roesel, and A. Winther, J. Phys. **G 3**, 889 (1977).

[4] R. Bass, *Nuclear Reactions with heavy ions* (Frankfurt, Germany, 1980).

[5] D. C. Biswas, R. K. Choudhury, B. K. Nayak, D. M. Nadkarni, and V. S. Ramamurthy, Phys. Rev. **C 56**, 1926 (1997).

[6] W. U. Schroder and J. R. Huizenga, Annu. Rev. Nucl. Sci. **27**, 465 (1977).

[7] D. Bodansky, Ann. Rev. Nucl. Sci. **12**, 79 (1962).

[8] N. Bohr, Nature **137**, 344 (1936).

[9] M. Beckerman, Rep. Prog. Phys. **51**, 1047 (1988).

[10] R. G. Stokstad, Y. Eisen, S. Kaplanis, D. Pelte, U. Smilansky, , and I. Tserruya, Phys. Rev. Lett. **41**, 465 (1978).

[11] J. X. Wei, J. R. Leigh, D. J. Hinde, J. O. Newton, R. C. Lemmon, S. Elfstrom, and J. X. Chen, Phys. Rev. Lett. **67**, 3368 (1991).

[12] C. R. Morton, M. Dasgupta, D. J. Hinde, J. R. Leigh, R. C. Lemmon, J. P. Lestone, J. C. Mein, J. O. Newton, and H. Timmers, Phys. Rev. Lett. **72**, 4074 (1994).

[13] C. H. Dasso, S. Landowne, and A. Winther, Nucl. Phys. **A405**, 381 (1983).

[14] C. H. Dasso, S. Landowne, and A. Winther, Nucl. Phys. **A407**, 221 (1983).

[15] R. A. Broglia, C. H. Dasso, S. Landowne, and G. Pollarolo, Phys. Lett. **B 133**, 34 (1983).

[16] C. H. Dasso and S. Landowne, Comput. Phys. Commun. **46**, 187 (1987).

[17] J. Fernandez-Niello, C. H. Dasso, and S. Landowne, Comput. Phys. Commun. **54**, 409 (1989).

[18] K. Hagino, N. Rowley, and A. T. Kruppa, Comput. Phys. Commun. **123**, 143 (1999).

[19] S. E. Vigdor, H. J. Karwowski, W. W. Jacobs, S. Kailas, P. P. Singh, F. Soga, and T. G. Throwe, Phys. Rev. **C 26**, 1035 (1982).

[20] J. Blatt and V. F. Weisskopf, *Theoretical Nuclear Physic* (John Wiley & Sons, Inc., New York, 1952).

[21] T. Ericson, Adv. Phys. **9**, 425 (1960).

[22] R. Stokstad, *Treatise on heavy-ion science, edited by D. A. Bromley*, vol. 3 (Plenum, New York, 1985).

[23] J. R. Huizenga and L. G. Moretto, Annu. Rev. Nucl. Sci. **22**, 427 (1972).

[24] H. Feshbach, *Nuclear Spectroscopy, Part B* (F. Ajzenberg-Selove, Ed. Academic Press, New York,, 1960).

[25] S. Okuducu, N. N. Akti, S. Akbas, and M. O. Kansu, Science and Technology of Nuclear Installations (2012), http://dx.doi.org/10.1155/2012/915496.

[26] T. Rauscher, F. K. Thielemann, and K. L. Kratz, Phys. Rev. **C 56**, 1613 (1997).

[27] S. Ayik and J. N. Ginocchio, Nucl. Phys. **A234**, 13 (1974).

[28] J. N. Ginocchio and M. M. Yen, Nucl. Phys. **A239**, 365 (1975).

[29] D. J. Morrissey, W. Benenson, and W. A. Friedman, Annu. Rev. Nucl. Sci. **44**, 27 (1994).

[30] H. A. Bethe, Rev. Mod. Phys. **9**, 69 (1937).

[31] V. F. Weisskopf, Phys. Rev. **52**, 295 (1937).

[32] H. A. Bethe, Phys. Rev. **50**, 332 (1936).

[33] A. Bohr and B. R. Mottelson, *Nuclear Structure*, vol. 1 (W. A. Benjamin, Inc., New York, 1969).

[34] A. Chbihi, L. G. Sobotka, N. G. Nicolis, D. G. Sarantites, D. W. Stracener, Z. Majka, D. C. Hensley, J. R. Beene, and M. L. Halbert, Phys. Rev. **C 43**, 666 (1991).

[35] H. Margenau, Phys. Rev. **59**, 627 (1941).

[36] C. Bloch, Phys. Rev. **93**, 1094 (1954).

[37] A. S. Iljinov, M. V. Mebel, N. Bianchi, E. D. Sanctis, C. Guaraldo, V. Lucherini, V. Muccifora, E. Polli, A. R. Reolon, and P. Rossi, Nucl. Phys. **A 543**, 517 (1992).

[38] International Atomic Energy Agency, *Handbook for nuclear calculations of nuclear reaction data:Reference Input Parameter Library, RIPL-2*, Vienna (2005), IAEA-Tecdoc-1506, URL http:/www-nds.iaea.org/RIPL-2/.

[39] L. G. Moretto and R. Stella, Phys. Lett. **B 32**, 558 (1970).

[40] M. Hillman and J. R. Grover, Phys. Rev. **185**, 1303 (1969).

[41] A. V. Ignatyuk, G. N. Smirenkin, and A. S. Tishin, Sov. J. Phys. **21**, 255 (1975).

[42] S. K. Kataria, V. S. Ramamurthy, and S. S. Kapoor, Phys. Rev. **C 18**, 549 (1978).

[43] M. Maruyama, Nucl. Phys. **A 131**, 145 (1969).

[44] A. A. Ross, Phys. Rev. **108**, 720 (1957).

[45] F. C. Williams, Jr., G. Chan, and J. R. Huizenga, Nucl. Phys. **A 187**, 225 (1972).

[46] H. Nakamura and T. Fukahori, Phys. Rev. **C 72**, 064329 (2005).

[47] A. Gilbert and A. G. W. Cameron, Can. J. Phys. **43**, 1446 (1965).

[48] S. Komarov, R. J. Charity, C. J. Chiara, W. Reviol, D. G. Sarantites, L. G. Sobotka, A. L. Caraley, M. P. Carpenter, and D. Seweryniak, Phys. Rev. **C 75**, 064611 (2007).

[49] S. M. Grimes, Phys. Rev. **C 78**, 057601 (2008).

[50] D. R. Chakrabarty, S. K. Rathi, V. M. Datar, S. Kumar, E. T. Mirgule, A. Mitra, and H. H. Oza, Nucl. Phys. **A712**, 23 (2002).

[51] J. R. Grover, Phys. Rev. **157**, 832 (1967).

[52] H. K. Vonach, R. Vandenbosch, and J. R. Huizenga, Nucl. Phys. **60**, 70 (1964).

[53] A. V. Ignatyuk, V. S. Stavinskii, and Y. H. Shubin, Sov. J. Phys. **11**, 563 (1970).

[54] L. G. Moretto, Nucl. Phys. **A 185**, 145 (1972).

[55] S. Hilaire, J. P. Delaroche, and A. J. Koning, Nucl. Phys. **A 632**, 417 (1998).

[56] N. Cerf, Phys. Rev. **C 50**, 836 (1994).

[57] B. K. Agrawal and A. Ansari, Phys. Lett. **B 339**, 7 (1994).

[58] B. K. Agrawal and A. Ansari, Nucl. Phys. **A 640**, 362 (1998).

[59] Y. Alhassid, G. F. Bertsch, L. Fang, and S. Liu, Phys. Rev. **C 72**, 064326 (2005).

[60] M. Gholami, M. Kildir, and A. N. Behkami, Phys. Rev. **C 75**, 044308 (2007).

[61] K. Kaneko and A. Schiller, Phys. Rev. **C 75**, 044304 (2007).

[62] T. D. Newton, Can. J. Phys. **34**, 804 (1956).

[63] A. G. W. Cameron, Can. J. Phys. **36,**, 1040 (1958).

[64] P. Wilhjelm, G. A. Keyworth, J. C. Browne, W. P. Beres, H. W. N. M. Divadeenam, and E. G. Bilpuch, Phys. Rev. **177**, 1553 (1969).

[65] J. C. Browne, H. W. Newson, E. G. Bilpuch, and G. E. Mitchell, Nucl. Phys. **A 153**, 481 (1970).

[66] A. A. Katsanos, J. R. Huizenga, and H. K. Vonach, Phys. Rev. **141**, 1053 (1966).

[67] G. Brown, A. E. Macgregor, and R. Middleton, Nucl. Phys. **77**, 385 (1966).

[68] T. Ericson and T. Mayer-Kuckuk, Annu. Rev. Nucl. Sci. **16**, 183 (1966).

[69] A. Mitra, D. R. Chakrabarty, V. M. Datar, S. Kumar, E. T. Mirgule, and H. H. Oza, Nucl. Phys. **A 707**, 343 (2002).

[70] A. Mitra, D. R. Chakrabarty, V. M. Datar, S. Kumar, E. T. Mirgule, H. H. Oza, V. Nanal, and R. G. Pillay, Nucl. Phys. **A 765**, 277 (2006).

[71] B. John, S. K. Kataria, B. S. Tomar, A. Goswami, G. K. Gubbi, and S. B. Manohar, Phys. Rev. **C 56**, 2582 (1997).

[72] B. John, R. K. Choudhury, B. K. Nayak, A. Saxena, and D. C. Biswas, Phys. Rev. **C 63**, 054301 (2001).

[73] D. Fabris and et al., Phys. Rev. **C 50**, R 1261 (1994).

[74] P. Hille, P. Sperr, M. Hille, K. Rudolph, W. Assmann, and D. Evers, Nucl. Phys. **A 232**, 157 (1974).

[75] C. C. Lu, L. C. Vaz, and J. R. Huizenga, Nucl. Phys. **A 197**, 321 (1972).

[76] A. J. Sierk, Phys. Rev. **C 33**, 2039 (1986).

[77] S. Henss, A. Ruckelshausen, R. D. Fischer, W. Kuhn, V. Metag, R. Novotny, R. V. F. Janssens, T.L.Khoo, D. Habs, D. Schwalm, et al., Phys. Rev. Lett. **60**, 11 (1988).

[78] R. Vandenbosch and J. R. Huizenga, *Nuclear Fission* (Academic, New York, 1973).

[79] D. C. Hoffman and M. M. Hoffman, Ann. Rev. Nucl. Science **24**, 151 (1974).

[80] O. Hahn and F. Strassmann, Naturwissenschaften **27**, 11 (1939).

[81] P. Armbruster, Annu. Rev. Nucl. Sci. **50**, 411 (2000).

[82] N. Bohr and J. A. Wheeler, Phys. Rev. **56**, 426 (1939).

[83] S. Cohen and W. J. Swiatecki, Anns. Phys. **22**, 406 (1963).

[84] J. R. Nix, Nucl. Phys. **A 130**, 241 (1969).

[85] P. Möller, D. G. Madland, A. J. Sierk, and A. Iwamoto, Nature **409**, 785 (2001).

[86] P. Möller and A. J. Sierk, Nature **422**, 485 (2003).

[87] V. M. Strutinsky, Nucl. Phys. **A 95**, 420 (1967).

[88] A. Saxena, A. Chatterjee, R. K. Choudhury, S. S. Kapoor, and D. M. Nadkarni, Phys. Rev. **C 49**, 932 (1994).

[89] J. R. Nix, Nucl. Phys. **A 502**, 609c (1989).

[90] D. Hilscher and H. Rossner, Anns. Phys. Fr. **17**, 471 (1992).

[91] H. A. Kramer, Physica **7**, 284 (1940).

[92] A. Bohr, B. R. Mottelson, and K. D. V. Selskab, Mat. Fys. Medd. **27**, 16 (1953).

[93] B. D. Wilkins, E. P. Steinberg, and R. R. Chasman, Phys. Rev. **C 14**, 1832 (1976).

[94] U. Brosa, S. Grossmann, A. Mull, and E. Becker, Nucl. Phys. **A502**, 423c (1989).

[95] D. J. Hinde, H. Ogata, M. Tanaka, T. Shimoda, N. Takahashi, A. Shinohara, S. Wakamatsu, K. Katori, and H. Okamura, Phys. Rev. **C 39**, 2268 (1989).

[96] K. Ramachandran, A. Chatterjee, A. Navin, K. Mahata, A. Shrivastava, V. Tripathi, S. Kailas, V.Nanal, R.G.Pillay, A. Saxena, et al., Phys. Rev. **C 73**, 064609 (2006).

[97] J. P. Lestone, J. R. Leigh, J. O. Newton, D. J. Hinde, J. X. Wei, J. X. Chen, S. Elfstrom, and M. Z. Pfabe, Nucl. Phys. **A 559**, 277 (1993).

[98] H. Ikezoe, N. Shikazono, Y. Nagame, Y. Sugiyama, Y. Tomita, K. Ideno, I. Nishinaka, B. J. Qi, H. J. Kim, A. Iwamoto, et al., Phys. Rev. **C 46**, 1922 (1992).

[99] P. Paul, Annu. Rev. Nucl. Sci. **44**, 65 (1994).

[100] N. Bohr, F. Kalckar, and et al., Mat. Fys. Medd. **14**, 10 (1937).

[101] K. T. R. Davies, A. J. Sierk, and J. R. Nix, Phys. Rev. **C 13**, 2385 (1976).

[102] J. Blocki, Y. Boneh, J. R. Nix, J. Randrup, M. Robel, A. J. Sierk, and W. J. Swiatecki, Anns. Phys. Fr. **113**, 330 (1978).

[103] A. J. Sierk and J. R. Nix, Phys. Rev. **C 21**, 982 (1980).

[104] N. Auerbach and S. Shlomo, Phys. Rev. Lett. **103**, 172501 (2009).

[105] V. E. Viola, K. Kwiatkowski, and M. Walker, Phys. Rev. **C 31**, 1550 (1985).

[106] A. Gavron, A. Gayer, J. Boissevain, H. C. Britt, J. R. Nix, A. J. Sierk, P. Grange, S. Hassani, H. A. Weidenmuller, J. R. Beene, et al., Phys. Lett. **B 176**, 312 (1986).

[107] D. J. Hinde, R. J. Charity, G. S. Foote, J. R. Leigh, J. O. Newton, S. Ogaza, and A. Chatterjee, Nucl. Phys. **A 452**, 550 (1986).

[108] W. P. Zank, D. Hilscher, G. Ingold, U. Jahnke, M. Lehmann, and H. Rossner, Phys. Rev. **C 33**, 519 (1986).

[109] J. P. Lestone, J. R. Leigh, J. O. Newton, D. J. Hinde, J. X. Wei, J. X. Chen, S. Elfstrom, and D. G. Popescu, Phys. Rev. Lett. **67**, 1078 (1991).

[110] J. P. Lestone, Phys. Rev. Lett. **70**, 2245 (1993).

[111] I. Halpern, Annu. Rev. Nucl. Sci. **21**, 245 (1971).

[112] A. K. Sinha, D. M. Nadkarni, and G. K. Mehta, Pramana J. Phys. **33**, 85 (1989).

[113] J. P. Lestone, Int. Jour. Mod. Phys. **E 17**, 323 (2008).

[114] Y. Boneh, Z. Fraenkel, and I. Nebenzahl, Phys. Rev. **156**, 1305 (1967).

[115] G. M. Raisbeck and T. D. Thomas, Phys. Rev. **172**, 1272 (1968).

[116] P. Fong, Phys. Rev. **C 16**, 251 (1977).

[117] R. K. Choudhury and V. S. Ramamurthy, Phys. Rev. **C 18**, 2213 (1978).

[118] R. K. choudhury, S. S. Kapoor, D. M. Nadakarni, P. N. R. Rao, and S. R. S. Murthy, Pramana J. Phys. **6**, 64 (1976).

[119] B. Krishnarajulu, G. K. Mehta, R. K. choudhury, D. M. Nadakarni, and S. S. Kapoor, Pramana J. Phys. **8**, 315 (1977).

[120] Z. Fraenkel, Phys. Rev. **156**, 1283 (1967).

[121] R. A. Atneosen, T. D. Thomas, and G. T. Garvey, Phys. Rev. **B 139**, 307 (1965).

[122] M. Rajagopalan and T. D. Thomas, Phys. Rev. **C 5**, 1402 (1972).

[123] T. D. Thomas and S. L. Whetstone, Phys. Rev. **144**, 1060 (1965).

[124] R. A. Noblest, Phys. Rev. **126**, 1508 (1962).

[125] I. Halpern, in *Proceedings of the IAEA Symp. Phys. Chem. Fission, Salzburg* (International Atomic Energy Agency, Vienna, 1965), vol. 2, p. 369.

[126] C. Wagemans, *The Nuclear Fission Process* (CRC Press, Boca Raton, 1991).

[127] J. P. Lestone, Phys. Rev. **C 70**, 021601 (R) (2004).

[128] M. R. Pahlavani and D. Naderi, Phys. Rev. **C 83**, 024602 (2011).

[129] B. Lindl, A. Brucker, M. Bantel, H. Ho, R. Muffler, L. Schad, M. G. Trauth, and J. P. Wurm, Z. Phys. A **328**, 85 (1987).

[130] M. Sowinski, M. Lewitowicz, R. Kupczak, A. Jankowski, N. K. Skobelev, and S. Chojnacki, Z. Phys. A **324**, 87 (1986).

[131] L. Schad, H. Ho, G.-Y. Fan, B. Lindl, A. Pfoh, R. Wolski, and J. P. Wurm, Z. Phys. A **318**, 179 (1984).

[132] K. Siwek-Wilczynska, J. Wilczynski, H. K. W. Leegte, R. H. Siemssen, H. W. Wilschut, K. Grotowski, A. Panasiewicz, Z. Sosin, and A. Wieloch, Phys. Rev. **C 48**, 228 (1993).

[133] W. W. Wilcke, J. P. Kosky, J. R. Birkelund, M. A. Butler, A. D. Dougan, J. R. Huizenga, W. U. Schroder, H. J. Wollersheim, and D. Hilscher, Phys. Rev. Lett. **51**, 99 (1983).

[134] R. Yanez, T. A. Bredeweg, E. Cornell, B. Davin, K. Kwiatkowski, V. E. Viola, R. T. de Souza, R. Lemmon, and R. Popescu, Phys. Rev. Lett. **82**, 3585 (1999).

[135] L. G. Moretto, D. Breus, L. Phair, and G. J. Wozniak, Phys. Rev. Lett. **85**, 2645 (2000).

[136] A. Gavron, Phys. Rev. **C 21**, 230 (1980).

[137] Y. K. Gupta, B. John, D. C. Biswas, B. K. Nayak, A. Saxena, and R. K. Choudhury, Phys. Rev. **C 78**, 054609 (2008).

[138] Y. K. Gupta, D. C. Biswas, B. John, B. K. Nayak, A. Saxena, and R. K. Choudhury, Phys. Rev. **C 80**, 054611 (2009).

[139] Y.K.Gupta, D. C. Biswas, R.K.Choudhury, A. Saxena, B. K. Nayak, B. John, K. Ramachandran, R. G. Thomas, L. S. Danu, B. N. Joshi, et al., Phys. Rev. **C 84**, 031603 (R) (2011).

[140] Y. K. Gupta, D. C. Biswas, B. John, B. K. Nayak, A. Chatterjee, and R. K. Choudhury, Phys. Rev. **C 86**, 014615 (2012).

[141] Y. K. Gupta, R. K. Choudhury, and A. Chatterjee, BARC News Letter **324 Jan.-Feb.**, 6 (2012).

[142] Y. K. Gupta, D. C. Biswas, P. Roy, B. K. Nayak, , R. G. Thomas, A.L.Inkar, R.P.Vind, B. John, A. Saxena, et al., Nucl. Instr. Meth. **A 629**, 149 (2011).

[143] J. P. Unik, J. E. Gindler, L. E. Glendenin, K. F. Flynn, A. Gorski, and R. K. Sjoblom, in *Proceedings of the Physics and Chemistry of Fission* (IAEA, Rochester, New York, 1973), vol. II, p. 19.

[144] D. C. Biswas, R. K. Choudhury, M. Cinausero, B. Fornal, D. V. Shetty, G. Viesti, D. Fabris, E. Fioretto, M. Lunardon, G. Nebbia, et al., Eur. Phys. J. **A 7**, 189 (2000).

[145] R. Verma, G. K. Mehta, R. K. Choudhury, S. S. Kapoor, B. K. Nayak, and V. S. Ramamurthy, Phys. Rev. **C 43**, 1850 (1991).

[146] B. K. Nayak, R. K. Choudhury, L. M. Pant, D. M. Nadkarni, and S. S. Kapoor, Phys. Rev. **C 52**, 3081 (1995).

[147] V. V. Verbinski, H. Weber, and R. E. Sund, Phys. Rev. **C 7**, 1173 (1973).

[148] *National Nuclear Data Center (NNDC)*, Brookhaven National Laboratory Upton, New York 11973-5000 (2012), URL `http://www.nndc.bnl.gov/`.

[149] S. S. Rattan, A. V. R. Reddy, V. S. Mallapurkar, R. J. Singh, S. Prakash, and M. V. Ramaniah, Phys. Rev. **C 27**, 327 (1983).

[150] G. F. Knoll, *Radiation Detection and Measurement* (John Wiley & Sons, Inc., New York, 1989), 3rd ed.

[151] W. R. Leo, *Techniques for Nuclear and Particle Physics Experiments* (Springer-Verlag Berlin Heidelberg, 1995), 2nd ed.

[152] M. N. Rao, D. C. Biswas, and R. K. Choudhury, Nucl. Instr. and Meth. **B 51**, 102 (1990).

[153] D. C. Biswas, M. N. Rao, and R. K. Choudhury, Nucl. Instr. and Meth. **B 53**, 251 (1991).

[154] R. K. Choudhury, S. S. Kapoor, D. M. Nadkarni, and P. N. R. Rao, Nucl. Instr. and Meth. **164**, 323 (1979).

[155] M. S. Sawant, R. P. Anand, R. K. Choudhury, D. M. Nadkarni, and S. S. Kapoor, Nucl. Instr. and Meth. **A 332**, 239 (1993).

[156] D. C. Biswas, V. S. Ambekar, L. M. Pant, B. V. Dinesh, and R. K. Choudhury, Nucl. Instr. Meth. **A 340**, 551 (1994).

[157] J. Pouthas and et al., Nucl. Instr. and Meth. **A 369**, 222 (1996).

[158] E. Norbeck and et al., Nucl. Instr. and Meth. **A 452**, 239 (2000).

[159] M. Alderighi and et al., Nucl. Instr. and Meth. **A 489**, 257 (2002).

[160] E. Fioretto and et al., Nucl. Instr. and Meth. **A 442**, 412 (2000).

[161] I. Valais and et al., Nucl. Instr. and Meth. **A 571**, 343 (2007).

[162] C. W. E. van Eijk, Phys. Med. Biol. **47**, R85 (2002).

[163] N. Colonna, G. J. Wozniak, A. Veeck, W. Skulski, G. W. Goth, L. Manduci, P. M. Milazzo, and P. F. Mastinu, Nucl. Instr. and Meth. **A 321**, 529 (1992).

[164] S. Aiello and et al., Nucl. Instr. and Meth. **A 369**, 50 (1996).

[165] C. J. W. Twenhofel and et al., Nucl. Instr. and Meth. **B 51**, 58 (1990).

[166] E. Valtonen, J. Peltonen, and J. J. Torsti, Nucl. Instr. and Meth. **A 286**, 169 (1990).

[167] P. Harihar, A. R. Knudson, W. J. Stapor, and A. B. Campbell, Nucl. Instr. and Meth. **A 283**, 62 (1989).

[168] J. Gal and *et. al.*, Nucl. Instr. and Meth. **A 366**, 120 (1995).

[169] R. B. Murray and A. Meyer, Phys. Rev. **122**, 815 (1961).

[170] A. Meyer and R. B. Murray, Phys. Rev. **128**, 98 (1962).

[171] B. John, A. Topkar, R. P. Vind, A. L. Inkar, D. C. Biswas, A. Saxena, Y. K. Gupta, and S. Kailas, Nucl. Instr. and Meth. **A 609**, 24 (2009).

[172] J. F. Ziegler, Nucl. Instr. and Meth. **B 219-220**, 1027 (2004).

[173] C. N. Fellas and W. B. Gilboy, IEEE Trans. Nucl. Sci. **NS-22**, 93 (1975).

[174] C. B. Fulmer, Phys. Rev. **108**, 1113 (1957).

[175] H. W. Schmitt and R. B. Leachman, Phys. Rev. **102**, 183 (1956).

[176] R. B. Leachman and H. W. Schmitt, Phys. Rev. **96**, 1366 (1954).

[177] J. Alarja and *et. al.*, Nucl. Instr. and Meth. **A 242**, 352 (1986).

[178] C. J. Crannell, R. J. Kurz, and W. Viehmann, Nucl. Instr. and Meth. **115**, 253 (1974).

[179] T. Nakamoto, Y. Fukazawa, T. Ohsugi, T. Kamae, , and J. Kataoka, Nucl. Instr. and Meth. **A 536**, 136 (2005).

[180] M. Laval, M. Moszynski, R. Allemand, E. Cormoreche, P. Guinet, R. Odru, and J. Vacher, Nucl. Instr. and Meth. **A 206**, 169 (1983).

[181] T. Bhattacharjee, S. K. Basu, C. C. Dey, and M. B. Chatterjee, Nucl. Instr. and Meth. **A 484**, 364 (2002).

[182] R. Farrell, F. Olschner, E. Frederick, L. Mcconchie, K. Vanderpuye, M. R. Squillante, and G. Entine, Nucl. Instr. and Meth. **A 288**, 137 (1990).

[183] M. Suffert, Nucl. Instr. and Meth. **A 322**, 523 (1992).

[184] A. Navin, M. Dasgupta, C. V. K. Baba, and A. Roy, in *Proceedings of DAE symopsium on Nuclear Physics* (1989), vol. B 32, p. 19.

[185] H. Ho and P. L. Gonthier, Nucl. Instr. and Meth. **190**, 75 (1981).

[186] V. S. Ramamurthy, R. K. Choudhury, and J. C. Mohankrishna, Pramana J. Phys. **8**, 322 (1977).

[187] K. Skarsvag, Phys. Rev. **C 22**, 638 (1980).

[188] S. Y. V. D. Werf, Nucl. Instr. and Meth. **153**, 221 (1978).

[189] R. Bass, Phys. Rev. Lett. **39**, 265 (1977).

[190] P. Moller, J. R. Nix, W. D. Myers, and W. J. Swiatecki, Atomic Data and Nuclear Data Tables **59**, 185 (1995).

[191] J. R. Huizenga and G. Igo, Nucl. Phys. **29**, 462 (1961).

[192] D. Cline and P. M. S. Lesser, Nucl. Instr. and Meth. **82**, 291 (1970).

[193] J. L. Wile, S. S. Datta, W. U. Schroder, J. Toke, D. Pade, S. P. Baldwin, J. R. Huizenga, B. M. Quendnau, R. T. deSouza, and B. M. Sazbo, Phys. Rev. **C 47**, 2135 (1993).

[194] M. Abe, KEK Report No. 86-26, KEK TH-128, 1986.

[195] J. F. Liang, J. D. Bierman, M. P. Kelly, A. A. Sonzogni, R. Vandenbosch, and J. P. S. van Schagen, Phys. Rev. Lett. **78**, 3074 (1997).

[196] I. M. Govil, R. Singh, A. Kumar, J. Kaur, A. K. Sinha, N. Madhavan, D. O. Kataria, P. Sugathan, S. K. Kataria, K. Kumar, et al., Phys. Rev. **C 57**, 1269 (1998).

[197] M. Aggarwal and S. Kailas, Phys. Rev. **C 81**, 047302 (2010).

[198] K. Banerjee, S. Bhattacharya, C. Bhattacharya, M. Gohil, S. Kundu, T. K. Rana, G. Mukherjee, R. Pandey, P. Roy, H. Pai, et al., Phys. Rev. **C 85**, 064310 (2012).

[199] J. P. Lestone, J. R. Leigh, J. O. Newton, and J. X. Wei, Nucl. Phys. **A 509**, 178 (1990).

[200] N. Majumdar, P. Bhattacharya, D. C. Biswas, R. K. Choudhury, D. M. Nadkarni, and A. Saxena, Phys. Rev. **C 51**, 3109 (1995).

[201] R. Raabe, C. Angulo, J. L. Charvet, C. Jouanne, L. Nalpas, P. Figuera, D. Pierroutsakou, M. Romoli, and J. L. Sida, Phys. Rev. **C 74**, 044606 (2006).

[202] R. P. Vind, A. L. Inkar, R. K. Choudhury, B. K. Nayak, A. Saxena, R. G. Thomas, D. C. Biswas, and B. V. John, Nucl. Instr. and Meth. **A 580**, 1435 (2007).

[203] A. Chatterjee, A. Navin, S. Kailas, P. Singh, D. C. Biswas, A. Karnik, and S. S. Kapoor, Phys. Rev. **C 52**, 3167 (1995).

[204] C. Y. Wong, Phys. Rev. Lett. **31**, 766 (1973).

[205] A. Fleury, F. H. Ruddy, M. N. Namboodiri, and J. M. Alexander, Phys. Rev. **C 7**, 1231 (1973).

[206] J. M. D'Auria, M. J. Fluss, L. Kowalski, and J. M. Miller, Phys. Rev. **168**, 1224 (1968).

[207] J. M. Alexander, D. Guerreau, and L. C. Vaz, Z. Phys. A **305**, 313 (1982).

[208] E. Holub, D. Hilscher, G. Ingold, U. Jahnke, H. Orf, and H. Rossner, Phys. Rev. **C 28**, 252 (1983).

[209] K. J. L. Couteur and D. W. Lang, Nucl. Phys. **13**, 32 (1959).

[210] J. Toke and W. J. Swiatecki, Nucl. Phys. **A 372**, 141 (1981).

[211] A. Saxena and et al., Nucl. Phys. **A 730**, 299 (2004).

[212] J. O. Newton, D. J. Hinde, R. J. Charity, J. R. Leigh, J. J. M. Bokhorst, A. Chatterjee, G. S. Foote, and S. Ogaza, Nucl. Phys. **A 483**, 126 (1988).

[213] R. Rafiei, R. du Rietz, D. H. Luong, D.J.Hinde, M. Dasgupta, M.Evers, and A. Diaz-Torres, Phys. Rev. **C 81**, 024601 (2010).

[214] D. H. Luong, M. Dasgupta, D.J.Hinde, R. du Rietz, R. Rafiei, C.J.Lin, A.Evers, and A. Diaz-Torres, Phys. Lett. **B 695**, 105 (2011).